Imperial College London

Department of Mechanical Engineering

Flow Control for Road Vehicle Drag Reduction

Faron Hesse
November 28, 2021

Submitted for the Degree of Doctor of Philosophy

"Ever tried, ever failed, no matter, try again,
fail again, fail better"

-Samuel Beckett

Declaration of Originality

I hereby declare that this dissertation is a result of my own work and research. Where information and arguments have been taken from published and unpublished sources, appropriate referencing has been done in the body of the text. These references are coupled to a list of sources provided at the end of the thesis.

Copyright Declaration

The copyright of this thesis rests with the author. Unless otherwise indicated, its contents are licensed under a Creative Commons Attribution-NonCommercial 4.0 International Licence (CC BY-NC). Under this licence, you may copy and redistribute the material in any medium or format. You may also create and distribute modified versions of the work. This is on the condition that: you credit the author and do not use it, or any derivative works, for a commercial purpose. When reusing or sharing this work, ensure you make the licence terms clear to others by naming the licence and linking to the licence text. Where a work has been adapted, you should indicate that the work has been changed and describe those changes. Please seek permission from the copyright holder for uses of this work that are not included in this licence or permitted under UK Copyright Law.

Abstract

This thesis covers topics that span bluff-body aerodynamics, hybrid RANS-LES CFD methods, flow control and model-order reduction. These topics arise from investigating the flow past three geometries: the bullet shaped D-body, the canonical squareback Ahmed body and the commerical Nissan NDP.

The study on the D-body was aimed at transitioning the research group from the restrictive block-structured formulated StreamLES solver to the more flexible OpenFOAM code that can use unstructured meshes. Linear feedback control for base pressure increase was applied as was done in the work by Dalla Longa *et al.* (2017). Identification of the plant, $G(s)$, that represents the wake's response to forcing was completed and correlated well with the results from Dalla Longa *et al.* (2017). The same can also be said of the sensitivity based designed feedback control law, $K(s)$. When applied in simulation, an attenuation of the base pressure fluctuations was, as desired, achieved, although the base pressure increased by 24.5% as opposed to the 38% achieved by Dalla Longa *et al.* (2017).

In the study on the squareback Ahmed body, wall-resolving (WRLES) and wall-modelled (WMLES) large eddy simulation were successfully applied. First, a simulation setup that is both able to resolve wake bimodality, while remaining reasonable in computational resource use, was created. Subsequently, variants of this setup were used to identify a flow feature that plays a critical role in forcing wake bimodality events. More specifically, a heavily under-resolved WMLES simulation in which both the near-wall and part of the outer-region of the turbulent boundary layer are Reynolds-averaged did not capture the front recirculation bubble near the Ahmed body nose; neither did it resolve a bimodal wake switching event. Meanwhile, the simulations with a more refined near-wall mesh did capture the front separation bubble as well as bimodal switching events of the wake. This front separation bubble sends out powerful hairpin vortices that interact with the rear wake. Specifically, these vortices go on to produce significant amounts of TKE, which, upon convection to the

rear of the Ahmed body, ultimately help trigger a bimodal event. The Ahmed body study also involved the application of linear feedback control for drag reduction as was done in the D-body study. In the short term, mean blowing did lead to a base pressure increase, but as the zero-net-mass-flux (ZNMF) jet settled, it oscillated around zero making its effects indiscernible.

The final geometry analyzed was the Nissan NDP. This was done by performing benchmark wall-resolving LES (WRLES). First, the benefit of appending a rear cavity to an otherwise "squareback" geometry was assessed. It was concluded that the cavity allows the wake to move more freely about the rear base. Specifically, the wake is freed from its more restricted motion that is present with the "squareback" Nissan NDP. In doing so, the drag reduction achieved with the cavity appendage is about 13.6%. Work on the Nissan NDP also involved an assessment of a moving ground in the simulation. It was concluded that, in the stationary ground simulation, flow detachment at the ground where the flow exits from the underbody has an adverse drag effect. In other words, although moving ground simulations better replicate the real-world conditions, the stationary ground variant is in this case more conservative, as it returns slightly higher drag values.

Acknowledgements

Where do I start? Acknowledging those without whom the PhD would not have been completed is for me by far possibly the most important part of the dissertation while for others it may just be a formality or right of passage.

First, I would like to express my immense gratitude to my supervisor, Professor Aimee S. Morgans. You secured the funding from Nissan, allowed me to explore a different solver for capturing wake bimodality when I simply was heading nowhere with StreamLES, were constantly open to new avenues of research even if they were not pursued in the end and, ultimately, always had the right advice for the moment at hand. You kept faith in me when the inherent chaos / turbulence that I bring with myself would have left many doubtful of my ability to complete the thesis. So, thank you! It can also not be forgotten that you supported my application to the 2018 Montestigliano Spring school on lattice Boltzmann CFD methods. I still had to step through the door and take advantage of the opportunities that presented themselves, but there is no doubt that this opened the door to a job at commercial lattice Boltzmann solution method provider Exa (now part of my employer Dassault Systèmes).

Second, a huge note of thanks to the members of Morgans' Lab. The group lunches, which included occasional visits to the best Thai restaurant in London, relaxing coffee breaks and more general comradery proved indispensable in our individual pursuits of a better world. Thank you to my fellow bluff-body buddies Dr. Olga Evstafyeva and Dr. Laurent Dalla Longa for helping me get started on my thesis, and thank you to Dania Ahmed for joining me on the bluff-body flow research endeavor and showing me how not to be afraid of more complex topics such as nonlinear flow control! A special thank you also to Dr. Steven (Yu) Xia, Dr. Dong Yang and Dr. Juan Guzmán Iñigo for going beyond what can be expected of a friend when I most needed help. Dr. Xiao Han and Dr. Davide Laera, it was a pleasure exchanging experiences made in the domain of love with you both.

Third, I would like to say thank you to my colleagues at Dassault Systèmes (3DS). Matthieu Plagnard (manager) as well as Dr. Christoph Classen (senior manager), you kept the PhD door open to me by supporting my decision to switch to an 80% 3DS and 20% PhD week. Also, thank you Svetlana Bludovskaia Jeronimo, Fabian Quintero and Clement Lambin for taking on any additional assignments that should have been on my plate during this one year long special arrangement.

Fourth, a sincere note of gratitude to my friends outside of Imperial College London and Dassault Systèmes. Jenn Li and Harry Thambirajah, it was a pleasure exploring Christianity with you and our little Italian get-away in spring 2018 will always be a fond memory of my PhD. Also, it was an honour being invited to your wedding in spring 2019 - the pants dilemma will not happen again. To my German-Japanese friend, Yukari Schrickel, our Franco Manca pizza therapy sessions proved invaluable during this trying PhD time. Our annual hikes were incredibly settling for the mind too. So, thank you for your time and friendship. The same goes for my dear friend Maggie (Bowen) Ma.

Finally, thank you to my family: Mummy, Daddy, Kerrick (my twin), and Angelene (my cousin). You supported me unconditionally during this, well, 11-12 year-long academic endeavour at Imperial College London that has spanned two masters degrees and, finally, this PhD. One could liken the 11-12 years at Imperial College to a full Ironman race where the 3.86km swim represents the MEng degree in mechanical engineering, the 180km biking portion symbolizes the MRes in fluid dynamics, and the marathon denotes the PhD in aerodynamics. As such, although I have never competed in a physical Ironman or marathon race, I have, thanks to my family, done so in the academic world.

Publications

Portions of this dissertation have featured in the following publication:

1. HESSE, F. & MORGANS, A. S. 2021 Simulation of wake bimodality behind squareback bluff-bodies using LES. *Computers & Fluids* **223**, 104901.

Conferences

Parts of this dissertation have been presented at the following conferences / events:

1. UK Fluids Conference 2019 at the DAMTP of Cambridge University
2. UK Turbulence Consortium 2019 at the Mechanical Engineering department of Imperial College London
3. Aerovehicles 4 2021 at the Technical University of Berlin

Other

Some of this work has featured in a video submitted to a UK Turbulence Consortium video competition in 2020. The video may be accessed through the following link:
https://www.youtube.com/watch?v=_EM4oHPMJA0.

Table of Contents

Page

1 Introduction **25**

1.1 Motivation 25

1.2 Project Objectives 27

2 Literature Review **29**

2.1 Bluff-Body Flow Features 29

2.1.1 Simplified Bluff-Body Geometries 30

2.1.2 On-Road Representative Bluff-Body Shapes 38

2.2 Flow Control 40

2.2.1 Passive Control 42

2.2.2 Active Open-Loop Control 44

2.2.3 Active Closed-Loop Control 48

2.3 Computational Fluid Dynamics 53

2.3.1 Finite Volume Method 53

2.3.2 Turbulence Modelling 54

2.3.3 Wall-Models 58

3 Research Methods **64**

3.1 Control Strategy 64

3.2 Flow Solver - OpenFOAM 71

3.3 Post-Processing Techniques 76

4 D-Body: Active Flow Control **81**

4.1 Simulation Set-up 81

4.2 Unforced Flow 85

4.3 Open-loop Forced Flow 89

4.4 Closed-loop Forced Flow 91

5 Ahmed Body: Bimodal Wake Dynamics **99**

5.1 Simulation Set-up 100

5.2 Detection of Wake Bimodality 113

5.3 Source of Wake Bimodality 125

5.4 Linear Feedback Control for the Ahmed Body 133

6 Nissan NDP: Passive Flow Control **142**

6.1 Simulation Set-up 143

6.2 Cavity based Passive Flow Control 149

6.3 Moving Ground Analysis 156

7 Closing Remarks **160**

7.1 Conclusions 160

7.2 Future Work 161

Bibliography **163**

Appendix A: Pressure-Velocity Coupling **178**

Appendix B: Figure Usage Permission **180**

Abbreviations

Abbreviation	Meaning
AIP	American Institute of Physics
APS	American Physical Society
ASME	American Society of Mechanical Engineers
CCAL	Creative Commons Attribution License
CCC	Copyright Clearance Center
CFD	Computational Fluid Dynamics
COP	Centre of Pressure
CV	Control Volume
DAMTP	Department of Applied Mathematics and Theoretical Physics
DES	Detached Eddy Simulation
DMD	Dynamic Mode Decomposition
DNS	Direct Numerical Simulation
FFT	Fast Fourier Transform
FRD	Frequency Response Data
FVM	Finite Volume Method
GHG	Greenhouse Gas
HPC	High Performance Computing
GTS	Ground Transportation System
IEA	International Energy Agency
IDDES	Improved Delayed Detached Eddy Simulation
IPCC	Intergovernmental Panel on Climate Change
LBM	Lattice Boltzmann Method
LES	Large Eddy Simulation
MIMO	Multi-Input Multi-Output
ODE	Ordinary Differential Equation
OECD	Organistation for Economic Cooperation and Development
PANS	Partially-Averaged Navier Stokes
PDF	Probability Density Function
PIV	Particle Image Velocimetry
POD	Proper Orthogonal Decomposition
RANS	Reynolds-Averaged Navier Stokes
RMS	Root-Mean-Square
SAE	Society of Automotive Engineers
SGS	Sub-Grid-Scale
SISO	Single-Input Single-Output
SVD	Singular Value Decomposition
WMLES	Wall-Modelled LES
WRLES	Wall-Resolving LES
ZNMF	Zero-Net-Mass-Flux

Nomenclature

Symbol	Explanation
P	Scalars (Zero-Order Tensors)
$\boldsymbol{B}$, x_i, y_j	Vectors (First-Order Tensors)
$\mathbf{A}$, y_{ij}	Second-Order Tensors

Greek Characters

Symbol	Units	Explanation
α	-	Amplitude, growth rate
Γ_ϕ	m^2s^{-1}	Diffusion coefficient of ϕ
δ	m	Boundary layer thickness
ϵ	m^2s^{-3}	Turbulent energy dissipation
ζ	-	Damping ratio
κ	-	von Kármán constant = 0.42
λ	-	Energy associated with mode, eigen-value, coefficient
λ_T	m	Taylor microscale
$\mathbf{\Lambda}$	-	Singular value matrix
μ	Pa·s	Dynamic shear viscosity, eigen-value
μ_B	Pa·s	Bulk viscosity
ν	m^2s^{-1}	Kinematic viscosity
ν_t	m^2s^{-1}	Turbulent eddy viscosity
$\nu_{t,wm}$	m^2s^{-1}	Wall-model eddy viscosity
ρ	$kg{\cdot}m^{-3}$	Density
σ	-	Standard deviation
σ_j	-	Eigen-vector
τ_w	Pa	Wall shear stress
ϕ	-	General quantity, arbitrary function, mode
$\mathbf{\Phi}$	-	Left singular matrix
$\mathbf{\Psi}$	-	Right singular matrix
ω	$rad{\cdot}s^{-1}$	Frequency
Ω	-	Flow domain

Roman Characters

Symbol	Units	Explanation
a	-	POD expansion coefficient
A	-	Undetermined constant
A_f	m^2	Cell face surface area
$\mathbf{A}$	-	DMD matrix of coefficients

Roman Characters Cont.

Symbol	Units	Explanation
$\tilde{\mathbf{A}}$	-	DMD matrix of coefficients
B	-	Log-law constant = 5.5
B_1	-	Reichardt law consant = 11
B_2	-	Reichardt law constant = 3
C	-	Reichardt law constant = 7.8
C_D	-	Drag coefficient
$C_D A$	m^2	Drag coefficient multiplied by frontal area
C_P	-	Coefficient of pressure
C_{PB}	-	Non-dimensional base pressure
C_{SGS}	-	Smagorinsky coefficient
C_μ	-	Momentum coefficient
C^*	-	Non-dimensional ground clearance $= C/W$
$\partial C_p/x_2$	m^{-1}	Vertical base pressure gradient
$\partial C_p/x_3$	m^{-1}	Horizontal base pressure gradient
D	N	Drag force
F_D	N	Drag force
F_L	N	Lift force
$F_p(s)$	-	Base pressure output
F_P	N	Pressure drag force
G	-	Filter function, ground clearance
G'	-	Non-dimensional ground clearance
$G(s)$	-	System transfer function, frequency response function
H	m	Bluff-body height
H^*	-	Aspect ratio $= H/W$
H'	-	Non-dimensional height
i	-	Imaginary number
k	m^2s^{-2}	Turbulent kinetic energy
k_c	m^{-1}	LES cut-off wavenumber
$K(s)$	-	Control law
l	m	Integral length-scale
l_e	m	Eddy cut-off length-scale
l_{int}	m	Hybrid RANS-LES interface height
L	m	Length
L'	-	Non-dimensional length
n	-	Counter
n_i	-	Cell face unit normal vector
P	Pa	Pressure (Pa)
$\boldsymbol{q}$	-	General data flow variable vector
Q	s^{-2}	Q-criterion

Roman Characters Cont.

Symbol	Units	Explanation
r	-	Economy SVD row and column number
R	m	Nose radius
R	-	Co-variance matrix
R'	-	Non-dimensional nose radius
Re	-	Reynolds number
s	m	Slot jet width, or Laplace transform variable s=$i\omega$
S	m^2	Surface area
S_{ij}	s^{-1}	Deformation tensor
S	s^{-1}	Deformation / strain-rate tensor
S_ϕ	-	Generic source term
Str	-	Strouhal number
t	s	Time
t^*	-	Non-dimensional time
T	s	Period
T_{ij}	m^2s^{-2}	Sub-grid-scale stresses
u_i	$m{\cdot}s^{-1}$	Component of velocity in i-th direction
u_τ	$m{\cdot}s^{-1}$	Friction velocity
$U_{j_{in}}$	$m{\cdot}s^{-1}$	Jet forcing amplitude
$U_j(s)$	-	Velocity jet input
U_∞	$m{\cdot}s^{-1}$	Free-stream velocity
V_p	m^3	Control volume
W	m	Width
W	s^{-1}	Vorticity tensor
W'	-	Non-dimensional width
x_i	m	Component of spatial position vector in the i-th direction
x^+	-	Spatial locations / dimensions in wall units
$\boldsymbol{y}$	-	Snapshot data vector
Y	-	m snapshots of data stacked into a matrix form for POD and DMD

List of Figures

Page

1.1 Transport sector direct GHG emissions (*image reproduced with permission from IPCC*) (Edenhofer *et al.*, 2014) 26

1.2 (a) Change in global oil demand and (b) electric car fleet growth (Cozzi *et al.*, 2017) 26

1.3 Nissan Qashqai CFD streamlines colored by velocity magnitude (Kremheller, 2014) . 27

1.4 Nissan Qashqai wind tunnel flow visualization (Kremheller, 2014) 27

2.1 (a) Locations of flow separation around a road vehicle with a particular emphasis on (b) the A-pillar and (c) the C-pillar vortex structures (*image reproduced with permission from Annual Reviews Inc.*) (Hucho, 1998; Hucho & Sovran, 1993) 30

2.2 Key time-averaged wake features for the Ahmed body (*image reproduced with permission from Annual Reviews Inc.*) (Choi *et al.*, 2014) 31

2.3 Bus geometry: ring vortex (W) visualized with iso-surface of $C_p = -0.20$ and longitudinal vortex (P) illustrated using streamlines (Krajnović & Davidson, 2003) 31

2.4 Reflectional symmetry breaking bifurcation diagram where $|ZW/W|$ is the non-dimensional spanwise offset of the wake (*image reproduced with permission from APS*) (Grandemange *et al.*, 2012) 33

2.5 Ahmed Body's laminar reflectional symmetry breaking behavior from the experimental work of Grandemange *et al.* (2012) (*image reproduced with permission from APS*) 33

2.6 (a) Bimodality occurrence map (*image reproduced with permission from AIP Publishing*) (Grandemange *et al.*, 2013*a*), (b) asymmetric wake topology with single horseshoe vortex system (*image reproduced with permission from Elsevier Ltd.*) (Evrard *et al.*, 2016), and (c) asymmetric wake topology with duel horseshoe vortex system (*image reproduced with permission from the authors*) (Perry *et al.*, 2016) 36

2.7 Top-to-bottom bimodal switching sequence: (a) instantaneous pressure on vertical symmetry plane (i.e. side view), (b) instantaneous iso-contours of pressure at C_p=-0.2, and (c) schematic of wake form during bimodal switching sequence (*image reproduced with permission from Open Access*) (Dalla Longa *et al.*, 2019) 37

2.8 Control method classification (*image reproduced with permission from Annual Reviews Inc.*) (Choi *et al.*, 2008) 41

2.9 Passive drag reduction on the Ahmed body using: (a) a splitter plate (*image reproduced with permission from Springer-Verlag*) (Gilliéron & Kourta, 2010), and (b) a boat-tail (*image reproduced with permission from Annual Reviews Inc.*) (Choi *et al.*, 2014) 44

2.10 Schematic of heavy vehicle (tractor-trailer) model with blowing slots, denoted by red rectangles, at the trailer's leading and trailing edge (Englar, 2001) 48

2.11 Schematic of feedback control loop 48

2.12 Turbulence energy spectrum where k_c is the LES filter cut-off wave-number (Temmerman, 2004) 56

2.13 Wall-stress-model application: LES flow information fed to wall-model for wall shear stress evaluation (*image reproduced with permission from Elsevier B.V.*) (Mukha *et al.*, 2019) 60

2.14 Turbulent boundary layer's universal velocity profile (*image reproduced with permission from Annual Reviews*) (Bose & Park, 2018) 60

2.15 Inner turbulent boundary layer with (a) WRLES and (b) WMLES (*image reproduced with permission from Annual Reviews*) (Piomelli & Balaras, 2002) 62

3.1 Instantaneous spanwise vorticity contours (red) and velocity vectors (blue) for (top row) full cavity simulation and (bottom row) modelled synthetic jets (*image reproduced with permission from International Journal of Flow Control*) (Aram *et al.*, 2010) 65

3.2 Open-loop system used for evaluation of $G(s)$ with system identification 69

3.3 Closed-loop system with control law $K(s)$ targeting pressure fluctuation attenuation for base pressure increase 69

3.4 Generic rule-of-thumb scalability of the OpenFOAM solver 76

4.1 Fluid domain of the D-body simulations (*image reproduced with permission from Open Access*)(Dalla Longa *et al.*, 2017) 83

4.2 Actuation and sensing positions in the D-body study (*image reproduced with permission from Open Access*) (Dalla Longa *et al.*, 2017) 83

4.3 Pointwise structured mesh for the D-body 85

4.4 Instantaneous wall "y-plus" for the D-body using the 10 million cell grid 85

4.5 Unforced base pressure spectra for the D-body (OpenFOAM) 86

4.6 Unforced base pressure spectra for the D-body (StreamLES) (*image reproduced with permission from Open Access*) (Dalla Longa *et al.*, 2017) 86

4.7 Average base pressure and probe data traces from Pastoor *et al.* (2008) (*image reproduced with permission from Cambridge University Press*) 87

4.8 x_3-vorticity comparison between present study and results from Dalla Longa *et al.* (2017) (*image reproduced with permission from Open Access*) 87

4.9 Vortex shedding mode from POD, Φ, - it is the first and most energetic mode . . . 88

4.10 Vortex shedding mode from DMD, ϕ ($Str_H \sim 0.25$) 88

4.11 First harmonic of vortex shedding mode from POD, Φ 88
4.12 First harmonic of vortex shedding mode from DMD, ϕ ($Str_H \sim 0.50$) 88
4.13 Bubble pumping mode from DMD, ϕ ($Str_H = 0.085$) 89
4.14 Gain plot of $G(s)$ for the D-body 90
4.15 Phase plot of $G(s)$ for the D-body 90
4.16 Gain and phase plot of $G(s)$ for the D-body from Dalla Longa *et al.* (2017) (*image reproduced with permission from Open Access*) 90
4.17 Percent change in D-body base pressure for open-loop forcing in OpenFOAM 91
4.18 Percent change in D-body base pressure for open-loop forcing in StreamLES (Dalla Longa, 2018) 91
4.19 Gain plot of $K(s)$ and $S(s)$ for the D-body 92
4.20 Phase plot of $K(s)$ and $S(s)$ for the D-body 92
4.21 Gain and phase plot of $K(s)$ and $S(s)$ for the D-body from Dalla Longa *et al.* (2017) (*image reproduced with permission from Open Access*) 93
4.22 Nyquist stability diagram for the D-body open-loop feedback law, $L(s)$ 93
4.23 Zero-net-mass-flux jet signal before and after control is switched "on" 94
4.24 D-body base pressure signal before and after control is switched "on" 95
4.25 Spectra of the base pressure traces in the uncontrolled and controlled state 95
4.26 Mean flow recirculation bubble aft of the D-body with (a) control "off" and (b) control "on" 96
4.27 Instantaneous x_3-vorticity aft of the D-body with (a) control "off" and (b) control "on" 96
4.28 DMD, ϕ, of vorticity magnitude aft of the D-body with (a) control "off" and (b) control "on" 97

4.29 Vorticity magnitude based DMD mode amplitude analysis for control "off" and control "on" 97

5.1 Ahmed body geometry: (a) side view and (b) rear view 101

5.2 Wall boundary condition flow chart 101

5.3 Ahmed body rear base pressure array 103

5.4 Sample volume mesh with (a) prism layer cells near the Ahmed body nose boundary, and trimmer cells in the majority of the flow domain visualized on the (b) x_1x_2 - middle plane and (c) the x_1x_3 - middle plane 104

5.5 Mesh refinement study for Ahmed body WRLES - base pressure spectra 107

5.6 Mesh refinement study for Ahmed body WRLES - base pressure gradients in the (a) vertical direction, $\partial C_P/\partial x_2$, and (b) horizontal direction, $\partial C_P/\partial x_3$ 107

5.7 Visualization of viscosity ratio with an (a) iso-contour plot at $\nu_t/\nu = 5$ colored by velocity magnitude and (b) a viscosity ratio contour plot 108

5.8 Histogram plots of wall "y-plus", $\overline{x_{2w}^+}$ 109

5.9 Histogram plots of $\overline{\Delta x_{1w}^+}$ and $\overline{\Delta x_{3w}^+}$ 110

5.10 Wall "y-plus" distribution projected onto the Ahmed body for (a) WRLES set-up with 11.1 million cells, (b) WMLES set-up using Spalding's law with 8.8 million cells and (c) WMLES set-up using the log-law with 8.3 million cells 112

5.11 Average turbulent boundary layer velocity profiles in wall units taken from the Ahmed body cross-stream side(s) downstream of the front separation bubble 113

5.12 Base pressure gradient in the (a) vertical direction, $\partial C_P/\partial x_2$, and (b) horizontal direction, $\partial C_P/\partial x_3$, for 11.1 million cells WRLES, 8.8 million cells WMLES with Spalding's law and 8.3 million cells WMLES employing the log-law. The black circles show bimodal wake shifting events 117

5.13 Base pressure gradient in the (a) vertical direction, $\partial C_P/\partial x_2$, and (b) horizontal direction, $\partial C_P/\partial x_3$, for 11.1 million cells WRLES, 8.8 million cells WMLES with the log-law and 8.3 million cells WMLES employing Spalding's law. The black circles show bimodal wake shifting events 118

5.14 Joint probability density function of base pressure gradients, PDF($\partial C_P/\partial x_2$,$\partial C_P/\partial x_3$), for (a) 11.1 million cells (MC) WRLES, (b) 8.8 million cells WMLES applying Spalding's law (SL) and (c) 8.3 million cells WMLES using the log-law (LL) 118

5.15 Wake bimodality visualized using the instantaneous pressure field projected onto the x_1x_3 - middle plane passing through the Ahmed body for the WRLES case 120

5.16 Wake bimodality visualized using the instantaneous velocity magnitude field with streamlines projected onto the x_1x_3 - middle plane passing through the Ahmed body for the WRLES set-up 121

5.17 Wake bimodality visualized using the instantaneous velocity magnitude field with streamlines projected onto the x_1x_3 - middle plane passing through the Ahmed body for the 8.8 million cell WMLES set-up that uses Spalding's law 121

5.18 Wake bimodality visualized using the instantaneous pressure field projected onto the x_1x_3 - middle plane passing through the Ahmed body for the 8.8 million cell WMLES case that uses Spalding's law 122

5.19 Vortex shedding frequency associated with front separation bubble 122

5.20 Wake bimodality visualized using $C_P = -0.3$ iso-contour plots coloured by velocity magnitude for (a) WRLES and (b) 8.8 million cell WMLES using Spalding's law . . 123

5.21 Contour plots of the mean velocity's x_1-component with streamlines projected onto the x_1x_3 - middle plane passing through the Ahmed body for (a) WRLES, (b) 8.8 million cell (MC) WMLES with Spalding's law (SL) and (c) 8.3 million cell WMLES using the log-law (LL) 127

5.22 Profiles of the mean velocity's x_1-component, $\overline{U_{x_1}}$, from the x_1x_3 - middle plane passing through the Ahmed body 127
5.23 Close-up of x_1-component mean velocity profiles in the vicinity of the front separation bubble. Markers denote cell centers 127
5.24 Visualization of flow structures captured around the Ahmed body using iso-contours of Q^*=5.30 for (a) WRLES, (b) 8.8 million cell (MC) WMLES with Spalding's law (SL) and (c) 8.3 million cell WMLES using the log-law (LL) 129
5.25 Visualization of flow structures captured around the Ahmed body using iso-contours of Q^*=5.30 for (a) WRLES, (b) 8.8 million cell (MC) WMLES with the log-law (LL) and (c) 8.3 million cell WMLES using Spalding's law (SL) 129
5.26 Contour plots of TKE projected onto the x_1x_3 - middle plane passing through the Ahmed body for (a) WRLES, (b) 8.8 million cell (MC) WMLES with Spalding's law (SL) and (c) 8.3 million cell WMLES using the log-law (LL) 131
5.27 Profiles of the TKE from the x_1x_3 - middle plane passing through the Ahmed body . 131
5.28 Close-up of TKE profiles in the vicinity of the front separation bubble. Markers denote cell centers 131
5.29 POD modes, Φ, from pressure data on the x_1x_3 - middle plane passing through the Ahmed body for the 8.8 million cell WMLES set-up using Spalding's law 133
5.30 POD modes, Φ, from pressure data on the x_1x_3 - middle plane passing through the Ahmed body for the 11.1 million cell WRLES set-up 133
5.31 Top-hat velocity profile actuation shape on the Ahmed body's rear base perimeter (marked in yellow) 134
5.32 Spectra of the unforced average base pressure signal 134
5.33 Gain plot of $G(s)$ for the Ahmed body 135
5.34 Phase plot of $G(s)$ for the Ahmed body 135

5.35 Change in mean base pressure, $\overline{C_{PB}}$, with open-loop forcing 136

5.36 Change in mean drag, $\overline{C_D}$, with open-loop forcing 136

5.37 Change in mean lift, $\overline{C_L}$, with open-loop forcing 136

5.38 Gain plot of $K(s)$ and $S(s)$ for the Ahmed body 137

5.39 Phase plot of $K(s)$ and $S(s)$ for the Ahmed body 137

5.40 Nyquist stability diagram for the Ahmed body open-loop feedback law, $L(s)$ 138

5.41 Closed-loop ZNMF jet signal for the Ahmed body 139

5.42 Average base pressure signal, $\overline{C_{PB}}$, when closed-loop control is "on" 139

5.43 Average drag coefficient signal, $\overline{C_D}$, when closed-loop control is "on" 139

5.44 Influence of jet actuation on the wake during mean blowing phase and during the phase with no noticeable impact of the jet 140

5.45 Symmetrizing effect of mean blowing on the wake's spanwise orientation: (a) general view and (b) close-up of horizontal base pressure gradient, $\frac{\partial C_P}{\partial x_3}$, during mean blowing 141

5.46 Comparison of average base pressure spectra without control and with control "on" 141

6.1 Nissan NDP: (a) front view and (b) rear view 143

6.2 Nissan NDP rear topology: (a) with cavity and (b) "squareback" 143

6.3 Base pressure probe array for the Nissan NDP 145

6.4 Sample fluid domain mesh with (a) prism layer cells near the Nissan NDP wall, and trimmer cells in the majority of the flow domain visualized on the (b) x_1x_2 - middle plane and (c) the x_1x_3 - middle plane 146

6.5 Histogram plot of wall "y-plus", $\overline{x_{2w}^+}$, for the Nissan NDP with moving ground . . . 149

6.6 Wall "y-plus" projected onto the Nissan NDP surface 149

6.7 Base pressure gradient in the (a) vertical direction, $\partial C_P/\partial x_2$, and (b) horizontal direction, $\partial C_P/\partial x_3$, for the Nissan NDP with and without cavity appendage. Filled-in circles denote times at which instantaneous pressure snapshots are taken for figures 6.10-6.11 150

6.8 Joint PDF of base pressure gradients for (a) Nissan NDP with cavity and (b) the "squareback" NDP 151

6.9 Mean pressure field snapshots highlighting the prominent vertical wake asymmetry for (a) the "squareback" NDP and (b) the NDP with a cavity at the rear 151

6.10 Pressure field snapshots highlighting short-lived moments of horizontal wake asymmetry for the "squareback" NDP. Times at which flow field snapshots are taken may be found in figure 6.7 152

6.11 Pressure field snapshots highlighting short-lived moments of horizontal wake asymmetry for the NDP with cavity. Times at which flow field snapshots are taken may be found in figure 6.7 152

6.12 Symmetric spanwise vortex shedding visualized through the application of POD, Φ, on instantaneous pressure data taken from the x_1x_3 - middle plane for (a) the "squareback" NDP and (b) the NDP with a rear cavity. This is the third POD mode. 154

6.13 Asymmetric top-to-bottom vortex shedding visualized through the application of POD, Φ, on instantaneous pressure data taken from the x_1x_2 - middle plane for (a) the "squareback" NDP and (b) the NDP with a rear cavity. This is the second POD mode. 154

6.14 Instantaneous pressure flow field for (a) moving ground and (b) stationary ground simulation of the Nissan NDP with a rear cavity 157

6.15 Instantaneous x_3-vorticity for (a) moving ground and (b) stationary ground simulation of the Nissan NDP with a rear cavity 158

6.16 Instantaneous velocity magnitude field for (a) moving ground and (b) stationary ground simulation of the Nissan NDP with a rear cavity 158

6.17 Ceiling hairpin vortex visualized through the application of POD, Φ, on instantaneous pressure data taken from the x_1x_2 - middle plane for (a) moving ground and (b) stationary ground simulation of the Nissan NDP with a rear cavity. This is the fourth POD mode. 159

6.18 Vortex structure visualization through Q^* criterion iso-contours of Q^*=59.8 for (a) moving ground and (b) stationary ground simulation of the Nissan NDP with a rear cavity 159

7.1 Semi-Implicit Method for Pressure Linked Equations (SIMPLE) algorithm (Versteeg & Malalasekera, 2007) 178

7.2 Pressure Implicit with Splitting Operators (PISO) algorithm (Versteeg & Malalasekera, 2007) 179

List of Tables

Page

4.1 D-body mesh refinement study 85

5.1 Mesh refinement study for Ahmed body WRLES - mean flow quantities 106

5.2 Mean aerodynamic quantities for the WMLES simulations where MC represents "million cells", SL denotes Spalding's law and LL stands for "log-law". Complementing wall-model results are written in *italics* 115

6.1 Mesh refinement study based on Nissan NDP with cavity appendage and moving ground - mean flow quantities 148

6.2 Integral flow quantities for the "squareback" NDP and NDP with a rear cavity . . . 155

6.3 Integral flow quantities for the stationary ground and moving ground simulation of the NDP with a rear cavity 157

7.1 Permission for Figure Reproduction from Copyright Holder 180

Chapter 1

Introduction

1.1 Motivation

In a report titled "Environmental Outlook to 2050", the Organization for Economic Co-operation and Development (OECD) states that climate change threatens basic life elements for the global population. This encompasses land use, water access, health, production of food, as well as natural and physical capital (Kitamori *et al.*, 2012). A Nature Perspective article titled "Choosing the Future of Antarctica" describes two scenarios for Antarctica's and the Southern Ocean's state in 2070: one where no serious measures were taken to lower greenhouse gas (GHG) emissions and climate change continued unchecked, and one where aggressive emission limiting measures were adopted to decelerate climate change. To avoid a global air temperature rise of approximately 3°C, a 23% reduction in ice shelf volume, a loss of more than 14% in average per-capita world consumption and many more adverse effects, it is clear that society needs to shift to "low-carbon and climate-resilient growth paths" (Rintoul *et al.*, 2018; Kitamori *et al.*, 2012; Stern, 2006).

According to the Intergovernmental Panel on Climate Change's (IPCC) 2014 report on climate change mitigation, GHG emissions caused by the transport sector are more than twice the amount emitted from this sector in 1970. In fact, by 2010, transport emissions had risen faster than

all other energy end-use divisions. Looking at figure 1.1, approximately 80% of this increase is a result of road vehicles alone (Edenhofer *et al.*, 2014). Also, based on the IEA's 2017 report on the world energy outlook to 2040, there may be a decline in passenger vehicle oil consumption due to a switch to electric power-trains (Fig. 1.2b), but there is a continued rise in truck oil demand (Fig. 1.2a) (Cozzi *et al.*, 2017). Thus, to advance society's transition to a low-carbon growth path, the efficiency of road vehicles must be improved. There would be a concomitant increase in electric vehicle range (Cozzi *et al.*, 2017). The target here is to enhance vehicle efficiency by acting upon its aerodynamics. Specifically, by lowering the drag, vehicle energy use is improved, since about 70% of driving resistance at motorway speeds ($\sim$ 140kph) is a result of aerodynamic drag (Hucho & Sovran, 1993; Hucho, 1998).

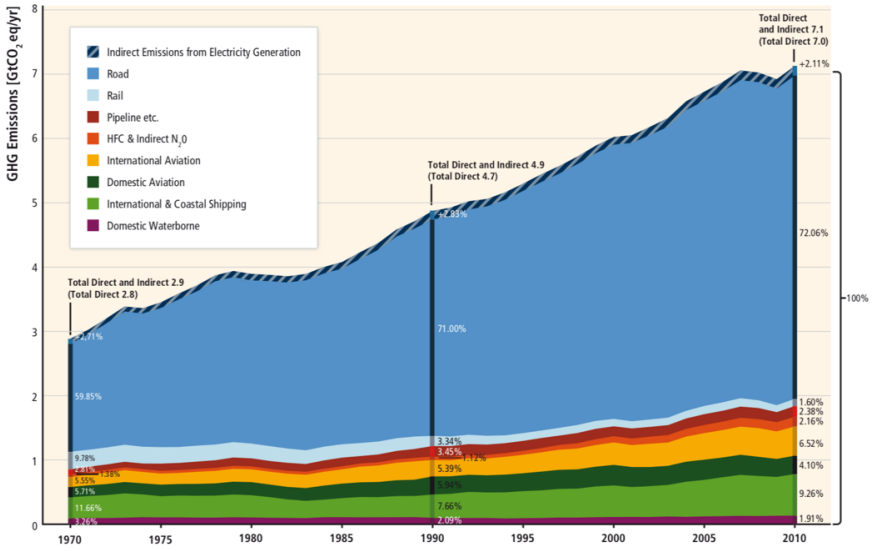


Fig. 1.1: Transport sector direct GHG emissions (*image reproduced with permission from IPCC*) (Edenhofer *et al.*, 2014)

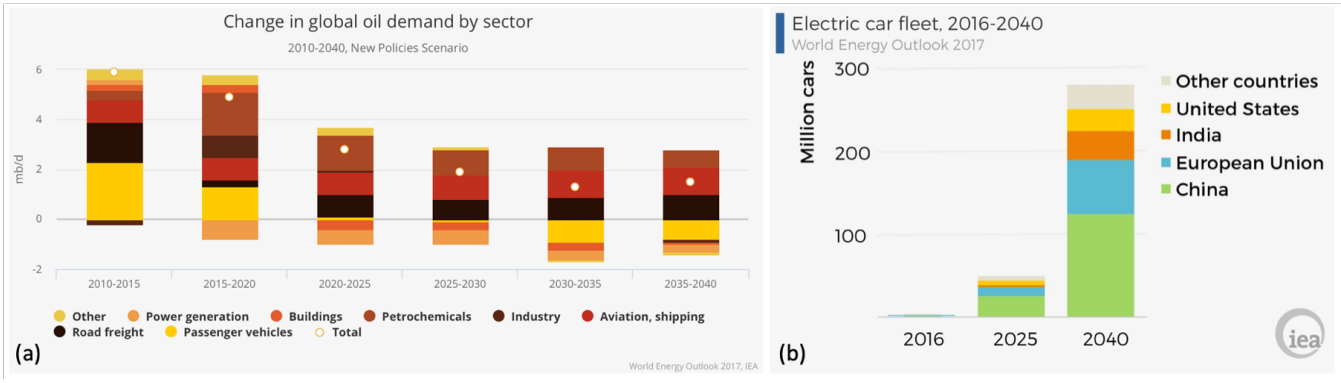


Fig. 1.2: (a) Change in global oil demand and (b) electric car fleet growth (Cozzi *et al.*, 2017)

Road vehicles are categorized as bluff-bodies in immediate proximity to the ground. Their

external flow fields are characterized by flow separations. The largest and most significant boundary layer flow separation is present at the rear-end of the vehicle where a substantial low pressure domain is formed. It is called a wake or "dead water" region (Fig. 1.3-1.4) and accounts for the majority of aerodynamic drag acting on the vehicle. The reason for this is that approximately 80% of total road vehicle aerodynamic drag is due to pressure drag (Hucho & Sovran, 1993; Hucho, 1998; Ahmed *et al.*, 1984). Therefore, an efficient and effective method to improve vehicle aerodynamics is to understand and control the rear-end wake's dynamics for increased base pressure - the ultimate target of this project.

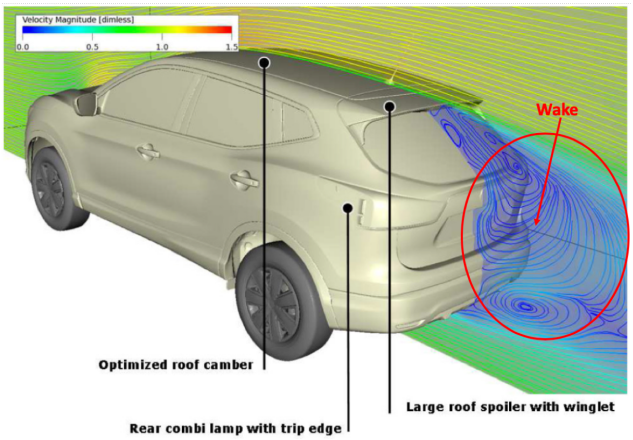


Fig. 1.3: Nissan Qashqai CFD streamlines colored by velocity magnitude (Kremheller, 2014)

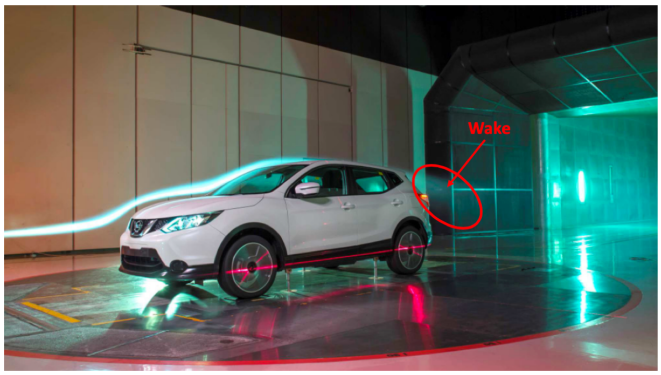


Fig. 1.4: Nissan Qashqai wind tunnel flow visualization (Kremheller, 2014)

1.2 Project Objectives

There are three main objectives for this dissertation:

1. The first objective is to validate the use of OpenFOAM for sensitivity based feedback control work targeting drag reduction. This is done by replicating the work of Dalla Longa *et al.* (2017) that was done on the bullet shaped D-body using StreamLES. The ultimate goal of this objective is to facilitate the research group's transition from StreamLES, a fluid solver that uses restrictive block-structured meshes, to OpenFOAM, a more versatile solver that allows the use of unstructured grids and, therefore, the simulation of more complex and road-vehicle representative bluff-body geometries.

2. The second objective is to construct a numerically efficient and tractable set-up for simulating and understanding wake bimodality, and to subsequently use highly resolved and heavily under-resolved variants of this setup to identify possible flow structures that could force a bimodal wake switching event at the rear of the canonical squareback Ahmed body geometry. A further target is to test linear feedback control on the Ahmed body.

3. The third objective is to assess the impact of appending a cavity to the "squareback" form of the Nissan NDP as well as to evaluate the use of a moving ground in the flow simulation.

The dissertation is structured as follows:

1. Chapter 2 is a literature review on bluff-body flow features, flow control, and computational fluid dynamics (CFD).

2. Chapter 3 reviews the precise research methods used. This entails the control strategy deployed, the flow solver used as well as any post-processing techniques that require further elaboration.

3. Chapter 4 discusses the active flow control work done on the bullet shaped D-body, which is used as a flow control simulation test case in transitioning to the OpenFOAM CFD solver.

4. Chapter 5 explains the work done to construct a computationally efficient mesh setup for simulating the bimodal wake dynamics aft of the Ahmed body as well as the work done to identify possible triggers of this drag enhancing phenomenon. It also investigates the use of linear feedback control to improve the drag characteristics of the Ahmed body.

5. Chapter 6 describes the passive flow control work done on the Nissan NDP and also assesses the use of a moving ground in the simulation.

6. Chapter 7 summarizes the key findings of this thesis and offers an outlook for future work.

Chapter 2

Literature Review

This chapter provides a brief overview of current knowledge on bluff-body aerodynamics and the control of bluff-body flows for lower drag. A section is also devoted to the CFD tools available and, in particular, the method employed in this project.

2.1 Bluff-Body Flow Features

Regions of flow separation are the key bluff-body flow field feature. Flow separations may be quasi 2D or fully 3D, and are found at multiple locations around the road vehicle (Fig. 2.1). As a result of these flow separations, the pressure drag force, F_P, is produced (Eq. 2.1.1). It is defined as the integral around the body surface, S, of the static pressure distribution, P, multiplied by its orientation relative to the free-stream flow's tangent, $\cos(\phi)$ (Ahmed *et al.*, 1984; Dahan, 2013):

$$F_P = \int_S P\cos(\phi)\mathrm{d}S \tag{2.1.1}$$

Large sources of pressure drag, which is responsible for about 80% of bluff-body drag (the remaining 20% is mainly attributable to skin friction drag), are the A-pillar and C-pillar vortex structures. But, the by far largest contributor is the body's rear-end wake (Fig. 1.3-1.4). As such, first a summary of present knowledge on the rear-end wake's time-averaged and instantaneous dynamics is provided.

This is done by looking at simplified bluff-body geometries. Subsequently, the flow field around more on-road representative bluff-body shapes is detailed to obtain an appreciation for its complexity (Ahmed *et al.*, 1984; Hucho, 1998).

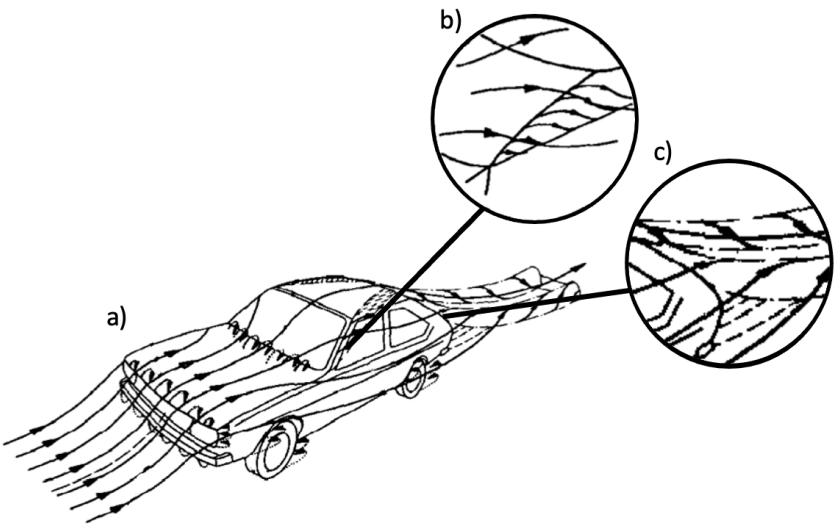


Fig. 2.1: (a) Locations of flow separation around a road vehicle
with a particular emphasis on (b) the A-pillar and (c) the C-pillar vortex structures
(*image reproduced with permission from Annual Reviews Inc.*) (Hucho, 1998; Hucho & Sovran, 1993)

2.1.1 Simplified Bluff-Body Geometries

The vehicle aerodynamics community possesses thorough knowledge on the time-averaged flow around simplified road vehicles. Some of the first quantitative information on the time-averaged rear-end wake is provided by Ahmed (1981). The work studied the flow past three characteristic vehicle rear-end shapes: the estate, fastback and notchback geometry. Qualitatively, it was shown that the near-wake for all three geometries consists of a separation bubble aft of which two counter-rotating vortices are formed. Quantitatively, it was assessed that there must be a base slant angle between 0° (estate) and 22.5° (fastback) where there is no rotational wake motion and, hence, no vortex drag (Ahmed, 1981). The first experimental work on the now widely used Ahmed body was performed by Ahmed *et al.* (1984). Their study illustrated that, encapsulated within the separation bubble, are two horseshoe vortices located above each other, while two longitudinal counter-rotating vortices are formed at and shed off the slanted side trailing edges (Fig. 2.2). If the bottom and top horseshoe

vortices are approximately of equal strength, a ring vortex is created. It is believed a merging process is initiated once equal vortex strength is reached (Ahmed *et al.*, 1984). Some of the first results for the streamwise development of time-averaged wake structures was provided by Barlow *et al.* (1999). They systematically varied the aspect ratio of a rectangular bluff-body to reconcile results for a commercial van that showed taller bluff-bodies possess lower drag than shorter vehicles with the opposite expected trend found in the literature. Bluff-body surface roughness at the bottom face was varied too (Barlow *et al.*, 1999). Meanwhile, some of the earliest computational work on the time-averaged wake dynamics of simplified bluff-bodies was performed by Han (1989). In this work, the flow past the Ahmed body was simulated using the Reynolds-averaged Navier-Stokes (RANS) equations coupled to the $k - \epsilon$ turbulence model. The simulated flow field compared favourably with the experimental data collected by Ahmed *et al.* (1984) (Han, 1989). Further time-averaged numerical data is provided by Krajnović & Davidson (2003), who simulated the flow past a simplified bus geometry at Reynolds number, Re, of 0.21×10^6 based on free-stream velocity, U_∞, and geometry height, H. They successfully resolved the symmetric ring vortex, W, and longitudinal counter-rotating vortex, P, described by Ahmed *et al.* (1984) (Fig. 2.3).

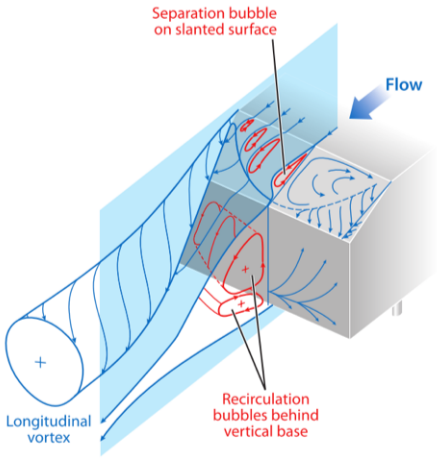


Fig. 2.2: Key time-averaged wake features for the Ahmed body (*image reproduced with permission from Annual Reviews Inc.*) (Choi *et al.*, 2014)

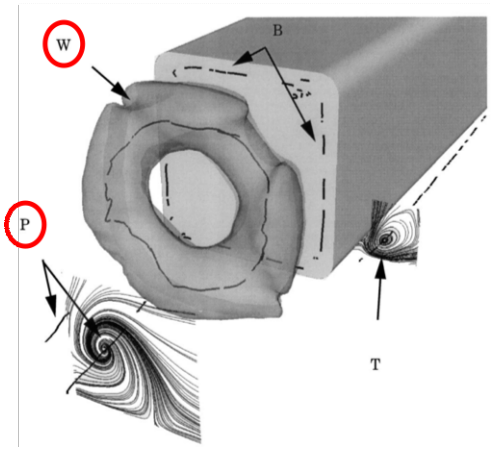


Fig. 2.3: Bus geometry: ring vortex (W) visualized with iso-surface of $C_p = -0.20$ and longitudinal vortex (P) illustrated using streamlines (Krajnović & Davidson, 2003)

In recent years, investigations have started to focus on the rear-end wake's instantaneous dynamics. The reason for this is that a road vehicle's aerodynamic properties, such as drag, lift,

general vehicle stability and wind noise, are directly related to the transient motions of the external flow field (Choi *et al.*, 2014). In a wind tunnel, Grandemange *et al.* (2012) carried out experiments on the Ahmed body for a Re range that generates a laminar 3D wake. Using flow visualization, they observed that, as Re is raised, the originally symmetric wake bifurcates to a state that breaks reflectional symmetry (Fig. 2.5). To bifurcate to a steady-asymmetric (SA) state, the steady-symmetric (SS) wake must always transition to an unsteady-symmetric (US) state first. This demonstrates that slight wake asymmetries initiated by flow unsteadiness are ultimately responsible for forcing the wake off center. As the Re is raised even further, the steady-asymmetric wake becomes an unsteady-asymmetric (UA) wake. This bifurcation process is illustrated in figure 2.4. It is crucial to note that, in the laminar Re regime, the asymmetric wake keeps its current off-axis location. This means there is no random wake migration from one off-axis location to an opposite one i.e. there is no switching of the wake's spanwise off-center location (Grandemange *et al.*, 2012). Using a block-structured finite volume method (FVM) solver that evaluates the incompressible Navier-Stokes equations with large-eddy simulation (LES) for turbulence modelling, Evstafyeva *et al.* (2017) were the first to numerically resolve the Ahmed body's laminar symmetry breaking states described by Grandemange *et al.* (2012). Their simulations offered access to the entire 3D flow field, which permitted a more thorough analysis of the dynamics responsible for wake symmetry destabilization. Specifically, Evstafyeva *et al.* (2017) concluded that horizontal wake symmetry (i.e. symmetry in the x_1x_3-plane) is broken once a Re is reached at which sufficient under-body flow is generated to allow the bottom and top shear layers to interact with each other and recirculate toward the bluff body's base. Evstafyeva *et al.* (2017) also visualized the wake using iso-contours of the Q-criterion. This showed that, as expected, the internal vortex is centred when the wake is symmetric, but forced to the side of the base when the wake breaks reflectional symmetry. Finally, just like with Grandemange *et al.* (2012)'s experimental runs, it was found that, for a given simulation run, the wake maintains its asymmetric position (Evstafyeva *et al.*, 2017).

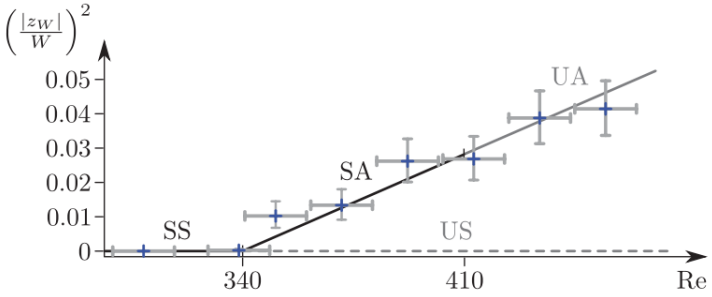


Fig. 2.4: Reflectional symmetry breaking bifurcation diagram where $|ZW/W|$ is the non-dimensional spanwise offset of the wake (*image reproduced with permission from APS*) (Grandemange *et al.*, 2012)

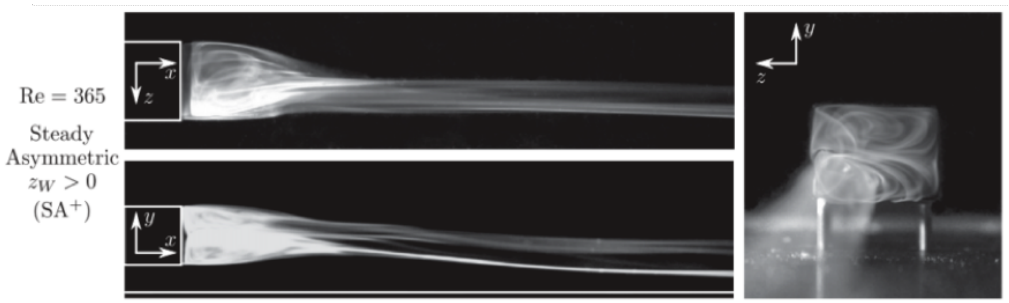


Fig. 2.5: Ahmed Body's laminar reflectional symmetry breaking behavior from the experimental work of Grandemange *et al.* (2012) (*image reproduced with permission from APS*)

Furthermore, it has recently been found that the broken symmetry of the wake persists at turbulent Re. Although the wake is symmetric in the long time-average, instantaneously the wake exhibits a broken symmetry. This translates to a feature known as wake bimodality for rectilinear 3D bluff-bodies (see e.g. figure 2.7) (Grandemange *et al.*, 2013*b*). Here, bimodality is a statistical term that refers to a physical process that leads to the presence of two peaks in a probability density function (PDF) plot of base pressure gradient, which can be either in the spanwise (x_1x_3-plane) or vertical (x_1x_2-plane) direction. The early experimental work by Grandemange *et al.* (2013*b*) on the Ahmed body's bimodal turbulent wake demonstrates that bimodality does not depend on the turbulent Re, that it only manifests itself for ground clearances over a critical value and that vortex-shedding, which is usually the 180° out-of-phase periodic shear layer roll-up from opposing sides of the body, is forced to be one-sided due to the wake asymmetry. Further work by Grandemange *et al.* (2014) showed that the wake's motion from opposing off-axis locations creates a time-dependent

side force that is believed to be responsible for approximately 3-7% of bluff-body drag. Meanwhile, in an additional study, Grandemange *et al.* (2013*a*) investigated experimentally the occurrence of wake bimodality for bluff-bodies with varying aspect ratio and ground clearance. Doing so, allowed the creation of a x_2 (i.e. vertical) versus x_3 (i.e. lateral) bimodality occurrence map in the aspect ratio, $H^* = H/W$, versus non-dimensional ground clearance, $C^* = C/W$, plane. As seen in figure 2.6a, there is a region where both horizontal and vertical wake bimodality are equally likely to occur for a given set-up. However, for a given experimental run, bimodality in only one direction is observed, not both (Grandemange *et al.*, 2013*a*). The bimodality occurrence space was augmented to include pitch and yaw by Bonnavion & Cadot (2018). It was found that above a critical ground clearance, regardless of the inclination, wake asymmetry is always present (Bonnavion & Cadot, 2018). Volpe *et al.* (2015) analysed wake bimodality as well, their work focusing on a full-scale Ahmed body model. Apart from identifying bimodality, they also picked-up signatures of important coherent structures (i.e. modes) in their wake pressure probe readings: the vortex-shedding mode at Strouhal number based on body height, Str_H, of 0.13 and the recirculation bubble pumping mode, where the recirculation bubble moves periodically toward and away from the body's base, at Str_H of 0.08 (Volpe *et al.*, 2015). Two experimental investigations have suggested topologies for the turbulent asymmetric wake. Using the data collected from two particle image velocimetry (PIV) planes, Evrard *et al.* (2016) proposed that the asymmetric wake is composed of a single horseshoe vortex system (Fig. 2.6b). Meanwhile, Perry *et al.* (2016) employed information obtained from three PIV planes to suggest an asymmetric wake topology consisting of two horseshoe vortices (Fig. 2.6c). In the long time-average, the wake retains its torus shape as shown in figure 2.3. Rigas *et al.* (2014) also experimentally studied the multi-stable nature of turbulent wakes, but for an axisymmetric bluff-body. Their study showed that, in a statistical sense, the 3D turbulent wake's large-scale coherent features maintain the structure that the laminar symmetry-breaking instabilities exhibit. However, contrary to the laminar wake, the turbulent wake here too is multi-stable and, for an axisymmetric

body, sustains an infinite number of states of broken symmetry (Rigas *et al.*, 2014). Additionally, the experimental and theoretical work of Rigas *et al.* (2015) suggests that turbulent fluctuations could be responsible for forcing the axisymmetric wake to undergo its multi-modal switching motion. Rigas *et al.* (2015) found that a 2D nonlinear Langevin equation, given by equations 2.1.2 in Cartesian coordinates, can accurately model the axisymmetric bluff-body's turbulent wake. The wake's broken symmetry in the radial direction that results from a supercritical spatial pitchfork bifurcation in the laminar flow regime is taken into account through the equations' deterministic part. These are the first two terms on the right-hand-side of equations 2.1.2. Meanwhile, the wake's random walk in the azimuthal direction is captured by the stochastic term, which is the third term on the right-hand-side of equations 2.1.2, and represents additive white noise. The variable α represents the unstable bifurcated mode's growth rate, the variable λ denotes the nonlinear saturation term's coefficient, and the variable σ^2 is the variance of the random turbulence forcing (Rigas *et al.*, 2015).

$$\dot{x}_1 = \alpha x_1 + \lambda x_1(x_1^2 + y_2^2) + \sigma\xi_{x_1}(t) \tag{2.1.2}$$

$$\dot{x}_2 = \alpha x_2 + \lambda x_2(x_1^2 + x_2^2) + \sigma\xi_{x_2}(t)$$

In theory, although the study was for a 3D wake created by an axisymmetric bluff-body and, thus, a wake that possesses an infinite amount of metastable states, the results should be applicable to rectilinear bluff-body wakes as well. And indeed this model was successfully adapted to the bimodal behavior of rectilinear bluff-body wakes in the experimental closed-loop flow control work by Brackston *et al.* (2016).

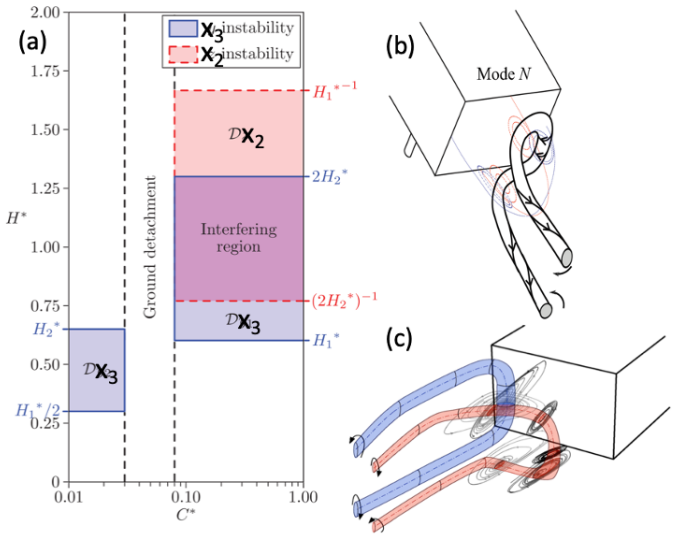


Fig. 2.6: (a) Bimodality occurrence map (*image reproduced with permission from AIP Publishing*) (Grandemange *et al.*, 2013*a*), (b) asymmetric wake topology with single horseshoe vortex system (*image reproduced with permission from Elsevier Ltd.*) (Evrard *et al.*, 2016), and (c) asymmetric wake topology with duel horseshoe vortex system (*image reproduced with permission from the authors*) (Perry *et al.*, 2016)

There is a fair amount of literature that discusses experimental results on wake bimodality (see above paragraph). Simulation results on this phenomenon are, however, scarce. A possible explanation for why it is hard to capture spatial bifurcations numerically is that the simulations require a high (spatial) mesh resolution and the subsequent capture of bimodality requires a comparatively long simulation time of at least 1000 convective flow units (Grandemange *et al.*, 2013*b*). In other words, the numerical resources needed for simulation are simply too high. It seems that merely a few numerical studies have resolved a turbulent asymmetric wake, while, until recently, only Dalla Longa *et al.* (2019) have numerically captured the asymmetric wake's bimodality (Fig. 2.7). Over the last year, two further papers on numerical simulations resolving wake bimodality have appeared: one by Fan *et al.* (2020) and one by Podvin *et al.* (2021). Pasquetti & Peres (2015) simulated the horizontally asymmetric wake aft of the Ahmed body using a spectral solver with LES for turbulence modelling and Lucas *et al.* (2017) achieved this using a lattice Boltzmann method (LBM) solver with LES for turbulence modelling as well. Meanwhile, Rao *et al.* (2018*a*,*b*) captured a vertically asymmetric wake for the ground transportation system (GTS) model using a FVM based solver

coupled to both LES and partially averaged Navier-Stokes (PANS) turbulence modelling. The results from the aforementioned numerical studies seem to suggest that the wake topologies proposed by Evrard *et al.* (2016) and Perry *et al.* (2016) are inaccurate. Specifically, the wake maintains its torus shape and is merely tilted to a side. This form of the asymmetric wake's topology is illustrated in figure 2.7 for the top-to-bottom bimodal wake switching event from Dalla Longa *et al.* (2019)'s FVM based LES study as well. Dalla Longa *et al.* (2019) go on to propose that, just prior to a bimodal switching event, a hairpin vortex is shed and that this vortex, therefore, helps trigger a bimodal event. This too was reported in the Improved Delayed Detached Eddy Simulation (IDDES) work by Fan *et al.* (2020). They also observed that a large hairpin vortex is shed from the shear layer during a wake switching event and/or attempt (Fan *et al.*, 2020). A low dimensional model of wake bimodality was built by Podvin *et al.* (2021). They applied proper orthogonal decomposition (POD) to the velocity field obtained from direction numerical simulation (DNS) of the flow aft of the Ahmed body. The first six velocity modes were then used to reconstruct the flow field's dynamics between and during switches. Their low-order model suggests that switching is triggered by an increase in vortex shedding activity as well, similar to the numerical results from Dalla Longa *et al.* (2019) and Fan *et al.* (2020) (Podvin *et al.*, 2021).

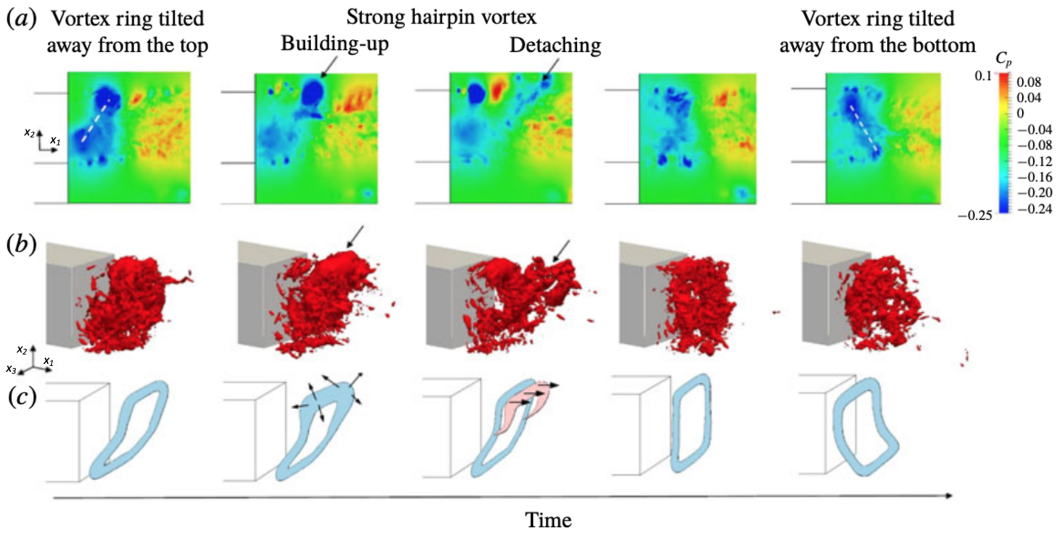


Fig. 2.7: Top-to-bottom bimodal switching sequence: (a) instantaneous pressure on vertical symmetry plane (i.e. side view), (b) instantaneous iso-contours of pressure at C_p=-0.2, and (c) schematic of wake form during bimodal switching sequence (*image reproduced with permission from Open Access*) (Dalla Longa *et al.*, 2019)

2.1.2 On-Road Representative Bluff-Body Shapes

Aerodynamic studies of road vehicles often rely on highly simplified geometry models. These include the aforementioned well known Ahmed body as well as the Ground Transportation System (GTS) model. Such models are well suited for relating observed aerodynamic flow features to specific geometry areas and are, therefore, ideal test cases for understanding fundamental flow structures. However, their high degree of abstraction excludes the influence of, for example, the vehicle under-body geometry as well as the wheels and their housings on the vehicle's external aerodynamics. Specifically, these simplified bluff-body geometries preclude the study of more complex flow phenomena that manifest themselves around on-road representative vehicle shapes (Heft *et al.*, 2012). In light of this, less generic car models have been proposed: the MIRA and VW reference car (Le Good & Garry, 2004).

Recently, a new on-road representative car model for academic aerodynamic studies has been released. It is derived from two production vehicles, the BMW 3 series and Audi A4, illustrating its departure from abstract shapes, and is called the DrivAer model. Heft *et al.* (2012) introduce the model and, therefore, provide the first set of extensive experimental results for the geometry that can be configured with the fastback, notchback and estate rear-end geometry. Their data includes a drag coefficient, C_D, study (e.g. its Re dependence) and C_P traces along selected planes for a broad range of test cases: detailed/simplified under-body, with/without mirrors, with/without wheels and with/without ground simulation. This extensive wind tunnel data set not only serves as a benchmark for future experimental and numerical studies of the DrivAer model, but also provides insight into the drag sources. It was identified that the following geometry "additions" contribute most to drag, in order of decreasing importance: wheels, detailed under-body and mirrors (Heft *et al.*, 2012). Strangfeld *et al.* (2013) studied the unsteady flow characteristics of the wake aft of the DrivAer fastback model. At the roof's trailing edge, a low pressure peak, attributed to a vortex responsible for keeping the flow attached as it passes over the rear window, is detected. Also,

PIV, used to visualize the velocity field in a vertical symmetry plane, identified large-scale structures in the near-wake that cause a meandering free stagnation point. However, no dominant frequencies are associated with these identified structures (Strangfeld *et al.*, 2013). Meanwhile, Wieser *et al.* (2014), who experimentally studied the DrivAer model with both fastback and notchback rear-end, did manage to identify dominant frequencies in time-resolved rear surface pressure measurements. They detected the base pumping mode at a $Str_H \sim 0.07$ and the shedding frequency at a $Str_H \sim 0.2$ (Wieser *et al.*, 2014). Aljure *et al.* (2018) performed a LES study of the DrivAer model with fastback rear-end. Although primarily done to assess the advantage and disadvantage of using FVM based wall-modelled LES (WMLES) over wall-resolving LES (WRLES), unsteady flow phenomena around the vehicle, particularly in the rear wake, were analysed in the process. The following characteristic frequencies were found: the bubble pumping mode at $Str_H \sim 0.08$, the mirror vortex's frequency at $Str_H \sim 0.15$, the rotation frequency of the wheel at $Str_H \sim 0.27$ and the high shedding frequency of small-scale structures in the fastback area at $Str_H \sim 2.5$ (Aljure *et al.*, 2018). Further numerical studies of the DrivAer model include a FVM based RANS and detached eddy simulation (DES) study by Ashton *et al.* (2016), and a LBM based implicit LES investigation by Pasquali *et al.* (2016). These numerical investigations agree well with each other. For instance, they identified the vortices stemming from the A-pillar and mirrors, the counter-rotating vortices generated by the under-body, and the large wake at the vehicle's rear (Ashton *et al.*, 2016; Pasquali *et al.*, 2016). The studies, experimental and numerical, described above were performed at Re of $\mathcal{O}(10^6)$.

Bimodality has also been observed experimentally for on-road representative vehicles. One study looked at two production cars from Renault: the Mégane and the Kangoo. The Renault Mégane, a hatchback car, exhibits bimodality in its flow reattachment behavior over the slanted rear window at a yaw angle of $\pm 8.6^\circ$. It is believed that the large-scale flow reattachment is made possible by the separated shear layer's curvature increase with increasing yaw angle. Meanwhile, for

the Renault Kangoo, a van, bimodality in the base pressure distribution is observed at a yaw angle of $\pm 4^{\circ}$. The vehicle's blunt trailing edge excludes the possibility of flow reattachment as a cause. Instead, the base pressure distribution's reversal in the vertical direction is believed to be due to the wake instability associated with the squareback Ahmed body's horizontal wake bimodality. This means that at a yaw angle of $\pm 4^{\circ}$ the Renault Kangoo's wake exhibits two distinct static modes in the vertical direction. For both vehicles, the wake's bimodal behavior was observed through analysis of the vertical base pressure gradient and lift coefficient (Bonnavion *et al.*, 2017). In a further study, the effects of ground clearance, yaw, pitch and an open/closed engine air-intake on the large-scale vertical wake instability of three blunt based road vehicles, the Peugeot Partner, the Peugeot 5008 and the Citroën Berlingo, was investigated (Bonnavion *et al.*, 2019). It was concluded that the drag coefficient associated with a wake tilted toward the top of the vehicle base is larger than for a wake tilted away from the top trailing edge. The ground clearance, yaw, pitch and open/closed engine air-intake parametric study also highlighted that conditions favoring low under-body flow intensity tend to be associated with a wake tilted away from the top trailing edge. This means that changes in car configuration that alter the under-body flow intensity can force a bimodal switch in the vertical direction. The study also demonstrated that rear side plate appendages (i.e. passive flow control) can lower the drag value attained by sealing the engine air-intake a further 3.7%; the appendages namely force the wake, initially tilted toward the top trailing edge, to be tilted away from the top trailing edge (Bonnavion *et al.*, 2019).

2.2 Flow Control

Due to the relevance of bluff-body flows to many engineering applications, such as high-rise buildings buffeted by wind, underwater pipelines and, in this case, particularly the automobile, a vast amount of research has been conducted on bluff-body flow control for improved system performance. The control target could be to reduce structural vibrations, to minimize noise or, for road vehicles, to

lower drag. To effectively summarize the research done on bluff-body flow control for lower drag, a control method classification is needed. A common approach is to group the methods into passive, active open-loop and active closed-loop control (Fig. 2.8). Passive control involves actuator(s) that are permanently "on", as they have no power input; such control methods typically involve geometric modifications/additions to the bluff-body. Active open-loop control entails actuator(s) that do have a power source; hence, these controls can be turned "on" and "off". Active closed-loop control encompasses methods that use actuators with a power source that respond to signals measured by sensors. Passive and active open-loop control techniques are more widespread due to their easier implementation. However, the advent of improved micro-electromechanical systems, advances in control theory and the rapid rise of computer power has made active closed-loop control an appealing alternative in recent times. Additional control method groupings are (Fig. 2.8): 2D forcing versus 3D forcing, and boundary layer control versus direct wake control. The former is based on whether the actuation varies in the spanwise/azimuthal coordinate direction, while the latter is based on whether the control method delays separation or acts directly on the wake (Choi *et al.*, 2008). Gad-el-Hak (2000) provides a thorough review of flow control.

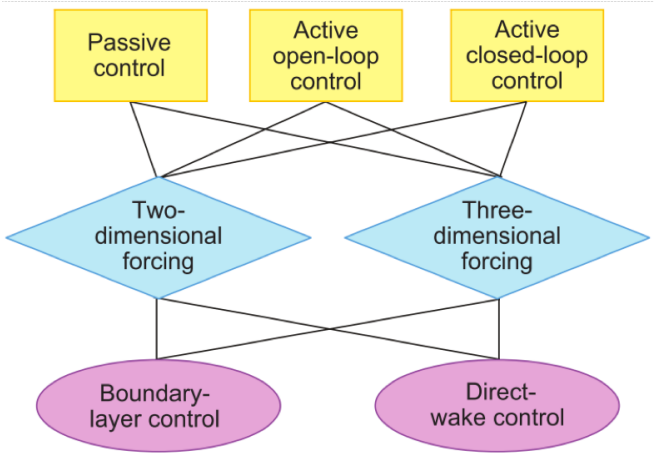


Fig. 2.8: Control method classification (*image reproduced with permission from Annual Reviews Inc.*) (Choi *et al.*, 2008)

2.2.1 Passive Control

In the passive control category, a broad range of geometrical modifications and additions have been successfully tested.

For one, in an experimental and numerical investigation on a 2D bluff-body with a blunt trailing edge known as the D-body, it was shown that tabs positioned at the lower and upper trailing edge can achieve a base pressure increase of more than 30%. The tabs perturb the 2D wake and, thereby, cause a spanwise phase mismatch in the vortex-shedding. This lowers the wake's vortical strength, which lengthens the recirculation bubble's length (Park *et al.*, 2006). By applying a segmented trailing edge to the D-body, a base pressure recovery of 38% is obtained. In this case, the geometry recesses formed by the segments generate pairs of counter-rotating vortices that replenish the fluid drawn from the base region, thereby reducing the quantity of fluid needed from the shear layers surrounding the wake and increasing the wake formation length (Petrusma, 1992). Studies on the D-body with a wavy trailing edge have also been performed. Here, the trailing edge causes vortex splitting, which is accompanied by spanwise variations in the vortex-shedding mode's phase. This increases the wake's formation length and raises the base pressure (Tombazis & Bearman, 1997).

Experimental work done on the Ahmed body showed that a splitter plate (Fig. 2.9a) placed in front of or downstream of the bluff-body can achieve a maximum drag reduction of 45% or 12%, respectively (Gilliéron & Kourta, 2010). Further experimental work done on the Ahmed body showed that a deflector positioned at the rear window's upper edge can, depending on the angle of the deflector, reduce drag by up to 9%. In essence, the deflector enlarges the rear window's flow separation region. This interferes with the counter-rotating longitudinal vortices' growth on the rear window's lateral edges (Fourrié *et al.*, 2011). Cylindrical roughness elements, when suitably positioned at the trailing edge, are able to suppress flow separation at the rear of the Ahmed body. These roughness elements force large-scale coherent streaks and this streaky base flow is able to "resist" the adverse pressure gradient. The modified wake topology is associated with a drag reduction of up to 10%

(Pujals *et al.*, 2010). A common successful passive drag device consists of extension plates at the bluff bodies rear that form a deep base cavity. Khalighi *et al.* (2001) document that the extension plates act similar to a boat-tail (Fig. 2.9b) by making the recirculation region narrower. The plates are shown to reduce the turbulence intensity within the wake by suppressing large-scale turbulent motions. In doing so, the drag on the Ahmed body is reduced by about 20% (Khalighi *et al.*, 2001). Also, Evrard *et al.* (2016) showed experimentally that the turbulent wake's asymmetry and, hence, bimodality is suppressed by the cavity. Their results indicate a 9% drag reduction (Evrard *et al.*, 2016). Meanwhile, Lucas *et al.* (2017)'s computational results correlate strongly with the experimental results from Evrard *et al.* (2016). For an Ahmed body with a curved rear body surface, vortex generators positioned close to the main separation point are shown to have a drag reducing effect. Typically, the vortex generators retard flow separation. However, here, they trigger early separation, which is accompanied by a larger recirculation bubble that suppresses the formation of the high drag counter-rotating longitudinal vortices. A maximum drag reduction of 12% is observed (Aider *et al.*, 2010). A similar drag reduction mechanism, where large-scale flow separation is encouraged and the longitudinal vortices are suppressed, was observed with the attachment of flaps to the Ahmed body's rear slanted surface. A maximum drag reduction of 25% was observed (Beaudoin & Aider, 2008). For an Ahmed body with part of its rear face slanted, a rounded trailing edge is able to suppress the 3D separation bubble on the slanted surface, thereby lowering drag by about 10% (Thacker *et al.*, 2012). A bio-mimetic drag reduction device for the Ahmed body was developed by Kim *et al.* (2016). Inspired by the feathers on a bird wing's suction surface that deflect upward when large-scale separation occurs for high angles of attack, Kim *et al.* (2016) applied a deflector plate to the slanted surface of the Ahmed body that is pushed upward when flow separates over it. The now "activated" deflector plate lowers the extent of flow separation and reduces the longitudinal vortices' strength, achieving drag reductions as large as 19% (Kim *et al.*, 2016).

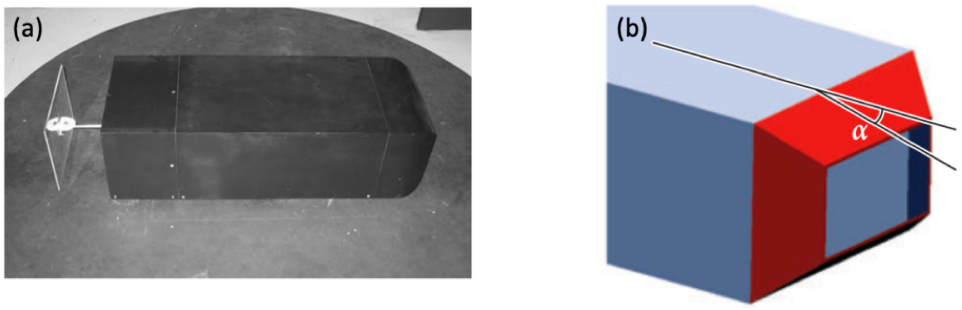


Fig. 2.9: Passive drag reduction on the Ahmed body using: (a) a splitter plate (*image reproduced with permission from Springer-Verlag*) (Gilliéron & Kourta, 2010), and (b) a boat-tail (*image reproduced with permission from Annual Reviews Inc.*) (Choi *et al.*, 2014)

2.2.2 Active Open-Loop Control

A rigorous review on actuators for flow control is provided by Cattafesta III & Sheplak (2011). The actuation techniques span methods that are fluidic based, surface motion based, plasma based and more (e.g. magnetohydrodynamic based). In the literature, the dominant actuation technique used for bluff-body flow control consists of the fluidic based zero-net-mass-flux (ZNMF) jet a.k.a. synthetic jet (see section 3.1).

Kim & Choi (2005) numerically investigated the flow past a circular cylinder that is perturbed at the upper and lower cylinder surfaces using blowing/suction profiles that vary sinusoidally in the spanwise direction. Between the upper and lower surfaces, both in-phase forcing and out-of-phase forcing were tested. Reynolds numbers from 40 to 3900 were considered. It was shown that for lower Reynolds numbers, in-phase forcing weakens or removes the von-Kármán vortex street, thereby lowering the average drag. Meanwhile, out-of-phase forcing seems to only be effective at higher Reynolds numbers where it influences the separating shear layer's evolution such that the mean drag is reduced (Kim & Choi, 2005).

For a cylindrical body aligned to the flow, Freund & Mungal (1994) experimentally looked at the capability of Coanda jet blowing to increase the base pressure and, thereby, lower drag. They found that the whole base flow domain can be significantly influenced by blowing through slot jets that are concentric with the bluff body's circumference. Both one and two slot jets were tested.

It is concluded that blowing through multiple slots is better than blowing through a single slot. In the best case, the recirculation bubble is suppressed and, through the Coanda jet blowing, replaced with entrained free-stream fluid. A maximum drag reduction of 30% is attained (Freund & Mungal, 1994). Similar tests were conducted by Morrison & Qubain (2009) of which the results were analysed in depth by Oxlade *et al.* (2015). They forced the wake formed by an axisymmetric bluff-body over a wide range of frequencies that went up to several times the shear layer instability frequency. This was done by using a high-fidelity speaker at the trailing edge to produce a ZNMF sinusoidal forcing. At low forcing frequencies of Strouhal number based on momentum thickness of $Str_\theta \leq 0.07$, undesired base pressure reduction was obtained due to shear layer amplification. Meanwhile, at higher forcing frequencies the recirculation zone's streamline curvature is changed such that there is a narrowing of the wake to produce a fluidic boat-tailing effect that raises the axisymmetric bluff-body's base pressure. This was understood by analysis of PIV data. Further investigation of the forcing's effects was done by modal decomposition techniques applied to pressure fluctuations. It was found that the jets pulsed at a high frequency produce vortex rings closely spaced in a row. Adjacent to these vortex rings are domains characterized by large shear that are associated with significant dissipation and prevent fluid entrainment, thereby producing a narrowed wake. Pressure recovery is found to be proportional to this vortex strength and an attenuation of base pressure fluctuations over all modes is also found. Overall, at forcing frequencies about five times larger than the shear layer instability frequency, the time-averaged base pressure rises by up to 35% (Morrison & Qubain, 2009; Oxlade *et al.*, 2015).

The steady, yet sinusoidally varying in the spanwise direction, blowing/suction technique applied by Kim & Choi (2005) on a cylinder was applied by Kim *et al.* (2004) on the 2D D-body to the top and bottom trailing edges. They performed both LES at a Re number based on body height of 4200, and wind tunnel experiments at Re numbers of 20000 and 40000. At all tested Re numbers it was found that the distributed forcing attenuates vortex-shedding and extends the recirculation

bubble's length, which leads to substantial base pressure recovery (Kim *et al.*, 2004). While for the previous study the jets were angled away from the D-body at 45°, in a further D-body study by Pasquetti & Peres (2015) synthetic micro-jet actuators positioned at the trailing edge were angled toward the D-body at 45°. Using a LES spectral solver and a Re of 20000, it was found that the jets confine the recirculation bubble producing an effect similar to that of a boat-tail; this leads to a rise of the base pressure (Pasquetti & Peres, 2015). Krajnović & Fernandes (2011) also performed a LES study of the flow behind the D-body using harmonic actuation consisting of top and bottom in-phase ZNMF jets. By forcing the vortex-shedding from the top and bottom trailing edges to be symmetric, at best a drag reduction of about 2.6% was achieved (Krajnović & Fernandes, 2011).

Littlewood & Passmore (2012) experimentally looked at the effect of steady blowing applied to the top trailing edge of a $1/4$ scale squareback vehicle called the Windsor model. Various angles were tested. Only when blowing was angled downward by approximately 45° relative to the horizontal plane was a drag reduction achieved. It was observed that most of the drag force modification is due to base pressure modifications. For the test case at Re of 3.01×10^6, drag reduction from blowing is determined to be a consequence of wake size reduction. This boat-tail effect is created by the upper shear layer's downward deflection. Active blowing is shown to have promise; unfortunately, it was concluded that application on production road vehicles is not possible due to the mass flow rate requirements (Littlewood & Passmore, 2012). Howell *et al.* (2003) also sought to improve the drag characteristics of the Windsor model using active open-loop forcing. Their technique consisted of bleeding flow from the base using varying amounts of porosity / different base porosity configurations. Generally, the drag reduction effect is larger for bigger bleed areas. Bleeding flow from the base is likely to force the low pressure domain downstream (Howell *et al.*, 2003).

Furthermore, Rouméas *et al.* (2009) performed 3D simulations using the LBM to assess the effect of continuous blowing at different angles positioned around the base periphery of the generic squareback Ahmed body, where only the flow past the rear is simulated. With blowing angles directed

toward the wake, the effect is to deflect the separating flow inward. This reduces the wake section and, therefore, the total pressure loss associated with the wake. Static pressure on the body's rear base rises. The efficiency of the open-loop control is also studied. It is found that control is most efficient for a jet velocity of 50% of the free-stream velocity and a wake-inward angle of 45°. For this actuation configuration, drag is reduced by 20%, while the actuation energy is seven times less than energy saved through control (Rouméas *et al.*, 2009). Pasquetti & Peres (2015), in addition to their D-body work, also simulated the flow past the squareback Ahmed body at a Re of 512000 using their LES spectral solver. With high frequency jets at the trailing edge pointing toward the Ahmed body base at 45°, a fluidic boat-tailing effect is produced that reduces wake cross-sectional area and, thereby, raises base pressure. The drag coefficient is reduced by 4.24% (Pasquetti & Peres, 2015). Barros *et al.* (2016) conducted an experimental study where the flow aft of the Ahmed body was forced with jets tangential to the main flow direction. A range of frequencies (Str_H of 0 to 12) and amplitudes was studied. They found that, at (broadband) actuation frequencies near the wake's vortex-shedding time-scale, wake entrainment is enhanced. This reduces the recirculation bubble's length, thereby increasing drag. Meanwhile, at actuation frequencies one to two orders of magnitude larger than the wake's vortex-shedding time-scale, the shear layers forming at the trailing edge are forced to deviate producing a fluidic boat-tailing effect, while turbulent kinetic energy in the shear layers is lowered reducing momentum entrainment toward the recirculation bubble. Combined, the mechanisms produce a base pressure increase, lowering Ahmed body drag. Through the addition of curved surfaces at the trailing edge, the jets deviate as a consequence of the Coanda effect; this strengthens flow deviation, which in turn enhances base pressure recovery. At best, a drag reduction of about 20% is attained (Barros *et al.*, 2016).

Englar (2001) conducted wind tunnel studies on a heavy vehicle (tractor-trailer) model with blowing slots positioned both at the trailer's leading edge and trailing edge (Fig. 2.10). Depending on the blowing slot combination selected, different control targets were achieved. For instance,

drag force was increased to aid braking. Also, by blowing solely through the rear top slot, the lift coefficient was augmented, thereby reducing tire rolling resistance. Meanwhile, blowing through the rear bottom slot only produced downforce for increased traction. Directional stability could be restored as well by activating a suitable side slot to produce a side force and a yawing moment. Most importantly, aerodynamic drag reductions of up to 80% were attained (Englar, 2001).

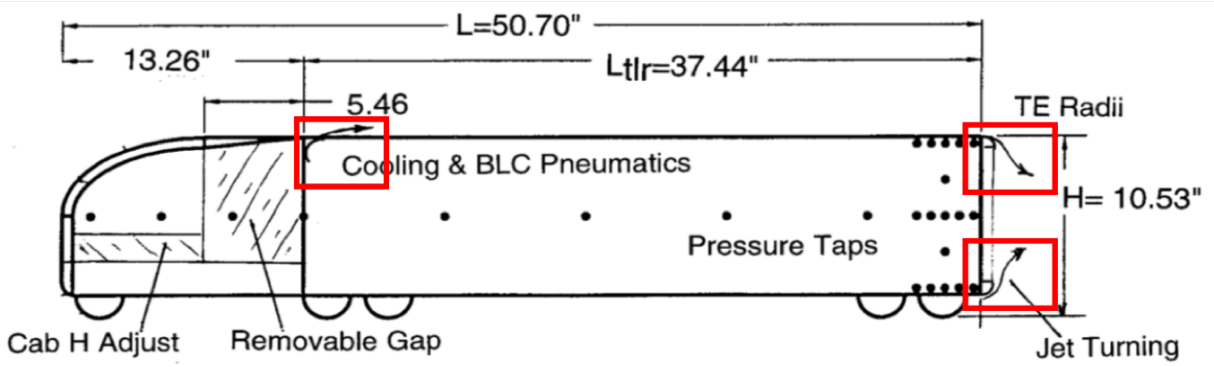


Fig. 2.10: Schematic of heavy vehicle (tractor-trailer) model with blowing slots, denoted by red rectangles, at the trailer's leading and trailing edge (Englar, 2001)

2.2.3 Active Closed-Loop Control

Compared to open-loop control, closed-loop control provides better actuation efficiency by permitting actuation parameters to react in real-time to changes in the flow field's coherent structures caused by actuation (Fig. 2.11). Closed-loop control is also more robust to disturbances and modelling uncertainties. Its implementation requires the identification of models that connect effects from the actuator with information provided by the flow field sensor. The derived model and accompanying controller must be chosen based on the flow's behaviour (Pastoor *et al.*, 2008).

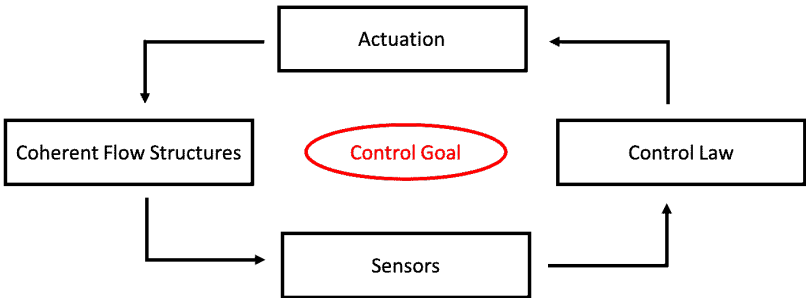


Fig. 2.11: Schematic of feedback control loop

One approach is to use controllers that are model independent. These controllers are typically

based on gradient methods, which are effective since the relationship between the actuator(s) and sensor(s) is characterised through a steady-state map that has an extremum. Henning & King (2005*a*) successfully employed an extremum seeking controller in their wind tunnel experiments on the D-body at Re_H of 40000. The designed controller synchronised vortex-shedding and, thereby, raised base pressure by a maximum of 35%. This was associated with a 10% drag reduction. It was also shown that this control approach required only about one half of the actuation energy that a robust controller designed using linear black-box models of the plant (i.e. wake) needed to achieve the same drag reduction. On the other hand, the extremum seeking controller behaved poorly at higher Re_H (Henning & King, 2005*a*). Beaudoin *et al.* (2006) also used an extremum seeking control method. In their case, the body under investigation within a wind tunnel setting at a Re_H up to 20000 is similar in shape to a backward-facing step; the bluff-body's separation point is altered through a rotating cylinder positioned at the trailing edge. Results from open-loop actuation clearly illustrate that the rotating cylinder delays separation. This reduces the size of the low pressure domain located aft of the body and, in turn, lowers drag. The goal of the extremum seeking controller was to find the point of lowest global energy consumed by the system i.e. to find the optimum balance between energy input for the actuator and energy saved from drag reduction. This was successfully implemented and it was also shown that the controller reacts well to external average flow modifications (Beaudoin *et al.*, 2006). Additionally, a slope-seeking feedback controller was developed by Henning *et al.* (2007) for wind tunnel flows past a D-body at Re_H ranging from 20000 to 60000. Here too a delayed vortex street formation resulted in a lengthened recirculation region aft of the D-body and a concomittant base pressure rise (Henning *et al.*, 2007). For the Ahmed body, Li *et al.* (2016) successfully employed a physically motivated opposition control strategy that combined a gradient feedback controller with open-loop periodic forcing consisting of slot jets to symmetrize the bimodal wake behind the Ahmed body and, thereby, achieve a modest recovery of base pressure (Li *et al.*, 2016).

In a further closed-loop control category, transfer functions are employed. These functions are based on the premise that the relationship between actuation (input signal) and flow field response (output signal) is dynamically linear. Controllers may then be designed using black-box models (Pastoor *et al.*, 2008). Roussopoulos (1993)'s transfer function based feedback control targeted attenuation (i.e. mode amplitude minimization) of vortex-shedding from cylinders for low Re in both wind tunnel and open water channel settings. It is possibly the earliest experimental application of closed-loop flow control, and used loudspeakers for actuation and velocity probes to measure flow response to actuation. The wake instability was successfully delayed, allowing the cylinder wake to remain stable for 20% higher Re when the following conditions were fulfilled: the flow field sensor(s) is positioned close to the cylinder's rear and, for wide cylinders, multiple sensors are positioned in the spanwise direction, thereby avoiding sensor local vortex-shedding attenuation (Roussopoulos, 1993). For the benchmark backward-facing step geometry, multiple transfer function based feedback control studies have been carried out over the past two decades. Black-box models, identified from wind tunnel data, were used by King *et al.* (2004), Henning & King (2005*b*), and Becker *et al.* (2005) to design robust H_∞-controllers for regulating the reattachment length of the flow behind the backward-facing step. Collectively, these studies showed that robust H_∞-controllers can enforce a desired flow reattachment length and compensate for flow disturbances up to a turbulent Re_H of 25000 (Becker *et al.*, 2005; Henning & King, 2005*b*; King *et al.*, 2004). Meanwhile, Dahan *et al.* (2012) employed linear feedback control in a LES study of the backward-facing step. The transfer function based controllers were designed to raise the base pressure, and thereby lower drag, by attenuating base pressure fluctuations. Actuation consisted of full-span ZNMF jets at the step's trailing edge and rear face, and pressure sensors to monitor flow response were positioned at the rear face. Both a laminar (2D) and turbulent (3D) case were investigated at momentum thickness based Re_θ of 280 and 1500, respectively. The disturbance attenuation based controllers produced sensible base pressure increases of approximately 70% for the laminar case and 20% for the turbulent case (Dahan *et al.*, 2012).

Several studies have also applied linear feedback control to the D-body. Henning & King (2005*a*) and Henning *et al.* (2007) developed a robust QFT-controller and H_∞-controller, respectively, to reduce the D-body's drag in wind tunnel settings for Re_H between 20000 and 60000. Unsurprisingly, the obtained drag reduction was a direct consequence of delaying the shear layers' roll-up, hence lengthening the recirculation bubble's length (Henning & King, 2005*a*; Henning *et al.*, 2007). Also, Dalla Longa *et al.* (2017) adopted the linear feedback control approach, using ZNMF jets as actuators and body-mounted pressure sensing, employed by Dahan *et al.* (2012) to successfully raise the D-body's base pressure by approximately 38% in an LES study. Here too shear layer roll-up was delayed, lengthening the recirculation bubble's length (Dalla Longa *et al.*, 2017). Transfer function based control for drag reduction has also been successfully applied to 3-D bluff-bodies that are more representative of road vehicles. For a 3D bluff-body, whose proportions are derived from the truck model investigated by Englar (2001), Pfeiffer & King (2012) identified dynamic black-box models from wind tunnel data and subsequently designed a robust multi-variable H_∞-controller to reduce the yaw moment and drag coefficient. Actuation consisted of Coanda jet blowing at the trailing edge and sensing was done via pressure sensors at the base. They successfully demonstrated the controller's ability to lower the drag coefficient by at least 20% and to minimize yaw moment disturbances from cross-wind gusts (Pfeiffer & King, 2012). Transfer function based feedback control was also applied by Brackston *et al.* (2016) on the squareback Ahmed body at high Re_H to suppress the wake's reflectional symmetry-breaking modes, and hence wake bimodality, through the use of oscillating flaps. Both streamwise and lateral forces were reduced. The controller's efficiency is particularly noteworthy; of the aerodynamic power saved, only 24% was needed for actuation (Brackston *et al.*, 2016). Finally, in a low Re_H LES study of the squareback Ahmed body, Evstafyeva *et al.* (2017) adopted the linear feedback control strategy used by Dahan *et al.* (2012) on the backward-facing step and Dalla Longa *et al.* (2017) on the D-body to attenuate base pressure fluctuations and, thereby, raise base pressure. The drag reduction associated with a 5% mean base pressure increase

was accompanied by the wake's re-symmetrisation from its (laminar) bifurcated state (Evstafyeva *et al.*, 2017).

The third closed-loop control category involves coherent structure models. Unlike black-box transfer function models that merely describe a linear connection between input and output signals, these model types, such as proper orthogonal decomposition (POD) and reduced-order vortex models, can directly capture the coherent structures that communicate the input signal's (i.e. actuation's) impact on the output signal (i.e. flow field response sensor). Thereby, the system's non-linear behavior is accounted for. By understanding the physical process(es) to be controlled, physically motivated controllers are typically developed (Pastoor *et al.*, 2008). Gerhard *et al.* (2003) employed a POD model of the system obtained from direct numerical simulation (DNS) data to successfully control the laminar vortex shedding behind a circular cylinder with a volumetric forcing term. Siegel *et al.* (2008) expanded on the use of POD by developing a low-dimensional model of the non-linear flow system around the circular cylinder using the double POD method. This form of the POD technique better accounts for an actuator's impact on the flow field. The low-dimensional model was successfully used to lower lift fluctuations by 90% in a feedback controlled simulation with forcing applied through transverse motion of the cylinder (Siegel *et al.*, 2008). Meanwhile, Pastoor *et al.* (2008) developed a reduced-order vortex model that accurately captures the shear layers' interaction with the wake behind the D-body. The low-order model was used as a guide for the development of a physically motivated feedback controller targeting phase control to force wake and shear layer dynamics to be desynchronized, thereby delaying vortex creation. Using ZNMF jets as actuators, the feedback controller was tested in a wind tunnel environment for Re_H between 23000 and 70000, and produced at best a base pressure increase of 40% (Pastoor *et al.*, 2008).

2.3 Computational Fluid Dynamics

External aerodynamics of road vehicles is a fluid flow problem set-up that is governed by the incompressible form of the continuity equation for mass conservation (Eq. 2.3.1) and the incompressible form of the Navier-Stokes equation for momentum conservation with body forces neglected as well (Eq. 2.3.2). This equation system is given below using tensor notation: u_i and x_i are the component of the velocity and spatial position vector in the i-th directon, t is time, ρ is density, P is pressure, and ν is the kinematic viscosity.

$$\frac{\partial u_j}{\partial x_j} = 0 \tag{2.3.1}$$

$$\frac{\partial u_i}{\partial t} + \frac{\partial u_i u_j}{\partial x_j} = -\frac{1}{\rho}\frac{\partial P}{\partial x_i} + \nu\frac{\partial^2 u_i}{\partial x_j^2} \tag{2.3.2}$$

A broad range of numerical methods exist to solve this equation system and they can be split into two groups: conventional "top-down" solvers that directly discretise the above macroscopic fluid dynamic equations, and particle-based "bottom-up" techniques that discretise microscopic or mesoscopic descriptions of the fluid flow. An example of a "bottom-up" approach is the mesoscopic particle based lattice Boltzmann method that through a stream and collide numerical algorithm recovers the behavior of the macroscopic continuity and Navier-Stokes equations (Krüger *et al.*, 2017; Viggen, 2014). This project uses the macroscopic finite volume method (FVM) with a suitable turbulence model. It also explores the use of wall-models to reduce the computational cost associated with fully resolving turbulent boundary layers.

2.3.1 Finite Volume Method

As the FVM is a well-established technique for numerically solving the macroscopic fluid dynamic equations, only a brief summary of its formulation is provided here. A rigorous overview is provided by Versteeg & Malalasekera (2007).

The FVM is based on dividing the flow domain of interest into many smaller control volumes

(CV), V_P, at the middle of which is a node where volume averages of flow quantities are stored. As the FVM is constructed to solve conservation equations, the first step is to recast the partial differential equations governing the problem in conservative form. For a general quantity, ϕ, whose diffusion coefficient is Γ_ϕ, the transport equation in conservative form is given by equation 2.3.3 where S_ϕ is a generic source term. Next, the equations are integrated in space over the CV and in time over a finite time-step, Δt. Volume integrals are subsequently converted into surface integrals using the divergence theorem. These surface integrals over the CV can be represented as sums over the CVs' faces. For equation 2.3.3, the above steps lead to equation 2.3.4 for a CV, V_P, with face surfaces, A_f, and respective face unit normal vectors, n_i, where S_c is the source term's constant part and S_P is the source term's non-linear part. Appropriate interpolation and differencing schemes are then applied to approximate the flow quantity's value at the CV face and to estimate the flow quantity's derivative at the CV face, respectively. Finally, the constructed linear algebraic equation system is solved for the discretised solution variables using a chosen solution algorithm. For the FVM based numerical solver used in this project, the selected interpolation and differencing schemes, as well as chosen solution algorithm are detailed in section 3.2.

$$\frac{\partial \rho\phi}{\partial t} + \frac{\partial \rho u_i \phi}{\partial x_i} - \frac{\partial}{\partial x_i}\Big[\rho\Gamma_\phi \frac{\partial \phi}{\partial x_i}\Big] = S_\phi \tag{2.3.3}$$

$$\int_t^{t+\Delta t} \Big[\Big(\frac{\partial \rho\phi}{\partial t}\Big)_P V_P + \Sigma_f (\rho u_i \phi)_f n_i A_f - \Sigma_f \Big(\rho\Gamma_\phi \frac{\partial \phi}{\partial x_i}\Big)_f n_i A_f\Big] \mathrm{d}t = \int_t^{t+\Delta t} (S_c V_P + S_P V_P \phi_P) \mathrm{d}t \tag{2.3.4}$$

2.3.2 Turbulence Modelling

The Re_H typical of the flows around road vehicles is of $\mathcal{O}(10^6)$. These flows are inherently turbulent and, thus, exhibit eddies across a broad range of time and length scales. A turbulence modelling method, whose eddy resolution and computational cost is suitable for the target application, needs to be selected.

At the lower end of the numerical cost spectrum lies Reynolds-averaged Navier-Stokes (RANS) turbulence modeling. Here, the focus is on the average flow and turbulence's effect on average flow properties. To obtain the RANS equations, the flow variables are decomposed into a mean and fluctuating component. The equations with decomposed flow quantities are subsequently time-averaged. This time-averaging results in the appearance of extra terms in the Reynolds-averaged equations. They are the result of interactions between the turbulent flow fluctuations and are called the Reynolds stresses. RANS turbulence modelling focuses on capturing the behavior of these Reynolds stresses. One of the best known models is the two-equation $k-\varepsilon$ model. RANS turbulence modelling is widely used in, for instance, the automotive industry where CFD complements wind tunnel tests (Versteeg & Malalasekera, 2007). A thorough review of RANS turbulence modelling, including its limitations, is provided by Wilcox (2006).

At the upper end of the computational cost spectrum is direct numerical simulation (DNS). Simulations in this category resolve the average flow as well as all turbulence scales; the word "model" is, therefore, not applicable here. The Navier-Stokes equations are solved using spatial grids of sufficient resolution to capture the Kolmogorov length scales (Fig. 2.12), where energy dissipation occurs, and using time steps small enough to capture the fastest flow fluctuations. Given DNS's computational cost, which scales with $Re^{2.25}$, it is only used in academia for flow set-ups that consist of simple configurations and geometries (Piomelli & Balaras, 2002; Pope, 2000). A comprehensive review on DNS is provided by Moin & Mahesh (1998).

The turbulence modelling approach selected for this project is large eddy simulation (LES) and is of intermediate computational cost. It provides the turbulence resolution needed by accurately capturing the time dependent behavior of the larger eddies that tends to be anisotropic, driven by the problem geometry, body forces and boundary conditions, while modelling the dynamics of the smaller eddies that are almost isotropic and at large enough Re_H essentially universal (Fig. 2.12). Also, LES remains computationally reasonable for the Re_H range investigated. An overview of its

implementation is provided below, and detailed reviews on LES are given by Meneveau & Katz (2000) and Piomelli (1999).

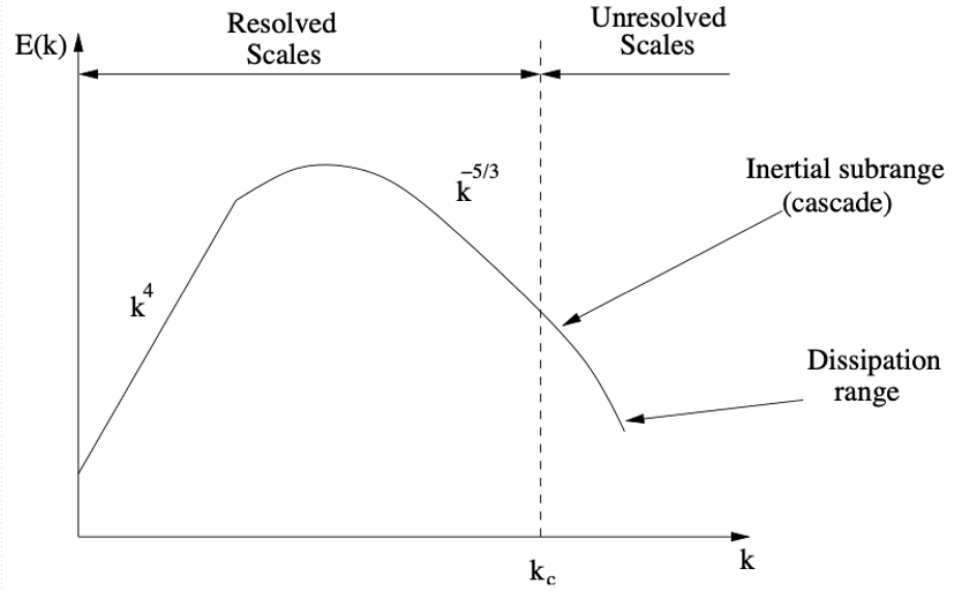


Fig. 2.12: Turbulence energy spectrum where k_c is the LES filter cut-off wave-number (Temmerman, 2004)

LES can be sensibly used to resolve all scales down to the Taylor microscale where viscosity begins to significantly affect the eddies' dynamics and the eddy scales are isotropic and, hence, the application of an eddy-viscosity based turbulence model becomes logical. The Taylor microscale is positioned at the higher wave-number end of the inertial subrange (Fig. 2.12) and its size scales with $Re_l^{-\frac{1}{2}}$ where l represents the integral (large) eddy length-scale (Tennekes & Lumley, 1972). To capture the dynamics of eddies whose size is greater than or equal to this order of magnitude, LES starts with an operation that spatially filters the Navier-Stokes equations. This spatial filtering is described by equation 2.3.5: $G(\boldsymbol{x},\boldsymbol{x'},l_e)$ is a filter function, l_e is an eddy cut-off length-scale, and ϕ is an arbitrary function. Variables with an over-bar have been spatially filtered (Versteeg & Malalasekera, 2007).

$$\bar{\phi}(\boldsymbol{x},t) = \int_{-\infty}^{\infty}\int_{-\infty}^{\infty}\int_{-\infty}^{\infty} G(\boldsymbol{x},\boldsymbol{x'},l_e)\phi(\boldsymbol{x'},t)\ \mathrm{d}x_1'\mathrm{d}x_2'\mathrm{d}x_3' \tag{2.3.5}$$

Through an unsteady flow calculation, LES resolves the eddies whose length-scale exceeds the l_e. In principle, l_e can be any value, which is the case in an explicit LES filtering scheme. However,

in the FVM, eddy length-scale cut-off values are intrinsically linked to the smallest cell size of the computational grid i.e. the eddy length-scale cut-off value is set implicitly. It is, therefore, common for the l_e to be of the smallest cell size's order of magnitude (Versteeg & Malalasekera, 2007). This means that the following relationship for the Taylor microscale, which was alluded to at the start of the paragraph, can be used as a reasonable estimate for the smallest cell size required to create a computational mesh appropriate for LES. Appropriate here denotes a mesh that resolves most of the anisotropic eddy scales. The relationship is derived under the assumption of a homogeneous and steady shear flow where turbulent energy production equals its viscous dissipation. A is taken to be an undetermined constant of $\mathcal{O}(1)$ (Tennekes & Lumley, 1972; Howard & Pourquie, 2002; Guilmineau *et al.*, 2018).

$$\lambda_T \sim 15^{\frac{1}{2}} A^{-\frac{1}{2}} Re_l^{-\frac{1}{2}} l \tag{2.3.6}$$

Additionally, while time-averaging momentum balance to derive the RANS equations creates additional quantities (i.e. the Reynolds stresses), spatially filtering the time-dependent and incompressible Navier-Stokes equations produces new terms in the (spatially filtered) equation system. These additional terms are called the sub-grid-scale (SGS) stresses, T_{ij} (Eq. 2.3.7) (Nicoud & Ducros, 1999):

$$T_{ij} = \bar{u}_i \bar{u}_j - \overline{u_i u_j} \tag{2.3.7}$$

The largest contributor to this stress is convective momentum transport caused by the unresolved eddies. As the small unresolved eddies are almost isotropic, Smagorinsky (1963) introduced a formula to account for their effect on the resolved flow field that is reminiscent of the Boussinesq hypothesis used to model the Reynolds stresses in RANS. This eddy-viscosity assumption used to construct the SGS stress model is given by equation 2.3.8, where $\bar{S}_{ij}$ represents the deformation tensor of the resolved flow field and ν_t is the eddy-viscosity (Nicoud & Ducros, 1999; Smagorinsky, 1963).

$$T_{ij} - \frac{1}{3} T_{kk} \delta_{ij} = 2\nu_t \bar{S}_{ij} \quad \text{where} \quad \bar{S}_{ij} = \frac{1}{2}\Big(\frac{\partial \bar{u}_i}{\partial x_j} + \frac{\partial \bar{u}_j}{\partial x_i}\Big) \tag{2.3.8}$$

To complete the above model and close the Navier-Stokes equation system for LES, an expression

for ν_t must be specified. The original expression proposed by Smagorinsky (1963), known as the Smagorinsky-Lilly SGS formalism, follows the form of Prandtl's mixing length model, and is given by equation 2.3.9: C_{SGS} is the Smagorinsky coefficient (Versteeg & Malalasekera, 2007; Smagorinsky, 1963).

$$\nu_t = C_{\mathsf{SGS}}^2 l_e^2 \sqrt{2\bar{S}_{ij}\bar{S}_{ij}} \tag{2.3.9}$$

An improved SGS stress model is used in the current project, as detailed in section 3.2.

2.3.3 Wall-Models

In academic turbulence research, LES has almost entirely displaced the RANS approach. However, in industrial engineering settings, LES has only made partial inroads. It is at most used in industry linked research centers and rarely influences the product engineering design process. The exorbitant computational resources associated with resolving high Re turbulent boundary layers fully is, to a large part, responsible for this situation (Larsson *et al.*, 2016). When one considers the computational cost associated with LES, the picture becomes clearer. Specifically, resolution requirements scale with $Re^{0.4}$ away from walls (i.e. computational cost depends only weakly on Re), but suddenly jump to $Re^{1.8}$ near / on approaching walls, where the turbulent eddy size reduces via a cascade edging closer to the Kolmogorov (i.e. dissipation) scale characteristic of the viscous sub-layer. The near-wall numerical resource scaling for LES approaches that of DNS, which is $Re^{2.25}$. In fact, Piomelli & Balaras (2002) demonstrate that a computational mesh suited to fully resolving a turbulent boundary layer of Re of $\mathcal{O}(10^6)$ in LES has 99% of its boundary layer grid points positioned in the inner region although the near-wall / inner-region only accounts for 10% of the whole boundary layer (Piomelli & Balaras, 2002; Reynolds, 1990; Piomelli, 2008). It is clear that solutions to this "near-wall problem of LES" must be adopted to make LES more viable for industrial applications and / or to investigate flow phenomena that occur over large time-scales (e.g. wake bimodality) (Larsson *et al.*, 2016).

In the past 50 years, a multitude of solutions to the "near-wall problem of LES" have been proposed. Although they are based on different arguments that target different objectives, they have one common global goal. They seek to model the inner region / near-wall boundary layer's turbulence, thereby eliminating the requirement to resolve any near-wall turbulent eddies. Merely the treatment of the turbulent boundary layer's outer region differs among the modelling techniques. Some model the outer region as well (e.g. detached eddy simulation), while others resolve the eddies there. The focus here is on methods that capture the outer boundary layer's energetic eddies, but model their dynamics in the near-wall region, thereby respecting a turbulent boundary layer's multi-scale characteristic (Larsson *et al.*, 2016). From this point forward, LES with these models "on" is called wall-modelled LES (WMLES) while LES that attempts to resolve the turbulent boundary layer fully is called wall-resolving LES (WRLES).

Different ways to categorize WMLES techniques are available. A useful approach is to group them into (a) hybrid LES/RANS and (b) wall-stress-models. In hybrid LES/RANS, the LES equations are only solved at a distance $x_2 \geq l_{\text{int}} > 0$, where l_{int} is an interface height, from the wall and below this interface the fluid flow governing equations themselves switch to the RANS equations. Meanwhile, with wall-stress-models, the LES equations are solved down to the wall with, typically, the wall-adjacent or wall-adjacent neighboring cell's flow information used to compute the wall shear stress, τ_w, via a RANS wall-model (Fig. 2.13). The computed τ_w is then used to compute a wall-model turbulent eddy viscosity, $\nu_{t,wm}$. This wall-model turbulent eddy viscosity, coupled with the impermeability condition, serves as the wall boundary condition, thereby modelling the no-slip condition. In this method, all the inner boundary layer dynamics, which consist of quasi-streamwise vortices, streaks, peak turbulence energy production and dissipation, are no longer part of the dynamical system; they are represented via a single value of τ_w. It is the RANS based wall-stress-model approach, where the LES and the wall-model region actually overlap, that is adopted in this work for WMLES (Larsson *et al.*, 2016).

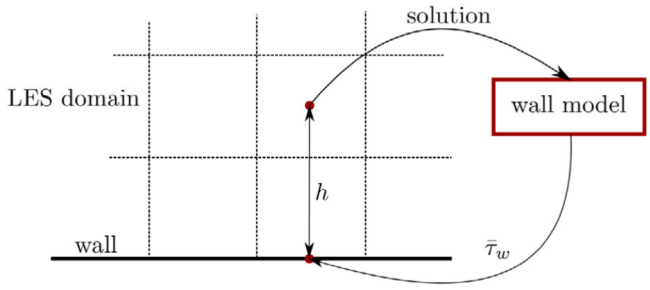


Fig. 2.13: Wall-stress-model application: LES flow information fed to wall-model for wall shear stress evaluation (*image reproduced with permission from Elsevier B.V.*) (Mukha *et al.*, 2019)

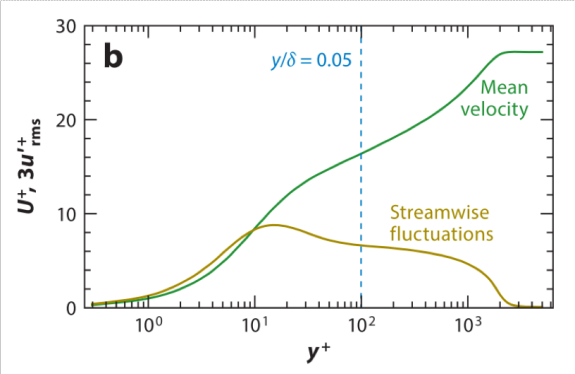


Fig. 2.14: Turbulent boundary layer's universal velocity profile (*image reproduced with permission from Annual Reviews*) (Bose & Park, 2018)

Most wall-stress-models are founded on momentum balance applied to a nearly parallel shear flow. By avoiding the resolution of turbulent eddies in the inner layer, the momentum balance equation can be viewed as low-pass filtered or ensemble-averaged in the inner turbulent boundary layer. Therein lies the resulting wall-stress-model's RANS nature; provided the near-wall grid is coarse enough for the near-wall cell(s) to contain a significant number of eddies, the wall-model must only account for the eddies' average effect i.e. statistical arguments hold (Fig. 2.15). The low-pass filtered / ensemble-averaged momentum balance equation for the streamwise direction of a wall-parallel flow is given below, where $<>$ denotes an averaged quantity (Larsson *et al.*, 2016; Piomelli & Balaras, 2002):

$$\frac{\partial < u_1 >}{\partial t} + \frac{\partial < u_1 >< u_j >}{\partial x_j} + \frac{1}{\rho}\frac{\partial < p >}{\partial x_1} = \frac{\partial}{\partial x_2}\left[(\nu + \nu_{t,wm})\frac{\partial < u_1 >}{\partial x_2}\right] \tag{2.3.10}$$

The most well-known wall-stress-model assumes equilibrium, where the pressure gradient and convection terms in equation 2.3.10 balance each other. An equilibrium assumption is not necessarily limiting in WMLES though. LES, which is active for up to 80% of the boundary layer's height, is namely perfectly capable of resolving any boundary layer non-equilibrium effects (e.g. the presence of an adverse pressure gradient). Thus, provided the LES in the turbulent boundary layer's outer region is accurate, the equilibrium wall-stress-model is given accurate instantaneous flow data, enabling the model to plausibly still account for non-equilibrium effects. Returning to equation 2.3.10,

a steady flow assumption is also applied. Thereby, the left-hand side of equation 2.3.10 is zero and an ordinary differential equation (ODE) is formed. This ODE can be solved directly to obtain $\nu_{t,wm}$. However, in terms of numerical resources, it is noticeably more cost effective to solve for $\nu_{t,wm}$ using an algebraic expression that is derived from the ODE (Larsson *et al.*, 2016). This algebraic expression has its roots in the works of Prandtl (1910) and Taylor (1916), who proposed that the turbulent boundary layer's universal velocity profile, illustrated in figure 2.14, should be divided into a laminar viscous sub-layer ($x_2^+ \leq 5$) and a fully turbulent section ($x_2^+ \geq 30$). The associated two-layer "law of the wall" is provided below, where $u_\tau = \sqrt{\tau_w/\rho}$ is the friction velocity, $x_2^+ = x_2 u_\tau/\nu$ is the wall normal distance in wall units, $u_1^+ = u_1/u_\tau$ is the wall parallel velocity in wall units, $\kappa = 0.42$ is the von Kármán constant and $B = 5.5$ (Larsson *et al.*, 2016; Spalding, 1961; Prandtl, 1910; Taylor, 1916):

$$< u_1 >^+ = \begin{cases} x_2^+ & \text{if} \quad x_2^+ \leq 5 \\ \frac{1}{\kappa}\ln(x_2^+) + B & \text{if} \quad x_2^+ \geq 30 \end{cases} \tag{2.3.11}$$

Although accurate in its modelling of the turbulent boundary layer velocity profile in the viscous sub-layer ($x_2^+ \leq 5$) and the fully turbulent section ($x_2^+ \geq 30$) (Fig. 2.14), this two-layer "law of the wall" (Eq. 2.3.11) suffers from two major drawbacks: (a) it requires two expressions, which are applicable for different x_2^+ ranges, to adequately describe the velocity profile and, more importantly, (b) it does not replicate the turbulent boundary layer's velocity profile to a satisfactory level in the buffer region ($5 < x_2^+ < 30$), a layer that, despite its importance to the boundary layer's turbulence energy budget, should be avoided for this wall-model according to best-practice guidelines. It is, therefore, desirable to have a single equation, which expresses the relationship $< u_1 >^+ (x_2^+)$, that is applicable over the entire x_2^+ range. Not only is the practical implementation of such an expression more convenient, but it allows a wider range of acceptable x_2^+ values for the wall-adjacent cell, as it models the critical buffer layer accurately too. Reichardt's law (Eq. 2.3.12), given below where $C = 7.8$, $B_1 = 11$ and $B_2 = 3$, is precisely such a formula that can model the entire turbulent boundary layer's universal velocity profile (Spalding, 1961; Mukha *et al.*, 2019; Reichardt, 1951;

Leschziner, 2015):

$$< u_1 >^+ = \frac{1}{\kappa}\ln(1 + \kappa x_2^+) + C\left(1 - e^{(-x_2^+/B_1)} - \frac{x_2^+}{B_1}e^{(-x_2^+/B_2)}\right) \tag{2.3.12}$$

In this project, both the log-law of the wall (Eq. 2.3.11) and a further single-equation wall-stress-model are adopted, as detailed in section 3.2.

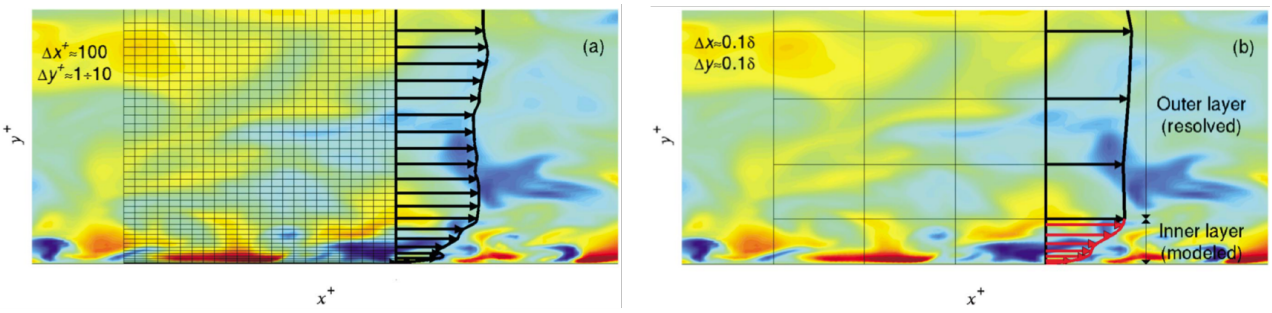


Fig. 2.15: Inner turbulent boundary layer with (a) WRLES and (b) WMLES (*image reproduced with permission from Annual Reviews*) (Piomelli & Balaras, 2002)

This section concludes with a summarized step-by-step overview of wall-stress-model application in FVM based CFD solvers. As mentioned above, the goal of wall-stress-modelling is to estimate and then enforce the τ_w at each wall boundary face (Mukha *et al.*, 2019).

1. First, the (spatially filtered) flow velocity is extracted from a cell centre within the domain where LES is active and is set equal to the ensemble-averaged flow velocity. Often the wall-adjacent or wall-adjacent neighboring cell's flow information is used (Fig. 2.13) (Mukha *et al.*, 2019).

2. Then, the sampled flow information is fed into the wall-stress-model (e.g. equation 2.3.11 or 2.3.12) to compute the wall shear stress, τ_w, for that cell's wall boundary (Mukha *et al.*, 2019).

3. Finally, using the following equation (Eq. 2.3.13), the wall-model turbulent eddy viscosity, $\nu_{t,wm}$, is calculated and, subsequently, applied as a boundary condition. Together with the impermeability condition, this models the no-slip boundary condition. Note, it is assumed here that direction $i = 2$ is the wall-normal direction and, therefore, Δx_2 represents the distance

of the sampling cell's centre, P, from the wall (Mukha *et al.*, 2019).

$$\nu_{t,wm} = \frac{\tau_w}{\left[(< u_{1,P} > /\Delta x_2)^2 + (< u_{3,P} > /\Delta x_2)^2\right]^{1/2}} - \nu \tag{2.3.13}$$

Having completed a brief literature review on several rather vast topics, it is now appropriate to be more specific and describe the precise methodologies used in this study.

Chapter 3

Research Methods

This chapter's first objective is to provide an overview of the control approach adopted in the project. Topics covered include the sensing configuration, the actuation layout, the feedback control loop and control strategy applied. The second objective of this chapter is to provide specific details on the flow solver used. Issues discussed encompass the chosen interpolation and differencing schemes, the implemented solution algorithm, the selected turbulence model, the adopted wall-models as well as any additional plug-ins used that do not come with the standard OpenFOAM functionality library. Finally, this section also serves to describe two model-order reduction techniques used to post-process the flow-field data: proper orthogonal decomposition (POD) and dynamic mode decomposition (DMD).

3.1 Control Strategy

There are two approaches to sense the rear wake's dynamics. The first method entails locating pressure (or velocity) probes directly in the wake. Although likely to pick-up strong signatures of the observable rear wake's dynamics, this approach is not very practical, particularly in experimental investigations where the apparatus for holding the probes will no doubt interfere with the fluid motion. The alternative approach is to use a sensing configuration mounted onto the rear of the

bluff-body. Aside from its feasibility in a computational test-bed, as is the case in this study, such an approach is well-suited for wind tunnel tests and real-world tests outside of the wind tunnel. Hence, in this investigation, rear body-mounted sensing is selected. The next question to ask is which quantity to sense: velocity or pressure. As body-mounted sensing is selected, the logical option is pressure. This is because velocity is zero on the body due to the no-slip condition. More importantly, pressure is the key drag component and the pressure field generated by the vortices propagates upstream making base pressure equivalent to drag. Finally, depending on the flow problem, different rear body-mounted pressure sensing configurations are used (e.g. top-to-bottom anti-phase sensing, lateral side-to-side anti-phase sensing or uniform base sensing). These are specified in the subsequent problem dependent chapters.

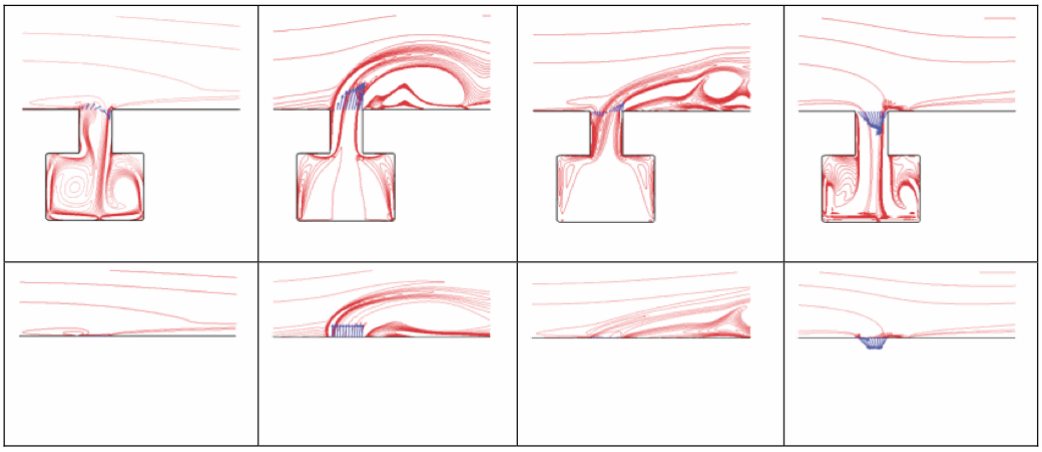


Fig. 3.1: Instantaneous spanwise vorticity contours (red) and velocity vectors (blue) for (top row) full cavity simulation and (bottom row) modelled synthetic jets (*image reproduced with permission from International Journal of Flow Control*) (Aram *et al.*, 2010)

Moving on, there are two actuation methodologies commonly implemented in active control studies for bluff-body drag reduction. The first consists of oscillating flaps positioned at the trailing edge of the bluff-body. Although a practical solution in experimental studies, as was done by Brackston *et al.* (2016), this approach is more difficult to achieve in computational investigations. One would have to implement a numerical solver that can handle moving meshes or integrate an oscillating body force term into the governing equations of fluid flow. Therefore, the second actuation technique is used in this investigation: zero-net-mass-flux (ZNMF) jets (a.k.a. synthetic

jets) positioned at the trailing edge of the bluff-body. They are well-suited for both experimental (e.g. Roussopoulos (1993) and Henning & King (2005*a*)) and numerical studies (e.g. Dahan *et al.* (2012) and Dalla Longa *et al.* (2017)). In the experimental domain, these jet flows can be formed by positioning small loudspeakers in a cavity. The vibrating membrane of the loudspeaker pulses air alternately in and out of the cavity and resonances in the cavity can help amplify the applied jet signal. Over one cycle, the net mass flow imparted to the system is zero, while the momentum given is non-zero (Glezer & Amitay, 2002). In the numerical domain, the details of the jet flow cavity, which would require very fine meshes and potentially the use of compressible codes to accurately model the motion of the diaphragm, need not necessarily be modelled. Leschziner & Lardeau (2011) as well as Aram *et al.* (2010) have shown that reasonably accurate (synthetic) jet flows can be obtained by specifying a time-varying top-hat incompressible velocity boundary condition on the exit-plane of the jet's cavity. This is visualized in figure 3.1 (Leschziner & Lardeau, 2011; Aram *et al.*, 2010). It is the ZNMF jet modelling strategy adopted throughout this study. Specifically, a time-varying top-hat velocity profile is applied on designated surfaces as a transient boundary condition. Also, depending on the bluff-body flow problem under investigation, different configurations of the ZNMF jets are adopted (e.g. top-to-bottom anti-phase forcing, lateral side-to-side anti-phase forcing or uniform trailing edge forcing). As with the precise sensing configuration, applied actuation layouts are detailed in the subsequent problem specific chapters.

Having identified the sensing and actuation techniques, it is now appropriate to detail the control strategy. In this investigation, the control technique is based on the premise that a mean (rear) base pressure increase and concomitant mean drag reduction can be achieved by altering the temporal fluctuations of the (rear) wake flow field. This premise has been justified by Dalla Longa *et al.* (2017). In their work, equation 3.1.1, which is essentially Newton's second law of motion and describes the sources of drag, was derived through an unsteady control volume analysis of the flow around a bluff-body. This time-dependent equation offers more insight than its steady

version, which is widely used in the automotive industry for drag analysis (Hucho, 1998; Van Dam, 1999). The left-hand-side term represents the drag force and the first term on the right-hand-side denotes the stagnation pressure loss. Meanwhile, the second term on the right-hand-side includes a streamwise velocity deficit component, a vortex induced drag component and a Reynolds-stress contribution. The control volume's x-momentum rate of change is denoted by the third term on the right-hand-side.

$$D(t) = \int_{\text{wake}} \Delta p_0(t)\mathrm{d}A + \frac{1}{2}\rho \int_{A_{\text{exit}}} (U_\infty^2 - u_1(t)^2 + u_2(t)^2 + u_3(t)^2 - 2 < u_1'(t)^2 >)\mathrm{d}A + \rho \frac{\partial}{\partial t} \int_V u_1(t)\mathrm{d}V \tag{3.1.1}$$

By decomposing the terms in equation 3.1.1 into a mean $< () >$ and fluctuating part ()', and then time-averaging the terms (i.e. one applies a process similar to the one used for obtaining the RANS equations), it is possible to discern which terms need to be manipulated to obtain a reduction of the mean drag, $< D(t) >$. One may try to alter the stagnation pressure loss or the term accounting for the control volume's rate of change of x-momentum. However, the fluctuating component of these terms disappears upon time-averaging, making the manipulation of their fluctuations ill-suited to mean drag reduction. The quadratic nature of the second term on the right-hand-side of equation 3.1.1 means that fluctuating terms of the velocity components remain upon time-averaging: $(u_2'(t)^2 + u_3'(t)^2 - u_1'(t)^2 - 2 < u_1'(t)^2 >)$. This means that a reduction in mean drag can be obtained by reducing the wake's velocity fluctuations in directions normal to the streamwise direction or increasing the velocity fluctuation magnitude in the streamwise direction, a plausible explanation for the high drag reduction obtained in Oxlade *et al.* (2015)'s experiments using streamwise slot jet actuation (Dalla Longa *et al.*, 2017). Having identified that mean drag reduction may be obtained through reduction of wake velocity fluctuations, it must be recognized that the measurement of such wake velocity fluctuations is not feasible without significantly disrupting the wake flow. As a working alternative, this project, therefore, targets the attenuation of rear base pressure fluctuations (as was alluded to previously) with the assumption that lowering base pressure fluctuations will lead to an

indirect lowering of wake velocity fluctuations. This assumption is valid, as pressure fluctuations are directly linked/coupled to velocity fluctuations through Newton's second law of motion or, more specifically, the Navier-Stokes equation (Eq. 2.3.2).

With the sensing technique, the actuation method and the control target set, it is now possible to describe the design process used to obtain the single-input single-output (SISO) system's feedback control laws for pressure drag reduction. To begin, the design of these feedback control laws is done in the frequency domain using Laplace transforms, where s is the Laplace transform variable and represents $i\omega$. This implies that the following assumptions apply to the system at hand: it is linear, causal and time-invariant (Astroem & Murray, 2010). The second and third conditions are deemed to be met by the high Re aerodynamic wake flow; the flow field is statistically stationary. It is, merely, the stipulation of linearity that could prove to be difficult to satisfy by a system that is governed by the inherently non-linear Navier-Stokes equations. As such, the assumption of linearity is checked when developing the control law (Dahan, 2013; Dalla Longa, 2018; Evstafyeva, 2018).

Crucially, operation with Laplace transforms means that one can relate system-input to system-output through a transfer function, which is a more compact representation of the system than its corresponding state-space description, another less condensed way to represent a system's possible configurations (Astroem & Murray, 2010). The first step, therefore, in the feedback control law development is to characterize the wake's response to actuation in the form of a transfer function. Specifically, by performing harmonic open-loop actuation, one needs to determine the transfer function, $G(s)$, that relates synthetic jet input, $U_j(s)$, to base pressure output, $F_p(s)$, as depicted in figure 3.2. For completeness, figure 3.2 also depicts terms that cancel-out during the subsequent control law derivation: $n(s)$, which represents surrounding flow noise in the form of upstream boundary and shear layer perturbations, and $H(s)$, which is the transfer function that determines the wake's response to those disturbances (Dahan, 2013; Dalla Longa, 2018; Evstafyeva, 2018). Returning to the construction of $G(s)$, once the harmonic open-loop forcing input and correspond-

ing wake pressure output data at various forcing frequencies and amplitudes is collected, one can perform system identification on the data to compute $G(s)$. In this work, $G(s)$ is determined by evaluating its gain, $|G(s)|$, and phase, $\angle G(s)$, curve from the collected data. The process used is called the correlation method, where at a given ZNMF jet (input) forcing frequency, ω_f, and forcing amplitude, $U_{j_{in}}$, the measured base pressure (output) signal, C_{PB}, is first decomposed into a Fourier series. Subsequently, the magnitude and phase associated with the Fourier component that oscillates at the forcing frequency, ω_f, is extracted (Astroem, 1975; Ljung, 1987). This system identification method is encapsulated in equation 3.1.2 and works well for (assumed) linear systems in which purely harmonic input actuation should produce a system response that is dominated by the forcing frequency once transients have died away. With the raw data representing $G(s)$ collected, a low-order mathematical fit to the frequency response data (frd) is computed using the MatLab command "fitfrd" (Dahan *et al.*, 2012).

$$a_f - ib_f = \frac{2}{T_f}\int_{T_f} C_{PB}(t)e^{-i\omega_f t}\mathrm{d}t \quad \rightarrow \quad |G(s)| = \frac{\sqrt{a_f^2 + b_f^2}}{U_{j_{in}}}, \quad \angle G(s) = \tan^{-1}\left(\frac{a_f}{b_f}\right) \tag{3.1.2}$$

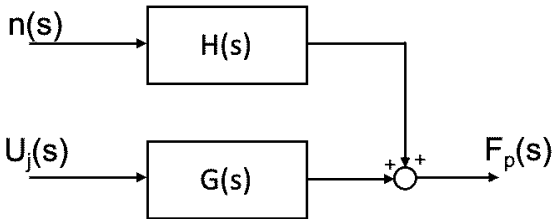


Fig. 3.2: Open-loop system used for evaluation of $G(s)$ with system identification

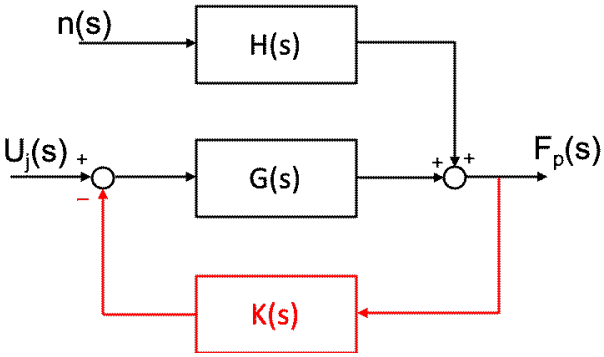


Fig. 3.3: Closed-loop system with control law $K(s)$ targeting pressure fluctuation attenuation for base pressure increase

Following the derivation of a low-order model, $G(s)$, that represents the wake's linear response to forcing, a control law, $K(s)$, may be computed to dictate the wake's behavior. The controller's position in the targeted negative feedback system is depicted in figure 3.3. By dividing the system's closed-loop characteristic, $F_p(s)_{CC}$, where "CC" denotes closed-loop control is ON, with its open-

loop counterpart, $F_p(s)_{OC}$, where "OC" indicates open-loop control is active, equation 3.1.3 is obtained. This equation returns the so-called sensitivity transfer function, $S(s)$, and illustrates that a reduction in base pressure fluctuation (for mean base pressure increase) can be obtained by ensuring that $|S(s)| < 1$ (Dahan *et al.*, 2012; Dahan, 2013). In control system design, reducing the magnitude of the frequency response uniformly over the entire spectrum is not possible. Instead, a waterbed effect pervades the system, where a reduction in frequency response magnitude over a targeted frequency range is offset by a concomitant increase in frequency response magnitude over other spectrum portions (Astroem & Murray, 2010). It is, therefore, paramount that attenuation of the system response (i.e. maintaining $|S(s)| < 1$) occurs over the frequency range where the unforced flow dynamics are strongest and this is achieved by tuning $K(s)$. In this work, $K(s)$, is composed of a second-order controller, $K_2(s)$, multiplied by a band-pass filter, $K_{BP}(s)$, as depicted in equation 3.1.4. The second-order controller is designed such that ω_n is set equal to the frequency of the dominant flow instability thereby damping it out with ζ, while the band-pass filter is specified such that the high-pass filter with ω_l removes mean actuation effects and the low-pass filter with ω_h removes high-frequency turbulent flow oscillations (Dalla Longa, 2015). After the derivation/tuning of the control law, $K(s)$, is done in the Laplace domain, it is checked for stability by plotting its Nyquist curve and ensuring that there are no net clockwise encirclements of the point (-1,0) (Astroem & Murray, 2010). Finally, $K(s)$ is converted from its Laplace transform description, in which it is easier to tune the controller, back into state-space form for implementation into the CFD solver, as described in section 3.2.

$$\frac{|F_p(s)_{CC}|}{|F_p(s)_{OC}|} = |S(s)| = \frac{1}{1 + G(s)K(s)} \tag{3.1.3}$$

$$K(s) = K_2(s)K_{BP}(s) = \frac{1}{s^2 + 2\zeta\omega_n s + \omega_n^2} \frac{s\omega_h}{(s + \omega_l)(s + \omega_h)} \tag{3.1.4}$$

3.2 Flow Solver - OpenFOAM

For this simulation based flow investigation, the open-source numerical toolbox OpenFOAM is used. Written in C++, it provides a host of finite volume method based solvers for fluid dynamic problems that span buoyancy-driven flows, compressible flows, combustion-driven flows, multiphase flow, etc. The reason for its choice in this project is the ability to use unstructured meshes for more complex bluff-body geometry simulations, and its widely used and, therefore, validated solvers. There is also an extensive amount of user-manuals available, which makes its use more amenable should in-house knowledge about the solver be lacking. Furthermore, usually the solver name provides an indication of the fluid equation forms solved and/or solution algorithms employed. For example, potentialFoam solves Laplace's equation for the velocity potential from which the velocity field is then computed.

The first step in setting-up the OpenFOAM computational fluid dynamics problem is the selection of the appropriate solver(s). As discussed previously, for external aerodynamics, one seeks solutions to the incompressible form of the continuity and Navier-Stokes equations (Eq.2.3.1-2.3.2). As such, a solver with suitable pressure-velocity coupling must be chosen, since there is no explicit equation for pressure despite its appearance in the Navier-Stokes equation (Eq. 2.3.2). For aerodynamics applications without the presence of porous media and/or rotating components, suitable OpenFOAM solvers are simpleFoam, pisoFoam and pimpleFoam. Each of these "packages" offer desirable iterative guess-and-solve pressure-velocity coupling algorithms. SimpleFoam is used exclusively for steady-state problems, while pisoFoam and pimpleFoam are suitable for transient problems. The nature of the (steady-state) simpleFoam solver makes it ideal for RANS simulations that, in this work, are used to initialise the more complex time-dependent 3D turbulent flow problems that are subsequently propogated forward in time using pisoFoam or pimpleFoam based LES (see chapters 5 and 6). SimpleFoam relies on the Semi-Implicit Method for Pressure Linked Equations (SIMPLE) algorithm developed by Patankar & Spalding (1972). The core of this iteration algorithm is the

solution of the pressure Poisson equation (Eq. 3.2.1).

$$\frac{1}{\rho}\frac{\partial^2 P}{\partial x_j^2} = -\frac{\partial^2 u_i u_j}{\partial x_i \partial x_j} \tag{3.2.1}$$

It is derived by taking the divergence of the incompressible Navier-Stokes equation (Eq. 2.3.2) and applying the incompressible continuity condition that $\partial u_i/\partial x_i = 0$ (Eq. 2.3.1). Solution of the pressure Poisson equation in so-called "outer correction" loops leads to the pressure correction term, p', that is used to "correct" the guessed pressure field to one closer to the true pressure distribution. A flow chart of the SIMPLE algorithm for a 2D flow can be found in Appendix A (Versteeg & Malalasekera, 2007). Moving on, pisoFoam uses a derivative workflow of the SIMPLE algorithm, namely the Pressure Implicit with Splitting Operators (PISO) scheme that was developed by Issa (1986). This scheme, well suited for transient incompressible flows, consists of a second Poisson equation based pressure correction step that is iterated over. Meanwhile, the first correction step is identical to the one in the SIMPLE algorithm. More specifically, for the PISO algorithm there is an "outer correction" loop that is analogous to the one present in the SIMPLE workflow, as well as an "inner correction" loop, both for the pressure term (Issa, 1986). Appendix A contains a workflow for the PISO algorithm applied to a 2D flow problem (Versteeg & Malalasekera, 2007). The final solver to consider is called pimpleFoam. Its pressure-velocity coupling algorithm is a hybrid of the SIMPLE and PISO numerical workflows. The earliest reference to the PIMPLE solution scheme is made in the paper by Barton (1998) who manipulated and added to the baseline SIMPLE and PISO codes to test for numerical performance and accuracy. The PIMPLE solver is in fact identical to its PISO counterpart if the number of "outer correction" loops is kept at unity. More importantly, through the use of more than one "outer correction" loop, the unique PIMPLE algorithm offers superior stability to the PISO code for large time-step sizes, albeit at a higher numerical cost (Barton, 1998). Overall, in this study the pimpleFoam solver with one "outer correction" loop was selected by default for transient simulations. Therefore, in essence the PISO solver was used. But, doing so through the pimpleFoam solver offered more room for stabilization should mesh quality (e.g. skewness and

non-orthogonality) be poor (Versteeg & Malalasekera, 2007; Barton, 1998).

Having identified the solver, attention may now be turned towards the differencing schemes adopted for the various terms in the governing equations of fluid dynamics. To begin, the flow is initialized with first order schemes. Although these schemes offer poor accuracy, they provide good solver stability, an imperative when initialising the flow field. To achieve the first order accuracy, the transient term was solved using the Euler method, while the gradient, divergence and Laplacian terms were solved for using Gauss upwind or central differencing in conjunction with limiters to avoid overshoots and undershoots, thereby keeping the initialized flow field total-variation-diminishing (TVD). Once the flow field was initialized, the numerical schemes were switched from first order accuracy to second order accuracy. Specifically, the transient term was solved for using the Crank-Nicolson scheme and the limiters for the gradient, divergence and/or Laplacian terms were reduced or switched off entirely. If the created mesh is non-orthogonal, then non-orthogonal correctors were also applied to, for instance, the computation of the Laplacian term (Versteeg & Malalasekera, 2007). More specifically, in this study a maximum mesh non-orthogonality of just over 70° was reached and as such a non-orthogonal correction scheme with limiting coefficient of 0.7 was used to make sure that the non-orthogonal corrector does not de-stabilize the solution.

Moving on, the next item to select for the simulation is the appropriate turbulence model. As for the previous two considerations above, this decision step is broken down into two parts: (1) flow field initialization, and (2) flow field propagation forward in time. In conjunction with SimpleFoam and first order schemes, the flow field is typically initialised with the very numerically robust Spalart-Allmaras single equation RANS model (Spalart & Allmaras, 1992). The word "typically" is used, as this form of flow field initialization is only applied for inherently 3D flow cases. For quasi-2D flow scenarios, stable first order accurate schemes are used, but within an LES turbulence formalism, as is subsequently done with second order accurate schemes following flow initialization. More specifically, for all time-advancing second order accurate simulations, the Wall-Adapting Local Eddy-viscosity

(WALE) sub-grid-scale LES turbulence model is used (Nicoud & Ducros, 1999). Developed by Nicoud & Ducros (1999), this sub-grid-scale turbulence model offers advantages over the classical Smagorinsky-Lilly model (1963) described previously and even its improved counterpart, the dynamic Smagorinsky model (1991) where the Smagorinksy coefficient, C_{SGS}, is allowed to vary in both space and time (Smagorinsky, 1963; Germano *et al.*, 1991). Based on the square of the velocity gradient tensor, WALE ensures the following:

1. It correctly accounts for the rotation rate and strain of the finest resolved turbulent fluctuations. This facilitates a more accurate representation of the energy transfer from the resolved to the unresolved scales and, in turn, the correct energy dissipation cascade (Nicoud & Ducros, 1999).

2. It replicates the correct x_2^3 scaling of the turbulent eddy viscosity, ν_t, near the wall where the dominating stresses are viscous and is naturally zero directly at the wall where the no-slip condition holds (Nicoud & Ducros, 1999).

3. It is a model that can handle both structured and unstructured meshes, both of which are used in this dissertation (Nicoud & Ducros, 1999).

4. It has also proven to handle laminar-to-turbulent flow transitions well (Nicoud & Ducros, 1999).

A further element to consider is which wall-model(s) to use. As mentioned in section 2.3.3, one wall-model construction used is the two-layer "law of the wall". Due to its poor performance in the buffer region of the turbulent boundary layer, a further wall-model is used. It is the single equation model called Spalding's law of the wall (Eq. 3.2.2) where the constants κ and B take on the same value as for the two-layer "law of the wall" (Eq. 2.3.11) (Spalding, 1961). Like Reichardt's law, it correctly captures the turbulent boundary layer's velocity profile across the viscous, buffer and log region. The reason why both the two-layer "law of the wall" (Eq. 2.3.11) as well as Spalding's

single equation law of the wall (Eq. 3.2.2) are used in this project, as opposed to for instance Reichardt's law (Eq. 2.3.12), is one of practicality. The two-layer "law of the wall" and Spalding's law are already programmed into the OpenFOAM library.

$$x_2^+ =< u_1 >^+ +\mathrm{e}^{-\kappa B}\Big[\mathrm{e}^{\kappa < u_1 >^+} - 1 - \kappa < u_1 >^+ - \frac{1}{2}(\kappa < u_1 >^+)^2 - \frac{1}{6}(\kappa < u_1 >^+)^3\Big] \quad (3.2.2)$$

It is also important to discuss two OpenFOAM plug-ins that were used during this project. To apply dynamic time-varying boundary conditions when doing closed-loop flow control, the plug-in swak4Foam was used. It stands for "SWiss Army Knife for OpenFOAM". The developers of this plug-in assert that, just like the army knife, it is not the best tool for a given task, but simply the most convenient, as opposed to, for example, changing the OpenFOAM source code. A further plug-in used is ccm26ToFoam. In chapters 5 and 6, the unstructured meshes are generated using the commercial solver Star-CCM+. This plug-in allows the meshes to be converted to OpenFOAM format.

Finally, every solver that can be used on a high performance computing (HPC) cluster operates at an optimum where the task division between cores complements the communication time between each core best. To obtain an approximation for the mesh cell count per core at which parallelisation is still beneficial, a scalability study was, therefore, conducted. Without giving too much consideration to the test-case used for this (it happens to be the D-body geometry of chapter 4), the subsequent graph (Fig. 3.4) allows the following rules-of-thumb to be deduced:

1. For mesh sizes of ≤ 10 million cells one can see an optimum decomposition ratio of $\sim 30,000$ cells per core.

2. Meanwhile, for mesh sizes of > 10 million cells one sees the best trade-off between task parallisation speed-up and communication time between cores at $\sim 35,000$ cells per core.

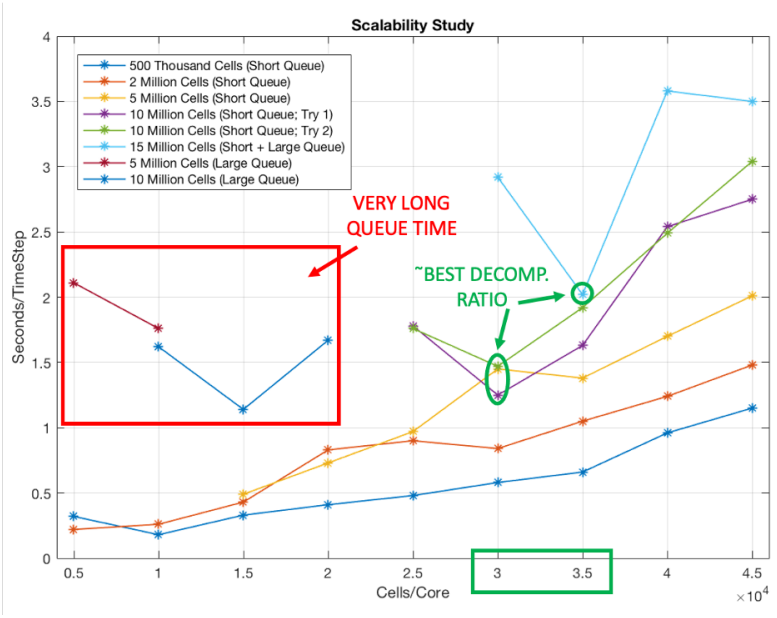


Fig. 3.4: Generic rule-of-thumb scalability of the OpenFOAM solver

3.3 Post-Processing Techniques

Given the flow complexity, expressed through broad spatio- and temporal-scales, that even simple flow configurations generate (e.g. flow past air-foils and cylinders or wall-bounded planar flows, etc.), it is indispensable to be able to apply post-processing techniques that allow the deconstruction of the generated flow field into physically important features, or so-called modes. This facilitates more targeted flow control algorithms and/or flow control targets, as one is creating a low-dimensional form of a very high-dimensional problem. Extraction of dominant flow modes can be achieved based on various criteria (e.g. frequency) and it is either data-based or operator-based. This work uses two data-based modal decomposition techniques for model-order reduction: (1) proper orthogonal decomposition (POD) and dynamic mode decomposition (DMD) (Taira *et al.*, 2017).

POD, also known as e.g. principal component analysis in statistics, was first introduced into the fluid dynamics field by Lumley (1967) where it has been and is heavily used to extract dominant flow modes, which includes coherent structures. It does so by providing an objective algorithm whose

target it is to break down a data set into a minimal number of basis functions / modes that collectively capture the pertinent / majority of the flow energy. In other words, POD identifies modes and ranks them in terms of energy content (Lumley, 1967; Berkooz *et al.*, 1993). Importantly, it does not take into account the dynamical relevance of the mode in its energy ranking. This is an issue addressed by the DMD method, as discussed subsequently. Returning to POD, the formal definition of its decomposition is provided below. A representation of the flow field through a Fourier series of basis functions with time-dependent expansion coefficients, where $\boldsymbol{q}$ represents a general data flow variable vector (e.g. pressure or velocity), ϕ the mode, and a the mode's expansion coefficient (Taira *et al.*, 2017).

$$\boldsymbol{q}(x_i, t) = \sum_j a_j(t)\phi_j(x_i) \tag{3.3.1}$$

It is important to note that the separation of time and spatial dependency is a result of modern POD applications. In the past, the dependencies were solely associated with the mode. Moving on, classical POD mode computation relies on first collecting a time series of finite dimensional flow field snapshots from which the mean of the considered variable is subtracted i.e. only the flow fluctuations represented by the data vector $\boldsymbol{y}$ are of relevance (Taira *et al.*, 2017).

$$\boldsymbol{y}(x_i, t) = \boldsymbol{q}(x_i, t) - \bar{\boldsymbol{q}}(x_i) \in \mathbb{R}^n, \quad t = t_1, t_2, ...t_m \tag{3.3.2}$$

With $\boldsymbol{y}$ in hand, the next step in classical POD computation is to compute the co-variance matrix, **R**. This is defined below where there is a summation over the m time series flow field snapshots (Taira *et al.*, 2017).

$$\mathbf{R} = \sum_{j=1}^{m} \boldsymbol{y}(t_j)\boldsymbol{y}^T(t_j) = \mathbf{Y}\mathbf{Y}^T \in \mathbb{R}^{n\times n} \tag{3.3.3}$$

Y denotes the m snapshots collated into a matrix of the following form (Taira *et al.*, 2017):

$$\mathbf{Y} = [\boldsymbol{y}(t_1), \boldsymbol{y}(t_2), ...\boldsymbol{y}(t_m)] \in \mathbb{R}^{n\times m} \tag{3.3.4}$$

With the co-variance matrix **R** defined, it is now possible to state the problem whose solution will lead to the best set of ortho-normal basis functions that represent the flow field. More specifically,

the problem takes on an eigenvalue-eigenvector form as stipulated below, where ϕ_j represents the mode(s) and λ_j the energy associated with each mode (the factor $1/m$ has been included in the variable λ_j) (Taira *et al.*, 2017):

$$\mathbf{R}\phi_j = \lambda_j \phi_j, \quad \phi_j \in \mathbb{R}^n, \quad \lambda_1 \geq ... \geq \lambda_n \geq 0 \tag{3.3.5}$$

One may choose to directly solve this eigenvalue-eigenvector problem for the POD modes, but an indirect method to the POD modes that is more robust against machine round-off errors is the singular value decomposition (SVD) of $\mathbf{Y}$. This matrix breakdown is illustrated below for $m < n$, where $\mathbf{\Phi} \in \mathbb{R}^{n \times n}$ is the left singular matrix, $\mathbf{\Psi} \in \mathbb{R}^{m \times m}$ is the right singular matrix and $\mathbf{\Lambda} \in \mathbb{R}^{n \times m}$ is a diagonal matrix that contains the corresponding singular values $(\Lambda_1, \Lambda_2, ...)$ (Taira *et al.*, 2017).

$$\mathbf{Y} = \mathbf{\Phi \Lambda \Psi}^T \tag{3.3.6}$$

The left singular matrix $\mathbf{\Phi}$ contains the eigenvectors of $\mathbf{YY}^T$ and, thus, the spatial structure of the POD modes, and the singular values relate to the eigenvalues and, therefore, POD mode energy, by the relationship $\lambda_j = \Lambda_j^2$. It is the SVD solution approach that is used in this thesis to compute POD modes (Taira *et al.*, 2017).

The next model-order reduction technique to describe is the DMD introduced to the fluid dynamics community for the first time by Schmid & Sesterhenn (2008) and rigorously in the seminal work by Schmid (2010). DMD is characterized by its ability to extract flow modes and rank them based on their dynamical importance, something alluded to in the previous paragraph. More specifically, it identifies modes based on their characteristic oscillation frequency and an associated growth/decay rate. In one sentence, DMD is an "eigendecomposition of a best-fit linear operator that approximates the dynamics present in the data" (Taira *et al.*, 2017). More specifically, DMD is a linear algebra based purely data-driven post-processing technique that can be viewed as the favorable merge of aspects from the discrete Fourier transform (temporal) and the POD (spatial) to identify coherent spatio-temporal structures. As was done for POD, the computation of the

DMD modes starts with collecting a series of flow field snapshots that are separated by a constant time-interval, Δt. These snapshots of the flow field are then re-arranged into two matrices, $\mathbf{Y}_\alpha$ and $\mathbf{Y}_\beta$, that are shifted by one data column relative to each other, as illustrated below (Taira *et al.*, 2017):

$$\mathbf{Y}_\alpha = [\boldsymbol{y}(t_1), \boldsymbol{y}(t_2), ...\boldsymbol{y}(t_m)] \in \mathbb{R}^{n\times m} \quad , \quad \mathbf{Y}_\beta = [\boldsymbol{y}(t_2), \boldsymbol{y}(t_3), ...\boldsymbol{y}(t_{m+1})] \in \mathbb{R}^{n\times m} \tag{3.3.7}$$

One subsequently assumes that there is a linear relationship between the snapshots such that the following equation holds (Taira *et al.*, 2017):

$$\mathbf{Y}_\beta = \mathbf{A}\mathbf{Y}_\alpha \tag{3.3.8}$$

At this point it is useful to point out that the assumption of linearity is one of the limitations of the DMD approach. Caution must be exercised when applying the method to data-sets of highly non-linear problems. Moving on, matrix $\mathbf{A}$ can, thus, be defined as the following, with $\mathbf{Y}_\alpha^{-1}$ as the pseudo-inverse of $\mathbf{Y}_\alpha$ (Taira *et al.*, 2017).

$$\mathbf{A} = \mathbf{Y}_\beta \mathbf{Y}_\alpha^{-1} \tag{3.3.9}$$

The eigenvalues and eigenvectors of $\mathbf{A}$ could, in theory, then be computed in order to directly obtain the DMD modes. However, as the number of grid-points is usually much higher than the number of snapshots (i.e. $n >> m$), it is more economical to adopt work-around algorithms such as the one proposed by Tu *et al.* (2013):

1. First, compute the SVD of $\mathbf{Y}_\alpha$ (Taira *et al.*, 2017; Tu *et al.*, 2013):

$$\mathbf{Y}_\alpha = \mathbf{\Phi}\mathbf{\Lambda}\mathbf{\Psi}^T \tag{3.3.10}$$

2. At this point, it is wise to truncate the result of the SVD computation to only include entries, r, that are associated with a non-zero singular value, thereby performing an "economy" SVD calculation and, most importantly, significantly reducing the computational over-head of subsequent numeric steps (Taira *et al.*, 2017; Tu *et al.*, 2013).

3. Next, the matrix $\tilde{\mathbf{A}}$ is determined from the following equation (Taira *et al.*, 2017; Tu *et al.*, 2013):

$$\tilde{\mathbf{A}} = \mathbf{\Phi}_r^T \mathbf{A} \mathbf{\Phi} = \mathbf{\Phi}_r^T \mathbf{Y}_\beta \mathbf{\Psi}_r \mathbf{\Lambda}_r^{-1} \tag{3.3.11}$$

4. It is the eigenvalues, μ_j, and eigenvectors, σ_j, of $\tilde{\mathbf{A}} \in \mathbb{R}^{r \times r}$ that are subsequently computed (Taira *et al.*, 2017; Tu *et al.*, 2013).

$$\tilde{\mathbf{A}} \sigma_j = \mu_j \sigma_j \tag{3.3.12}$$

5. The eigenvalues are then converted to their needed form with the following equation. Real parts of λ_j indicate whether the mode decays (negative) or grows (positive), while the imaginary part gives the mode's characteristic frequency (Taira *et al.*, 2017; Tu *et al.*, 2013).

$$\lambda_j = \frac{1}{\Delta t} \log(\mu_j) \tag{3.3.13}$$

6. The evaluated eigenvectors are converted to their projection-ready modal form, ϕ_j, by pre-multiplying the eigenvectors with the left singular matrix of $\mathbf{Y}_\alpha$ (Taira *et al.*, 2017; Tu *et al.*, 2013).

$$\phi_j = \mathbf{\Phi} \sigma_j \tag{3.3.14}$$

7. Finally, the amplitude of each mode may too prove insightful when attempting to attenuate a certain mode. To compute the amplitude associated with each mode, the following operation is carried out (Tu *et al.*, 2013).

$$\alpha_j = \phi_j^{-1} \boldsymbol{y}(t_1) \tag{3.3.15}$$

With the control strategy, the flow solver and two key post-processing techniques described, it is now apt to describe the results collected.

Chapter 4

D-Body: Active Flow Control

The purpose of this chapter is to validate the use of OpenFOAM for active feedback control targeting drag reduction. Prior bluff-body aerodynamics research in the group had namely used the in-house LES code StreamLES whose simulations are performed with block-structured structural meshes. The code permitted rigorous active feedback control studies for drag reduction to be performed on canonical geometries, such as the backward facing step, but its mesh limitations preclude its use for more complex and, therefore, industry relevant cases such as the Nissan NDP (see chapter 6) (Evstafyeva *et al.*, 2017; Dahan *et al.*, 2012; Dalla Longa *et al.*, 2017). This chapter will, therefore, focus on the replication of StreamLES drag reduction work done by Dalla Longa *et al.* (2017) on the D-body, thereby facilitating the group's transition from using StreamLES to the more flexible OpenFOAM CFD toolbox. The chapter is divided into the following sections: (a) simulation set-up, (b) unforced flow, (c) open-loop forced flow and (d) closed-loop forced flow.

4.1 Simulation Set-up

A schematic of the D-body flow set-up is illustrated in figure 4.1. This 2D bullet shaped geometry has also been the subject of feedback control investigations by Henning & King (2005*a*), Henning *et al.* (2007) and Pastoor *et al.* (2008). The flow domain size is $\Omega = (L_{in}, L_{x_1}, L_{x_2}, L_{x_3}) =$

$(4H, 24H, 9H, 4H)$ where H is the D-body height and is equal to 1m. In non-dimensional terms, the geometry exactly replicates the one used by Dalla Longa *et al.* (2017).

Furthermore, as this is a quasi-2D flow with cross-stream periodic boundary conditions, no flow initialisation was performed using the RANS based simpleFoam solver with the very robust Spalart Allmaras turbulence model. Instead, the flow was immediately allowed to develop forward in time from uniform initial conditions of $\boldsymbol{U_\infty} = (0, 0, 0)$m·s^{-1} flow velocity and $P_\infty = 0$Pa gauge pressure in the full domain using the LES based pimpleFoam solver with the WALE turbulence model, as described in section 3.2. The following boundary conditions were applied to the domain, Ω, consisting of air at 20°C with kinematic fluid viscosity, ν, equal to 1.511×10^{-5}m^{2}s^{-1}.

1. At $\partial\Omega_{in}$, a Blasius boundary layer profile with boundary layer thickness, δ, equal to $0.1H$ and free-stream velocity, U_∞, equal to 0.1511m·s^{-1} was specified. This free-stream flow velocity was chosen, as this leads to a Reynolds number based on body height, Re_H, of 10000, and is also the Reynolds number set in Dalla Longa *et al.* (2017).

2. In the cross-stream direction, x_3, a periodic boundary condition is applied.

3. At $\partial\Omega_{top}$ and $\partial\Omega_{bottom}$, a free-slip condition is stipulated.

4. At $\partial\Omega_{out}$, an advective pressure outlet condition is specified.

5. At the D-body walls, the no-slip condition is applied i.e. wall-resolving (WRLES) is performed.

This set of boundary conditions holds for the unforced flow simulations, the open-loop forced flow simulations, and the closed-loop forced flow simulations. However, for the forced flow simulations, an additional boundary condition is specified on the D-body surface. It spans a length of $\sim 0.04H$ just upstream of the top and bottom D-body trailing edges. Specifically, anti-phase top-hat velocity profiles (as shown in figure 3.1) at an angle of 45° with respect to the x_1-coordinate axis are applied (Fig. 4.2). Ideally, one would want to test a broad range of jet orientations and see which one has the largest impact on the shear layers developing at the trailing edge. However, in this work, the

orientation of jets is chosen to be consistent with the work of Dalla Longa *et al.* (2017) and because past experimental work by Kim *et al.* (2004), Henning & King (2005*a*) and Pastoor *et al.* (2008) successfully adopted a 45° jet orientation to raise the base pressure of the bullet shaped D-body. For open-loop forced flow, these anti-phase top-hat velocity profiles are sinusoidal in time, while for closed-loop forced flow their time-dependent profiles are determined by the output of the groovyBC used with the swak4Foam plug-in.

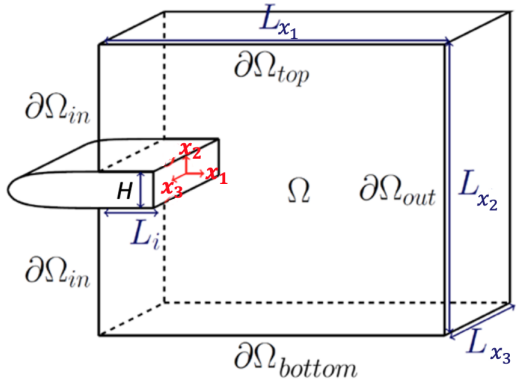


Fig. 4.1: Fluid domain of the D-body simulations (*image reproduced with permission from Open Access*)(Dalla Longa *et al.*, 2017)

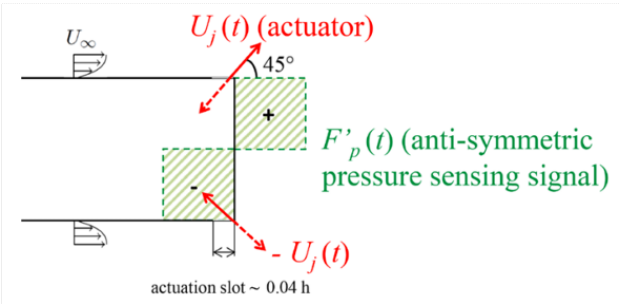


Fig. 4.2: Actuation and sensing positions in the D-body study (*image reproduced with permission from Open Access*) (Dalla Longa *et al.*, 2017)

The mesh for this bluff-body configuration was created using the commercial mesh generation software Pointwise. It was selected to create the structured mesh (Fig. 4.3) - at the time of its creation, the research group's expertise involved this tool. Pointwise also has the added benefit that no OpenFOAM plug-in is needed to convert the mesh to OpenFOAM compatibility - meshes from Pointwise can be immediately saved in OpenFOAM format. To ensure that wall-resolving LES (WRLES) is performed and, thereby, that the mesh resolves the boundary layer down to the wall, a mesh with wall "y-plus" of $\overline{x_{2w}^+} \sim 1$ was created. Its distribution for the D-body surface is visualized in figure 4.4 using curvilinear coordinates, thus ensuring that $\overline{x_{2w}^+}$ really does refer to a wall-normal distance. This is a benchmark value that has been universally accepted to be required to resolve the boundary layer down to the wall - see for example the work by Fan *et al.* (2020). Meanwhile, near-wall resolution in the streamwise direction and spanwise direction were also specified to meet the requirements of wall-resolving LES, as dictated in the work by Choi & Moin (2012). Specifically,

$\overline{\Delta x_{1w}^+}$ was made to equal approximately 5.6, thereby fulfilling the requirement that the value lie below 50 to 130, while $\overline{\Delta x_{3w}^+}$ was made to equal about 16.4, thereby meeting the requirement that the value lie near 15 to 30 (Choi & Moin, 2012). The selection of the final mesh to use in this study was primarily made based on a mesh refinement study. Table 4.1 illustrates that mesh independency is achieved, at first, with a mesh of about 10 million cells, where upon a second plateau is achieved with about 20 million cells. It was deemed intractable to use the 20 million cell mesh for the current feedback control study though, as identification of a black-box model of the wake's response to forcing (see section 4.3) requires ~ 36 simulation runs, and those with low forcing frequency need to be run for a comparatively long time in order to capture sufficient forced flow cycles. As such, the mesh with ~ 10 million cells was selected as the best compromise between simulation cost and fidelity. This mesh also aligns well with the 9.4 million cell sized block-structured mesh used in the study by Dalla Longa *et al.* (2017), although this comparison should merely be used as a guide, as Dalla Longa *et al.* (2017) used a different solver and, therefore, encountered a different amount of inherent numerical diffusivity. Somewhat counter-intuitively, it was decided to change the solver schemes post mesh refinement study, switching from ones that are inherently second order accurate (e.g. backward for the time-dependent term and Gauss linear for the divergence terms) to ones that can blend from first order accuracy to second order accuracy based on the limiters applied. Specifically, Crank-Nicolson with a factor 1.0 for a purely second order accurate time-dependent scheme, and limited Gauss linear schemes for the gradient and divergence terms with the limiters switched off for second order accuracy were used. The switch to this more general scheme format, which was described in section 3.2, was done in anticipation of the unstructured meshes used in the subsequent two studies (see chapters 5 and 6), where, for stability reasons, a purely second order accurate scheme may not be tractable. This scheme switch produced a $\overline{C_{PB}}$ value of ~ -0.53, which correlates very well, even better than previously, with the experimental values of Pastoor et al. (2008), which were obtained at Re numbers between 23000 and 70000 - the data from Pastoor

et al. (2008) resides at about $\overline{C_{PB}} \sim -0.520$ (Fig. 4.7). While this comparison should be made with caution, as the Re numbers are different, it should be noted that the base pressure coefficient values in the work by Pastoor *et al.* (2008) seem to be independent of the Re; there is not much variability between the value recorded at $Re = 23000$ and $Re = 70000$.

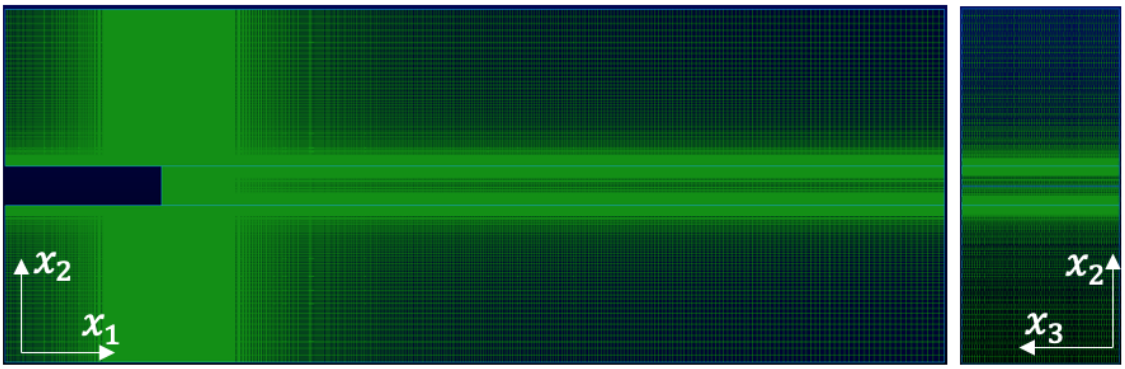


Fig. 4.3: Pointwise structured mesh for the D-body

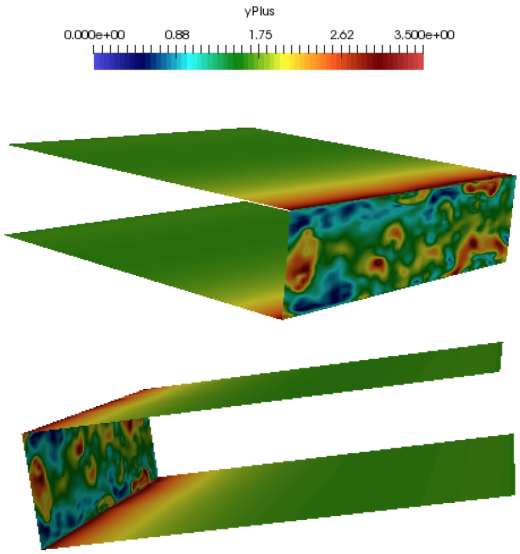


Fig. 4.4: Instantaneous wall "y-plus" for the D-body using the 10 million cell grid

Mesh size	$\bar{C}_{PB}$
500 thousand	-0.590
2 million	-0.484
5 million	-0.442
10 million	-0.436
15 million	-0.437
20 million	-0.420
25 million	-0.421
Dalla Longa et al. (2017)	-0.399
Pastoor et al. (2008)	-0.520

Table 4.1: D-body mesh refinement study

4.2 Unforced Flow

To be able to apply the sensitivity based feedback control described in section 3.1, it is imperative that the coherent flow structure(s), whose attenuation is sought, be identified. This is done by computing the spectra of the symmetric as well as anti-symmetric base pressure data trace.

In this case, the symmetric base pressure is equivalent to the average base pressure. Meanwhile, anti-symmetric is used here to denote the delta between the base pressure average of the D-body's top half and bottom half. The second measurement ensures that a strong signature of the vortex shedding mode is picked up. The spectra are depicted in figure 4.5 for the current simulations with OpenFOAM. A corresponding spectral plot of the base pressure data traces from Dalla Longa *et al.* (2017) are presented in figure 4.6.

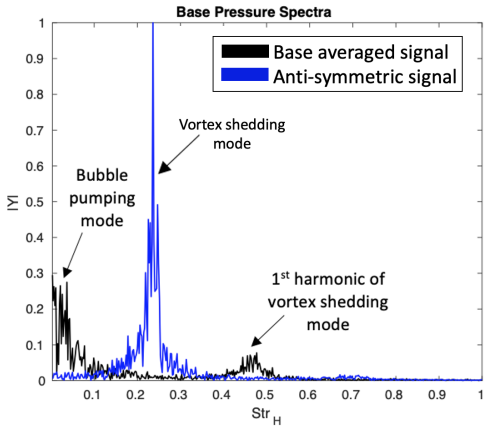


Fig. 4.5: Unforced base pressure spectra for the D-body (OpenFOAM)

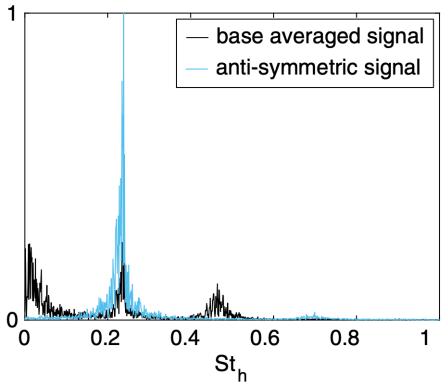


Fig. 4.6: Unforced base pressure spectra for the D-body (StreamLES) (*image reproduced with permission from Open Access*) (Dalla Longa *et al.*, 2017)

The vortex shedding mode, where shear layers roll-up periodically and 180° out-of-phase from opposing top and bottom sides of the D-body, is detected in the anti-symmetric pressure data trace for both the current OpenFOAM results and the past results from Dalla Longa *et al.* (2017). Meanwhile, the averaged base pressure data profile for both current OpenFOAM results and the past StreamLES results pick-up the so-called bubble pumping mode, where the recirculation bubble moves periodically toward and away from the D-body base, and the first harmonic of the vortex shedding mode. Upon closer inspection, the averaged base pressure trace from Dalla Longa *et al.* (2017) also has a signature of the vortex shedding mode. This is not detected in the OpenFOAM data. By inspecting pressure data traces from the experimental and analytical work of Pastoor *et al.* (2008), it may be observed that the average base pressure signal has a frequency of twice that from data probes placed at the top and bottom trailing edge of the D-body, and whose signals would, therefore, be

dominated by the vortex shedding mode (Fig. 4.7). It, thus, appears that the experimental and analytical results from Pastoor *et al.* (2008) corroborate the OpenFOAM results more than they do the StreamLES results, illustrating that the base averaging performed by Dalla Longa *et al.* (2017) may not be sufficiently (or correctly) done. Nonetheless, the flow fields simulated in OpenFOAM and StreamLES generally do compare well qualitatively. This can be seen by looking at the instantaneous x_3-vorticity component on a plane positioned at (0,0,0) and with a normal pointing in the x_3-direction (Fig. 4.8). A direct back-to-back comparison between these two flow field snapshots is not entirely possible though, as the visualization tool used and, therefore, colormap is not identical. But, one may observe similar flow structures with the main difference being that the amount of numerical diffusion appears stronger in OpenFOAM when comparing the far-field vortex street.

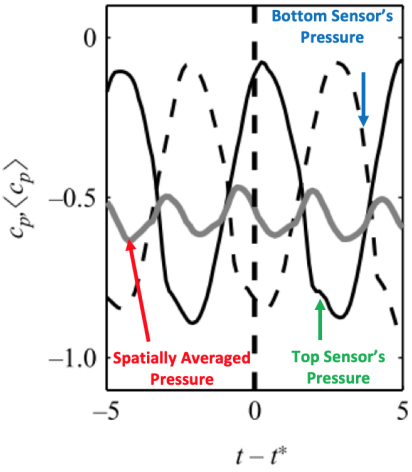


Fig. 4.7: Average base pressure and probe data traces from Pastoor *et al.* (2008) (*image reproduced with permission from Cambridge University Press*)

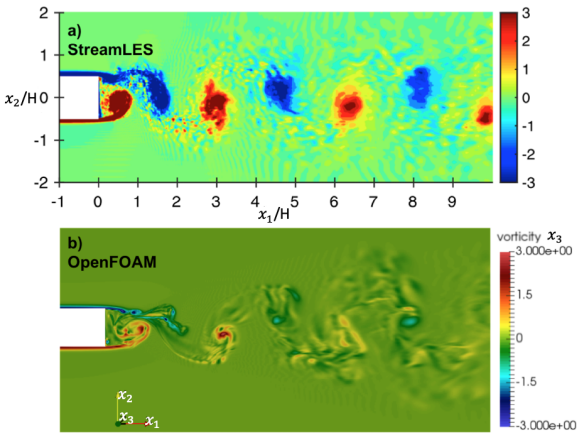


Fig. 4.8: x_3-vorticity comparison between present study and results from Dalla Longa *et al.* (2017) (*image reproduced with permission from Open Access*)

Further analysis of the coherent structures relevant to this quasi-2D flow past the D-body is performed using the model-dimensionality reduction techniques explained in section 3.3. Applying POD and DMD to the vorticity magnitude data on a plane whose normal is pointing in the x_3-direction and is positioned just downstream of the D-body trailing edge, one is able to conclude the following (flow is from left to right for the resulting modes shown in figures 4.9 to 4.13):

1. The vortex shedding mode at $Str_H \sim 0.25$ is the most energetic mode. It is namely the first

POD mode. Furthermore, POD and DMD both illustrate that the top and bottom layers of this vortex shedding mode are anti-phase. This is in line with expectations (Fig 4.9-4.10).

2. Furthermore, POD and DMD both illustrate that the first harmonic of the vortex shedding mode involves top and bottom shear layer dynamics that are in-phase with each other (Fig 4.11-4.12).

3. The bubble pumping mode is rather difficult to identify, even with DMD, which is frequency based. However, a structure was identified in the frequency range of the bubble bumping mode that, when cycled through its time-dependent frames, presents a pumping sequence. The basis of this DMD mode is shown in figure 4.13.

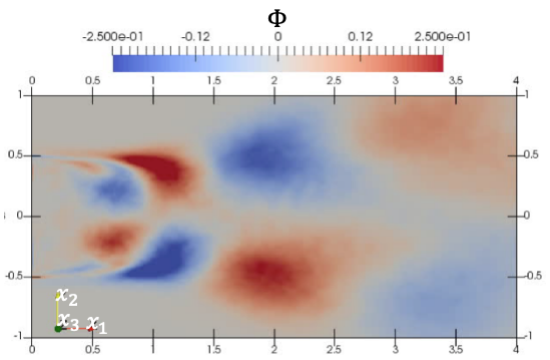


Fig. 4.9: Vortex shedding mode from POD, Φ, - it is the first and most energetic mode

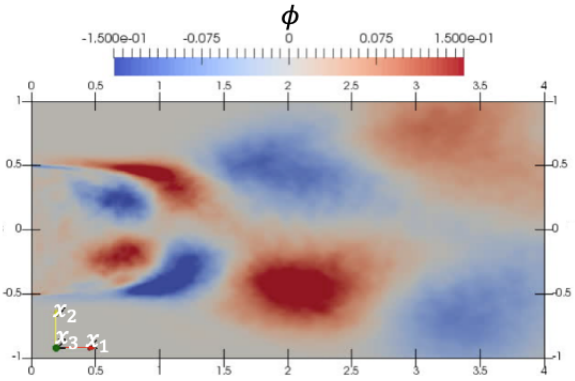


Fig. 4.10: Vortex shedding mode from DMD, ϕ ($Str_H \sim 0.25$)

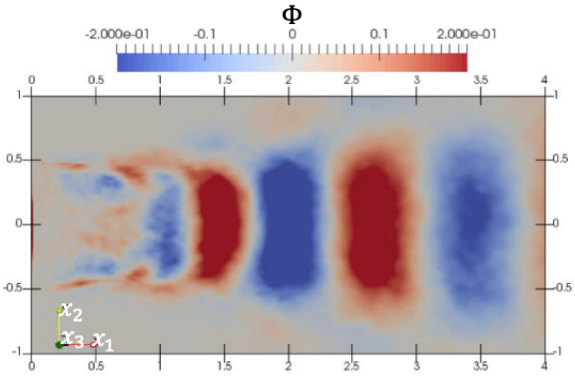


Fig. 4.11: First harmonic of vortex shedding mode from POD, Φ

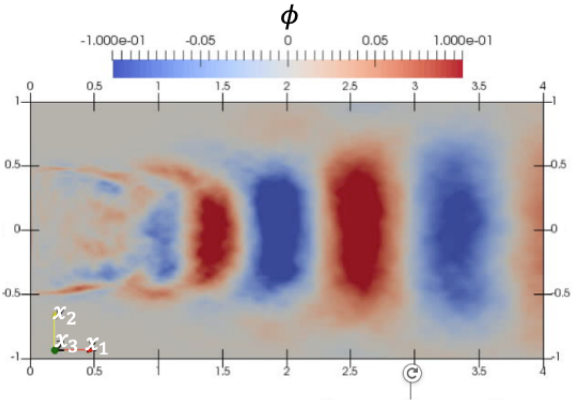


Fig. 4.12: First harmonic of vortex shedding mode from DMD, ϕ ($Str_H \sim 0.50$)

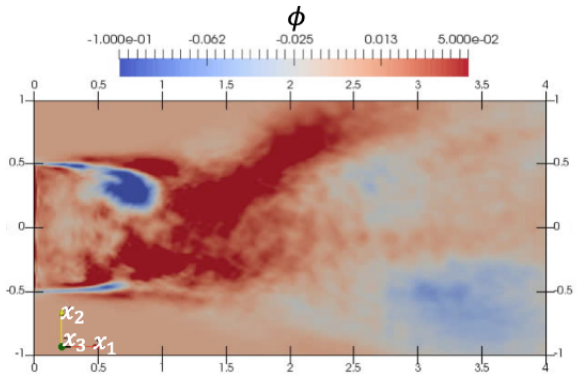


Fig. 4.13: Bubble pumping mode from DMD, ϕ ($Str_H = 0.085$)

4.3 Open-loop Forced Flow

With the unforced flow field past the D-body characterized, one may now seek to parameterize the system transfer function $G(s)$ i.e. the wake's response to forcing using the correlation method from the system identification toolbox, as has been described in section 3.1. Specifically, having determined that the strongest coherent structure, the vortex shedding mode, is associated with a $Str_H \sim \mathcal{O}(0.1)$, harmonic anti-phase (top-to-bottom) actuation is performed at a range of Strouhal numbers between 0.01 and 1. This Strouhal number range has been chosen, as this will allow the tuning of a sensitivity transfer function, $S(s)$, that is below unity in the vortex shedding mode's frequency window. Also, in order to test whether the assumption of dynamic linearity holds, the amplitudes of the harmonic forcing functions are set to U_f/U_∞ equal to 0.1, 0.2 and 0.3 at each frequency. The data collected from these open-loop forcing simulation runs is depicted in figure 4.14-4.15. MatLab's "fitfrd" function has been used to fit a 5th-order state-space function to the magnitude and phase plot of $G(s)$. The transfer function that corresponds to this state-space model is provided below:

$$G(s) = \frac{-8.89s^5 + 9.56s^4 - 0.96s^3 + 0.34s^2 - 0.02s - 0.002}{s^5 + 47.34s^4 + 0.29s^3 + 4.14s^2 + 0.009s + 0.092} \tag{4.3.1}$$

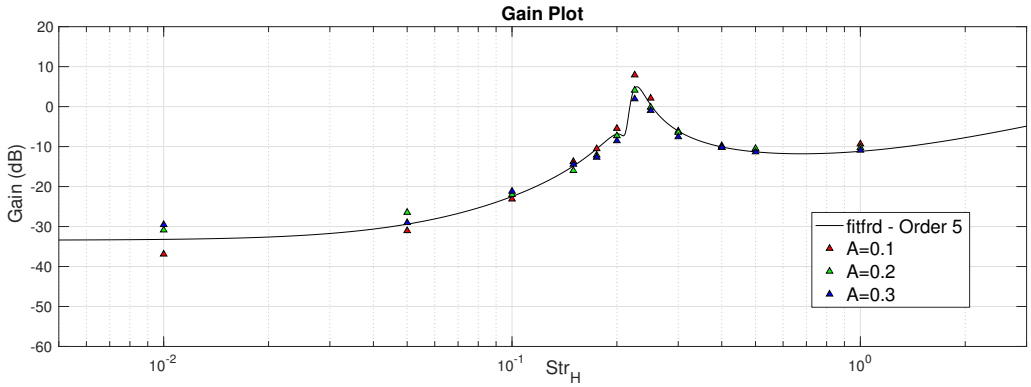


Fig. 4.14: Gain plot of $G(s)$ for the D-body

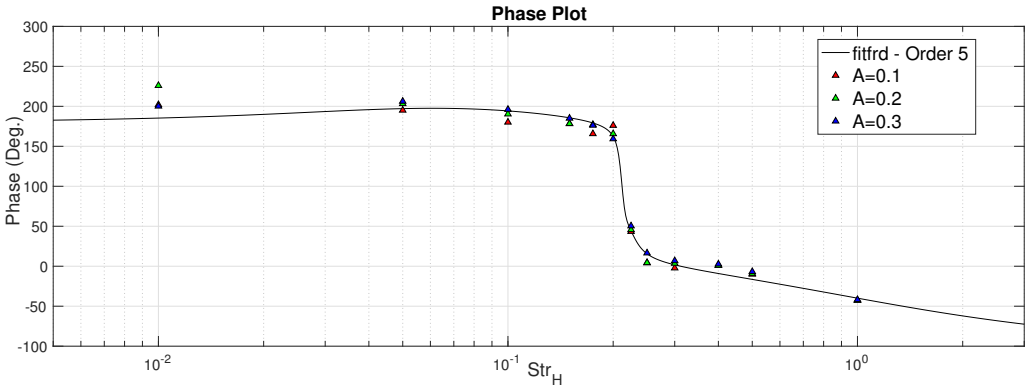


Fig. 4.15: Phase plot of $G(s)$ for the D-body

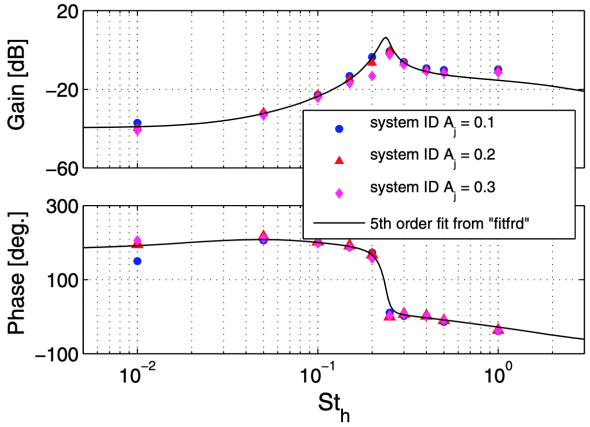


Fig. 4.16: Gain and phase plot of $G(s)$ for the D-body from Dalla Longa *et al.* (2017) (*image reproduced with permission from Open Access*)

These plots compare favourably with their counterpart, figure 4.16, in Dalla Longa *et al.* (2017). Additionally, the assumption of dynamic linearity has proven to be valid: (a) spectral analysis of the forced wake is dominated by the forcing frequency without too much scattering into higher harmonics and (b) there is no noticeable gain and phase dependency on forcing amplitude (Fig. 4.14-4.15).

Before moving on to the construction and simulation of the closed-loop system, one may assess the immediate impact of open-loop forcing on the D-body's wake. As figure 4.17 shows, in the open-loop configuration, there is at most a decrease in base pressure. This is in disagreement with open-loop forcing's direct impact on the D-body wake from Dalla Longa *et al.* (2017) for which figure 4.18 shows an increase in base pressure in the vicinity of the vortex shedding mode's characteristic frequency. Nonetheless, these OpenFOAM results do not preclude a base pressure increase in the closed-loop configuration. They merely indicate that, although one is solving the same governing equations, one can expect some code dependency on the results, not just in the open-loop, but also in the closed-loop configuration. More specifically, the different numerical codes, OpenFOAM and StreamLES, have a different amount of numerical diffusivity associated with them, as was seen in figure 4.8, and this will impact the control associated results.

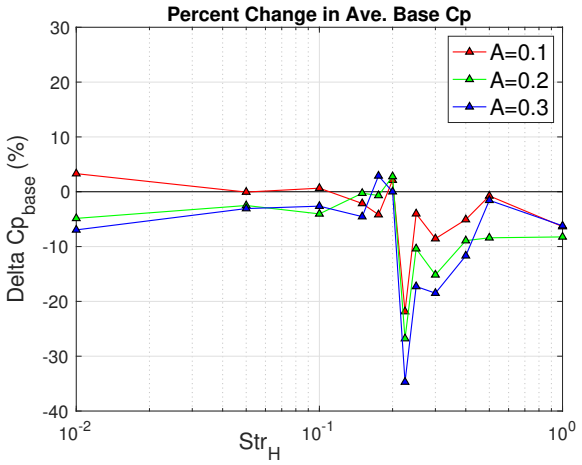


Fig. 4.17: Percent change in D-body base pressure for open-loop forcing in OpenFOAM

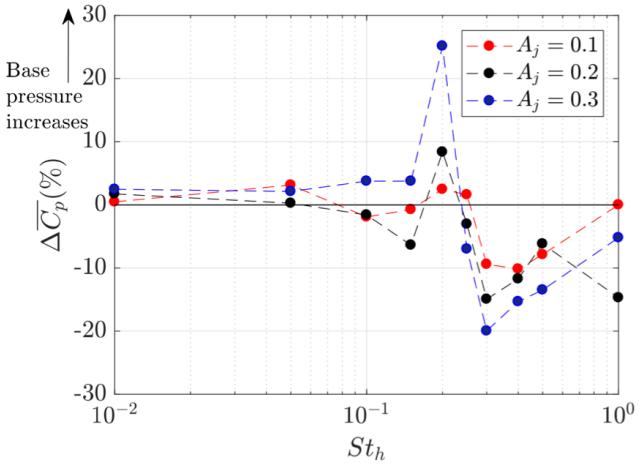


Fig. 4.18: Percent change in D-body base pressure for open-loop forcing in StreamLES (Dalla Longa, 2018)

4.4 Closed-loop Forced Flow

Using equations 3.1.3-3.1.4 as a guide, a feedback control law, $K(s)$, is tuned via trial and error to produce a sensitivity transfer function, $S(s)$, whose magnitude is below unity and, therefore, negative in decibels, for the frequency range most pertinent to the vortex shedding mode. While tuning the control law, $K(s)$, it is made sure that the feedback system is kept stable by computing the Nyquist diagram of the (open-) loop feedback transfer function equal to $L(s) = G(s)K(s)$.

Specifically, it is ensured that there are no net clockwise encirclements of the point (-1,0) in the Nyquist diagram, thereby ensuring that no input signal can grow unbounded (Astroem & Murray, 2010). The result of the control law, $K(s)$, designed is illustrated in figures 4.19-4.20. One can see that, as desired, the sensitivity transfer function, $S(s)$, is below unity in magnitude in the vicinity of the vortex shedding mode ($Str_H \sim 0.25$) and the open-loop feedback law has no net encirclements of the point (-1,0) in the Nyquist diagram (Fig. 4.22). The gain and phase plot of $S(s)$ also compare well with the work from Dalla Longa *et al.* (2017) (Fig. 4.21). One may, therefore, expect a similiar percentage in base pressure recovery with feedback control active.

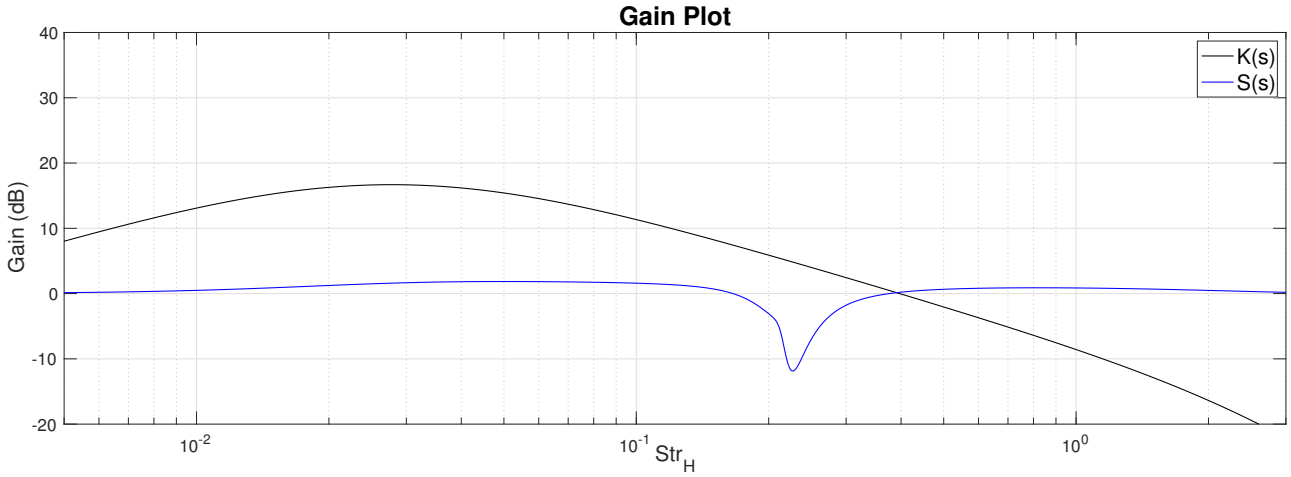


Fig. 4.19: Gain plot of $K(s)$ and $S(s)$ for the D-body

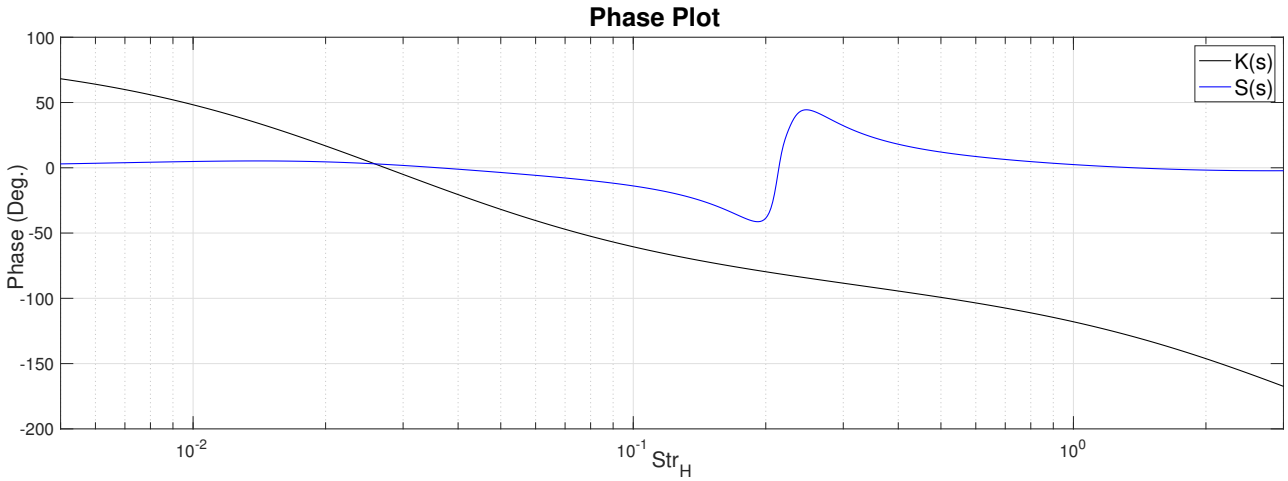


Fig. 4.20: Phase plot of $K(s)$ and $S(s)$ for the D-body

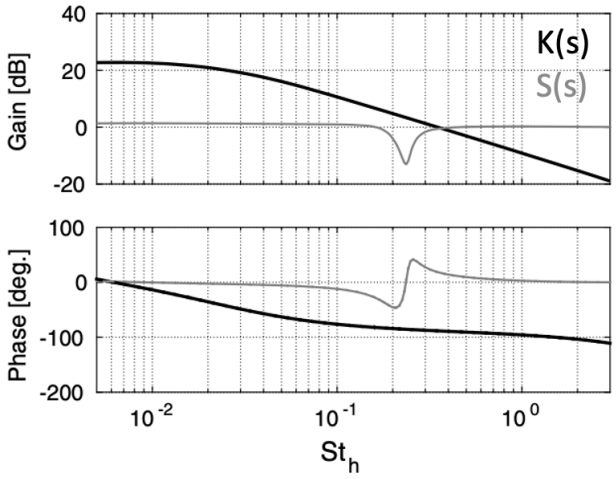


Fig. 4.21: Gain and phase plot of $K(s)$ and $S(s)$ for the D-body from Dalla Longa *et al.* (2017) (*image reproduced with permission from Open Access*)

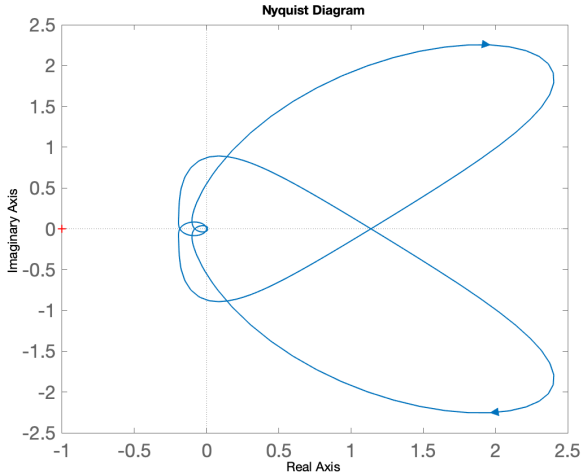


Fig. 4.22: Nyquist stability diagram for the D-body open-loop feedback law, $L(s)$

It is now pertinent to look at the result of implementing the designed feedback control law, $K(s)$, given by equation 4.4.1.

$$K(s) = \frac{4.747s}{s^4 + 7.405s^3 + 12.77s^2 + 0.7005s + 0.008595} \tag{4.4.1}$$

The plug-in swake4Foam mentioned in section 3.2 is used in conjunction with the groovyBC to do so. This namely enables the specification of a dynamic (i.e. time-varying) boundary condition without altering the OpenFOAM source code. The value of the time-varying boundary condition is dependent on the anti-symmetric base pressure sensor reading (Fig. 4.2) that is fed into a discretized state-space model of the control law, $K(s)$. In other words, the control law was designed in the frequency

domain, but it is implemented into the solver in its state-space form. Figure 4.23 illustrates the magnitude of the velocity component U_{j_i}, where i equals 1 or 2 before and after control is switched "on" - the x_1- and x_2- components of velocity are equal in magnitude as the jet is angled at 45° relative to the x_1-axis. Evidently, at the start of control being switched "on", the magnitude of the velocity components is comparatively large. The control system is attempting to obtain control of the chaotic D-body wake. Once this control is established, the velocity jet settles into a low energy state. Meanwhile, the direct impact of the closed-loop synthetic jet actuation on the D-body's base pressure is illustrated in figure 4.24. One can observe that the D-body base pressure rises from an average of $\overline{C_{PB}} \sim -0.53$ to an average of $\overline{C_{PB}} \sim -0.40$. This represents a 24.5% increase in base pressure as opposed to the 38% achieved by Dalla Longa *et al.* (2017) for the same configuration and control strategy, but different CFD solver. This highlights the code dependency of the control results that was alluded to in previous sections - as one has different amounts of numerical diffusivity associated with a given code, one should expect some differences in the numerical results with the hope that trends are maintained. Moving on, figure 4.24 also shows that feedback control attenuates the base pressure fluctations, especially for the anti-symmetric base pressure. In other words, the controller is doing what it is designed to do. This mode attenuation can be more clearly seen in figure 4.25 that compares the spectra for the anti-symmetric and symmetric base pressure signal in both the uncontrolled and the controlled state. A frequency shift that accompanies mode damping is also noticed.

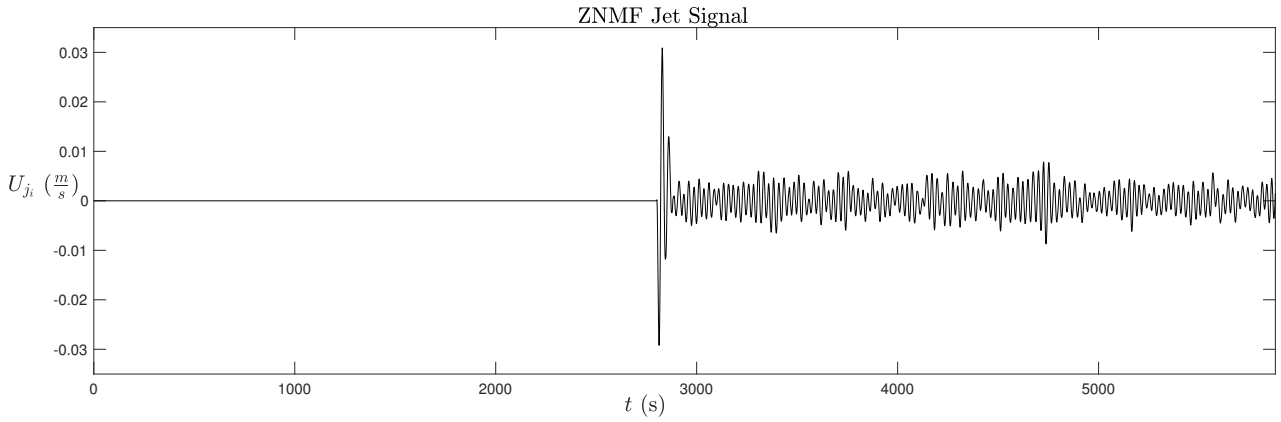


Fig. 4.23: Zero-net-mass-flux jet signal before and after control is switched "on"

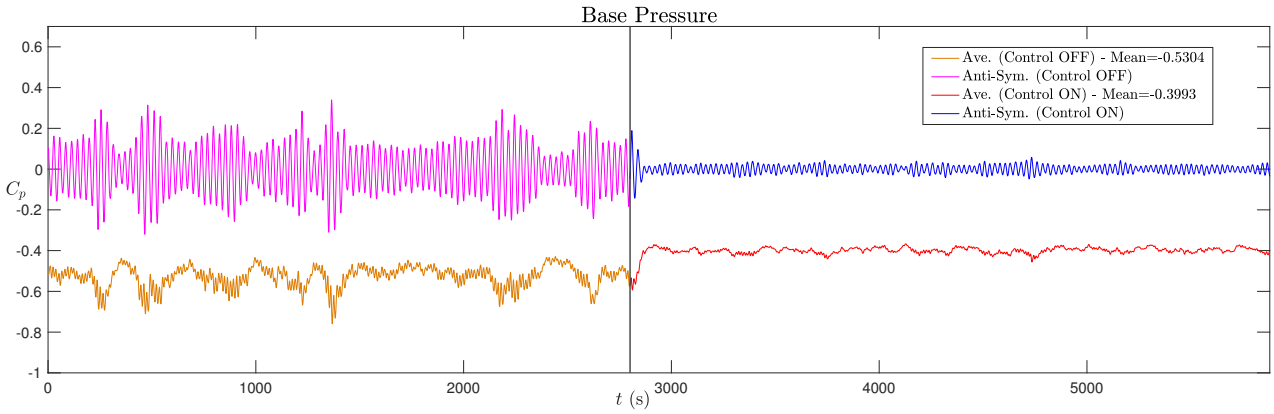


Fig. 4.24: D-body base pressure signal before and after control is switched "on"

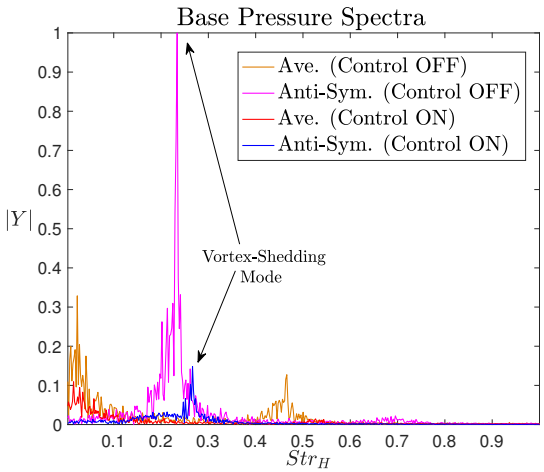


Fig. 4.25: Spectra of the base pressure traces in the uncontrolled and controlled state

Having looked at integral quantities of the flow field, it is now necessary to inspect the flow field itself in order to better understand why the changes observed occurred. Looking at the mean flow field just aft of the D-body, one can see that the recirculation bubble length has increased in the controlled state compared to the uncontrolled state (Fig. 4.26). This already sufficiently explains why the base pressure increased with control "on". According to Roshko (1993), classic potential flow theory for inviscid detached flows dictates that the recirculation zone aft of a bluff-body has a larger radius of curvature the lower the associated base pressure is. This seems logical - a greater suction zone will curve the flow inward toward the bluff-body more rapidly. Looking at instantaneous x_3-vorticity (Fig. 4.27), one can observe that in the controlled state shear layers roll-up far later than in the uncontrolled state. This directly means that the low pressure cores of these shear layer

roll-ups have a far smaller influence on the D-body base's pressure field, further supporting the increase in the integral base pressure measurement(s).

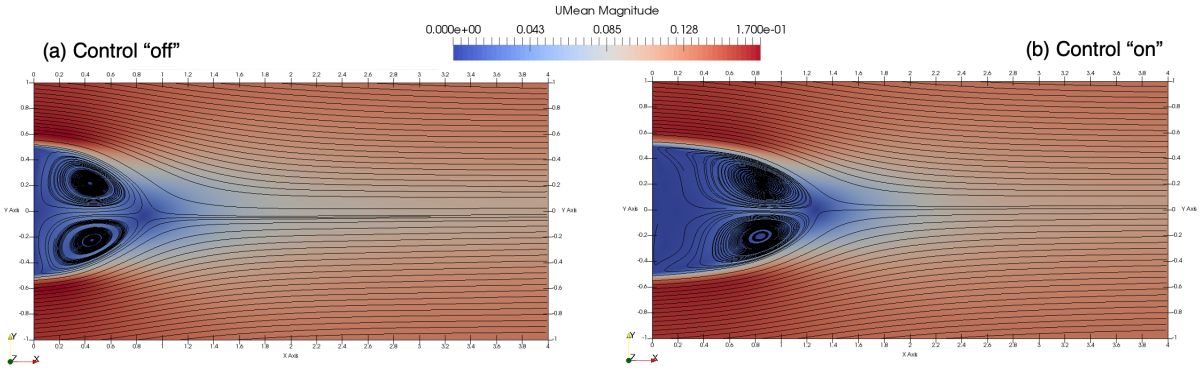


Fig. 4.26: Mean flow recirculation bubble aft of the D-body with (a) control "off" and (b) control "on"

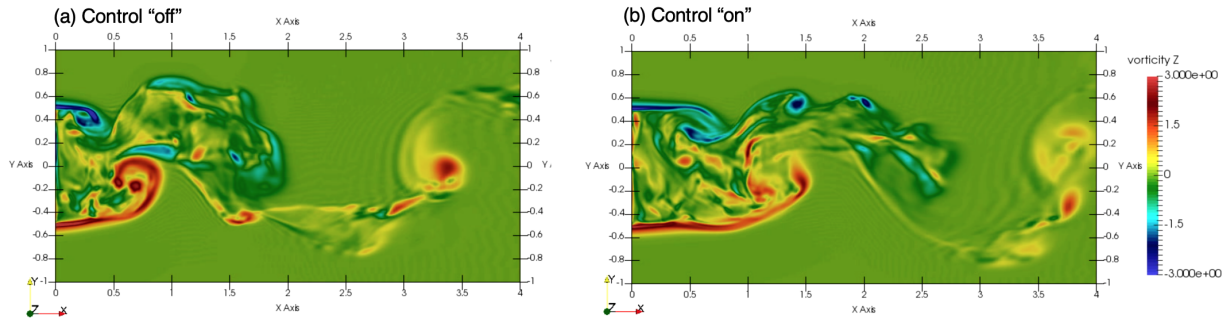


Fig. 4.27: Instantaneous x_3-vorticity aft of the D-body with (a) control "off" and (b) control "on"

Both the POD and DMD model reduction techniques have been applied to the vorticity magnitude flow field with control "off" and with control "on", respectively. As it has previously been observed in figures 4.9- 4.10 that the vortex shedding mode at $Str_H \sim 0.25$ is the most energetic and, therefore, first POD mode as well, only the DMD mode representation of this coherent structure is illustrated in figure 4.28 for both its uncontrolled and controlled state. It may be observed that the anti-symmetric structures pulse further away from the D-body base in the controlled case than in the uncontrolled case. This re-emphasizes the feedback controller's influence on the flow field - it pushes the vortex shedding mode further away from the D-body diminishing its influence on the base pressure. Finally, the accompanying DMD mode amplitude analysis (Fig. 4.29) corroborates the successful attenuation of the vortex shedding mode, albeit at the expense of a phase shift as was found in the base pressure's spectral analysis.

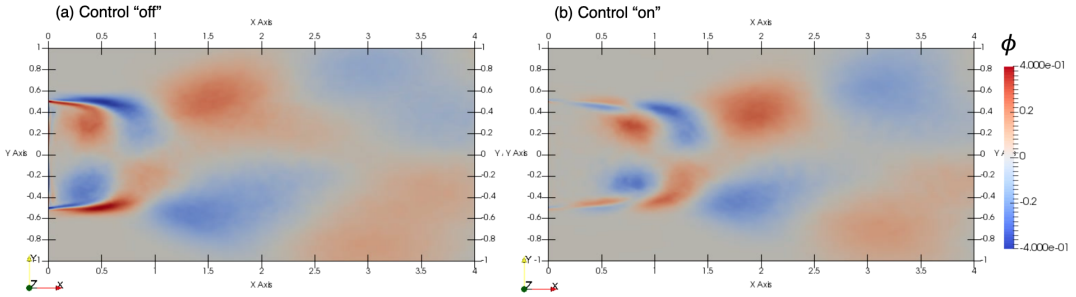


Fig. 4.28: DMD, ϕ, of vorticity magnitude aft of the D-body with (a) control "off" and (b) control "on"

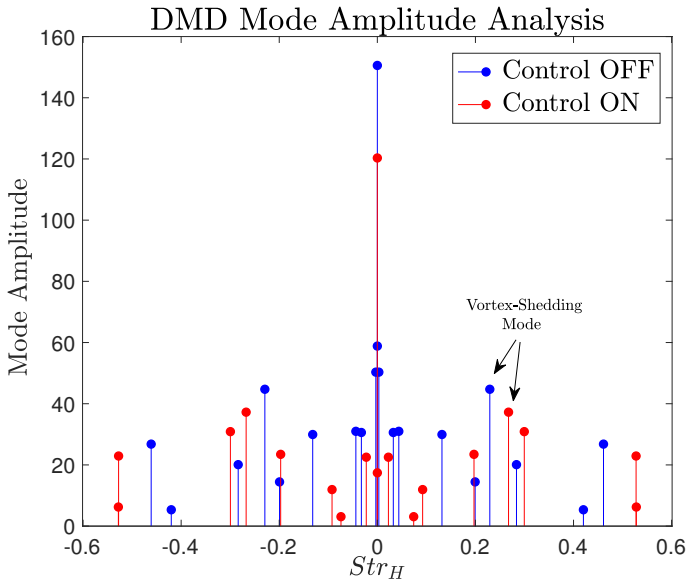


Fig. 4.29: Vorticity magnitude based DMD mode amplitude analysis for control "off" and control "on"

Before closing this chapter on feedback control for the D-body, an indication of energy input requirements must be given. Is this feedback control system operating efficiently? For this, the momentum coefficient associated with the control system is computed and compared to the values calculated by Dalla Longa *et al.* (2017) and Pastoor *et al.* (2008) for identical and similar set-ups, respectively. The equation for momentum coefficient, C_μ is given below, where s is the slot jet width:

$$C_\mu = \frac{sU_j^2}{HU_\infty^2} \tag{4.4.2}$$

For the current simulation C_μ has a maximum value of about 3.15×10^{-3} and an average peak value once control of the flow has been established of about 3.307×10^{-4}. The present maximum value of C_μ is lower than the maximum from Dalla Longa *et al.* (2017), which resides at about

1.18×10^{-2}, while the present average value is slightly above that of Dalla Longa *et al.* (2017), which lies at 2.60×10^{-4}. The order of magnitude of the computed C_μ values also match those found in Pastoor *et al.* (2008). It may, therefore, be concluded that the present feedback simulation is performing, at the very least, as efficiently as past studies.

Chapter 5

Ahmed Body: Bimodal Wake Dynamics

The first purpose of this chapter is to rigorously explore the bimodal wake dynamics aft of the squareback form of the Ahmed bluff-body with a computationally efficient setup. As elaborated upon in section 2.1.1, this phenomenon produces an unsteady side force that can be responsible for as much as 7% of the bluff-body's drag (Grandemange *et al.*, 2014). Unfortunately, most of the work on this flow feature is experimental, which precludes the analysis of the full flow field in order to better understand bimodality's dynamics, including its contributing triggers (Rigas *et al.*, 2014; Grandemange *et al.*, 2013*b*,*a*; Volpe *et al.*, 2015; Evrard *et al.*, 2016; Perry *et al.*, 2016). Dalla Longa *et al.* (2019), Fan *et al.* (2020), and Podvin *et al.* (2021) have numerically captured the phenomenon, but their analysis did not explicitly cover what a possible source of this wake behavior could be. Equally important, the mesh sizes used by Dalla Longa *et al.* (2019), work originating from this research group, were quite large, which makes parametric studies for drag reduction rather intractable. The main part of this chapter, therefore, focuses on the following two topics, which also form the core of a recently published paper by Hesse & Morgans (2021): (a) creating a computational set-up that is both reasonable in cell count and able to capture bimodality, and (b) identifying contributing trigger(s) of bimodality in order to develop more targeted drag reduction control algorithms. The second and smaller part of this chapter tests the linear feedback control

strategy that was previously validated for the quasi-2D D-body wake flow on the more complex and 3D turbulent bluff-body wake aft of the Ahmed body. Hence, the chapter is divided into the following sub-sections: (a) simulation set-up, (b) detection of wake bimodality, (c) source of wake bimodality, and (d) linear feedback control of the Ahmed body wake.

5.1 Simulation Set-up

The geometry under investigation is the Ahmed body, specifically the 1/4 scale squareback form (Fig. 5.1) (Ahmed *et al.*, 1984). It has the subsequent dimensions: height of $H = 0.072$m, length of $L = 0.261$m, nose radius of $R = 0.025$m, width of $W = 0.09725$m, and ground clearance of $G = 0.0125$m. Based on these dimensions, for which $C^* = 0.129$ and $H^* = 0.740$ in figure 2.6a, one expects horizontal (i.e. in the x_3-direction) wake bimodality to occur. Furthermore, this scale size was selected in order to match the dimensions employed by Grandemange *et al.* (2013*b*) for their seminal work on the bimodal wake behind the squareback Ahmed body. When the above mentioned dimensions are non-dimensionalized by body height, H, the non-dimensional specifications provided in figure 5.1 are computed. While a * was used to denote non-dimensional size specifications in figure 2.6a, in figure 5.1 an apostrophe, $'$, is used. Additionally, for bluff-body flows, the European Research Community on Flow, Turbulence and Combustion (ERCOFTAC) recommends a computational domain, Ω, with approximate dimensions of $\Omega = (L_{in}, L_{x1}, L_{x2}, L_{x3}) = (2L, 8L, 2L, 2L)$, where L denotes the bluff-body's length (Manceau & Bonnet, 2002). It is this domain size that has been adopted in the subsequent study.

Unlike the quasi-2D D-body wake flow with periodic cross-stream boundary conditions, the Ahmed body wake flow is fully 3D. Therefore, as described in section 3.2, the flow field is first initialised using the simpleFoam solver with the very numerically robust Spalart Allmaras RANS turbulence model, and subsequently is marched forward in time using the pimpleFoam solver with the WALE LES turbulence model. The initial conditions for the RANS simpleFoam simulation are

$\boldsymbol{U_\infty} = (6.996, 0, 0)\text{m·s}^{-1}$ and $P_\infty = 0\text{Pa}$ gauge pressure. The fluid is again air at 20°C with $\nu = 1.511 \times 10^{-5}\text{m}^2\text{s}^{-1}$. Additionally, the following boundary conditions were applied:

1. At the domain inlet, a uniform flow velocity of $\boldsymbol{U_\infty} = (6.996, 0, 0)\text{m·s}^{-1}$ without artificial forcing (i.e. turbulence is allowed to develop naturally) is stipulated. This corresponds to a $Re_H = 33333$ flow around the $1/4$ scale squareback Ahmed body.

2. A free-slip condition is specified at the computational domain's sides as well as top upper boundary i.e. at boundaries far-away from the Ahmed body.

3. An advective pressure condition is applied at the domain's outlet.

4. Meanwhile, at the Ahmed body walls and the ground, three boundary condition types are specified. Whether wall-resolving LES (WRLES) or WMLES is performed, as indicated in the flow chart of figure 5.2, determines which boundary condition type is applied. For WRLES, one tries to resolve the boundary layer in its entirety through the explicit enforcement of the no-slip condition. If a WMLES simulation is performed, either of the following two RANS based equilibirum wall-stress models is adopted with information fed into the wall-model from the wall-adjacent cell: Spalding's law of the wall (Eq. 3.2.2) or the log-law of the wall (Eq. 2.3.11).

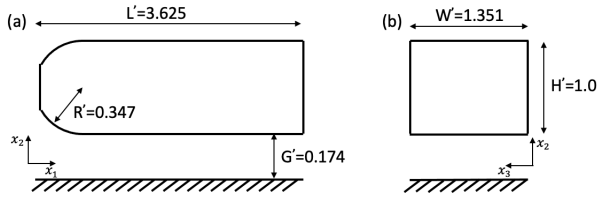


Fig. 5.1: Ahmed body geometry: (a) side view and (b) rear view

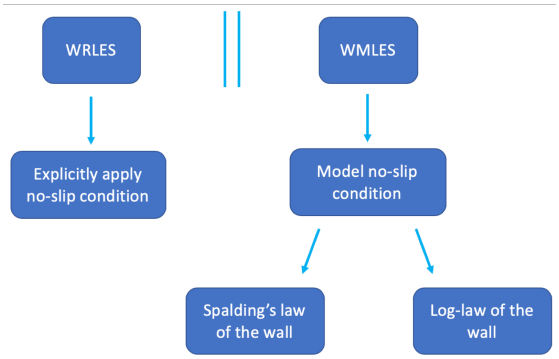


Fig. 5.2: Wall boundary condition flow chart

Next, several key variables that, in addition to flow velocity, $\boldsymbol{U}$, and pressure, P, are used throughout this chapter need to be defined. The non-dimensional coefficients employed in this study

are the drag coefficient, C_D, lift coefficient, C_L, as well as the pressure coefficient, C_P, that is used to compute the base pressure coefficient, C_{PB}, for a base area of $A = WH$ and $n = 300$ pressure probes. These variables are defined below, where the drag force is F_D, the lift force is F_L, the free-stream pressure is P_∞, the free-stream density is ρ_∞, the Ahmed body cross-sectional area projected onto the x_2x_3-plane is $A_{x_2x_3}$ and the Ahmed body cross-sectional area projected onto the x_1x_3-plane is $A_{x_1x_3}$ (Eq. 5.1.1-5.1.3).

$$C_D = \frac{F_D}{\frac{1}{2}\rho_\infty |\boldsymbol{U}_\infty|^2 A_{x_2x_3}} \tag{5.1.1}$$

$$C_L = \frac{F_L}{\frac{1}{2}\rho_\infty |\boldsymbol{U}_\infty|^2 A_{x_1x_3}} \tag{5.1.2}$$

$$C_P = \frac{P - P_\infty}{\frac{1}{2}\rho_\infty |\boldsymbol{U}_\infty|^2} \quad \rightarrow \quad C_{PB} = \frac{\sum_{i=1}^{n=300} C_{P_i} \mathrm{d}A}{WH} \tag{5.1.3}$$

Two quantities that are of crucial importance to this study on the bimodal wake dynamics of the Ahmed body are the vertically oriented base pressure gradient, $\partial C_P/\partial x_2$, and the horizontally oriented base pressure gradient, $\partial C_P/\partial x_3$. These gradients are defined using figure 5.3. It portrays the whole array of rear base pressure probes associated with the Ahmed body and, most importantly, four 1D color-coded pressure probe arrays: two x_3-oriented arrays that are marked as BOTTOM (B) and TOP (T), and two x_2-oriented arrays highlighted as LEFT (L) and RIGHT (R). $\partial C_P/\partial x_2$ is computed by taking the delta between the TOP probe array's average and the BOTTOM probe array's average. Meanwhile, $\partial C_P/\partial x_3$ is determined by taking the difference between the LEFT probe array's mean and the RIGHT probe array's mean (Eq. 5.1.4-5.1.5). The separation distance between horizontally and vertically oriented pressure probe arrays is denoted by ΔL_{x_2} and ΔL_{x_3}, respectively. The reason for choosing the 1D probe arrays denoted by BOTTOM (B), TOP (T), LEFT (L) and RIGHT (R) is that the low pressure imprint of the wake is strongest for these probe locations. This can be more easily visualized by looking at figures 5.15 and 5.18 for pressure on an x_1x_3-plane passing through the middle of the Ahmed body. As these figures illustrate, the extremity

of the wake with the lowest pressure is just inside of the blunt trailing edge(s).

$$\frac{\partial C_P}{\partial x_2} = H\frac{\overline{C_{P_T}} - \overline{C_{P_B}}}{\Delta L_{x_2}} \tag{5.1.4}$$

$$\frac{\partial C_P}{\partial x_3} = H\frac{\overline{C_{P_L}} - \overline{C_{P_R}}}{\Delta L_{x_3}} \tag{5.1.5}$$

Furthermore, the Q-criterion is employed to identify vortex structures. It is defined as the Laplacian of pressure, P. This can be reformulated to return the delta between the double contraction of the vorticity tensor, **W**, and the strain rate tensor, **S**, respectively. As equation 5.1.6 illustrates, when Q is positive, rotation dominates in the flow, demonstrating the Q-criterion's suitability for vortex structure identification. Q-criterion can be non-dimensionalized with the free-stream velocity's magnitude, $|\boldsymbol{U}_\infty|$, and Ahmed body base height, H, to give Q^* (Eq. 5.1.7).

$$Q = \nabla^2 P = \mathbf{W}\cdot\cdot\mathbf{W} - \mathbf{S}\cdot\cdot\mathbf{S} \tag{5.1.6}$$

$$Q \quad \rightarrow \quad Q^* = \frac{QH^2}{|\boldsymbol{U}_\infty|^2} \tag{5.1.7}$$

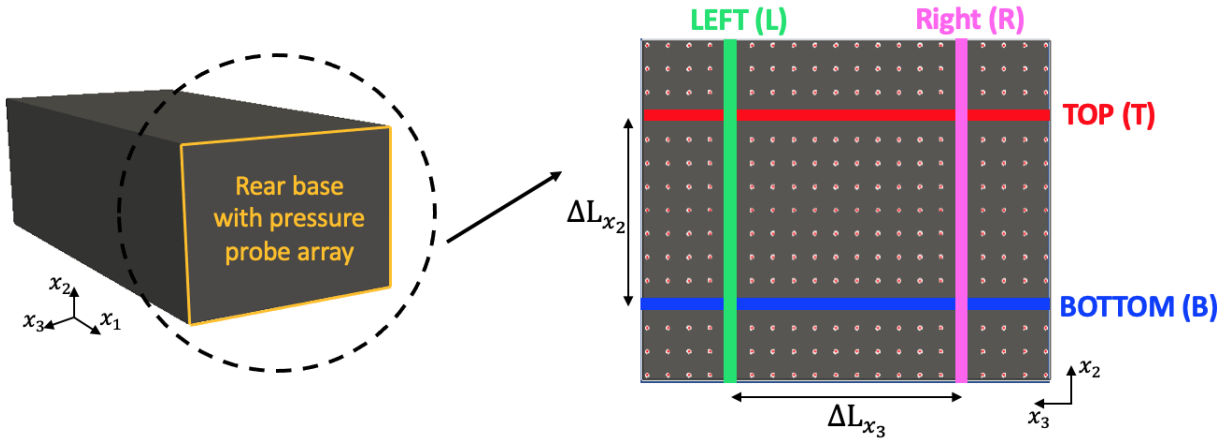


Fig. 5.3: Ahmed body rear base pressure array

Unlike for the D-body work, the meshes for this study were generated using Star-CCM+'s meshing functionalities. To convert the mesh outputs from this commercial code to OpenFOAM format, the plug-in ccm26ToFoam was used, as alluded to in section 3.2. The majority of the fluid domain was disctretized using so-called trimmer cells (Fig. 5.4b-5.4c). They are hexahedral cells

that get "trimmed" to polyhedral cells on approach to a boundary, thereby accomodating a complex geometry's shape. Hexahedral cells were selected, as they are computationally efficient for simulating fluid flows that have a main/primary flow direction. When nearing wall boundaries, in this case the ground and Ahmed body wall, prism layer cells are created (Fig. 5.4a). These orthogonal cells are ideally suited for capturing a boundary layer's large velocity gradient and doing so without raising the cell number in the domain's far-field exorbitantly. Overall, the created mesh consisting of prism layer and trimmer cells is an unstructured mesh.

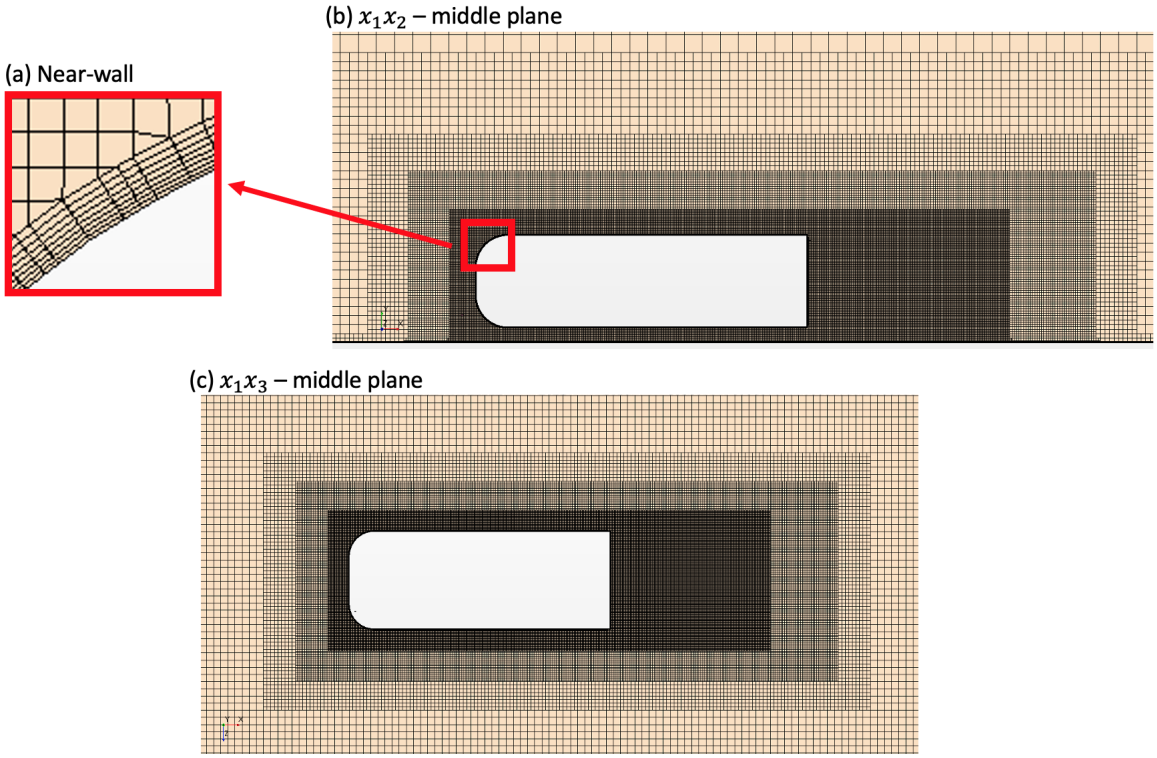


Fig. 5.4: Sample volume mesh with (a) prism layer cells near the Ahmed body nose boundary, and trimmer cells in the majority of the flow domain visualized on the (b) x_1x_2 - middle plane and (c) the x_1x_3 - middle plane

To identify the baseline/reference wake and free-stream mesh for this study, a mesh refinement study with WRLES was carried out. An estimate of the required wake cell size, ΔL_{wake}, that is needed to try to resolve scales down to the Taylor microscale, λ_T, where viscosity begins to affect the eddies' dynamics and where eddy scales are isotropic and, hence, application of an eddy-viscosity based LES turbulence model becomes reasonable, was acquired by using equation 5.1.8, a scaling relationship for λ_T that was first mentioned in section 2.3.2 (Tennekes & Lumley, 1972). It is

paramount to obtain this estimate, as the Taylor microscale can serve as an upper bound of the finest anisotropic eddy scales that LES should be able to resolve. As has been done in prior Ahmed body simulation work, A is set to equal 0.5 and l is taken to equal the Ahmed body height, H (Howard & Pourquie, 2002; Guilmineau *et al.*, 2018).

$$\lambda_T \sim 15^{\frac{1}{2}} A^{-\frac{1}{2}} Re_l^{-\frac{1}{2}} l \quad \rightarrow \quad \lambda_T \sim 5.5 Re_H^{-\frac{1}{2}} H \tag{5.1.8}$$

In total, three meshes were analysed as part of the mesh refinement study. The cell counts of these meshes are 5.4 million, 11.1 million and 25.6 million. In the far-field and near-wall region, the cell size remained unchanged among the three meshes. It is only their wake cell size that differs. For the 5.4 million, 11.1 million and 25.6 million cell meshes, the wake cell size is $0.825\lambda_T$, $0.413\lambda_T$ and $0.205\lambda_T$, respectively.

Table 5.1 contains the mean drag coefficient, $\overline{C_D}$, lift coefficient, $\overline{C_L}$, base pressure coefficient, $\overline{C_{PB}}$, and re-circulation bubble length, $\overline{L_B}$, for the three meshes. It may be observed that $\overline{C_{PB}}$ and $\overline{L_B}$ appear to converge between the 5.4 million and 11.1 million cell set-up and the comparison to experimental values from Grandemange *et al.* (2013*a*), who investigated the squareback Ahmed body at $Re_H = 33333$, substantiates this claim. Meanwhile, there is no apparent mesh convergence when looking at $\overline{C_D}$ and $\overline{C_L}$. This does not necessarily mean that we have to discard our meshes though. It is very difficult to obtain converged values from surface CFD measurements, as this is where the intersection between the surface and volume mesh occurs. It is one major reason why wind tunnels with their more robust surface measurement qualities will for the foreseeable remain in use and not be entirely replaced by CFD runs. This difficulty in obtaining converged CFD surface measurements was illustrated in the work of Fan *et al.* (2020) as well. In their IDDES work using the commercial Star-CCM+ solver, there was a 2.6% variation in $\overline{C_D}$ between their coarsest and finest mesh, while in this instance it is 3.2%. Thus, if only mean flow quantities are considered, it seems plausible to employ the coarsest mesh, which consists of 5.4 million cells.

Mesh size	ΔL_{wake}	$\overline{C_D}$	$\overline{C_L}$	$\overline{C_{PB}}$	$\overline{L_B}$
5.4 million	$0.825\lambda_T$	0.375	-0.0542	-0.203	1.417H
11.1 million	$0.413\lambda_T$	0.364	-0.0548	-0.201	1.417H
25.6 million	$0.205\lambda_T$	0.376	-0.0564	-0.214	1.375H
Grandemange *et al.* (2013*a*)	-	-	-	-0.190	1.418H

Table 5.1: Mesh refinement study for Ahmed body WRLES - mean flow quantities

However, upon closer inspection of the instantaneous flow, it becomes evident that indeed a finer mesh must be employed. Figure 5.5 portrays the base pressure spectra and figure 5.6 exhibits the base pressure gradients over 300 non-dimensional time units, $t^* = t|\boldsymbol{U}_\infty|/H$, for all three meshes. The average base pressure spectra show that the amplitude of the base pressure signal is heavily under-predicted for the 5.4 million cell mesh (Fig. 5.5). There is a significantly larger amplitude in the mean base pressure signal for the 11.1 million and 25.6 million cell mesh at Strouhal numbers based on body height, Str_H, of $\mathcal{O}(0.01)$. Additionally, although one cannot discern a difference in the vertical base pressure gradient, $\partial C_P/\partial x_2$, among the three set-ups (Fig. 5.6a), this cannot be said of the horizontal base pressure gradient, $\partial C_P/\partial x_3$ (Fig. 5.6b). The magnitude of the horizontal base pressure gradient is noticeably smaller for the 5.4 million cell mesh than for the 11.1 million and 25.6 million cell mesh (Fig. 5.6b). It was, thus, deemed necessary to use the 11.1 million cell mesh for all subsequent WRLES simulations performed in the considered study. Furthermore, it is important to mention that all three WRLES meshes considered here present a bimodal event in the illustrated time-span of figure 5.6: at $t^* \sim 70$ for the 5.4 million cell mesh, at $t^* \sim 135$ for the 11.1 million cell mesh, and at $t^* \sim 110$ for the 25.6 million cell mesh. This demonstrates that one objective of this study has been achieved as part of the mesh refinement study: the construction of a numerically tractable set-up that captures bimodality for future drag reduction work performed with

LES. More specifically, the adopted 11.1 million cell WRLES mesh is 80% smaller in cell count than the fully block-structured WRLES meshes employed in the only further published computational investigation on wake bimodal switching from this research group, which was carried out by Dalla Longa *et al.* (2019).

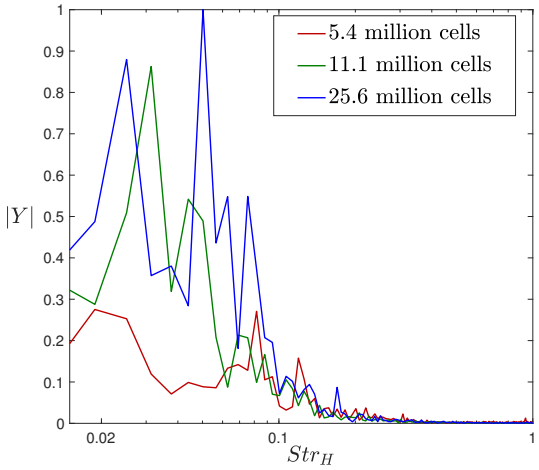


Fig. 5.5: Mesh refinement study for Ahmed body WRLES - base pressure spectra

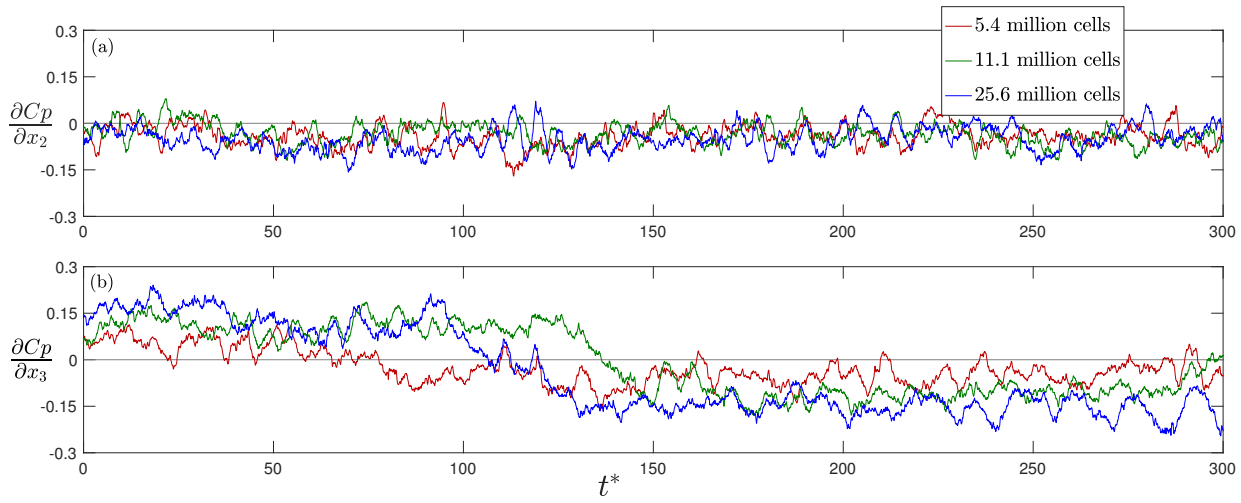


Fig. 5.6: Mesh refinement study for Ahmed body WRLES - base pressure gradients in the (a) vertical direction, $\partial C_P/\partial x_2$, and (b) horizontal direction, $\partial C_P/\partial x_3$

The use of the 11.1 million cell WRLES mesh is further justified through its favourable comparison to other general LES mesh resolution criteria both near the wall and away from the wall. To begin, away from the wall, the mesh satisfies the LES viscosity ratio criterion of $\nu_t/\nu \sim\leq 5$ (Fauconnier & Dick, 2014). As made clear in the instantaneous iso-contour plot of $\nu_t/\nu = 5$ (Fig. 5.7a) and the complementary viscosity ratio contour plot (Fig. 5.7b), ν_t/ν is only greater than 5

in eddy cores nearer to the Ahmed body as well as in the far-field wake region. At this stage, it is important to distinguish between the different reasons for these elevated viscosity ratio values. As Howard & Pourquie (2002) state in their LES study of the Ahmed reference model, there are both the artificial grid effects in the wake's far-field region as well as the physical strain effects near the Ahmed body wall. In the far-field, the large cell size amplifies even negligible strain effects. This is a result of the eddy viscosity output from the WALE turbulence model having a grid dependent length-scale. It is, therefore, justified to ignore the larger viscosity ratio values in the far-field. From this point onward, both the wake and far-field mesh remain unaltered from the, thus far, discussed baseline WRLES mesh. Specifically, subsequently constructed WMLES meshes have the same wake as well as far-field mesh topology.

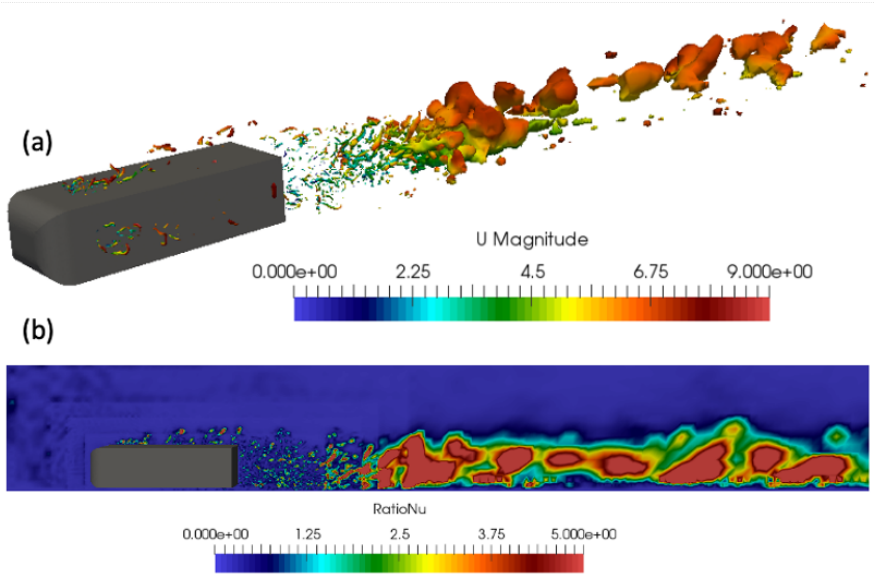


Fig. 5.7: Visualization of viscosity ratio with an (a) iso-contour plot at $\nu_t/\nu = 5$ colored by velocity magnitude and (b) a viscosity ratio contour plot

The baseline 11.1 million cell WRLES mesh's near-wall construction is now examined more closely. It has 8 prism layers (Fig. 5.4a) in order to try to fully capture the large velocity gradient inherent with a turbulent boundary layer. The average wall "y-plus" must be centered about 1 (Fan *et al.*, 2020). Histogram plots of figure 5.8 demonstrate that this criteria is fulfilled. Further, by projecting the $\overline{x_{2w}^+}$ distribution onto the Ahmed body, it is clear that $\overline{x_{2w}^+} > 1$ values are positioned around the

nose of the Ahmed body (Fig. 5.10a). It is deemed acceptable to have such near-wall wall-normal mesh resolution, as the flow is likely still laminar near the nose. The flow's transition to a turbulent state is expected to happen due to flow separation just behind the Ahmed body nose, where a bubble of separated flow forms (see section 5.3). In fact, traces of this separation bubble may be seen in the $\overline{x_{2w}^+}$ distribution (figure 5.10a). Additional WRLES mesh criteria for the near-wall mesh construction include an average streamwise cell spacing, $\overline{\Delta x_{1w}^+}$, of at most 50-130, and cross-stream grid spacing, $\overline{\Delta x_{3w}^+}$, of at most 15-30, as well as at least 10-30 grid-points populated across the turbulent boundary layer's inner region ($\overline{x_2^+} < 100$) (Choi & Moin, 2012). In this work, meshes have $\overline{\Delta x_{1w}^+}$ equal to $\overline{\Delta x_{3w}^+}$ i.e. in the streamwise and cross-stream directions the cells are isotropic. In figure 5.9, the histogram plots show that the WRLES grid is characterized by $\overline{\Delta x_{1w}^+}$ and $\overline{\Delta x_{3w}^+}$ values centered about 20. The WRLES grid, therefore, satisfies both the streamwise and cross-stream grid metrics as provided by Choi & Moin (2012) for wall-resolving LES. Finally, the near-wall mesh requirement that at least 10 cells be positioned in the inner turbulent boundary layer region is also satisfied as figure 5.11 shows.

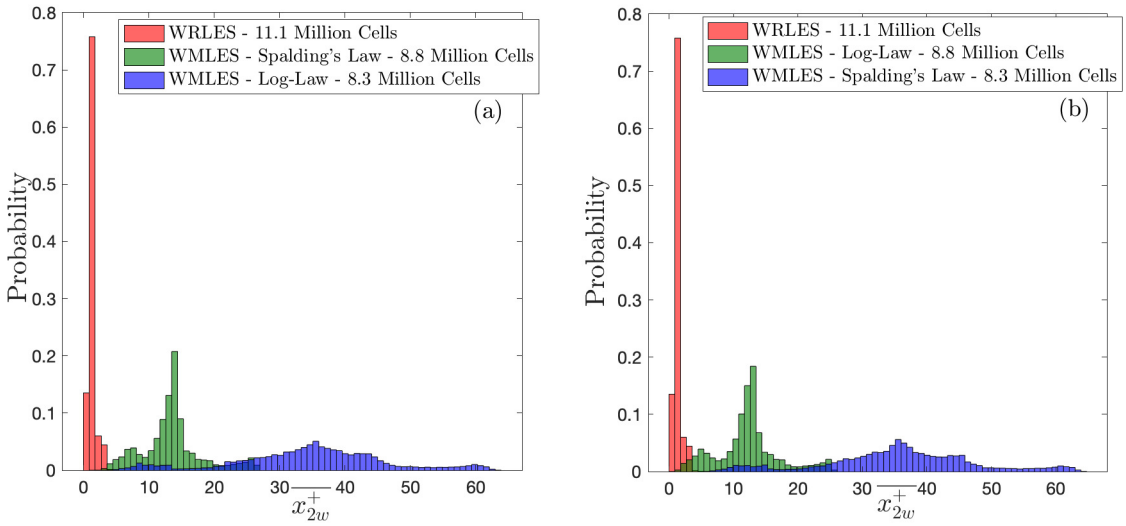


Fig. 5.8: Histogram plots of wall "y-plus", $\overline{x_{2w}^+}$

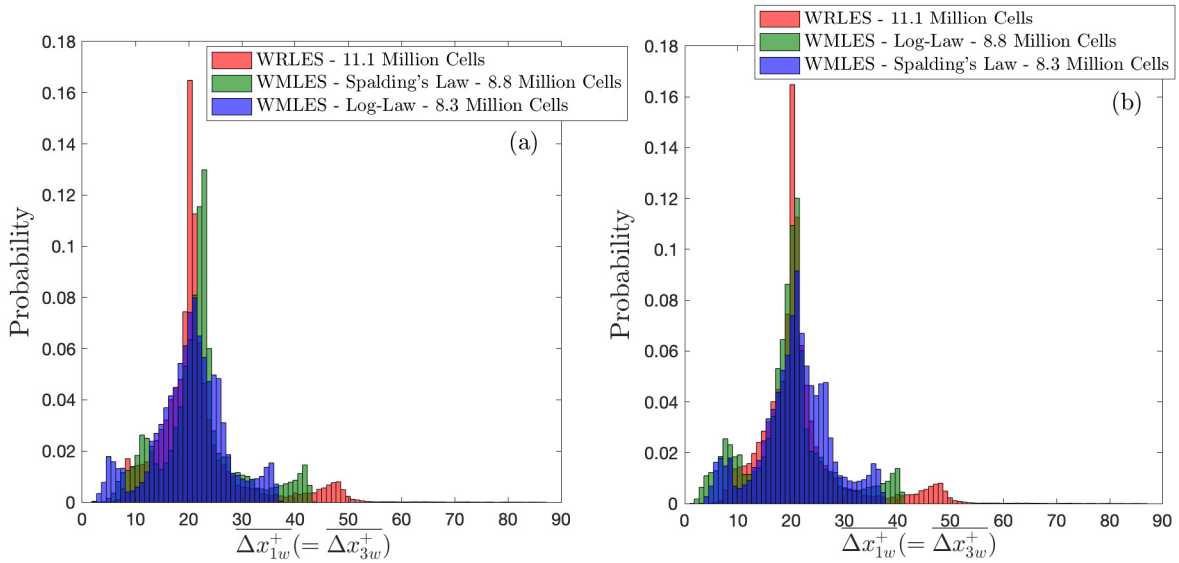


Fig. 5.9: Histogram plots of $\overline{\Delta x^+_{1w}}$ and $\overline{\Delta x^+_{3w}}$

With the baseline WRLES grid consisting of 11.1 million cells conclusively chosen, two WMLES meshes were derived from it. As stated previously, the mesh away from walls is fixed and, thus, only the prism layer mesh construction at the wall was changed. In the first WMLES mesh, the original eight prism layers are replaced with a mere two prism layers. This mesh consists of about 8.8 million cells, which constitutes a reduction of approximately 20% in terms of cell number when compared to the reference 11.1 million cell WRLES mesh. Spalding's law (Eq. 3.2.2) and the log-law (Eq. 2.3.11) were both applied to this mesh in a simulation. An assessment of the average wall "y-plus" distribution for these two simulations is provided in figure 5.8: (a) for Spalding's law and (b) for the log-law. The histogram plots indicate that the wall-model applied has a negligible impact on the resolved flow. Almost identical $\overline{x^+_{2w}}$ spreads are obtained with the centers of the histogram plot distributions positioned beyond $\overline{x^+_{2w}} > 10$, thereby adhering to best-practice guidelines for using wall-models. Additionally, one may project the $\overline{x^+_{2w}}$ spread upon the Ahmed body itself, as was done for the WRLES simulation. Figure 5.10b illustrates the result for Spalding's law applied to the 8.8 million cell mesh. The contours on the Ahmed body closely replicate those found for the WRLES simulation (Fig. 5.10a), particularly the trace of the front bubble of separated flow. Although the imprint of the front separation bubble is captured for the 8.8 million cell mesh with Spalding's law

applied, it is important to note one significant difference compared to the WRLES simulation. In the case of the wall-modelled set-up, the front recirculation bubble appears slightly further downstream of the nose-to-side junction. This seems plausible. One is enforcing, or in other words "tripping", a turbulent boundary layer in the wall-model set-up. This suppresses the front separation bubble and forces it to occur further downstream compared to the WRLES case. Furthermore, to ensure that the Reynolds-averaging effect is enough to allow wall-models to be used, Piomelli & Balaras (2002) state that $\overline{\Delta x_{1w}^{+}} \sim 1500$ and $\overline{\Delta x_{3w}^{+}} \sim 70$. These criteria are, unfortunately, not fulfilled by the created WMLES mesh that is currently under scrutiny. The condition is not met, since altering the mesh spacing in the streamwise and spanwise directions would inadvertently also modify the wall-normal mesh spacing. Therefore, $\overline{\Delta x_{1w}^{+}}$ and $\overline{\Delta x_{3w}^{+}}$ continue to encapsulate the value of 20 at their centers, as is the case for the 11.1 million cell WRLES mesh (Fig. 5.9). It remains, however, appropriate to still designate these simulations as WMLES. The reason for this is that the wall-normal mesh spacing has been enlarged to an acceptable value (Fig. 5.8) and, ultimately, the simulations employ modelled no-slip conditions. Moving on, the final mesh created is also one for WMLES. It now has only one prism layer cell applied and, therefore, a cell count of approximately 8.3 million cells. The two wall-models considered in this study were also both used in conjunction with this mesh (Fig. 5.8): (a) log-law and (b) Spalding's law. It can be discerned that the wall "y-plus" distributions do not differ too much and that both are centred beyond the 30 mark. A coarser near-wall mesh results in a greater amount of Reynolds-averaging being applied to the wall-normal fluctuations. This leads to a distinct change in the flow structures that are projected on the Ahmed body wall through visualization of the wall "y-plus" distribution. For instance, figure 5.10c for the log-law does not present indications that a front separation bubble is captured in the simulation. One may interpret this as the tripping of a turbulent boundary layer that never separates. However, upon closer inspection in section 5.3, it becomes clear that the reason for this lacking front separation bubble is insufficient near-wall mesh resolution.

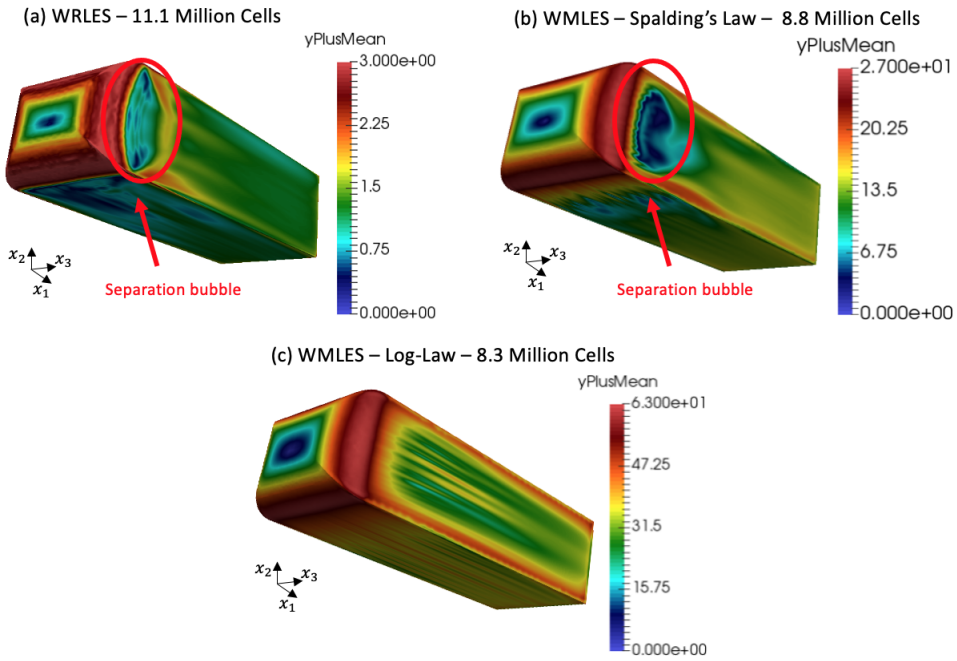


Fig. 5.10: Wall "y-plus" distribution projected onto the Ahmed body for (a) WRLES set-up with 11.1 million cells, (b) WMLES set-up using Spalding's law with 8.8 million cells and (c) WMLES set-up using the log-law with 8.3 million cells

Looking at the data on $\overline{x^+_{2w}}$ (wall "y-plus"), $\overline{\Delta x^+_{1w}}$ and $\overline{\Delta x^+_{3w}}$, it does not appear too unreasonable to state that both wall-models, Spalding's law (Eq. 3.2.2) and the log-law (Eq. 2.3.11) can be used in conjunction with the 8.3 million cell and 8.8 million cell WMLES meshes. However, there are differences. These become noticeable when analysing average turbulent boundary layer velocity profiles measured at a position downstream of the front separation bubble on the cross-stream side of the Ahmed body where the flow has recovered from the front separation bubble. These profiles are presented in non-dimensional wall units (Fig. 5.11). It appears that greater correlation with the WRLES curve is achieved when using Spalding's law of the wall on the 8.8 million cell mesh. This corroborates the observation that the log-law of the wall should, ideally, be employed when the wall-adjacent cell center is beyond the buffer layer of the turbulent boundary layer i.e. $x^+_{2w} \gg 30$. This is a stipulation that the 8.8 million cell grid does not satisfy. Nevertheless, the 8.8 million cell grid in conjunction with the log-law does still better resolve the high energy buffer layer of the turbulent boundary layer than both of the two simulations carried out with the 8.3 million cell grid. A likely reason for this is that the 8.3 million cell mesh is, in fact, ill-suited for both Spalding's law

and the log-law of the wall. Its wall "y-plus" is centred about 35 (Fig. 5.8), which bounds the extremities of the buffer region and log-law region of the turbulent boundary layer (see Eq. 2.3.11). In other words, the wall-models are not used correctly for this mesh, as the cells do not directly fall into either region, which makes the modelling of their velocity value difficult, returning wall unit turbulent boundary layer velocity profiles that do not conform with the WRLES curve. This means that the slope imposed by $1/\kappa$ in the log-law is not returned for the 8.3 million cell mesh (Fig. 5.11). The 8.3 million cell grid's inability to accurately capture the transition from the buffer region to the fully turbulent log region of the boundary layer with both wall-models means that critical physics is not resolved. This is physics that appears to be required for resolving wake bimodality as shown in section 5.3. The remainder of the work presented in this chapter focuses mainly on three simulations: WRLES with the 11.1 million cell grid, WMLES with Spalding's law of the wall applied to the 8.8 million cell grid, and the log-law of the wall applied to the 8.3 million cell grid.

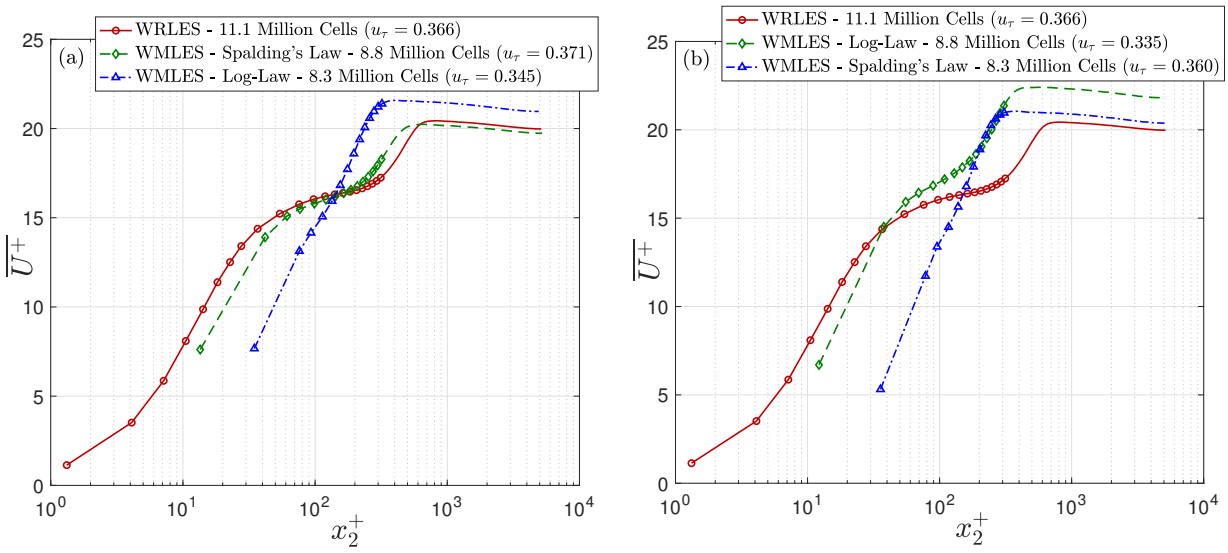


Fig. 5.11: Average turbulent boundary layer velocity profiles in wall units taken from the Ahmed body cross-stream side(s) downstream of the front separation bubble

5.2 Detection of Wake Bimodality

This section is devoted to graphical representations that assess whether simulations have captured wake bimodal switching events. Specifically, the goal is to graphically assess which simulations

with varying near-wall resolution, in this case the two WMLES mesh constructions and the one WR-LES mesh, resolve wake bimodality.

Before analyzing the occurrence of bimodality, mean aerodynamic flow quantities for the WM-LES simulations are considered (table 5.2). Positioned next to these values are the corresponding numbers for the WRLES simulation. When taking the WRLES data as the benchmark, one can discern some variability amongst the quantities on display: drag varies by up to 5%, lift varies by up to a staggering 30%, base pressure varies by up to 22%, and the wake length varies by up to 6%. In aerodynamic investigations, it often occurs that it is more difficult to obtain converged lift values and, therefore, the noticeably higher variability and poorer correlation among the lift values is not completely unexpected. This was encountered by Ashton *et al.* (2016) in their computational investigation of different DrivAer models with a broad range of RANS and DES turbulence models. The lift coefficient could vary beyond 100% of its reference value, while the drag coefficient varied by as little as just over 5% of its baseline value. Importantly, one can see that for this study variability is quite high for $\overline{C_L}$, which lies at 27.2%, and $\overline{C_{PB}}$, which lies at 23.9%, with the 8.3 million cell mesh used for WMLES simulations. As elaborated upon in section 5.3, this suggests the simulations carried out with the 8.3 million cell mesh capture flow features that are fundamentally different to the benchmark flow features in the WRLES simulation of 11.1 million cells.

Simulation	ΔL_{wake}	$\overline{C_D}$	$\overline{C_L}$	$\overline{C_{PB}}$	$\overline{L_B}$
WRLES - 11.1 MC	$0.413\lambda_T$	0.364	-0.0548	-0.201	1.417H
WMLES - SL - 8.8 MC	$0.413\lambda_T$	0.365	-0.0506	-0.204	1.403H
WMLES - LL - 8.8 MC	*$0.413\lambda_T$*	*0.346*	*-0.0526*	*-0.203*	*1.444H*
WMLES - LL - 8.3 MC	$0.413\lambda_T$	0.369	-0.0405	-0.157	1.500H
WMLES - SL - 8.3 MC	*$0.413\lambda_T$*	*0.375*	*-0.0383*	*-0.158*	*1.472H*
Grandemange *et al.* (2013*a*)	-	-	-	-0.190	1.418H

Table 5.2: Mean aerodynamic quantities for the WMLES simulations where MC represents "million cells", SL denotes Spalding's law and LL stands for "log-law". Complementing wall-model results are written in *italics*

Moving to visual representations indicating the occurence of wake bimodality, figure 5.12 displays base pressure gradients in the horizontal direction, $\partial C_P/\partial x_3$, and the vertical direction, $\partial C_P/\partial x_2$, for all three simulation cases that are looked at more closely in this study. Covering a non-dimensional time-span of 1050 convective time-scales, this temporal window should be enough to assess if wake bimodality can be captured in simulation. At least one bimodal switch should be resolved in this time window, since it has been shown both experimentally and computationally that the time-scale characterizing the occurence of bimodal events is up to $t^* \sim 10^3$ convective time-scales (Grandemange *et al.*, 2013*b*; Fan *et al.*, 2020; Dalla Longa *et al.*, 2019). One can discern a mild vertical wake asymmetry for all three simulations (Fig. 5.12a). To be more specific, the wake tilts to its top trailing edge. The reason for this is the ground proximity of the Ahmed body. This causes an acceleration of the flow in the under-body gap to the ground, which drags the wake's bottom side further downstream at the exit of the gap. Such a weak asymmetry in the vertical direction is found as well in the experimental work by Grandemange *et al.* (2013*a*) and Grandemange *et al.* (2013*b*) for flow Re_H of 33333 and 92000, respectively. One can, therefore, conclude that the balance between the wake's bottom and top shear layers is simulated accurately.

This is paramount to resolving bimodal dynamics of the wake, as illustrated by the laboratory work of Perry *et al.* (2016). They reduced the likelihood of bimodality developing behind the Windsor reference model via the use of top and bottom trailing edge tapers, which altered the distribution of the base pressure and, thereby, the wake balance in the vertical direction (Perry *et al.*, 2016). Additionally, a distinctly visible horizontal wake asymmetry is present in all three simulations, which indicates that the wake balance between the side shear layers (i.e. in the horizontal / cross-stream direction) is accurately represented as well (Fig. 5.12b). Of the three mesh set-ups presented, only two capture bimodal events: the WRLES grid with 11.1 million cells and the simulation that uses the 8.8 million cell WMLES grid in conjunction with Spalding's law. This means there is a further 21% reduction in mesh size that is needed to capture wake bimodality. Going back to the results, the wake moves its horizontal off-axis position at t^*-values of 378, 713 and 836 for the WRLES set-up. In the same time-span, the 8.8 million cell grid with Spalding's law applied as the wall-model presents large-scale wake motions at t^*-values of approximately 222, 300, 698 and 941. Capturing up to four bimodal switching events within a non-dimensional convective time-scale window of just over $t^* \sim 10^3$ suggests that it is, in fact, not so clear-cut to say that a single bimodal switching event is expected to occur in $t^* \sim 10^3$ convective time-scales, as suggested by other studies. Based on these simulation results, the period between (random) switching is actually much shorter. It is also worth pointing out that associating a period with an inherently random and stochastically driven phenomenon is already in itself questionable. In any case, figure 5.14 depicts joint probability density functions (PDF) of the $\partial C_P/\partial x_2$ and $\partial C_P/\partial x_3$ distributions found in figure 5.12, this offering an additional way to highlight the presence of wake bimodality. When wake bimodality does exist, the PDF has two attractors: one centered at $\partial C_P/\partial x_3 >$0 and another at $\partial C_P/\partial x_3 <$0 (Fig. 5.14a and 5.14b). Therefore, figure 5.14a represents three bimodal switching realizations, while figure 5.14b constitutes four bimodal switching events. Two attractors with a more similar heat-map are found in figure 5.14a as opposed to figure 5.14b because, although figure 5.14b is associated with

more bimodal switching events, the total time that the wake spends in any given off-axis position is more evenly distributed for the WRLES case in figure 5.14a. Meanwhile, the WMLES simulation that uses the 8.3 million cell grid and the log-law only possesses one attractor (Fig. 5.14c). It is centered at $\partial C_P/\partial x_3 > 0$, thereby showing the mesh's inability to resolve wake bimodality. When extending the simulation time to $t^* \rightarrow \infty$ and, therefore, capturing more bimodal events, one can expect the two attractors seen in both figures 5.14a and 5.14b, respectively, to exhibit a more similar color intensity distribution, indicating that equal quantities of time are spent in each asymmetric wake state. To further highlight the grid dependency related to resolving wake bimodality, figure 5.13 presents a base pressure gradient plot that supplements figure 5.12. Specifically, the plot illustrates that bimodality can be resolved with the log-law used on the 8.8 million cell grid, while the phenomenon remains elusive with the 8.3 million cell grid despite the use of Spalding's law of the wall.

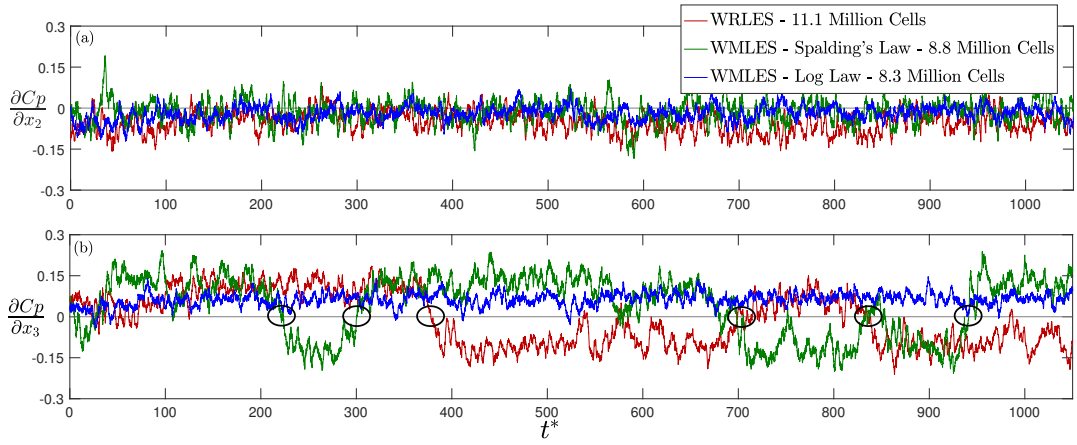


Fig. 5.12: Base pressure gradient in the (a) vertical direction, $\partial C_P/\partial x_2$, and (b) horizontal direction, $\partial C_P/\partial x_3$, for 11.1 million cells WRLES, 8.8 million cells WMLES with Spalding's law and 8.3 million cells WMLES employing the log-law. The black circles show bimodal wake shifting events

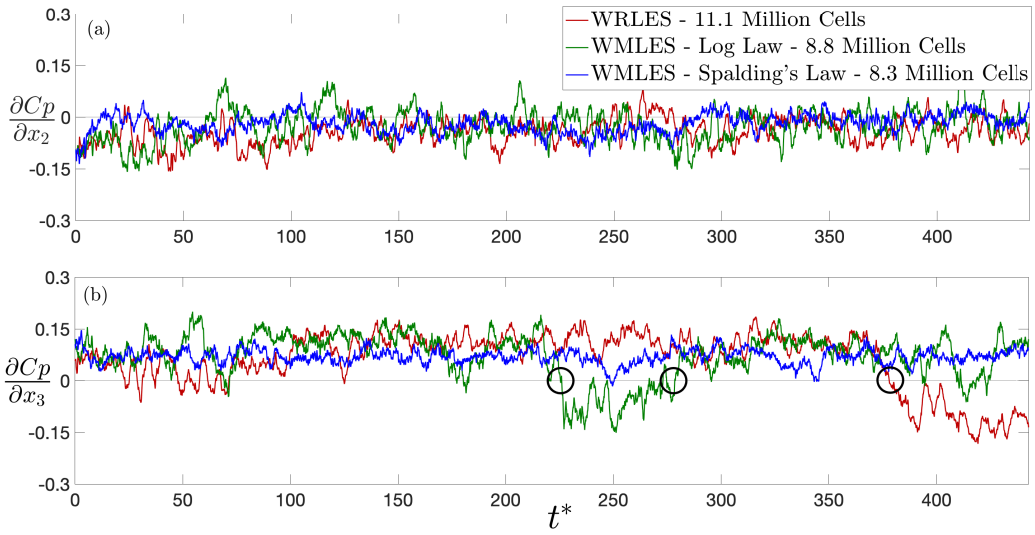


Fig. 5.13: Base pressure gradient in the (a) vertical direction, $\partial C_P/\partial x_2$, and (b) horizontal direction, $\partial C_P/\partial x_3$, for 11.1 million cells WRLES, 8.8 million cells WMLES with the log-law and 8.3 million cells WMLES employing Spalding's law. The black circles show bimodal wake shifting events

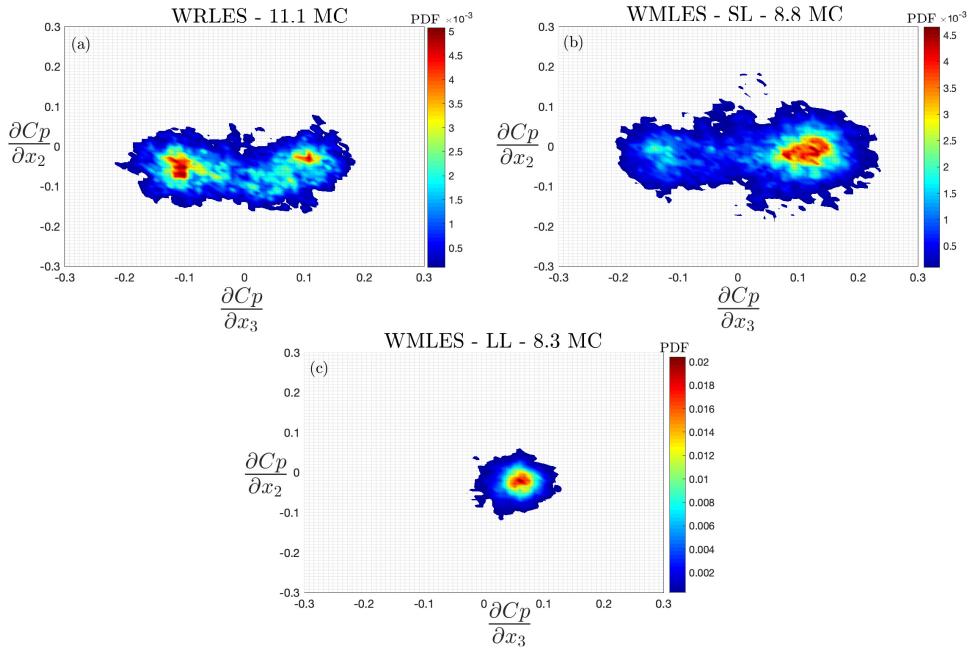


Fig. 5.14: Joint probability density function of base pressure gradients, PDF($\partial C_P/\partial x_2$,$\partial C_P/\partial x_3$), for (a) 11.1 million cells (MC) WRLES, (b) 8.8 million cells WMLES applying Spalding's law (SL) and (c) 8.3 million cells WMLES using the log-law (LL)

Additionally, velocity magnitude and pressure contour plots on an x_1x_3 - middle plane through the Ahmed body also serve as good identifiers of wake bimodality. Figure 5.15 presents one "cycle" of wake bimodality for the WRLES simulation with an 11.1 million cell grid using instantaneous contour plots of pressure. More specifically, it shows the wake tilted towards opposing off-axis locations, i.e. to the left-hand side and to the right-hand side of the Ahmed body, as well as a

transitory symmetric state of the wake. These states are separated by a Δt^* of approximately 15 convective time-scales (see figure 5.12). At the nose, one can identify a separation bubble with a low pressure core from which derivative low pressure vortex structures are shed. The vortex structures grow as they are convected downstream. Once at the rear of the Ahmed body, these structures interact with the wake. Section 5.3 focuses in more detail on this separation bubble and the shed vortices, since they may play a major role in triggering a bimodal event. Moving on, in figure 5.17, the instantaneous velocity magnitude with streamlines is presented for the 8.8 million cell grid that uses Spalding's law as a wall model. Here too, the states are separated by a Δt^* of approximately 15 convective time-scales (see figure 5.12). The wake is initially tilted to the Ahmed body's right-hand side and subsequently shifts its low pressure core to the left-hand side. One can discern that a large recirculation core is "fixated" to the spanwise side to which the asymmetric wake is tilted. The left and right recirculation cores become more evenly distributed, i.e. the wake is symmetric, as the wake moves from one side to another. The previously described front separation bubble and shed vortices are also noticeable in these snapshots of the flow field. It is insightful to further compare the front separation bubbles for the different simulations. In the case of the WRLES simulation with the 11.1 million cell grid, the separation bubble is moderately more prominant in size and is positioned slightly further upstream than the bubble captured by the 8.8 million cell WMLES simulation with Spalding's law. This point is corroborated by the following two figures: figure 5.16 for the WRLES simulation with the 11.1 million cell grid and figure 5.18 for the WMLES simulation with Spalding's law applied to the 8.8 million cell grid. A plausible explanation for this observation is that, as mentioned previously, the application of Spalding's law as a wall-model "trips" a turbulent boundary layer at the nose of the Ahmed body, thereby delaying separation and the associated front recirculaton bubble. Spectra (Fig. 5.19) were also evaluated by using the fast Fourier transform of pressure data that is recorded at a fixed point downstream of the recirculation bubble (Fig. 5.15 and 5.17). Despite the varying bubble size, the results indicate that, for the selected probe location, the

vortex shedding amplitude of the vortices is large for both the WRLES simulation, and the WMLES set-up using the 8.8 million cell grid and Spalding's law. The shedding amplitude is, however, largest for the latter WMLES simulation. This is likely simply due to the marginally closer probe position to the recirculation bubble in this set-up (Fig. 5.17). Finally, one can see that the amplitude of the front bubble's shedding frequency is negligible for the coarser WMLES grid consisting of 8.3 million cells and that, here, uses the log-law. This suggests that no front separation bubble is captured when using the coarser wall-model grid. It is a theme that pervades section 5.3.

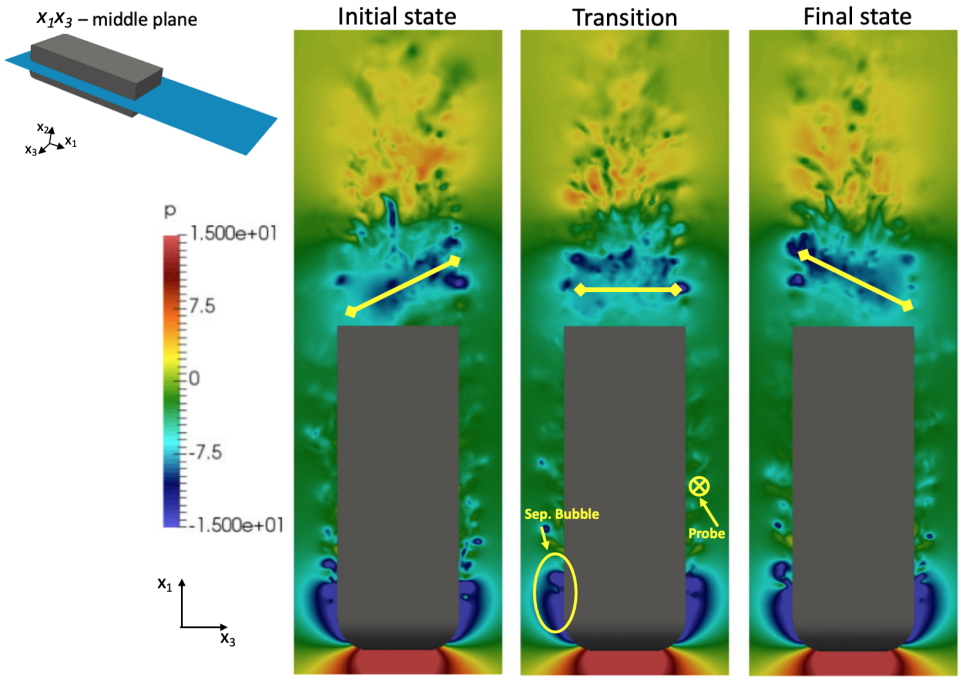


Fig. 5.15: Wake bimodality visualized using the instantaneous pressure field projected onto the x_1x_3 - middle plane passing through the Ahmed body for the WRLES case

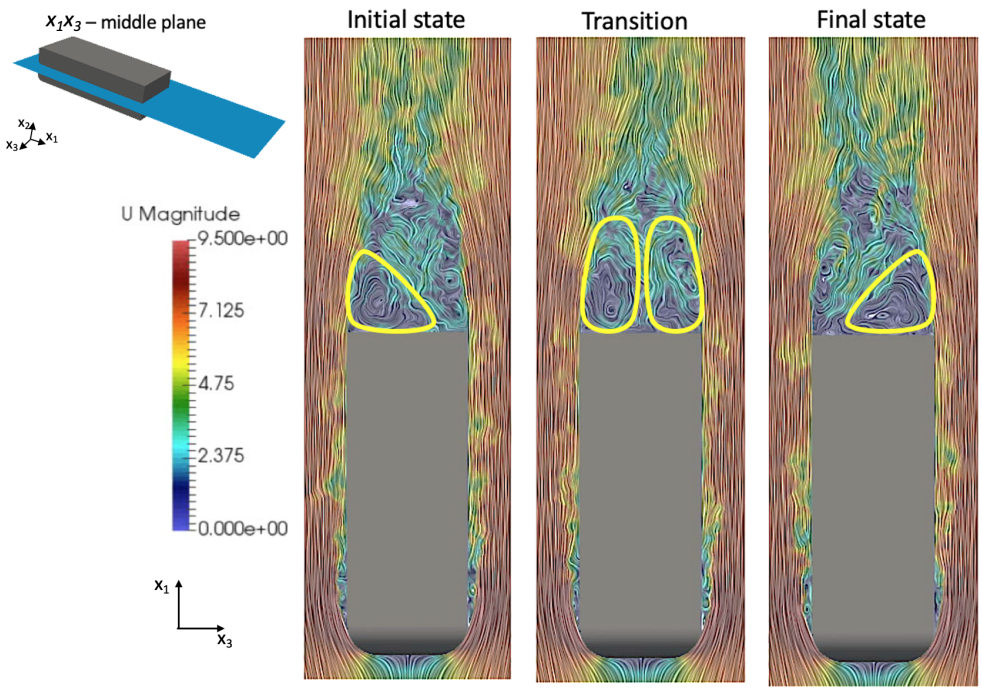


Fig. 5.16: Wake bimodality visualized using the instantaneous velocity magnitude field with streamlines projected onto the x_1x_3 - middle plane passing through the Ahmed body for the WRLES set-up

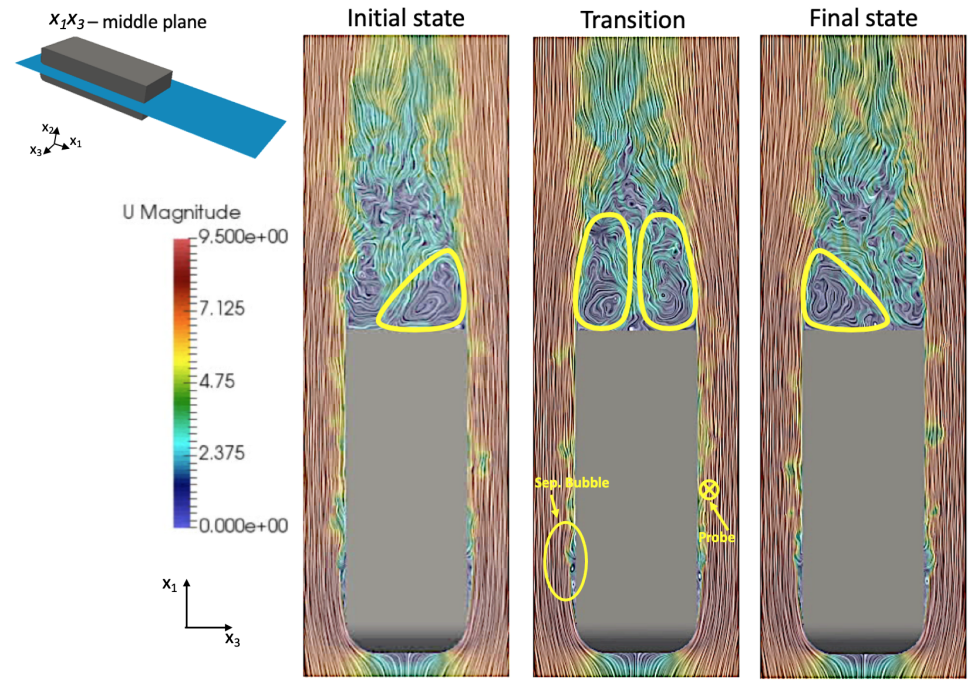


Fig. 5.17: Wake bimodality visualized using the instantaneous velocity magnitude field with streamlines projected onto the x_1x_3 - middle plane passing through the Ahmed body for the 8.8 million cell WMLES set-up that uses Spalding's law

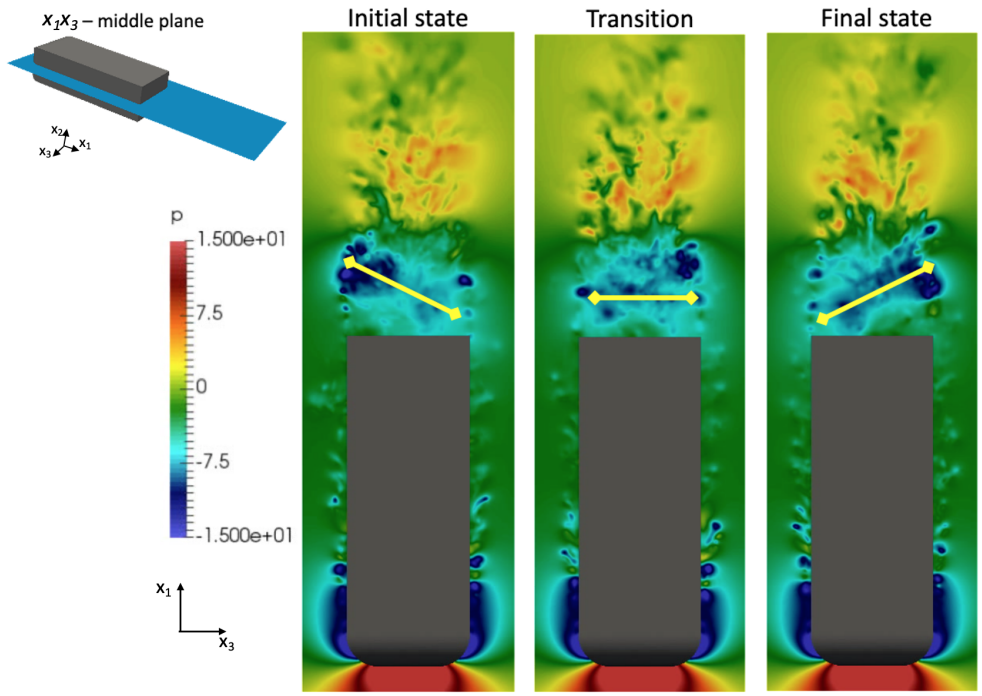


Fig. 5.18: Wake bimodality visualized using the instantaneous pressure field projected onto the x_1x_3 - middle plane passing through the Ahmed body for the 8.8 million cell WMLES case that uses Spalding's law

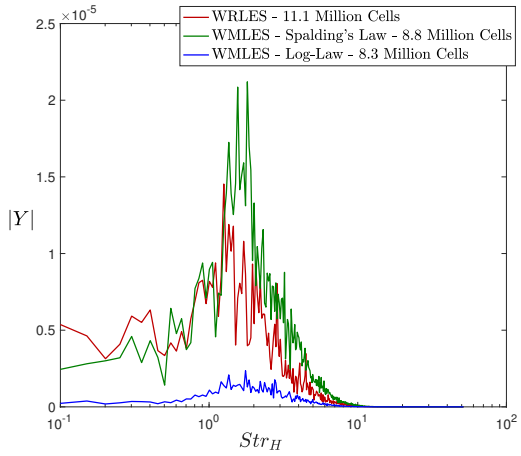


Fig. 5.19: Vortex shedding frequency associated with front separation bubble

Additionally, one can visualize the presence of wake bimodality in 3D by analyzing instantaneous iso-contour plots of $C_P = -0.3$ coloured by velocity magnitude. In figure 5.20a, the instantaneous plots are presented for WRLES. Meanwhile, in figure 5.20b the instantaneous plots are illustrated for the 8.8 million cell WMLES simulation with Spalding's law applied as wall-model. Both figures focus on the rear of the Ahmed body, and the wake transitions in opposite directions for the two setups. As observed in the numerical studies by Lucas *et al.* (2017), Rao *et al.* (2018*a*), Rao *et al.* (2018*b*) and Dalla Longa *et al.* (2019), the simulations capture an instantaneously asymmetric

wake that keeps its toroidal time-averaged structure and is merely tilted to a preferred side. This goes against the observations made by Evrard *et al.* (2016), Perry *et al.* (2016) and Pavia *et al.* (2018) who used 2D PIV planes to propose that the instantaneously asymmetric wake is made up of single or multiple horseshoe vortices that, in the long time-average, "merge" to form the closed toroidal structure that characterizes the time-averaged wake. Furthermore, the numerical study on wake bimodality by Dalla Longa *et al.* (2019) and Fan *et al.* (2020) explains that the bimodal switch from one side to the other is accompanied by the release of a large hairpin vortex that drags the wake to its opposing off-axis location. The presented simulations do not capture this. Instead, throughout a bimodal switching event, the toroidal pressure structure simply "disconnects" from the Ahmed body rear base side to which it is tilted at first and subsequently, after the bimodal motion is complete, "reconnects" to the Ahmed body rear base, but at the opposing side.

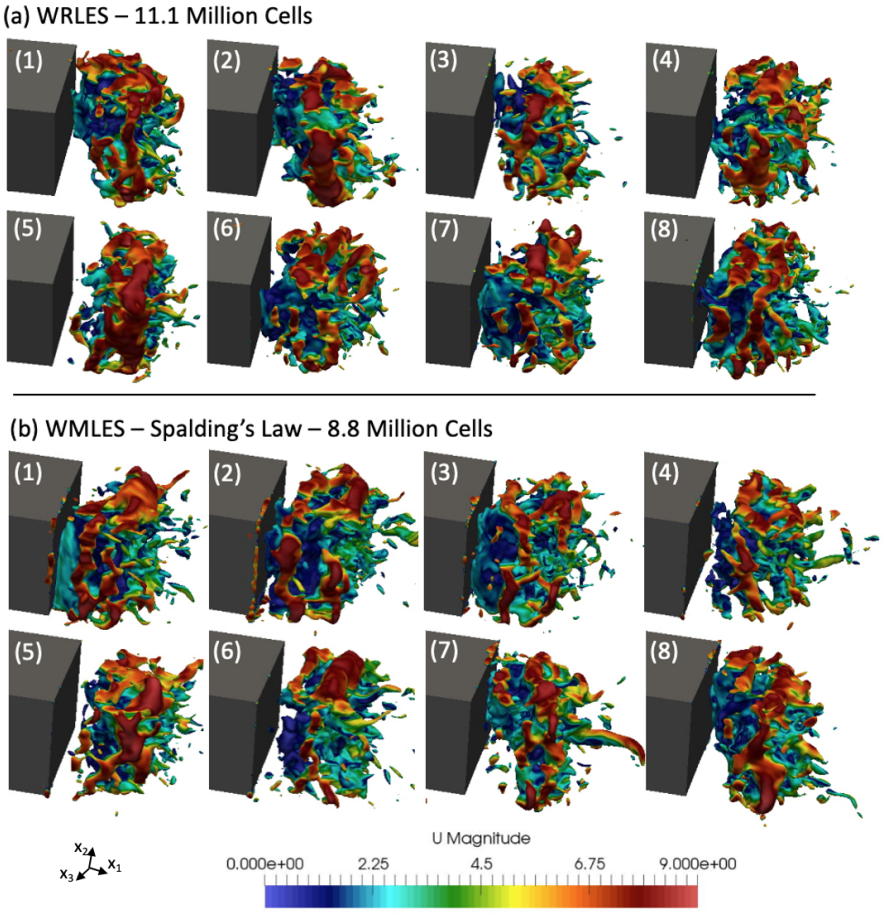


Fig. 5.20: Wake bimodality visualized using $C_P = -0.3$ iso-contour plots coloured by velocity magnitude for (a) WRLES and (b) 8.8 million cell WMLES using Spalding's law

Overall, the presence of spanwise large-scale shifts in the wake's position at irregular intervals (Fig. 5.12b) shows that bimodality is inherently random and that it must, therefore, be driven by stochastic processes that are introduced to the flow due to the turbulent nature of the fluid's state. Such information supports the previously mentioned theoretical and experimental work done by Rigas *et al.* (2015) on a 3D wake created by an axisymmetric blunt bluff-body. The investigation illustrated that the turbulent wake's motions, consisting of an infinitely large quantity of metastable states in the azimuthal direction and about a mean radial position that is determined by a supercritical spatial pitchfork bifurcation from the laminar regime, can be correctly modelled by a 2D nonlinear Langevin equation: the deterministic component accounts for the broken symmetry while the stochastic term captures the turbulent fluctuations forcing the wake to undergo a random walk (Eq. 2.1.2) (Rigas *et al.*, 2015). Additionally, it has already been shown in this research group through the work of Dalla Longa *et al.* (2019) that WRLES can resolve bimodality. Their study presents one bimodal switching event for the squareback Ahmed body in a t^*-window of $\sim$1400. In the current study, it is demonstrated for the first time that, with enough near-wall resolution, WMLES can resolve bimodality as well. As the coarser of the two WMLES grids, namely the 8.3 million cell grid with just one prism layer cell, fails to capture bimodality with both of the two considered equilibrium wall-models tested in this work, the following may be concluded: only when the turbulent boundary layer's near-wall region, which is made up of the viscous sub-layer and buffer layer, is modelled, can one still resolve bimodality. As the coarser 8.3 million cell grid treats both the turbulent boundary layer's near-wall region and part of its outer region, which consists of the log-layer, in a Reynolds-averaged sense, it fails the above criterion. Meanwhile, the slightly more refined 8.8 million cell grid with two prism layer cells only models the near-wall dynamics of the turbulent boundary layer, thereby fulfilling the criterion for still resolving bimodality. This information indicates that larger scale flow structures found within the turbulent boundary layer's outer region, such as the vortices produced by the front recirculation bubble, contribute immensely to the flow stochasticity / intermittency that

ultimately forces a transition of the wake's horizontal off-axis location. Section 5.3 delves deeper into this idea.

5.3 Source of Wake Bimodality

First, average flow features present in the three main simulations under investigation in this chapter are analysed. To do this, the focus is placed on the front recirculation bubbles and not the wake. This flow feature can be clearly visualized by looking at contour plots for the average velocity's x_1-component with streamlines projected on to it (Fig. 5.21). Averages are taken over the whole simulation duration i.e. there is no conditional averaging. As such, plots that indicate rear-wake symmetry are, here, actually the time-average over multiple bimodal switching events (see e.g. figure 5.21a for the WRLES) and instantaneously would indicate rear-wake spanwise asymmetry. The x_1x_3-plane used for this visualization is the one used for figures 5.15 to 5.18. It can be seen that the two grids capable of capturing wake bimodality, the baseline WRLES grid with 11.1 million cells (Fig. 5.21a) and the slightly under-resolved near-wall grid with 8.8 million cells (Fig. 5.21b), resolve the front recirculation bubble. Meanwhile, the heavily under-resolved near-wall grid with 8.3 million cells that does not simulate wake bimodality also does not present the upstream front recirculation bubble (Fig. 5.21c). As was noted in the previous section, in the WRLES simulation, the separation bubble is very distinct, while in the 8.8 million cell grid's under-resolved wall-modelled near-wall region, the separation bubble manifests itself slightly downstream of the nose-to-side junction and is also slimmer in shape. Separation bubbles like these are visible on the top surface as well as the side surfaces of the Ahmed body. Ground proximity at the Ahmed body's bottom side hinders flow detachment at the nose. For the 8.3 million cell WMLES set-up (Fig 5.21c), the near-wall region that is treated in a Reynolds-averaged sense extends too far into the turbulent boundary layer and, thus, no front recirculation bubble is captured on any of the Ahmed body's four sides. By overlaying profiles of the average velocity's x_1-component, $\overline{U_{x_1}}$, that are taken from the x_1x_3-middle plane

in the vicinity of the front recirculation bubble (Fig 5.22), one can more precisely demonstrate the variation in the average flow structures resolved by each of the core simulation test cases for this chapter. Figure 5.23 presents a magnified view of the profiles in figure 5.22 at the precise location of the front separation bubble with cell center markers to more visibly illustrate the impact of the mesh's resolution. Slightly downstream of the nose-to-side junction, where x_1 takes on values between 0.03m and 0.08m, the recirculation bubble is visible for both the reference WRLES set-up and the 8.8 million cell WMLES set-up, which is depicted here with data acquired when using Spalding's law. In this highlighted region, $\overline{U_{x_1}}$ presents itself with values less than zero, which is an indicator of flow separation. There are, however, visible differences between the recirculation bubbles captured for the WRLES setup and the 8.8 million cell WMLES setup. More specifically, as noted earlier, separation and subsequent flow reattachment occurs further upstream for the WRLES case. The separation bubble also protrudes further into the wall-adjacent flow domain for WRLES. Furthermore, the $\overline{U_{x_1}}$ profiles for the two set-ups that capture a separation bubble are almost coincident from x_1 =0.12m onward. This further corroborates the application of a grid for Ahmed body aerodynamic simulations in which the near-wall region is slightly under-resolved. Also, looking at the $\overline{U_{x_1}}$ profiles of the 8.3 million cell WMLES grid setup that is used here in conjunction with the log-law (Fig. 5.23), one can see that the flow remains attached downstream of the nose of the Ahmed body. This supports the previous finding that no front recirculation bubble is resolved for this coarsened WMLES set-up. In total, there are very visible discrepancies between wall-region $\overline{U_{x_1}}$ curves captured with the 8.3 million cell grid and the other two main test cases of this chapter that, unlike the 8.3 million cell grid set-up, do capture wake bimodality. Therefore, despite the 8.3 million cell mesh's ability to capture the horizontal rear wake asymmetry, it does not correctly resolve the upstream turbulent boundary layers' profile, including its shedding dynamics, which influences its ability to resolve bimodal switching events.

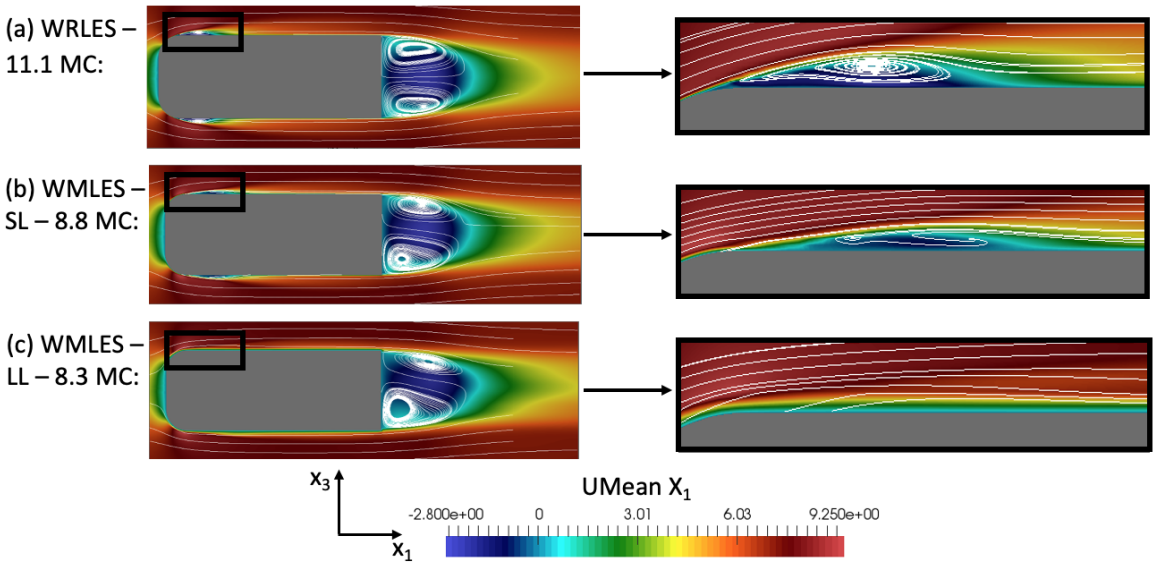


Fig. 5.21: Contour plots of the mean velocity's x_1-component with streamlines projected onto the x_1x_3 - middle plane passing through the Ahmed body for (a) WRLES, (b) 8.8 million cell (MC) WMLES with Spalding's law (SL) and (c) 8.3 million cell WMLES using the log-law (LL)

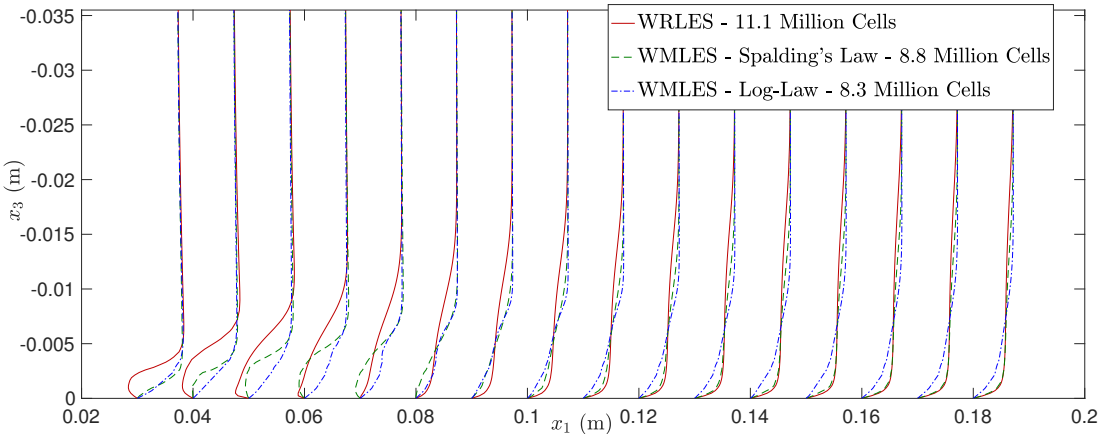


Fig. 5.22: Profiles of the mean velocity's x_1-component, $\overline{U_{x_1}}$, from the x_1x_3 - middle plane passing through the Ahmed body

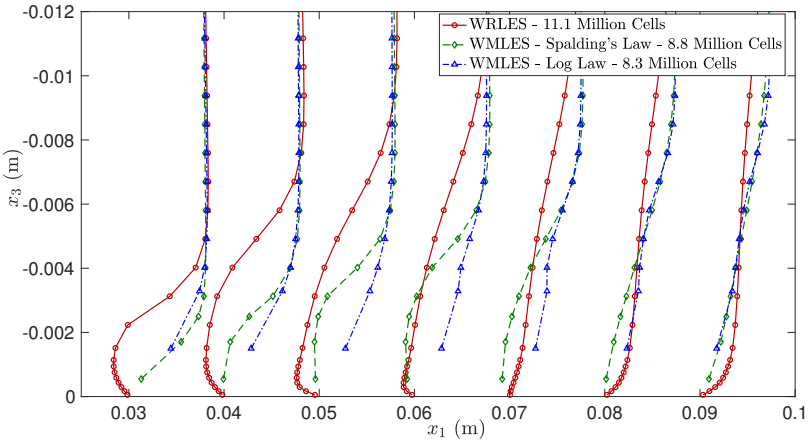


Fig. 5.23: Close-up of x_1-component mean velocity profiles in the vicinity of the front separation bubble. Markers denote cell centers

Moving on, instantaneous flow features captured in the Ahmed body's vicinity for the three main simulations are considered. This is done using 3D visualizations consisting of Q^* iso-contour plots coloured by velocity magnitude (Fig 5.24). The iso-value chosen is $Q^* = 5.30$. This highlights structures with low pressure cores and high rotation. As in the previous paragraph's analysis, the focus is on the vicinity upstream of the wake and, in particular, the nose-to-side junction as well as the domain just downstream of this junction. Figure 5.24a for the WRLES simulation with the 11.1 million cell grid, and figure 5.24b for the WMLES simulation with 8.8 million cell grid and the application of Spalding's law depict similar vortex shedding patterns from the Ahmed body nose. The origin of these shed vortex structures are the prominent front recirculation bubbles (Fig. 5.21a and 5.21b) that were identified in the previous paragraph. These shed vortices grow into sizable hairpin vortices that are convected along the sides of the Ahmed body to its rear. It is precisely these flow structures that are not illustrated in figure 5.24c for the WMLES set-up using the 8.3 million cell grid and the log-law. This set-up's inability to resolve the front recirculation bubbles (Fig. 5.21c) directly leads to its inability to capture the large hairpin vortices that should be emitted by the bubbles. Instead, smaller scale hairpin vortices that form a streaky structure manifest themselves on the sides of the Ahmed body. Figure 5.25 contains a corresponding plot for figure 5.24 in which the WMLES grid order is switched: Spalding's law is applied to the 8.3 million cell mesh and the log-law of the wall is applied to the 8.8 million cell mesh. This complementing figure further substantiates the claim that wake bimodality is sensitive to the near-wall Ahmed body's upstream mesh resolution. Overall, it appears that the lack of large-scale hairpin vortices shed from the Ahmed body nose, a direct consequence of the 8.3 million cell grid's inability to resolve the front recirculation bubble, is associated with the grid's deficiency in capturing rear wake bimodal behavior. One may, therefore, assert that capturing the correct dynamics associated with the front recirculation bubble is a necessity for resolving wake bimodality.

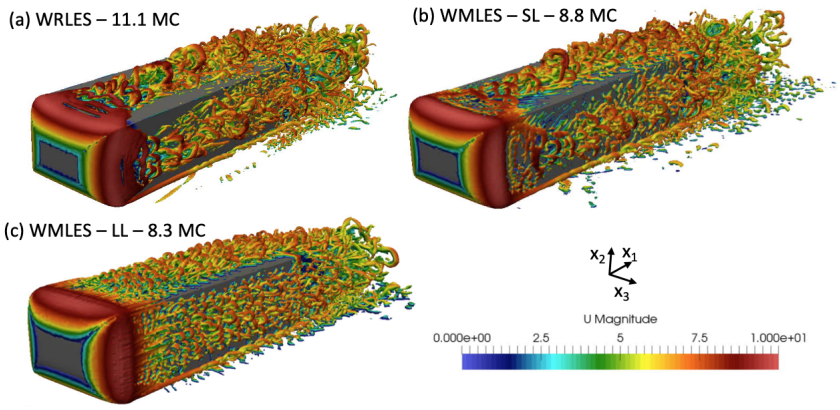


Fig. 5.24: Visualization of flow structures captured around the Ahmed body using iso-contours of Q^*=5.30 for (a) WRLES, (b) 8.8 million cell (MC) WMLES with Spalding's law (SL) and (c) 8.3 million cell WMLES using the log-law (LL)

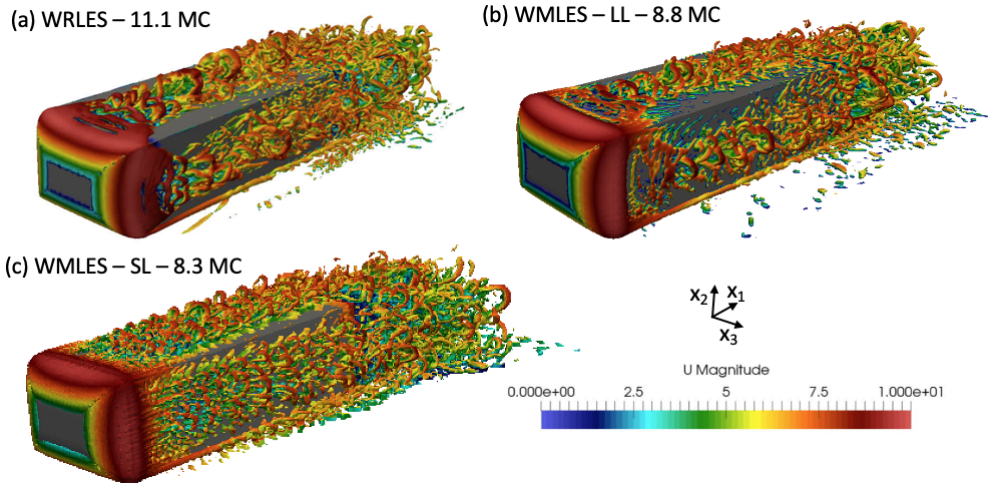


Fig. 5.25: Visualization of flow structures captured around the Ahmed body using iso-contours of Q^*=5.30 for (a) WRLES, (b) 8.8 million cell (MC) WMLES with the log-law (LL) and (c) 8.3 million cell WMLES using Spalding's law (SL)

The noticeable difference in the instantaneous flow features captured translates directly to a different flow intermittency level that is produced at the nose of the Ahmed body. By analyzing the level of turbulent kinetic energy (TKE) that is generated by the flow features around the Ahmed body, one can immediately discern the crucial role that the front recirculation bubbles play in producing flow intermittency via the shedding of large hairpin vortices. Presented in figure 5.26 are contour plots of this TKE on the x_1x_3 - middle plane that passes through the Ahmed body. It is possible to see that non-negligible quantities of TKE are generated at the front recirculation bubble for the 11.1 million cell WRLES simulation (Fig. 5.26a) and the 8.8 million cell WMLES simulation that is presented here for data with Spalding's law applied (Fig. 5.26b). In other words, for the two grids

that are able to capture bimodal wake switches, TKE at the front of the Ahmed body is significant. TKE levels are particularly high for the WRLES case. The level of TKE is, however, negligible for the 8.3 million cell WMLES set-up illustrated here with the application of the log-law; the near-wall dynamics are simply under-resolved by too much (Fig. 5.26c). This is made even clearer by looking at TKE profiles in figure 5.27. A close-up of this figure, where markers denote cell centers, is portrayed in figure 5.28. It can be concluded that the reason for this behavior of the 8.3 million cell grid is that it is unable to resolve the flow feature responsible for the high level of TKE, namely, the front recirculation bubble. The TKE profile cuts in figures 5.27 and 5.28 clearly show significantly higher levels of TKE for the two meshes that do capture wake bimodality in comparison to the coarse 8.3 million cell grid that is unable to resolve bimodality. Amounts of TKE that are non-negligible spread out into the wall-adjacent flow domain furthest for the WRLES simulation. It may also be noted that the levels of TKE build-up earliest for the 11.1 million cell WRLES. The TKE profiles of this WRLES simulation eventually match those of the 8.8 million cell WMLES simulation with Spalding's law from approximately $x_1 = 0.15$m onward. Overall, it may be concluded that the resolution of bimodal switching events requires the presence of the front recirculation bubbles, as these generate significant levels of TKE through the shedding of large hairpin vortices. Hairpin vortices that, when convected to the rear of the Ahmed body, interact with the wake in a manner that can culminate in a bimodal switching event. Meanwhile, one still captures the wake's spanwise asymmetry with the highly under-resolved near-wall 8.3 million cell grid, as the rear wake unsteadiness associated with the spatial bifurcation in the laminar regime at Re_H of $\mathcal{O}(100)$ is still simulated; it is only the near-wall mesh that is under-resolved and not the wake mesh as well.

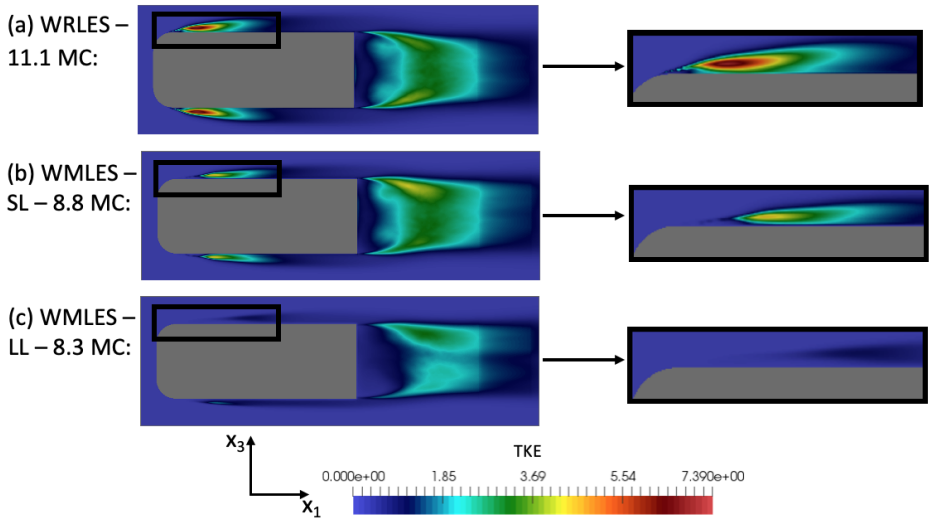


Fig. 5.26: Contour plots of TKE projected onto the x_1x_3 - middle plane passing through the Ahmed body for (a) WRLES, (b) 8.8 million cell (MC) WMLES with Spalding's law (SL) and (c) 8.3 million cell WMLES using the log-law (LL)

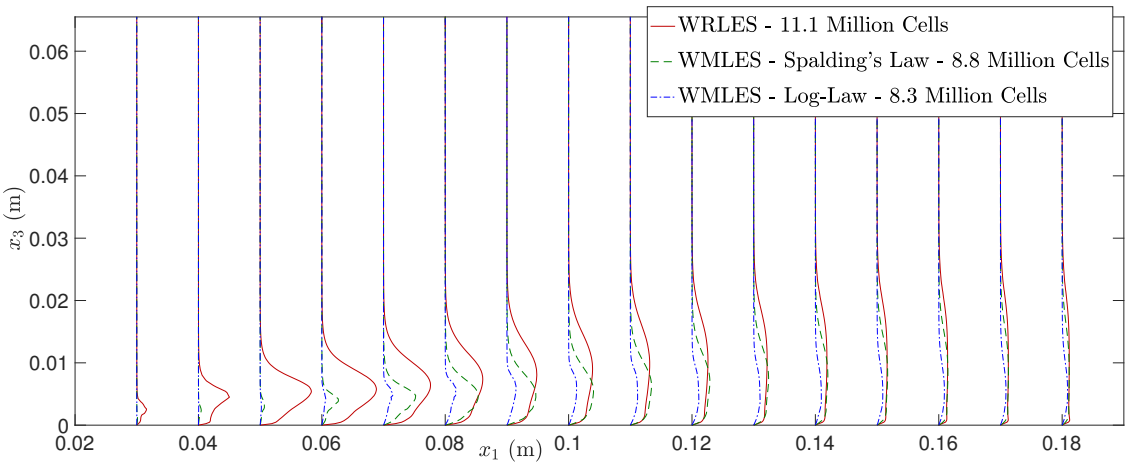


Fig. 5.27: Profiles of the TKE from the x_1x_3 - middle plane passing through the Ahmed body

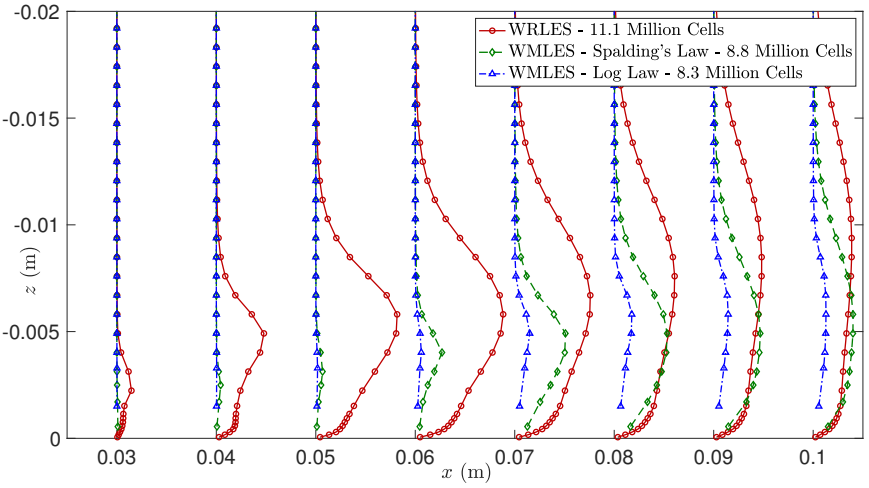


Fig. 5.28: Close-up of TKE profiles in the vicinity of the front separation bubble. Markers denote cell centers

Having conclusively shown that front recirculation bubbles release large hairpin vortices into

the domain and, thereby, produce large amounts of TKE, POD is now applied to snapshots of pressure data from the x_1x_3 - middle plane. This is to show the coherent flow structures that are captured in the respective simulation and, in turn, to further illustrate how significant the presence of the front recirculation bubble is in generating the flow intermittency that, upon convection to the Ahmed body rear, can force bimodal switching events. Figure 5.29 contains the POD modes captured with the 8.8 million cell WMLES grid in conjunction with Spalding's law of the wall. Mode 1 is the bimodal mode. It is static and, thus, is not complemented by a 90° out-of-phase mode that, upon being coupled to it, generates a convective motion of the mode. The other three modes do, however, appear in pairs, which illustrates that they are associated with a convective motion. Represented by mode 2 is the front recirculation bubble and its shedding dynamics. The asymmetric rear vortex shedding modes are represented by modes 3 and 4. They are each associated with different horizontal wake tilts. Found in figure 5.30 are the POD modes derived from pressure field data snapshots of the 11.1 million cell WRLES simulation. They are similar in structure to the ones shown in figure 5.29 for the 8.8 million cell WMLES simulation with Spalding's law. This similarity should come as no surprise. The WRLES set-up resolves the front recirculation bubble, although slightly upstream in location, and its complementing shedding dynamics. It, therefore, captures wake bimodal events coupled to which are two vortex shedding modes located in opposing spanwise locations. Meanwhile, by using the POD reduced-order-modelling technique on pressure field data snapshots derived from the 8.3 million cell WMLES grid set-up, a far more limited selection of modes is generated. More specifically, only a single coherent structure is detected. It is an asymmetric rear vortex shedding mode whose spanwise center of pressure location (COP) is fixed by the side that the wake is tilted to throughout the simulation's time-span. No mode that represents the front recirculation bubble's shedding motions is derived and, thus, the presence of the bimodal static mode is lacking as well. Overall, this simply stresses the significance that the front recirculation bubble's dynamics carries for generating the necessary flow intermittency that can culminate in a bimodal

switching event at the Ahmed body's rear.

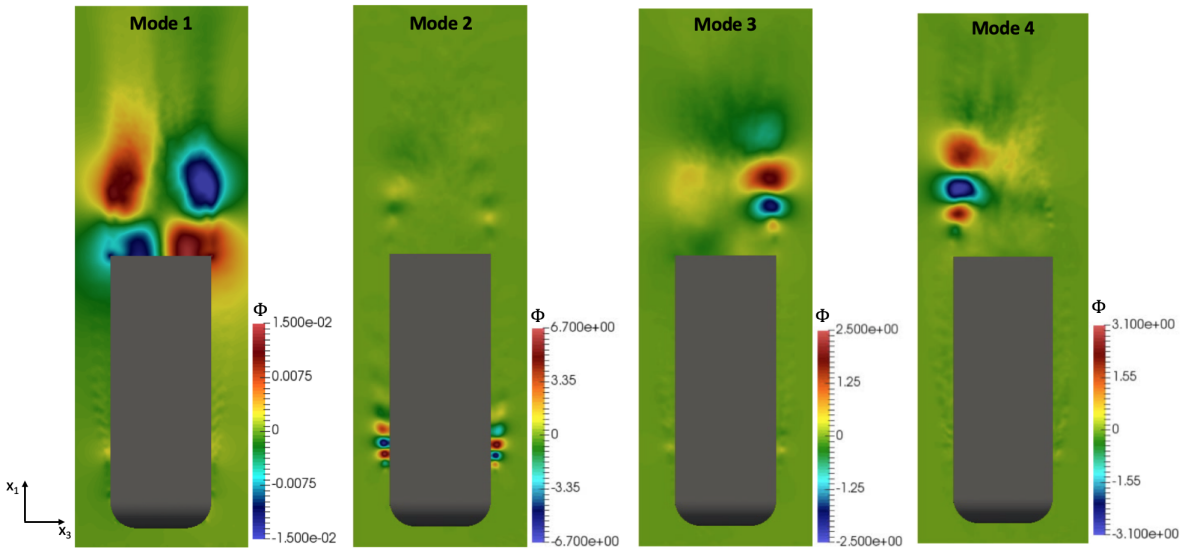


Fig. 5.29: POD modes, Φ, from pressure data on the x_1x_3 - middle plane passing through the Ahmed body for the 8.8 million cell WMLES set-up using Spalding's law

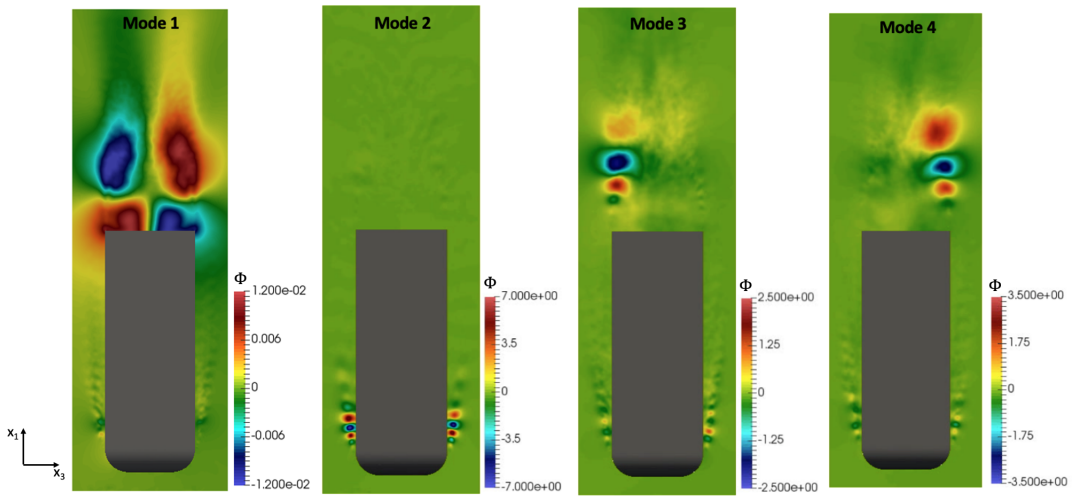


Fig. 5.30: POD modes, Φ, from pressure data on the x_1x_3 - middle plane passing through the Ahmed body for the 11.1 million cell WRLES set-up

5.4 Linear Feedback Control for the Ahmed Body

With the dynamics of wake bimodality extensively explored, this section will test the linear feedback control method validated for the bullet-shaped D-body on the Ahmed body. Does this linear feedback control strategy work when applied to an inherently 3D turbulent wake?

To save on numerical cost, all simulations performed for this section of the Ahmed body chapter are performed with the 8.8 million cell WMLES grid. The wall-model chosen is Spalding's law

of the wall. Meanwhile, the actuation shape chosen is illustrated in figure 5.31 where it is applied on the Ahmed body's rear base perimeter (marked in yellow), which has a slot width of $0.05H$. For open-loop forcing, actuation takes the form of sinusoidal in-phase top-hat velocity profiles oriented at 0° relative to the x_1-axis. This deviates slightly from the actuation shape adopted by Evstafyeva *et al.* (2017) in their successful flow control study for drag reduction of the Ahmed body's laminar wake, where the jets were angled outward at 10° relative to the x_1-axis. In closed-loop forcing, the velocity actuation shape is maintained, while the time dependent dynamics is set by the derived control law, $K(s)$, which is fed with the spatial average of the base pressure sensor readings - the pressure probes remain positioned as illustrated in figure 5.3. This is the only additional boundary condition that has been specified. The remaining surfaces are associated with the boundary conditions detailed at the start of section 5.1.

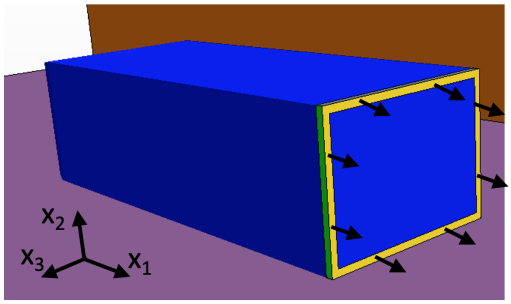


Fig. 5.31: Top-hat velocity profile actuation shape on the Ahmed body's rear base perimeter (marked in yellow)

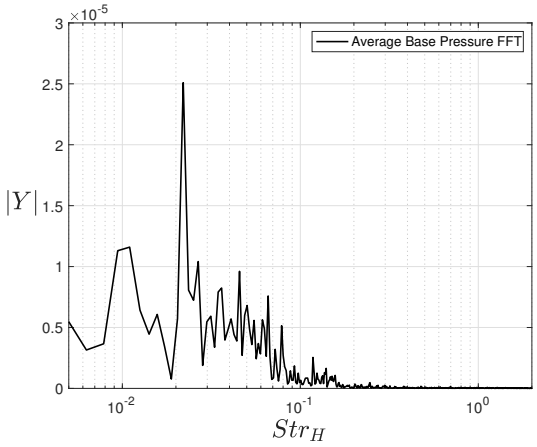


Fig. 5.32: Spectra of the unforced average base pressure signal

Before moving to the open-loop sinusoidal actuation for system identification of the wake's response to forcing (Fig. 3.2), the frequency range upon which to actuate needs to be assessed. This is achieved by looking at the spectral content of the average base pressure signal. Figure 5.32 depicts the results of this desired fast Fourier transform (FFT) operation. It is clear that the Strouhal number range that should be actuated upon is approximately 10^{-2} to 2×10^{-1}. As was done for the D-body, multiple actuation amplitudes are tested to assess whether the wake's response to forcing remains unaffected by the varying actuation amplitude, indicating that a linear assumption

of the wake's dynamical behavior is valid. The actuation amplitudes are here chosen to be 0.05, 0.1 and 0.2. Figures 5.33 and 5.34 portray the system identification results for the chosen matrix of amplitudes and forcing frequencies. One can observe that there is some amplitude dependence in the lower half of the $\mathcal{O}(0.01)$ Strouhal number range for the magnitude of $G(s)$ and some amplitude dependence in the the higher half of the $\mathcal{O}(0.01)$ Strouhal number range for the phase of $G(s)$. Now, as was done for the D-body's system identification of $G(s)$, a state-space function is fit to the collected data using MatLab's "fitfrd" command. Conveniently, as was the case for the D-body, a 5th-order state-space model was deemed to return the best fit to the collected system identification data for the Ahmed body (Eq. 5.4.1).

$$G(s) = \frac{-38.71s^5 - 1.82e4s^4 - 2.25e6s^3 - 9.74e7s^2 - 2.92e9s - 4.95e10}{s^5 - 1.49e4s^4 - 7.19e6s^3 - 3.37e8s^2 - 1.19e10s - 1.47e11} \tag{5.4.1}$$

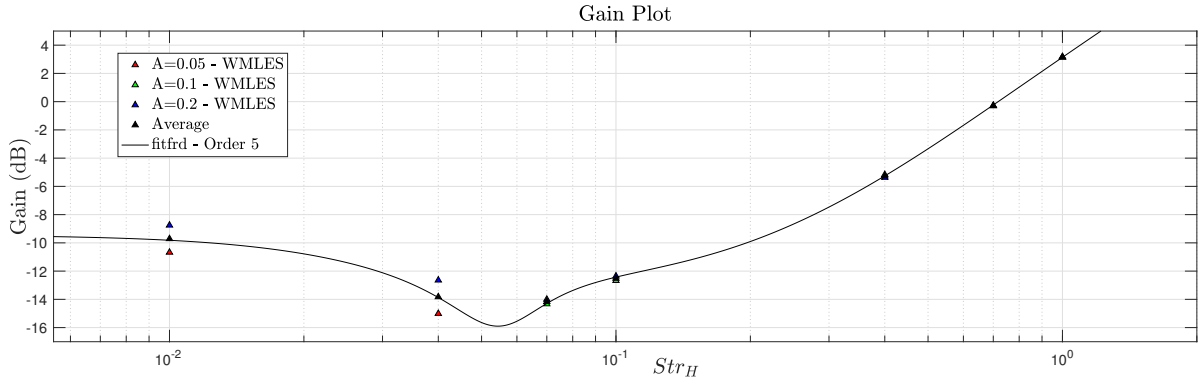


Fig. 5.33: Gain plot of $G(s)$ for the Ahmed body

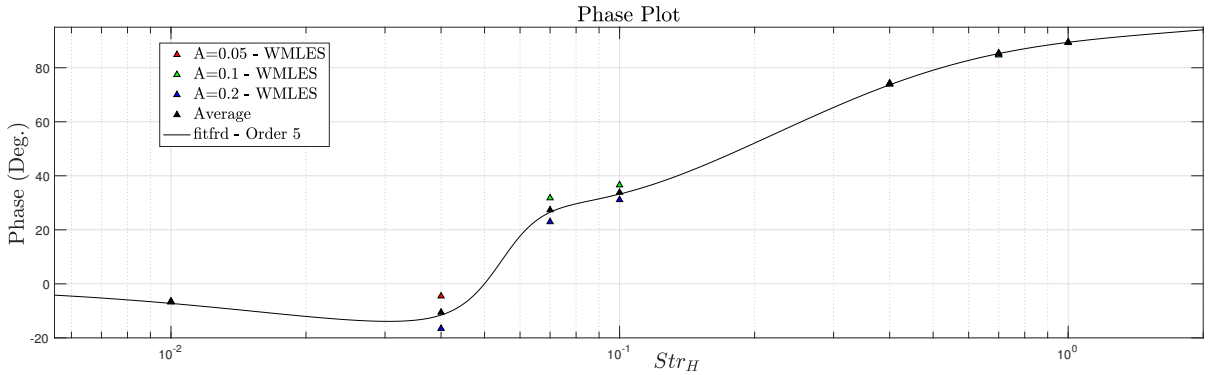


Fig. 5.34: Phase plot of $G(s)$ for the Ahmed body

Before moving on to the tuning of a sensitivity transfer function, $S(s)$, to attenuate the base pressure fluctuation(s) identified in figure 5.32, it is interesting to observe what the direct impact of open-

loop actuation is on the mean base pressure, $\overline{C_{PB}}$, the drag coefficient, $\overline{C_D}$, and the lift coefficient, $\overline{C_L}$. As figures 5.35 to 5.37 depict, the application of open-loop forcing lowers $\overline{C_{PB}}$ further and this is accompanied by a rise in $\overline{C_D}$. Meanwhile, there is also a tendency for the $\overline{C_L}$ to be raised, which would lead to a destabilization of the real-world vehicle. Despite these observations, there may be a benefit when incorporating a feedback system into the problem i.e. when in closed-loop mode.

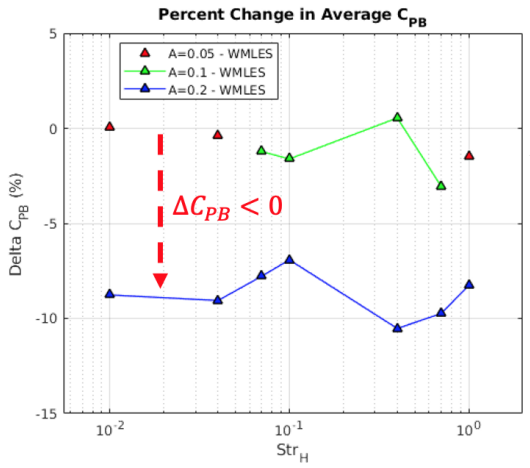


Fig. 5.35: Change in mean base pressure, $\overline{C_{PB}}$, with open-loop forcing

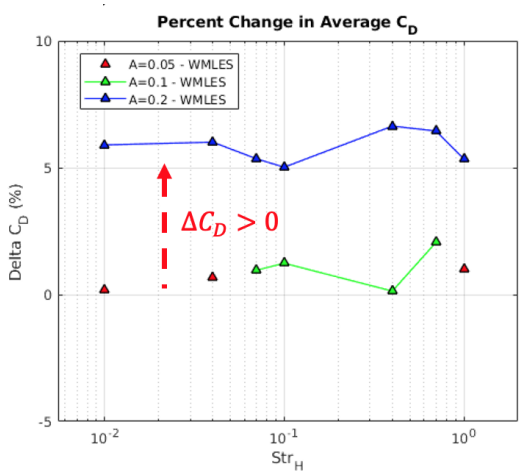


Fig. 5.36: Change in mean drag, $\overline{C_D}$, with open-loop forcing

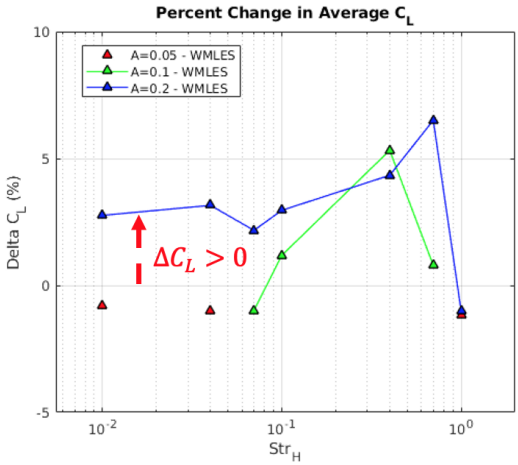


Fig. 5.37: Change in mean lift, $\overline{C_L}$, with open-loop forcing

With the model $G(s)$ of the Ahmed body wake's response to forcing, one may now determine the control law $K(s)$ via tuning of the parameters in equations 3.1.3 to 3.1.4. It is ensured that the sensitivity transfer function, $S(s)$, is below unity in the Str_H number range which exhibits the most dynamics (as observed in the spectral plot in figure 5.32). Figures 5.38 and 5.39 depict the gain

and phase plot of the designed control law, $K(s)$ (Eq. 5.4.2). As desired, the magnitude of the sensitivity transfer function, $S(s)$, is below unity in the Strouhal number range of 10^{-2} to $2{\times}10^{-1}$. It can be observed that $S(s)$ is also kept below unity for a Strouhal number down to $5{\times}10^{-4}$. This is because the FFT of the average base pressure signal does not conclusively approach zero for Strouhal numbers smaller than 10^{-2} (Fig. 5.32); the resolution of the FFT was not small enough and obtaining such resolution would require running the unforced simulation for an unreasonably large physical time. As was the case for the bullet shaped D-body in chapter 4, stability of the designed control system is ensured by looking at the Nyquist diagram of the open-loop feedback system $L(s) = G(s)K(s)$. No net encirclements of the point (-1,0) in the complex plane means the designed control law and feedback system should be stable (Fig. 5.40).

$$K(s) = \frac{8.55e7s}{s^4 + 2516s^3 + 1.86e5s^2 + 1.32e7s + 8e6} \tag{5.4.2}$$

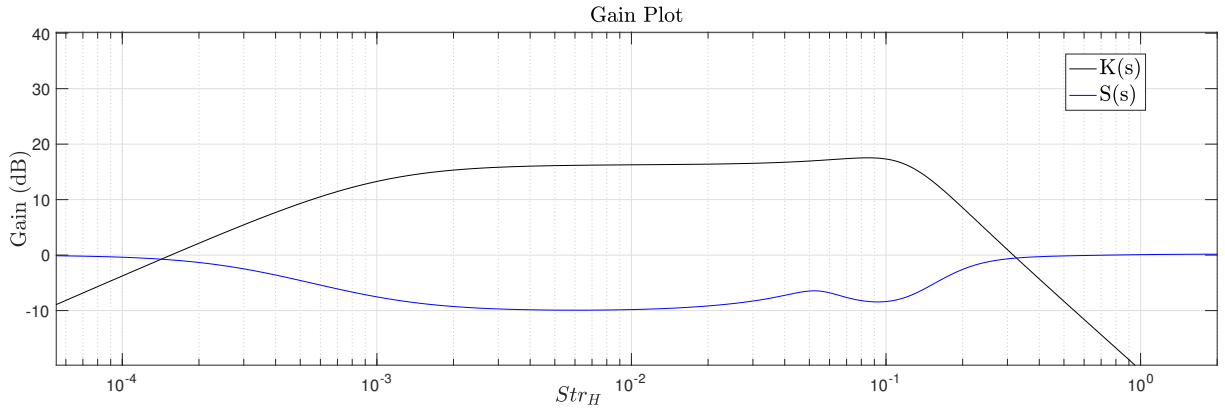


Fig. 5.38: Gain plot of $K(s)$ and $S(s)$ for the Ahmed body

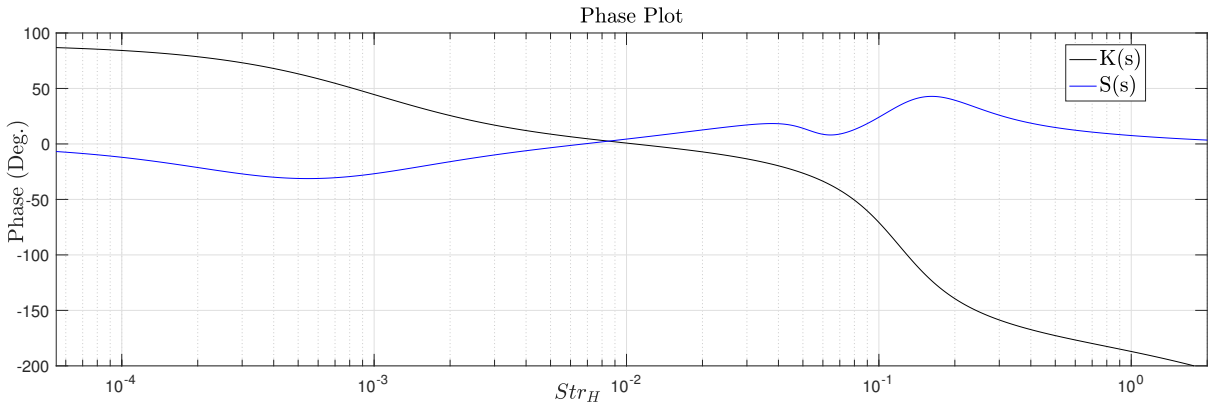


Fig. 5.39: Phase plot of $K(s)$ and $S(s)$ for the Ahmed body

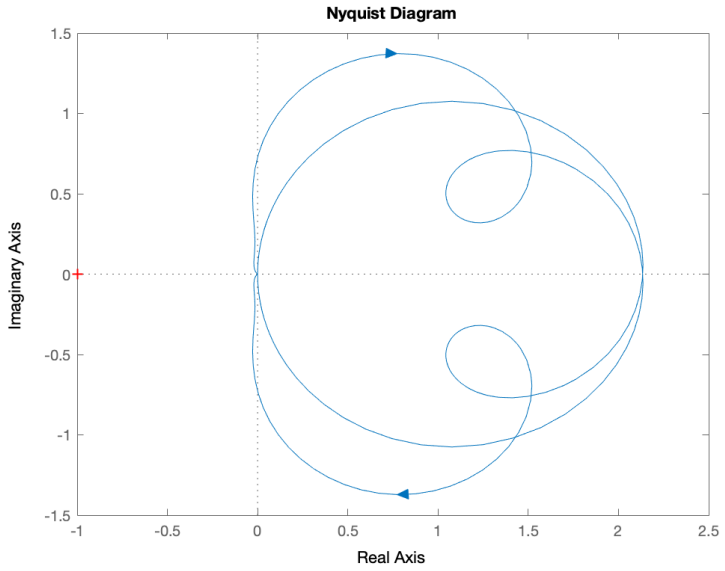


Fig. 5.40: Nyquist stability diagram for the Ahmed body open-loop feedback law, $L(s)$

Having designed the control law, $K(s)$, in the frequency domain, it is converted to state-space form where upon it is subsequently implemented into the OpenFOAM closed-loop simulation by using the swak4Foam plug-in and the groovyBC. The process is identical to the one used for setting-up the closed-loop D-body flow simulation (section 4.4). Upon activating the feedback controller, the ZNMF jet signal (Fig. 5.41) is seen to exhibit a mean blowing effect in the first approximately 300 non-dimensional time units. This in effect means that the jet is not acting like a ZNMF jet. The signal does, however, settle into a more ZNMF shape for $t^* >\sim 300$. Unfortunately, this corresponds to any positive effects of the jet actuation disappearing. This can be seen in figures 5.42 and 5.43 for Ahmed body average base pressure and drag coefficient, respectively. The base pressure signal drops down to its unforced value, while the drag coefficient rises to its unforced value as well (see table 5.2 for reference). This in effect means that the magnitude of the ZNMF jet signal appears to be too small for the jets to have a noticeable impact on the flow; the flow seems to behave as if it were unforced.

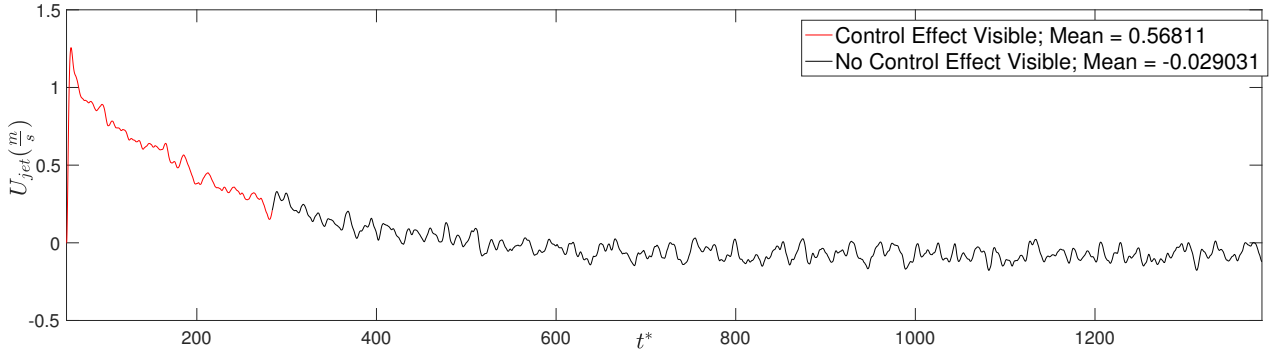


Fig. 5.41: Closed-loop ZNMF jet signal for the Ahmed body

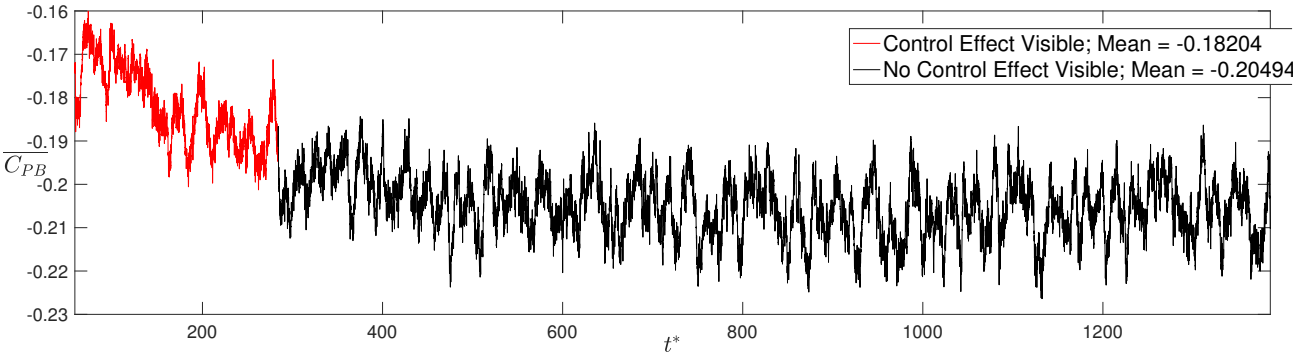


Fig. 5.42: Average base pressure signal, $\overline{C_{PB}}$, when closed-loop control is "on"

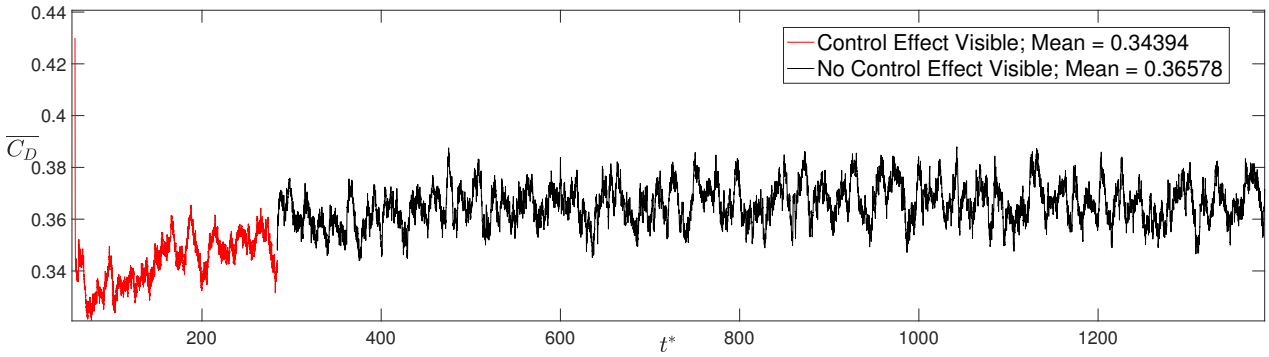


Fig. 5.43: Average drag coefficient signal, $\overline{C_D}$, when closed-loop control is "on"

The initial impact of the jet on the Ahmed body wake can be visualized more clearly by looking at pressure contour plots (Fig. 5.44). In this figure, it can be observed that during the initial 300 non-dimensional time-units, the jet "pushes" the low pressure wake away from the Ahmed body's base, thereby leaving a higher pressure domain just aft of the Ahmed body's rear. This leads to, as was mentioned above, a higher average base pressure coefficient (Fig. 5.42) and lower drag coefficient (Fig. 5.43). A further curious observation is that under mean blowing, the wake is

symmetric in the spanwise direction. This can be seen in figure 5.45 for the average base pressure gradients, particularly in the close-up view. It suggests that the mean blowing forces the wake away from the immediate impact of the asymmetric trailing edge vortex shedding. These observations are in line with the laminar wake findings of Evstafyeva *et al.* (2017): a re-symmetrization of the wake (even if only transient) is associated with a mean drag reduction. Moving on, the goal of the control algorithm was to attenuate the base pressure fluctuations with the hope that this would be associated with a mean base pressure rise and drag reduction (as concluded from the analysis and decomposition of equation 3.1.1). Figure 5.46 does show that there is an attenuation of the dominant signal contained in the average base pressure readings. Thus, the feedback controller is successfully attenuating oscillations as it was designed to do. Unfortunately, there is no associated mean drag reduction benefit.

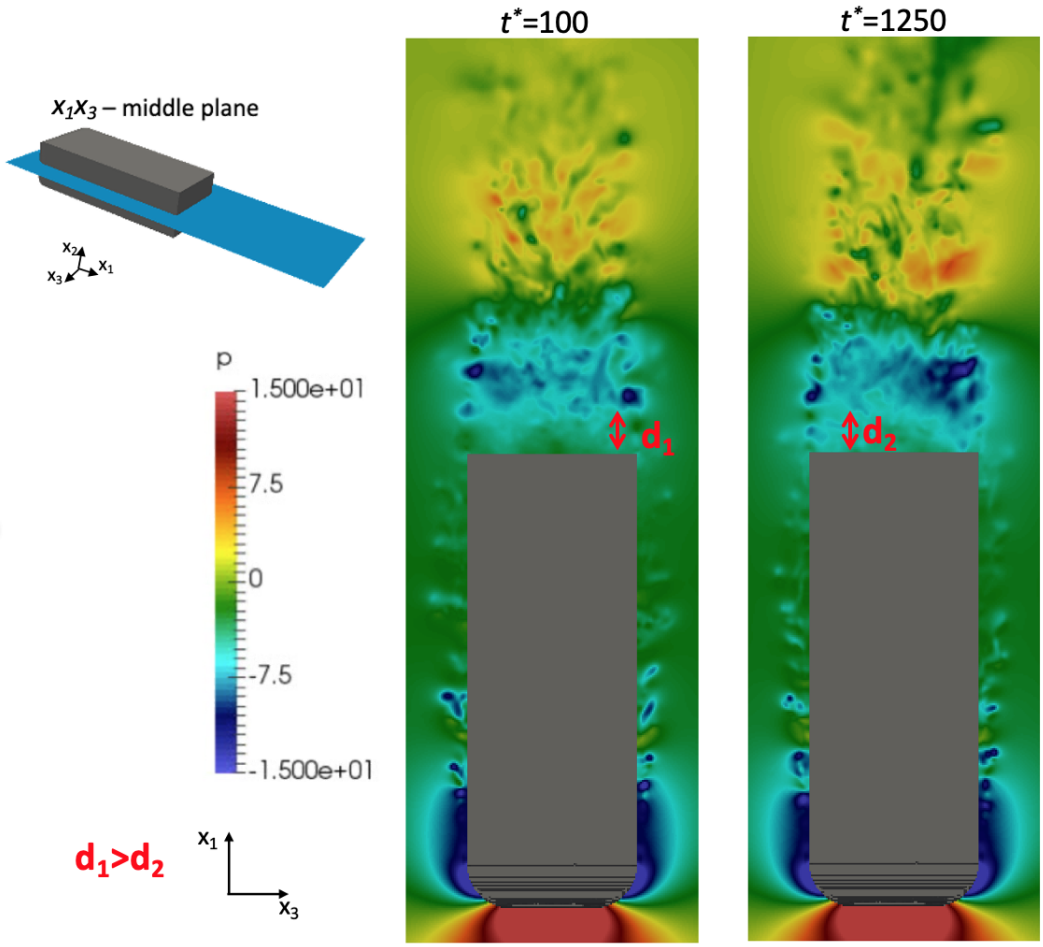


Fig. 5.44: Influence of jet actuation on the wake during mean blowing phase and during the phase with no noticeable impact of the jet

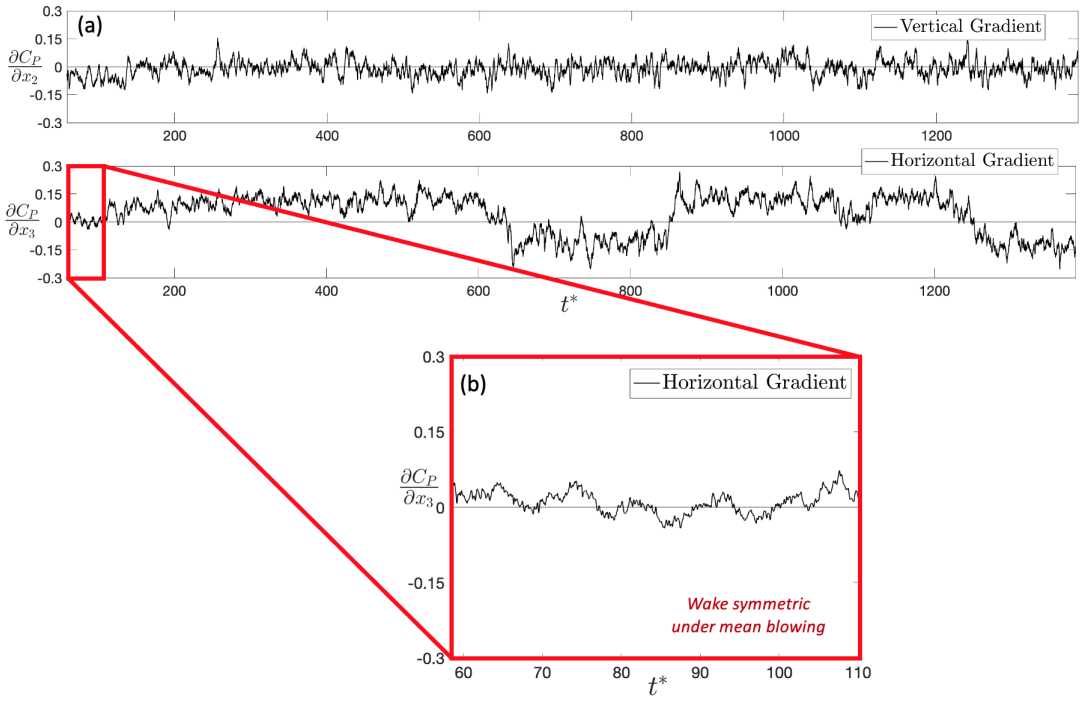


Fig. 5.45: Symmetrizing effect of mean blowing on the wake's spanwise orientation: (a) general view and (b) close-up of horizontal base pressure gradient, $\frac{\partial C_P}{\partial x_3}$, during mean blowing

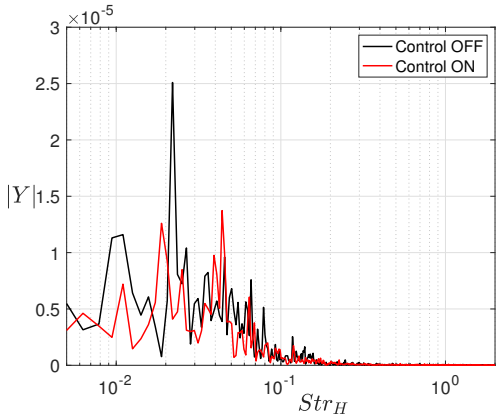


Fig. 5.46: Comparison of average base pressure spectra without control and with control "on"

It must be noted that this is not the first time that linear feedback control for drag reduction has failed on 3D turbulent wakes generated by academic squareback bluff-bodies. Both Evstafyeva (2018) and Dalla Longa (2018) were unable to make the linear based feedback control transfer functions work on their Ahmed body and truck-like setups, respectively. This suggests that the premise that attenuating base pressure fluctuations will yield a mean drag reduction may not be valid for these fully turbulent 3D bluff-body wakes. Perhaps new non-linear feedback control approaches that target drag reduction through wake (re-)symmetrization should be adopted and tested.

Chapter 6

Nissan NDP: Passive Flow Control

Having looked at two more academic bluff-body geometries, it is apt to explore an industry relevant and, therefore, more road vehicle representative geometry. The considered vehicle is the so-called Nissan NDP (Fig. 6.1). It is a derivative of the Nissan NV200, a production vehicle. Nissan primarily developed the concept vehicle as part of an optimization study that sought to maximise loading bay volume for a given vehicle length while at the very least recovering the baseline C_DA value. This was accomplished and the C_DA value was lowered by 18.63% from its baseline value (Kremheller *et al.*, 2015). Nissan then also sought to assess whether vehicle development under steady zero-yaw conditions (the convention) leads to dramatically different design conclusions / optimizations than when doing development tests under more unsteady and non-zero yaw conditions. The study concluded with the result that the global trends in drag and lift remain captured in both conditions. However, when it comes to fine-tuning smaller vehicle features (e.g. spoiler influences or side mirrors) where absolute drag and lift values become more pertinent, different conclusions may be obtained (Kremheller *et al.*, 2016). The main topic(s) covered in this chapter are the influence of the cavity, i.e. passive flow control, on the Nissan NDP's aerodynamics as well as what the differences are between moving ground and stationary ground simulations. As such the chapter is structured as follows: (a) simulation set-up, (b) cavity based passive flow control, and (c) moving

ground analysis.

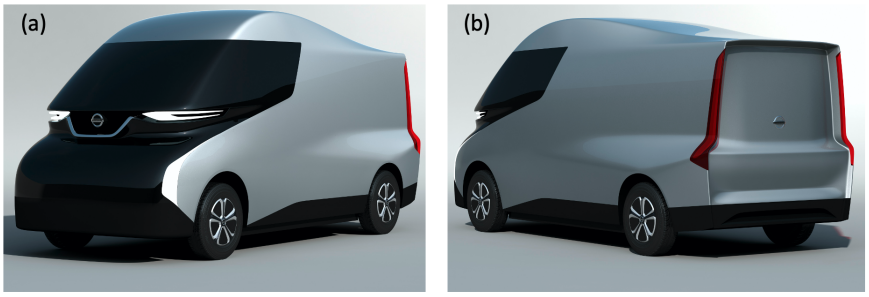


Fig. 6.1: Nissan NDP: (a) front view and (b) rear view

6.1 Simulation Set-up

Instead of using the full-scale Nissan NDP, this work uses a 15% scale model, which corresponds to the following dimensions: length of L=0.657m, height of H=0.309m, and width of W=0.257m. The ground clearance is measured as G=0.0251m. Based on these dimensions, for which C^*= 0.098 and H^*=1.2 in figure 2.6a, one could expect horizontal (i.e. in the x_3-direction) and vertical (i.e. in the x_2-direction) wake bimodality to occur. Furthermore, details of the tire spokes are disregarded in this work. Instead a simple flat hub-cap is used to facilitate easier meshing; there are then fewer cells with high skewness that need to be taken into account. The Nissan logo has also been removed for the same reason. Throughout this chapter, two Nissan NDP versions are explored: the default with a cavity at the rear (Fig. 6.2a) and a "squareback" version where the cavity has been truncated off (Fig. 6.2b). The domain size is again based on ERCOFTAC guidelines. As such, the computational domain, Ω, has dimensions $\Omega = (L_{in}, L_{x1}, L_{x2}, L_{x3}) = (2L, 8L, 2L, 2L)$, where L denotes the bluff-body's length (Manceau & Bonnet, 2002).

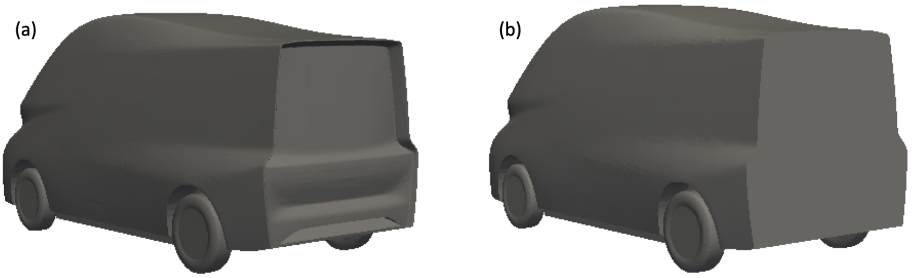


Fig. 6.2: Nissan NDP rear topology: (a) with cavity and (b) "squareback"

As was done for the fully 3D turbulent Ahmed body simulation, the flow fields are first initialised using the simpleFoam solver with the inherently numerically robust Spalart Allmaras RANS turbulence model. Following this initialisation, the simulations move forward in time using the pimpleFoam solver in conjunction with the WALE LES turbulence model. The initial conditions that are set for the RANS simulation are $\boldsymbol{U_\infty} = (4.893, 0, 0)$m·s^{-1} and $P_\infty = 0$Pa gauge pressure. The fluid is again air at 20°C with $\nu = 1.511 \times 10^{-5}$m^{2}s^{-1}. Furthermore, the following boundary conditions were applied:

1. At the domain inlet, a uniform flow velocity of $\boldsymbol{U_\infty} = (4.893, 0, 0)$m·s^{-1} without artificial forcing (i.e. turbulence is allowed to develop naturally) is stipulated. This corresponds to a Re_H=100000. A Re_H of this magnitude is still an order of magnitude lower than the ones typically encountered in external vehicle aerodynamics wind tunnel runs or more computationally accessible CFD runs that use hybrid RANS-LES methods (Heft *et al.*, 2012; Ashton *et al.*, 2016). Nonetheless, it bridges the gap between such high Re_H setups, and the lower Re_H yet more academic Ahmed body runs presented in chapter 5.

2. A free-slip condition is specified at the computational domain's sides as well as top upper boundary i.e. at boundaries far away from the Nissan NDP.

3. An advective pressure condition is applied at the domain's outlet.

4. At the walls of the Nissan NDP, the no-slip condition is explicitly enforced i.e. wall-resolving LES (WRLES) is performed and not WMLES. In light of the results from chapter 5, where WMLES was successfully applied, it may seem intuitive to actually continue with WMLES, or better yet, adaptive WMLES, for the Nissan NDP and, thereby, save on computational expenses. However, this option was not opted for, as there have already been some past hybrid RANS-LES simulations performed for the NDP in the form of DES (albeit for a different Re_H) (Kremheller *et al.*, 2015). As such, the rare opportunity to perform wall-resolving LES on a

rather complex industry geometry was capitalized upon. The data from the simulations would then also be able to serve as a benchmark for future wind tunnel and/or cheaper CFD runs.

5. At the "ground" of the domain, the no-slip condition is applied if a stationary ground simulation is performed, or it is set to a velocity boundary condition of $\boldsymbol{U}_\infty = (4.893, 0, 0)\text{m}\cdot\text{s}^{-1}$ for moving ground simulations. Ideally, when a moving ground simulation is performed, the boundary conditions applied to the wheels should be such that rotational effects are included through, for example, a moving reference frame or a sliding mesh. However, to remain consistent in this study with simplified wheel behavior modelling, when a moving ground simulation is performed, wheels are kept stationary to save on both simulation cost and complexity.

The variables, such as drag coefficient, C_D, or the Q-criterion, keep their definitions from chapter 5 on the Ahmed body. Only the position and number of the probes used to compute the base pressure gradients, $\partial C_P/\partial x_2$ and $\partial C_P/\partial x_3$, has changed. The probes now total 633 (this is important for computing the average base pressure using equation 5.1.3), and their position and orientation are illustrated in figure 6.3. Although illustrated for the NDP with cavity, they apply equally to its "squareback" form as well.

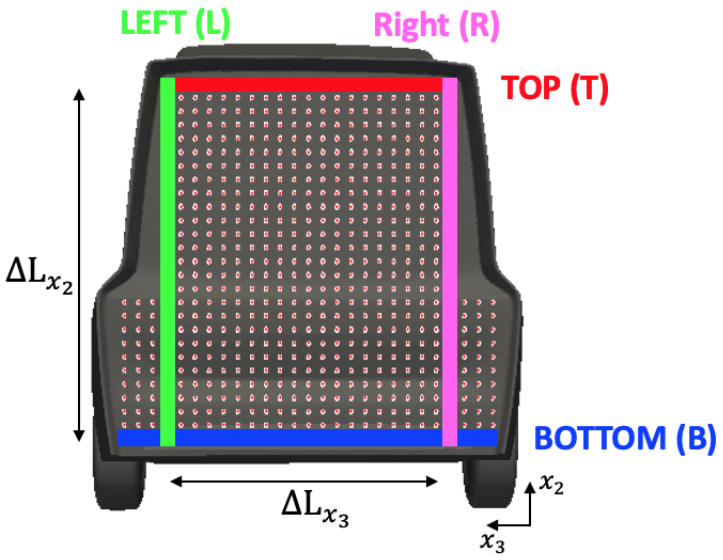


Fig. 6.3: Base pressure probe array for the Nissan NDP

Furthermore, the meshing procedure adopted for the Nissan NDP is identical to the Star-CCM+ based method used for the Ahmed body in chapter 5, except for one step. Prior to creating the fluid domain mesh, the Nissan NDP had to have its surface wrapped. This is because the received CAD geometry was very poorly faceted (e.g. there were many self-intersecting and overlapping facets). After this step, an unstructured fluid domain mesh consisting of both trimmer cells away from the wall and prism layer cells near the wall was created, and then converted to OpenFOAM format using the plug-in ccm26ToFoam (Fig. 6.4).

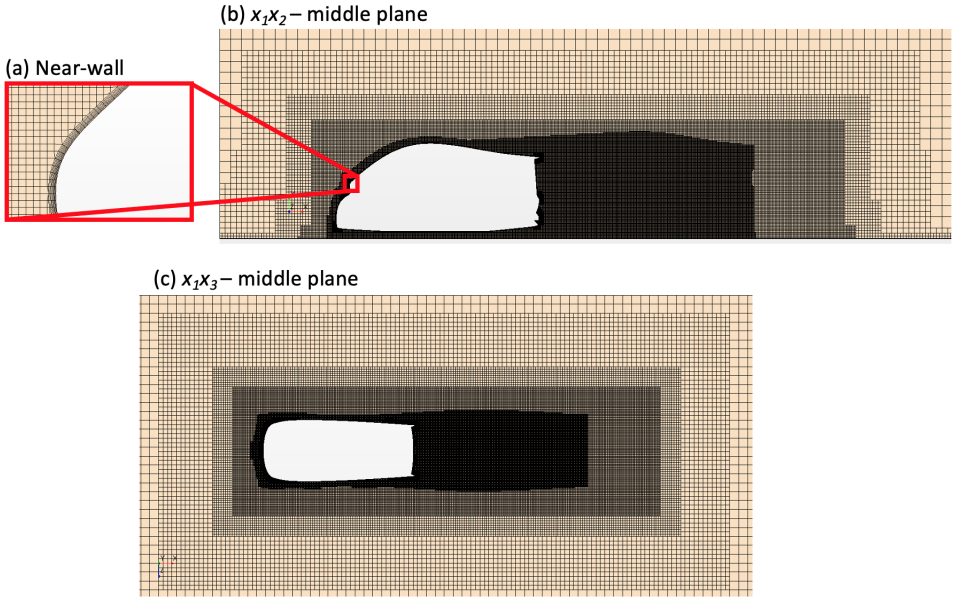


Fig. 6.4: Sample fluid domain mesh with (a) prism layer cells near the Nissan NDP wall, and trimmer cells in the majority of the flow domain visualized on the (b) x_1x_2 - middle plane and (c) the x_1x_3 - middle plane

To identify the baseline mesh settings for use, a mesh refinement study was performed. This refinement study was done using a moving ground simulation of the Nissan NDP with its default cavity appendage. The reason for using the moving ground simulation is that there is no need to then apply prism layer cells near the ground, thereby reducing the absolute value of the cells required. In other words, performing a mesh refinement study with the moving ground simulation should take, in total, fewer CPUhrs than when doing the mesh refinement study with the stationary ground variant. The necessary, but not necessarily sufficiently small, wake cell size was again estimated using relationship 5.1.8 for the Taylor microscale, a reference eddy size from and below which viscosity begins to affect the eddies' dynamics and isotropy of the eddy scales can be sensibly

assumed. As mentioned previously, it, therefore, serves as a good eddy scale reference length below which the application of an eddy-viscosity based LES turbulence model for accounting for the eddies' macroscopic flow field effects becomes reasonable. Results of the mesh refinement study are presented in table 6.1. Three meshes were simulated, each with a wake cell size by a factor of two smaller than its coarser predecessor. In the end, it was decided to use the second of the three mesh set-ups, which consists of approximately 26.7 million cells. It is of intermediate wake resolution, is not too expensive in terms of CPUhrs, and has a moderately stabilized average base pressure, $\overline{C_{PB}}$, and recirculation bubble length, $\overline{L_B}$. Although there is some variation between the second and third finer meshes for $\overline{C_D}$ and $\overline{C_L}$, it was simply not deemed computationally tractable to go with the finest mesh set-up if one hopes to consider the large time-scales over which wake bimodality occurs (up to $t^* \sim 10^3$) (see section 6.2). The difficulty in achieving mesh convergence for $\overline{C_D}$ and $\overline{C_L}$ again highlights the issue that obtaining converged surface measurements in CFD, where the volume mesh intersects with the surface mesh, is not simple. It is a problem that was already highlighted for the Ahmed body in section 5.1. One may wonder, however, will using a coarser mesh not influence the possibility of capturing bimodality for the Nissan NDP? By looking at the flow fields, as is done in sections 6.2 and 6.3, one can see that the pertinent flow structures appear to be captured with the mesh of intermediate resolution. Specifically, the prominent vertical wake asymmetry is captured (Fig. 6.9), which means the vertical wake balance is correctly resolved, along with the shedding of a large hairpin vortex from the ceiling of the vehicle (Fig. 6.14-6.17). Based on the results for the Ahmed body, where it was assessed that the shedding of high TKE generating large hairpin vortices from the front recirculation bubble are likely to contribute to triggering a bimodal switch (section 5.3), resolution of the aforementioned structures with the Nissan NDP mesh of intermediate resolution should suffice for capturing bimodality, if it is present. In fact, based on this assertion, one could even choose to proceed analysis here with the coarsest mesh of 19.1 million cells - it too resolves the relevant flow structures mentioned above. However, to ensure

sufficient unsteadiness in the wake is resolved, one has chosen to use the intermediate mesh of 26.7 million cells. Unfortunately, there are currently no experimental results available with which one may assess the simulation data's correlation with real-world tests.

Mesh size	ΔL_{wake}	$\overline{C_D}$	$\overline{C_L}$	$\overline{C_{PB}}$	$\overline{L_B}$
19.1 million	$0.832\lambda_T$	0.263	-0.0828	-0.188	0.797H
26.7 million	$0.417\lambda_T$	0.265	-0.0888	-0.190	0.754H
49.6 million	$0.205\lambda_T$	0.271	-0.0918	-0.192	0.780H

Table 6.1: Mesh refinement study based on Nissan NDP with cavity appendage and moving ground - mean flow quantities

Furthermore, performing wall-resolving LES (WRLES) requires that the wall "y-plus" must be centered about 1 (Fan *et al.*, 2020). This is indeed true as the histogram plot in figure 6.5 demonstrates. When projecting the wall "y-plus" distribution onto the vehicle surface (Fig. 6.6), one can observe that the values beyond $\overline{x_{2w}^+}$=1 are located in the vicinity of the tires. It is, in fact, notoriously difficult to capture the flow dynamics generated by tires, whose contact patch is handled in this study through the placement of the tires on small pedestals. The reason for this difficulty in tire behavior modelling is that rotation and deformation need to be considered. Since these effects are not taken into account and as the hub-caps are simplified as well, errors are already introduced when modeling the flow about the tire. Furthermore, as the large-scale separation at the trailing edge of the Nissan NDP is the main focus of this work, the errors introduced by under-resolving the flow features near the tire are deemed acceptable, particularly if this leads to a computationally more efficient mesh. The subsequently derived meshes, one for the Nissan NDP with cavity and stationary ground as well as one for the "squareback" NDP with stationary ground, keep the same prism layer and trimmer cell construction for near and away from the NDP walls, respectively, as the currently described 26.7 million cell moving ground mesh.

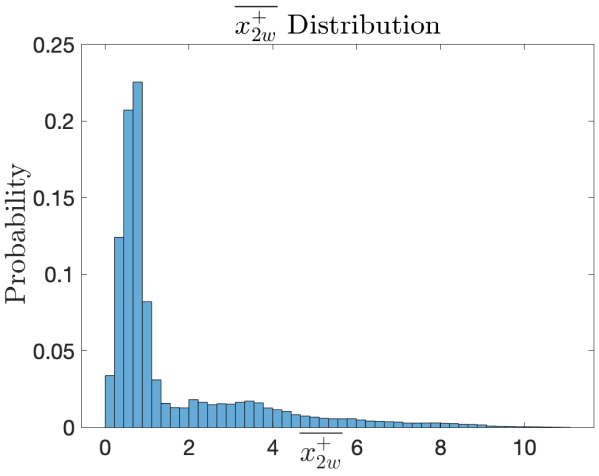


Fig. 6.5: Histogram plot of wall "y-plus", $\overline{x^+_{2w}}$, for the Nissan NDP with moving ground

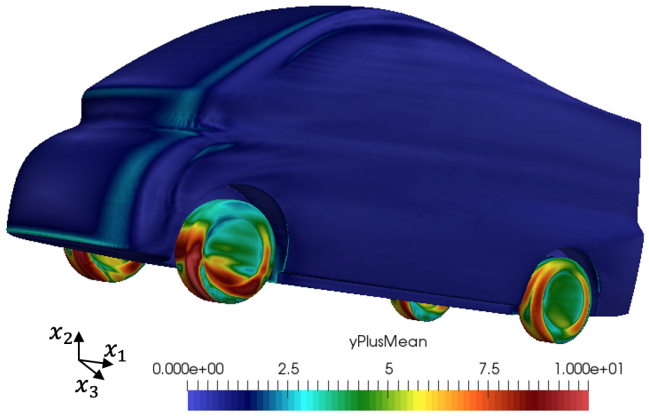


Fig. 6.6: Wall "y-plus" projected onto the Nissan NDP surface

6.2 Cavity based Passive Flow Control

With the simulation set-up described, this section compares the "squareback" NDP with its cavity appended counterpart in order to assess the drag benefit of the latter as well as the underlying physics from which this benefit is derived. The two simulations conducted for this part are both with a stationary ground. An additional focus of this section and chapter in general is whether any evidence of wake bimodality, either horizontally or vertically, is present in the simulated set-ups. Only a fraction of the characteristic non-dimensional time that one can expect bimodality to occur in, which is $t^* \sim 10^3$, was simulated though. The available computational resources and project time simply did not permit simulation over such a large non-dimensional time-scale for this model. With 800+ cores and almost 10 job submissions of 48 hours each on the UK's largest supercomputing facility, ARCHER (now ARCHER2), only a simulation time period of $t^* \sim 70$ was achieved (Fig. 6.7). This period sufficiently covers the vortex shedding mode time-scale of $t^* \sim 5$, but means that the discussed results on wake bimodality are not 100% conclusive (Grandemange *et al.*, 2013*b*).

Figure 6.7 is a direct comparison between the base pressure gradients for the cavity appended NDP and the "squareback" version. On a first glance, one can discern a very clear wake asymmetry

in the vertical direction (Fig. 6.7a) for both setups. This is due to the asymmetry introduced in the vertical direction through the ground's presence and, as is visually shown in section 6.3, the detachment of a powerful hairpin vortex occurs from the top of the NDP midway between the front and rear axle (Fig. 6.14-6.18). It may also be seen that the NDP with cavity explores a larger vertical base pressure gradient space than its "squareback" form. Meanwhile, looking at the horizontal base pressure gradient (Fig. 6.7b), no noticeable long-term spanwise wake asymmetry is discernible; the horizontal base pressure gradient PDF is centered about zero for both setups. However, in the case of the NDP with cavity, the horizontal base pressure gradient PDF is wider about the zero point. This accompanies the cavity wake's larger rear base exploration in the vertical direction.

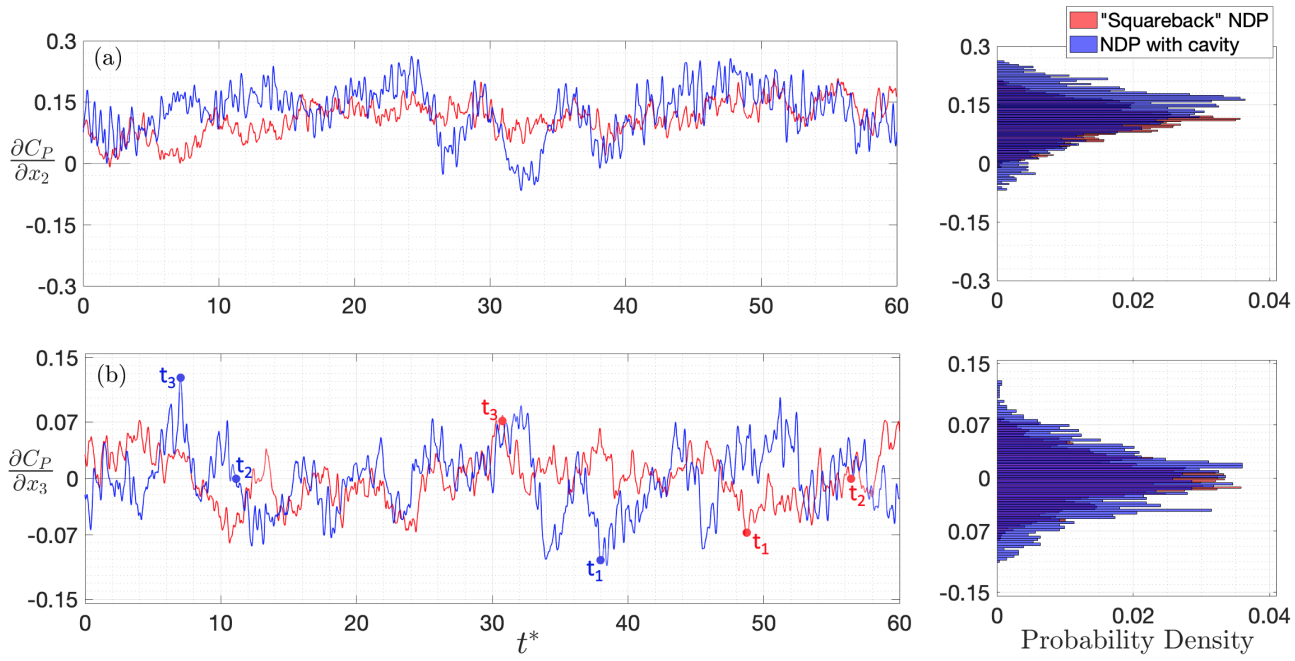


Fig. 6.7: Base pressure gradient in the (a) vertical direction, $\partial C_P/\partial x_2$, and (b) horizontal direction, $\partial C_P/\partial x_3$, for the Nissan NDP with and without cavity appendage. Filled-in circles denote times at which instantaneous pressure snapshots are taken for figures 6.10-6.11

By looking at the joint PDF of the base pressure gradients for both set-ups (Fig. 6.8), one can conclusively see that the cavity appendage releases the wake from a more restricted motion about the rear base that is present with the "squareback" NDP. Overall, looking at the base pressure gradient distribution, one cannot conclusively identify or exclude the presence of wake bimodality, vertically or horizontally; the simulated time is simply not enough (Fig. 6.7). Nonetheless, one can still extract

a time-averaged contour plot of pressure illustrating the prominent vertical wake asymmetry present in both setups (Fig. 6.9) and, more interestingly, one can also extract instantaneous flow snapshots from the available data that exhibit the wake's rapid exploration of spanwise asymmetric states for both the "squareback" NDP and the NDP with cavity (Fig. 6.10-6.11).

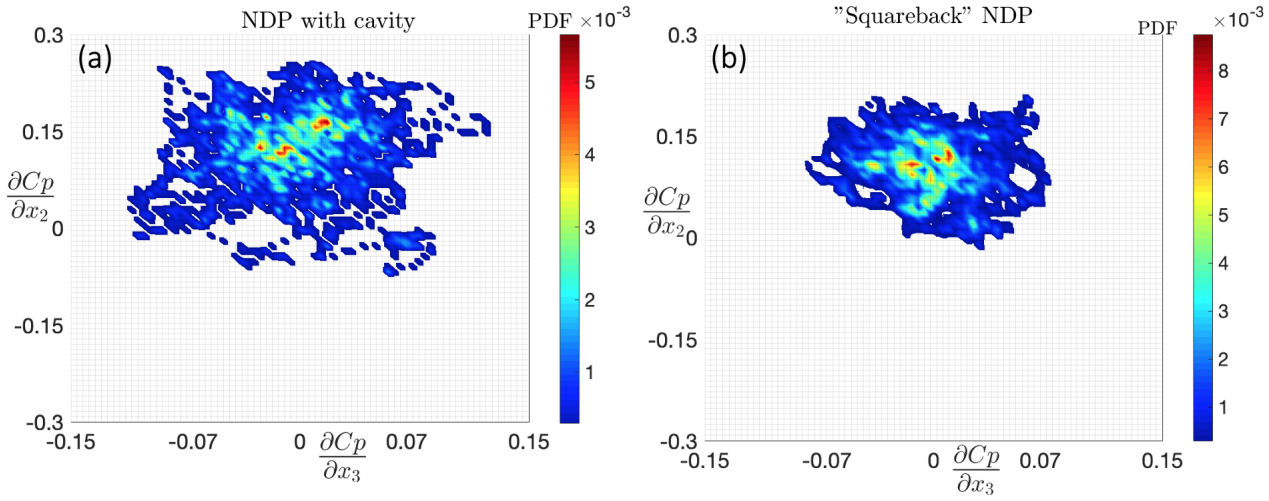


Fig. 6.8: Joint PDF of base pressure gradients for (a) Nissan NDP with cavity and (b) the "squareback" NDP

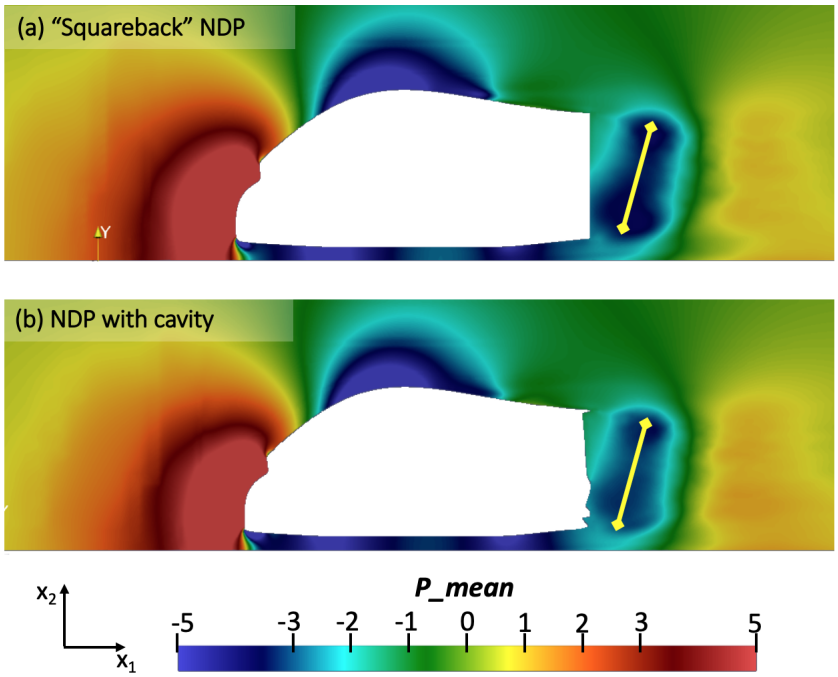


Fig. 6.9: Mean pressure field snapshots highlighting the prominent vertical wake asymmetry for (a) the "squareback" NDP and (b) the NDP with a cavity at the rear

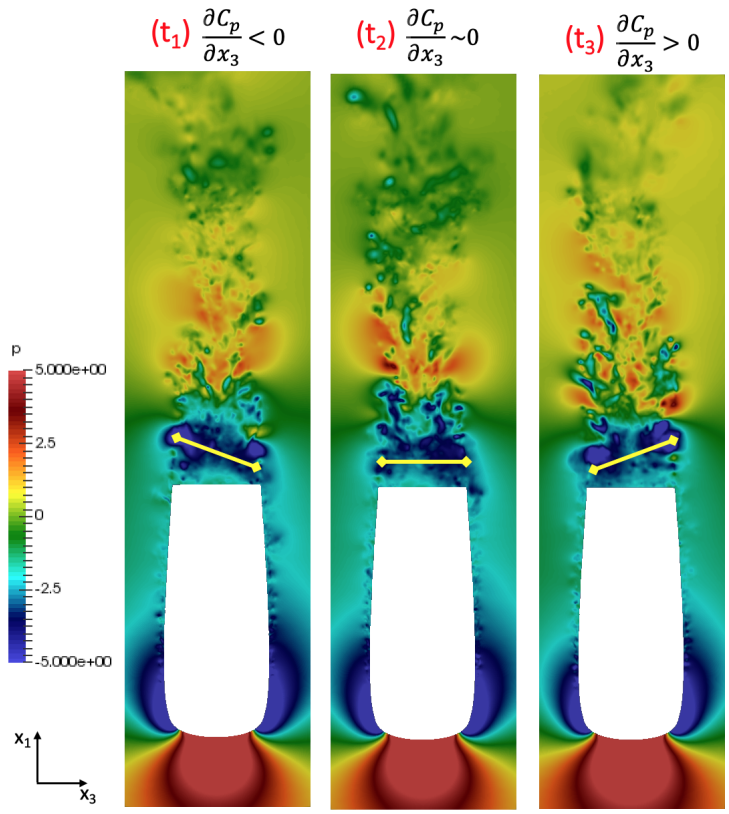


Fig. 6.10: Pressure field snapshots highlighting short-lived moments of horizontal wake asymmetry for the "squareback" NDP. Times at which flow field snapshots are taken may be found in figure 6.7

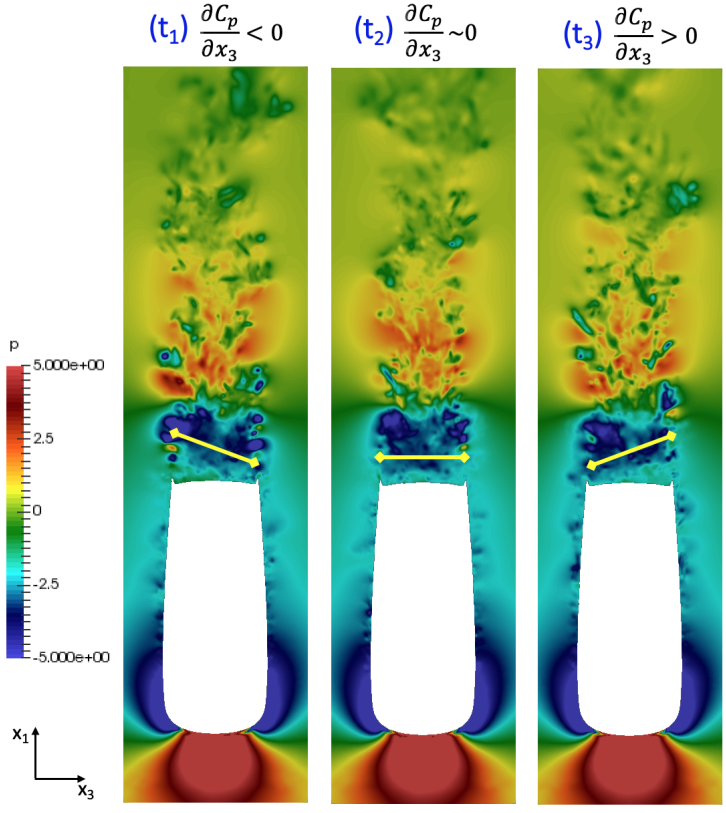


Fig. 6.11: Pressure field snapshots highlighting short-lived moments of horizontal wake asymmetry for the NDP with cavity. Times at which flow field snapshots are taken may be found in figure 6.7

Having looked at base pressure gradients and the corresponding wake tilts through pressure contour plots, modal analysis using POD is now performed in order to better understand the coherent flow structures underlying these wake tilts. In figures 6.12 and 6.13, one can discern the third POD mode computed from snapshots taken on the x_1x_3 - middle plane passing through the two NDP variants, and the second POD mode derived from snapshots taken on the x_1x_2 - middle plane passing through the two NDP test cases, respectively. The energy associated with the POD modes computed for both planes is very distributed. At most, the first mode, which in all cases did not present any clean clearly discernible coherent structure, contained $\sim 10\%$ of the flow energy. Meanwhile, subsequent modes 2 to 3 contained between 3% to 6% of the total flow energy. This highly distributed flow energy content seems to indicate that there is no dominating flow structure, at least not based on energy content. Nonetheless, one is still able to identify what the coherent flow structures represent. Figure 6.12 depicts the symmetric spanwise vortex shedding pattern, which is present for both the "squareback" NDP (Fig.6.12a) and the NDP with a rear cavity (Fig. 6.12b). This pattern is in stark contrast to the asymmetric spanwise rear vortex shedding modes that were picked-up as two separate modes for the Ahmed body (Fig. 5.29). As these asymmetric rear vortex shedding modes for the Ahmed body are a direct consequence of the wake spending extended periods in two opposing spanwise off-axis positions, and the concomitant bimodal wake switching events, this evidence for the two NDP geometry variants (Fig. 6.12) seems to indicate that no spanwise wake bimodality will occur. Meanwhile, figure 6.13 illustrates the highly asymmetric rear vortex shedding mode that occurs in the top-to-bottom vertical plane for both NDP variants. In light of the previously discussed asymmetric spanwise modes picked-up for the Ahmed body, this modal evidence suggests that one can simulate vertical wake bimodality for the Nissan NDP, both in its "squareback" and cavity form. To confirm this, one needs to extend the currently available non-dimensional simulation time, t^*, by at least an order of magnitude (Fig. 6.7) (Grandemange *et al.*, 2013*b*).

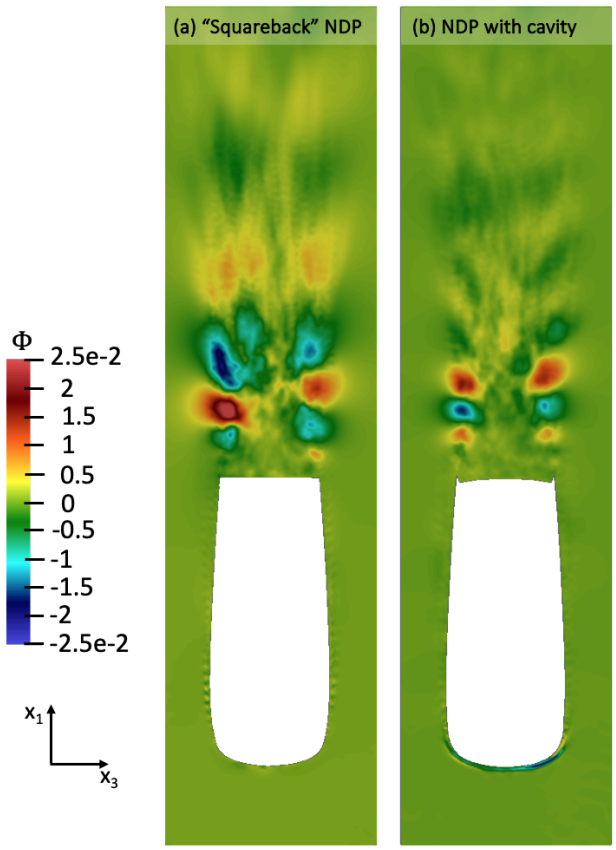


Fig. 6.12: Symmetric spanwise vortex shedding visualized through the application of POD, Φ, on instantaneous pressure data taken from the x_1x_3 - middle plane for (a) the "squareback" NDP and (b) the NDP with a rear cavity. This is the third POD mode.

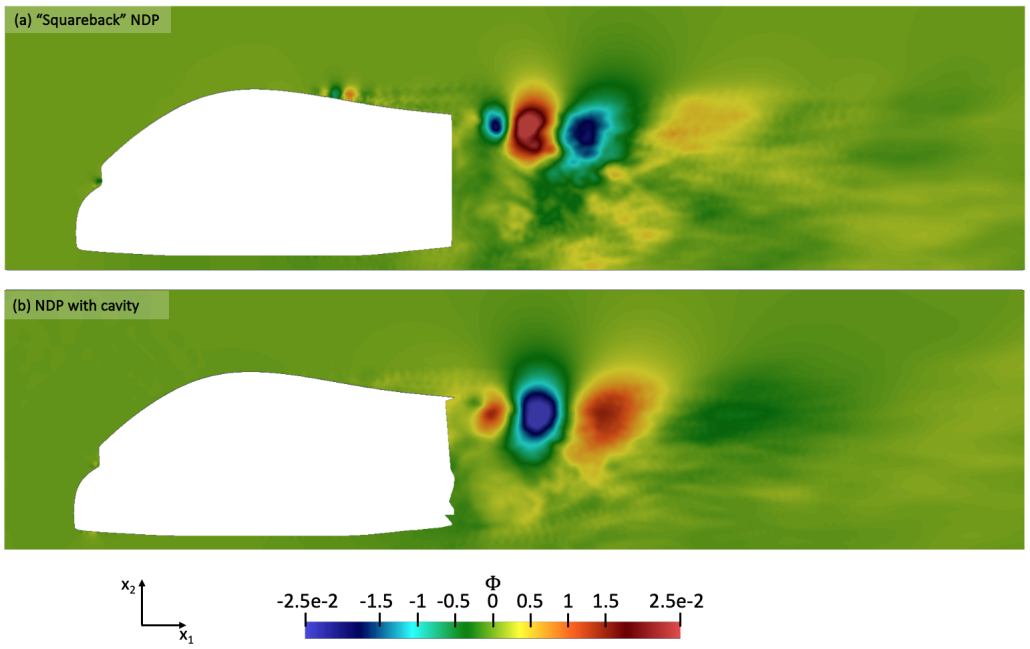


Fig. 6.13: Asymmetric top-to-bottom vortex shedding visualized through the application of POD, Φ, on instantaneous pressure data taken from the x_1x_2 - middle plane for (a) the "squareback" NDP and (b) the NDP with a rear cavity. This is the second POD mode.

Moving on, the direct impact of the cavity on average integral flow quantities, C_D and C_L, is

now looked at. The average and root-mean-square (RMS) value of these variables, as well as the percentage delta between the "squareback" and cavity variants are displayed in table 6.2. For one, the direct impact of the cavity on the absolute drag value is to lower it. This corroborates the work of Lucas *et al.* (2017) who achieved drag reductions between 3% and 9.5% when appending cavities of varying depth to the canonical Ahmed body. In this case, the cavity reduces the drag experienced by the Nissan NDP by 13.6%, illustrating that it is a beneficial passive flow control device. Equally notable is the cavity's influence on the RMS values of drag and lift. It reduces the RMS drag value, $\overline{C_D'^2}$, by 68.7% and the RMS lift value, $\overline{C_L'^2}$, by 32.7%, respectively. This indicates that the cavity reduces fluctuations in the flow field around the Nissan NDP, which should translate to improved ride comfort e.g. less roadway noise. Unfortunately, the cavity increases the lift force experienced by the vehicle. This reduction in downforce on the vehicle means the Nissan NDP with cavity will experience less stability when travelling at high speeds through corners. Fortunately, high speed cornering is not a design target for vans. In light of the failure to achieve truly converged values for drag coefficient and lift coefficient with both the Ahmed body (section 5.1) and the Nissan NDP (section 6.1), it is important to note here that these percentage deltas between the "squareback" and cavity variant of the NDP cannot be viewed as absolute. They must be viewed in the context of some plus and minus variability (i.e. margin of error), which for the Nissan NDP's drag is about 3% and lift is about 10% (see table 6.1) based on the set-up's mesh sensitivity study. This means that the error margin in lift exceeds the percentage delta, which reinforces the notion that the variability in lift with CFD is quite high, as encountered in the work of Ashton *et al.* (2016).

Set-up	$\overline{C_D}$	$\%\Delta$	$\overline{C_D'^2}$	$\%\Delta$	$\overline{C_L}$	$\%\Delta$	$\overline{C_L'^2}$	$\%\Delta$
"Squareback" NDP	0.317	-	0.0163	-	-0.0815	-	0.0107	-
NDP with cavity	0.274	-13.6	0.0051	-68.7	-0.0750	8.0	0.0072	-32.7

Table 6.2: Integral flow quantities for the "squareback" NDP and NDP with a rear cavity

6.3 Moving Ground Analysis

This final more qualitative section analyzes what it means to have a moving ground in simulation for vehicle development. To do so, stationary ground and moving ground simulations of the Nissan NDP with cavity appendage are compared. Figures 6.14, 6.15, and 6.16 illustrate the instantaneous pressure distribution, x_3-vorticity, and velocity magnitude around the vehicle, respectively, for both setups. All three representations highlight the separation of a vortex from the vehicle's ceiling. It was this structure that was alluded to previously and highlighted as a reason for a strong vertical tilt of the wake away from the Nissan NDP's top trailing edge. One is able to isolate this coherent structure and, thereby, visualize it more clearly through the use of POD. POD analysis indicates that this hairpin vortex structure is the fourth most energetic mode of this highly energy distributed system - the mode contains about 3.5% of the total system energy. Also, its moving ground and stationary ground manifestation are indistinguishable (Fig. 6.17). Meanwhile, all three representations of the flow around the NDP (Figs. 6.14-6.16) highlight the existence of a stationary ground by indicating the presence of clockwise rotating low pressure cores that are brought on by the onset of flow detachment from the ground. This flow detachment is triggered by the flow going from a low pressure area to a higher pressure one as it passes beyond the vehicle under-body into the far-field wake region. Furthermore, figure 6.18 portrays the vortex structures around the vehicle through visualization of Q^* criterion iso-contours at $Q^* = 59.8$ coloured by velocity magnitude. The influence of the moving ground is to drag the vortex structures further downstream (Fig. 6.18a) away from the vehicle so that their negative impact on the vehicle is mitigated. Looking at drag, one can see that the mean value for the stationary ground simulation therefore lies at 0.274, while for the moving ground simulation it rests at 0.265 (table 6.3). This indicates that, for the Nissan NDP vehicle geometry, although a moving ground is more representative of real-world conditions, a more conservative design based on aerodynamics is achieved by considering the results from a stationary ground simulation. Whether or not moving ground simulations always predict a lower drag value

than their fixed ground counterparts is not absolute though. It depends very heavily on whether the underbody is detailed or smooth, whether one is accounting for the presence of tires and even whether side mirrors are present. This was nicely illustrated when Heft *et al.* (2012) introduced the open-source DrivAer model. Additionally, looking at lift, one can see that the effect of a moving ground in accelerating the flow under the vehicle body is to drop the lift value (i.e. more downforce is generated), leaving lift for the moving ground simulation at -0.089 compared to its stationary ground value at -0.075 (table 6.3). Finally, the results on RMS of drag and lift are inconclusive. More specifically, RMS of drag increases and RMS of lift decreases by a similar amount between the stationary ground and moving ground simulation (table 6.3).

Set-up	$\overline{C_D}$	$\%\Delta$	$\overline{C_D'^2}$	$\%\Delta$	$\overline{C_L}$	$\%\Delta$	$\overline{C_L'^2}$	$\%\Delta$
Stationary ground	0.274	-	0.0051	-	-0.075	-	0.0072	-
Moving ground	0.265	-3.3	0.0064	25.5	-0.089	-18.7	0.0060	-16.7

Table 6.3: Integral flow quantities for the stationary ground and moving ground simulation of the NDP with a rear cavity

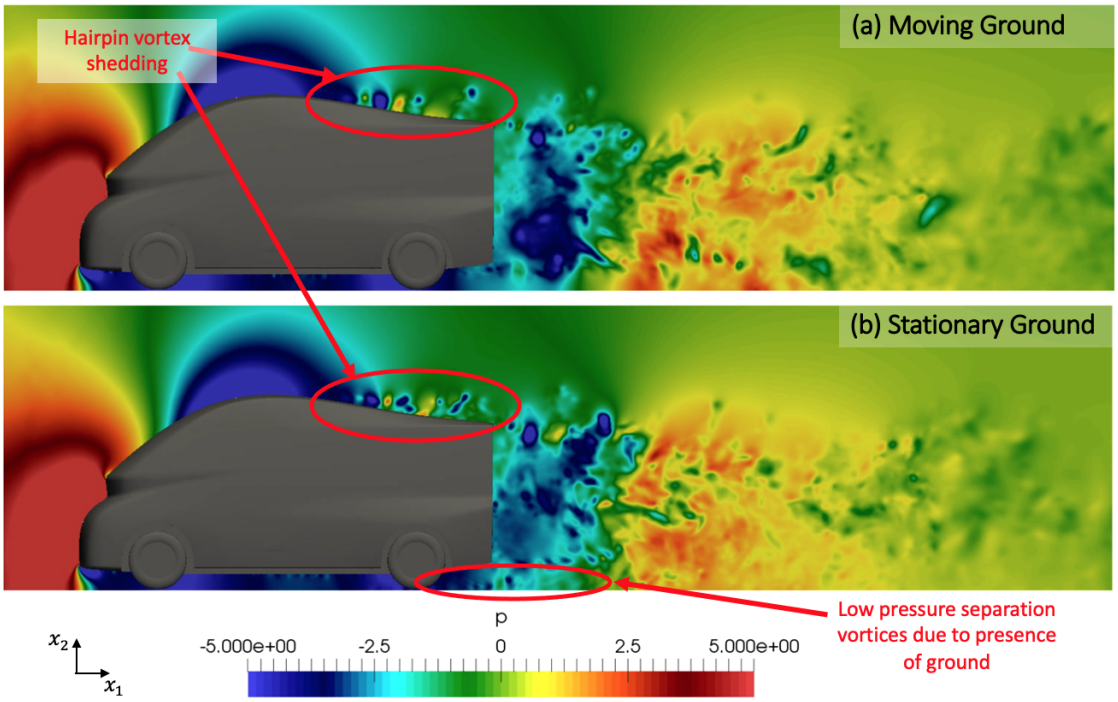


Fig. 6.14: Instantaneous pressure flow field for (a) moving ground and (b) stationary ground simulation of the Nissan NDP with a rear cavity

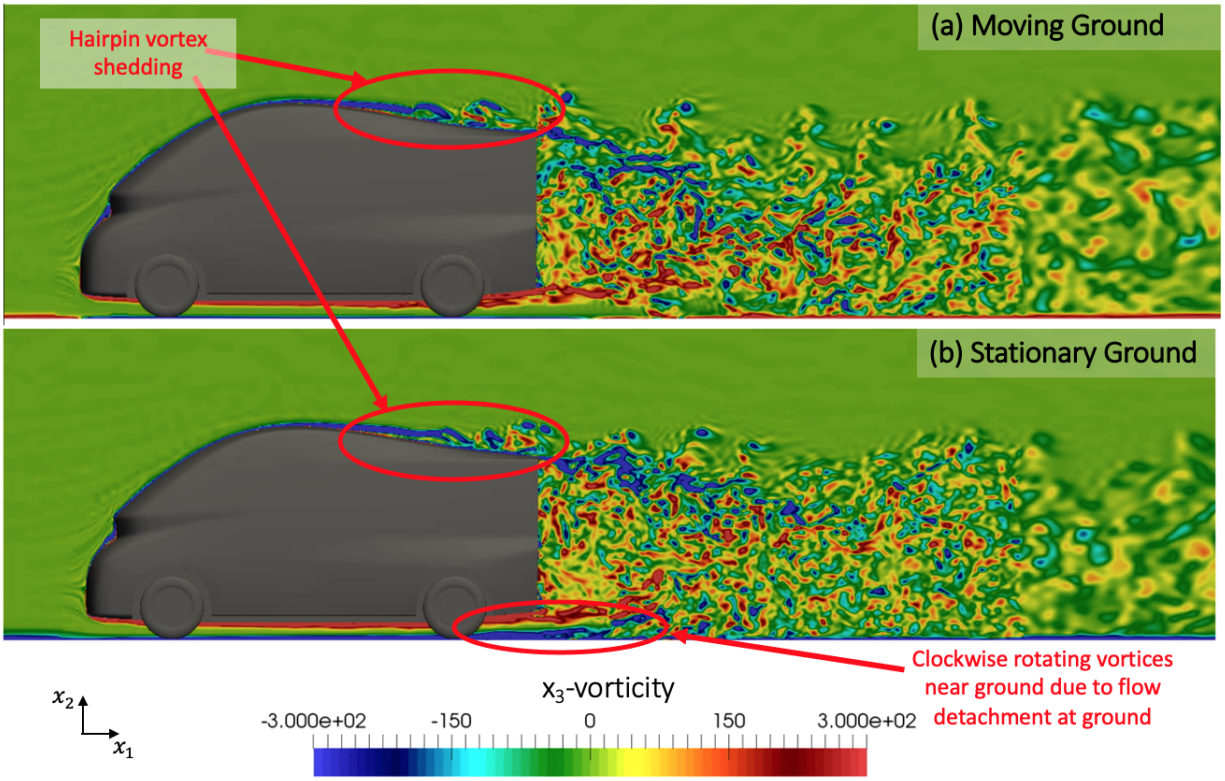


Fig. 6.15: Instantaneous x_3-vorticity for (a) moving ground and (b) stationary ground simulation of the Nissan NDP with a rear cavity

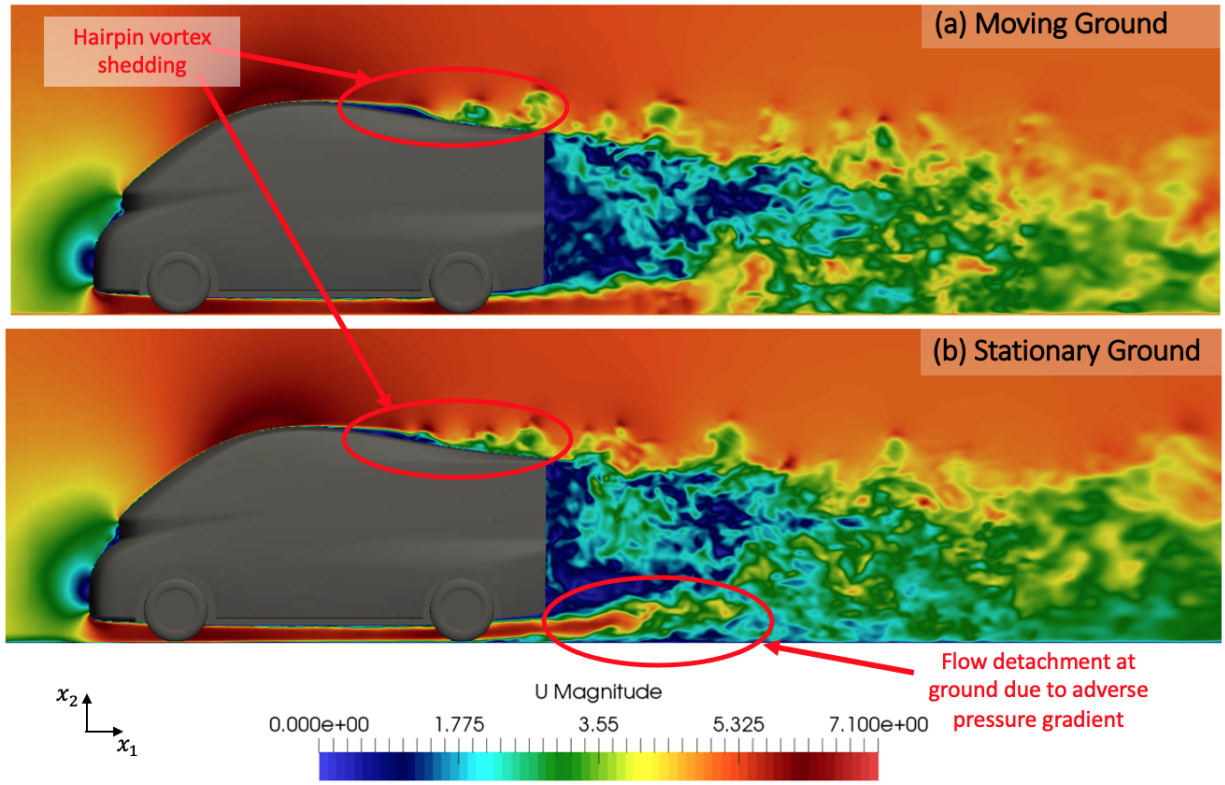


Fig. 6.16: Instantaneous velocity magnitude field for (a) moving ground and (b) stationary ground simulation of the Nissan NDP with a rear cavity

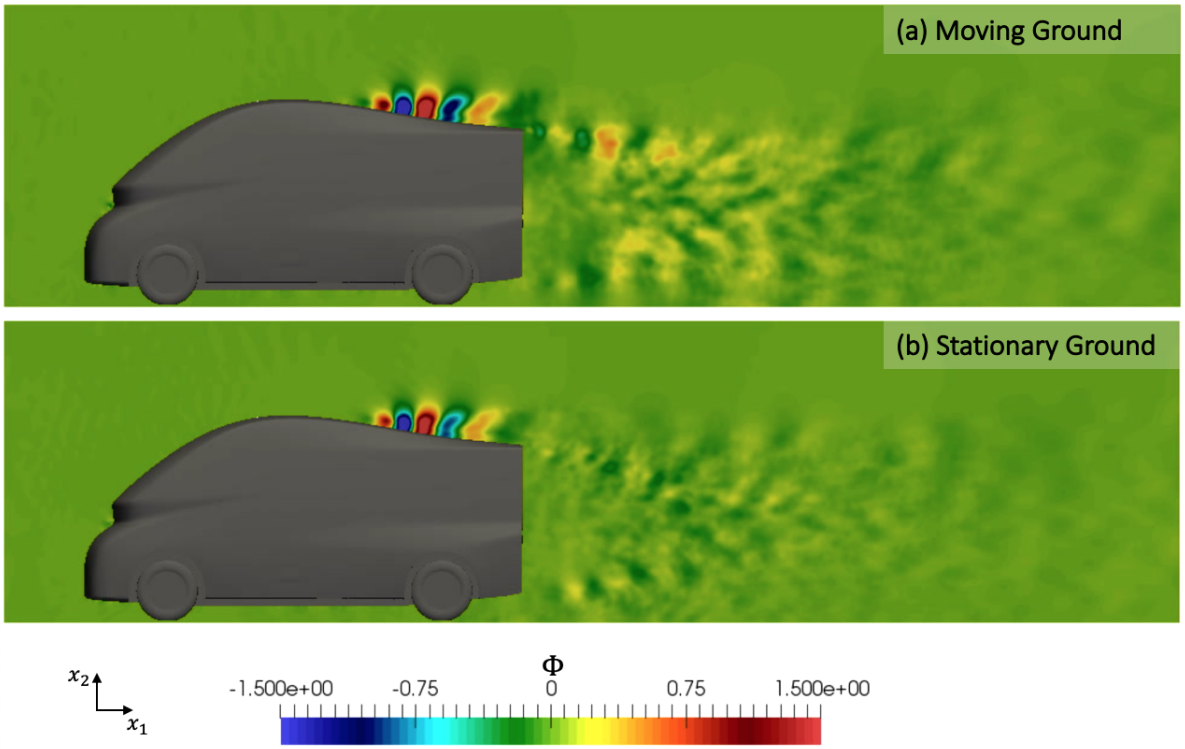


Fig. 6.17: Ceiling hairpin vortex visualized through the application of POD, Φ, on instantaneous pressure data taken from the x_1x_2 - middle plane for (a) moving ground and (b) stationary ground simulation of the Nissan NDP with a rear cavity. This is the fourth POD mode.

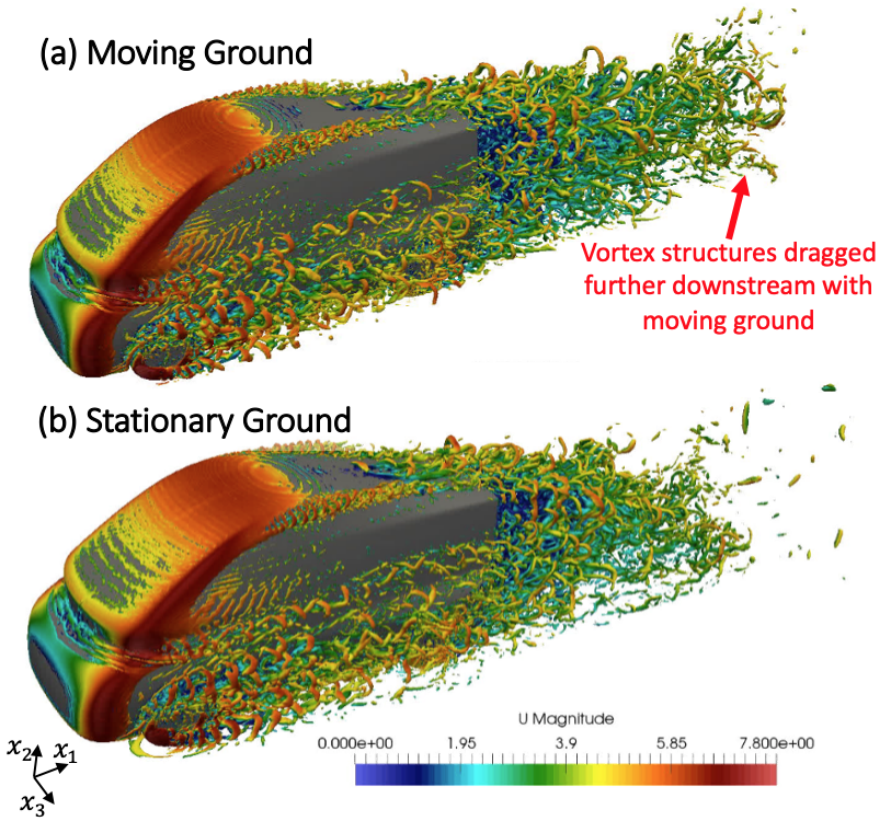


Fig. 6.18: Vortex structure visualization through Q^* criterion iso-contours of Q^*=59.8 for (a) moving ground and (b) stationary ground simulation of the Nissan NDP with a rear cavity

Chapter 7

Closing Remarks

This chapter ties up the thesis by summarising its main findings and offering suggestions / avenues for future work.

7.1 Conclusions

The set-ups covered in this thesis span from very academic cases consisting of the bullet shaped D-body and the Ahmed body to an industry relevant road vehicle geometry provided by Nissan, the NDP. The following conclusions may be drawn from the three simulation studies:

1. The work of Dalla Longa *et al.* (2017) on the linear feedback control of the D-body wake has been successfully replicated in OpenFOAM by achieving a base pressure recovery of 24.5%, thereby transitioning the research group from StreamLES to OpenFOAM.

2. A computationally efficient mesh setup was constructed for the rigorous analysis of wake bimodality aft of the squareback Ahmed body. Hybrid RANS-LES in the form of WMLES versus wall-resolving LES (WRLES) was then used to assess that the front recirculation bubble, a source of high TKE generating large hairpin vortices, is a strong candidate for triggering rear wake bimodality. Furthermore, it was determined that linear feedback control for drag reduction, while successful in attenuation of base pressure fluctuations, does not work on fully

turbulent 3D wakes as it does for more quasi-2D 3D turbulent wakes. The results suggest that, for flows passed fully 3D bluff-bodies, one must focus on control strategies that symmetrize the wake - they have been shown on multiple occasions to reduce drag.

3. For the Nissan NDP, benchmark wall-resolving LES (WRLES) was performed to assess the benefits of passive flow control through the appendage of a rear cavity and to assess the influence of a moving ground on the simulation. It was observed that the application of the rear cavity results in a 13.6% drag reduction. Meanwhile, a comparison between a stationary ground simulation and a moving ground simulation for the Nissan NDP with rear cavity illustrated that a higher drag value is obtained from the stationary ground simulation, thereby showing that stationary ground simulations can actually be more conservative.

7.2 Future Work

The thesis explores a broad range of topics that each on their own already could form individual branches of research: bluff-body aerodynamics, hybrid RANS-LES methods, flow control and model-order reduction. As such, there is an array of complex topics spanning combinations of these disciplines that could be explored as part of further research:

1. More complexity could be introduced into the bluff-body simulations performed by better accounting for the dynamics of tire motion. This can be done through moving reference frames or sliding meshes.

2. A major limitation of the Nissan NDP work was that there was no experimental data to assess the CFD result's correlation to real-world tests. Nissan have donated a foam model of the Nissan NDP to Imperial College. It should be tested in future wind tunnel runs and, thereby, make experimental data available for CFD correlation exercises.

3. To overcome the exorbitantly large CPUhr requirements for using wall-resolving LES (WRLES) to simulate the flow past the Nissan NDP up to and beyond a non-dimensional time, t^*, of

1000, the time-scale at which one could expect bimodality to occur, cheaper hybrid RANS-LES methods could be adopted e.g. detached eddy simulation (DES) or simply WMLES (as was used for the Ahmed body in this dissertation).

4. One should look to adopt more complex control methods such as non-linear feedback control, multi-input multi-output (MIMO) control or dynamic control.

Bibliography

Ahmed, S. R. 1981 Wake structure of typical automobile shapes. *Journal of Fluids Engineering* **103** (1), 162–169.

Ahmed, S. R., Ramm, G. & Faltin, G. 1984 Some salient features of the time-averaged ground vehicle wake. *SAE Technical Paper* .

Aider, J.-L., Beaudoin, J.-F. & Wesfreid, J. E. 2010 Drag and lift reduction of a 3D bluff-body using active vortex generators. *Experiments in Fluids* **48** (5), 771–789.

Aljure, D. E., Calafell, J., Baez, A. & Oliva, A. 2018 Flow over a realistic car model: Wall modeled large eddy simulations assessment and unsteady effects. *Journal of Wind Engineering and Industrial Aerodynamics* **174**, 225–240.

Aram, E., Mittal, R. & Cattafesta, L. 2010 Simple representations of zero-net mass-flux jets in grazing flow for flow-control simulations. *International Journal of Flow Control* **2** (2).

Ashton, N., West, A., Lardeau, S. & Revell, A. 2016 Assessment of RANS and DES methods for realistic automotive models. *Computers & Fluids* **128**, 1–15.

Astroem, K. J. 1975 Lectures on system identification - frequency response analysis. *Tech. Rep.* 3093. Department of Automatic Control, Lund Institute of Technology (LTH).

Astroem, K. J. & Murray, R. M. 2010 *Feedback systems: an introduction for scientists and engineers*. Princeton University Press.

Barlow, J., Guterres, R., Ranzenbach, R. & Williams, J. 1999 Wake structures of rectangular bodies with radiused edges near a plane surface. *SAE Technical Paper Series* .

Barros, D., Borée, J., Noack, B. R., Spohn, A. & Ruiz, T. 2016 Bluff body drag manipulation using pulsed jets and Coanda effect. *Journal of Fluid Mechanics* **805**, 422–459.

Barton, I. E. 1998 Comparison of SIMPLE-and PISO-type algorithms for transient flows. *International Journal for Numerical Methods in Fluids* **26** (4), 459–483.

Beaudoin, J.-F. & Aider, J.-L. 2008 Drag and lift reduction of a 3D bluff body using flaps. *Experiments in Fluids* **44** (4), 491.

Beaudoin, J.-F., Cadot, O., Aider, J.-L. & Wesfreid, J.-E. 2006 Drag reduction of a bluff body using adaptive control methods. *Physics of Fluids* **18** (8), 085107.

Becker, R., Garwon, M., Gutknecht, C., Bärwolff, G. & King, R. 2005 Robust control of separated shear flows in simulation and experiment. *Journal of Process Control* **15** (6), 691–700.

Berkooz, G., Holmes, P. & Lumley, J. L. 1993 The proper orthogonal decomposition in the analysis of turbulent flows. *Annual Review of Fluid Mechanics* **25** (1), 539–575.

Bonnavion, G. & Cadot, O. 2018 Unstable wake dynamics of rectangular flat-backed bluff bodies with inclination and ground proximity. *Journal of Fluid Mechanics* **854**, 196–232.

Bonnavion, G., Cadot, O., Évrard, A., Herbert, V., Parpais, S., Vigneron, R. & Délery, J. 2017 On multistabilities of real car's wake. *Journal of Wind Engineering and Industrial Aerodynamics* **164**, 22–33.

Bonnavion, G., Cadot, O., Herbert, V., Parpais, S., Vigneron, R. & Délery, J. 2019 Asymmetry and global instability of real minivans' wake. *Journal of Wind Engineering and Industrial Aerodynamics* **184**, 77–89.

Bose, S. T. & Park, G. I. 2018 Wall-modeled large-eddy simulation for complex turbulent flows. *Annual Review of Fluid Mechanics* **50** (1), 535–561.

Brackston, R. D., García de la Cruz, J. M., Wynn, A., Rigas, G. & Morrison, J. F. 2016 Stochastic modelling and feedback control of bistability in a turbulent bluff body wake. *Journal of Fluid Mechanics* **802**, 726–749.

Cattafesta III, L. N. & Sheplak, M. 2011 Actuators for active flow control. *Annual Review of Fluid Mechanics* **43**, 247–272.

Choi, H., Jeon, W.-P. & Kim, J. 2008 Control of flow over a bluff body. *Annual Review of Fluid Mechanics* **40**, 113–139.

Choi, H., Lee, J. & Park, H. 2014 Aerodynamics of heavy vehicles. *Annual Review of Fluid Mechanics* **46**, 441–468.

Choi, H. & Moin, P. 2012 Grid-point requirements for large eddy simulation: Chapmans estimates revisited. *Physics of Fluids* **24** (1), 011702.

Cozzi, L., Gould, T., Guel, T., McNamara, K., McGlade, C. & Trueby, J. 2017 *World Energy Outlook 2017.*. Paris, France: International Energy Agency.

Dahan, J. 2013 Linear feedback control for form-drag reduction on bluff-bodies with a blunt trailing edge. PhD thesis, Imperial College London.

Dahan, J. A., Morgans, A. S. & Lardeau, S. 2012 Feedback control for form-drag reduction on a bluff body with a blunt trailing edge. *Journal of Fluid Mechanics* **704**, 360–387.

Dalla Longa, L. 2015 First year report: Simulation, modelling and feedback control of the flow around a square-back road vehicle. *Tech. Rep.*. Imperial College London.

Dalla Longa, L. 2018 Simulation, modelling and feedback control of the flow around a simplified square-back road vehicle. PhD thesis, Imperial College London.

Dalla Longa, L., Evstafyeva, O. & Morgans, A. S. 2019 Simulations of the bi-modal wake past three-dimensional blunt bluff bodies. *Journal of Fluid Mechanics* **866**, 791–809.

Dalla Longa, L., Morgans, A. S. & Dahan, J. A. 2017 Reducing the pressure drag of a D-shaped bluff body using linear feedback control. *Theoretical and Computational Fluid Dynamics* **31** (5-6), 567–577.

Edenhofer, O., Sokona, Y., Farahani, E., Kadner, S., Seyboth, K. & Adler, A. 2014 *Climate Change 2014: Mitigation of Climate Change.*, 1st edn. New York, USA: Cambridge University Press.

Englar, R. J. 2001 Advanced aerodynamic devices to improve the performance, economics, handling and safety of heavy vehicles. *SAE Technical Paper* .

Evrard, A., Cadot, O., Herbert, V., Ricot, D., Vigneron, R. & Délery, J. 2016 Fluid force and symmetry breaking modes of a 3D bluff body with a base cavity. *Journal of Fluids and Structures* **61**, 99–114.

Evstafyeva, O. 2018 Simulation and feedback control of simplified vehicle flows. PhD thesis, Imperial College London.

Evstafyeva, O., Morgans, A. S. & Dalla Longa, L. 2017 Simulation and feedback control of the Ahmed body flow exhibiting symmetry breaking behaviour. *Journal of Fluid Mechanics* **817**.

Fan, Y., Xia, C., Chu, S., Yang, Z. & Cadot, O. 2020 Experimental and numerical analysis of the bi-stable turbulent wake of a rectangular flat-backed bluff body. *Physics of Fluids* **32** (10), 105111.

Fauconnier, D. & Dick, E. 2014 Analytical and numerical study of resolution criteria in large-eddy simulation. *Physics of Fluids* **26** (6), 065104.

Fourrié, G., Keirsbulck, L., Labraga, L. & Gilliéron, P. 2011 Bluff-body drag reduction using a deflector. *Experiments in Fluids* **50** (2), 385–395.

Freund, J. B. & Mungal, M. G. 1994 Drag and wake modification of axisymmetric bluff bodies using Coanda blowing. *Journal of Aircraft* **31** (3), 572–578.

Gad-el-Hak, M. 2000 *Flow Control: Passive, Active, and Reactive Flow Management*. Cambridge, UK: Cambridge University Press.

Gerhard, J., Pastoor, M., King, R., Noack, B., Dillmann, A., Morzynski, M. & Tadmor, G. 2003 Model-based control of vortex shedding using low-dimensional Galerkin models. In *33rd AIAA Fluid Dynamics Conference and Exhibit*, p. 4262.

Germano, M., Piomelli, U., Moin, P. & Cabot, W. H. 1991 A dynamic subgrid - scale eddy viscosity model. *Physics of Fluids A: Fluid Dynamics* **3** (7), 1760–1765.

Gilliéron, P. & Kourta, A. 2010 Aerodynamic drag reduction by vertical splitter plates. *Experiments in Fluids* **48** (1), 1–16.

Glezer, A. & Amitay, M. 2002 Synthetic jets. *Annual Review of Fluid Mechanics* **34** (1), 503–529.

Grandemange, M., Cadot, O. & Gohlke, M. 2012 Reflectional symmetry breaking of the separated flow over three-dimensional bluff bodies. *Physical review E* **86** (3), 035302.

Grandemange, M., Gohlke, M. & Cadot, O. 2013*a* Bi-stability in the turbulent wake past parallelepiped bodies with various aspect ratios and wall effects. *Physics of Fluids* **25** (9), 095103.

Grandemange, M., Gohlke, M. & Cadot, O. 2013*b* Turbulent wake past a three-dimensional blunt body. part 1. global modes and bi-stability. *Journal of Fluid Mechanics* **722**, 51–84.

Grandemange, M., Gohlke, M. & Cadot, O. 2014 Turbulent wake past a three-dimensional blunt body. part 2. experimental sensitivity analysis. *Journal of Fluid Mechanics* **752**, 439–461.

Guilmineau, E., Deng, G. B., Leroyer, A., Queutey, P., Visonneau, M. & Wackers, J. 2018 Assessment of hybrid RANS-LES formulations for flow simulation around the Ahmed body. *Computers & Fluids* **176**, 302–319.

Han, T. 1989 Computational analysis of three-dimensional turbulent flow around a bluff body in ground proximity. *AIAA Journal* **27** (9), 1213–1219.

Heft, A., Indinger, T. & Adams, N. A. 2012 Introduction of a new realistic generic car model for aerodynamic investigations. *SAE Technical Paper* **2012-01-0168**.

Henning, L. & King, R. 2005*a* Drag reduction by closed-loop control of a separated flow over a bluff body with a blunt trailing edge. In *Proceedings of the 44th IEEE Conference on Decision and Control, and the European Control Conference 2005*, pp. 494–499. IEEE.

Henning, L. & King, R. 2005*b* Multivariable closed-loop control of the reattachment length downstream of a backward-facing step. *IFAC Proceedings Volumes* **38** (1), 235–240.

Henning, L., Pastoor, M., King, R., Noack, B. R. & Tadmor, G. 2007 Feedback control applied to the bluff body wake. *Springer - Active flow control* pp. 369–390.

Hesse, F. & Morgans, A. S. 2021 Simulation of wake bimodality behind squareback bluff-bodies using LES. *Computers & Fluids* **223**, 104901.

Howard, R. & Pourquie, M. 2002 Large eddy simulation of an Ahmed reference model. *Journal of Turbulence* **3** (012), 1–18.

Howell, J., Sheppard, A. & Blakemore, A. 2003 Aerodynamic drag reduction for a simple bluff body using base bleed. *SAE Technical Paper* .

Hucho, W.-H. 1998 *Aerodynamics of Road Vehicles.*, 4th edn. United States of America: Society of Automotive Engineers, Inc.

Hucho, W.-H. & Sovran, G. 1993 Aerodynamics of road vehicles. *Annual Review of Fluid Mechanics* **25** (1), 485–537.

Issa, R. I. 1986 Solution of the implicitly discretised fluid flow equations by operator-splitting. *Journal of computational physics* **62** (1), 40–65.

Khalighi, B., Zhang, S., Koromilas, C., Balkanyi, S. R., Bernal, L. P., Iaccarino, G. & Moin, P. 2001 Experimental and computational study of unsteady wake flow behind a bluff body with a drag reduction device. *SAE Technical Paper* .

Kim, D., Lee, H., Yi, W. & Choi, H. 2016 A bio-inspired device for drag reduction on a three-dimensional model vehicle. *Bioinspiration & biomimetics* **11** (2), 026004.

Kim, J. & Choi, H. 2005 Distributed forcing of flow over a circular cylinder. *Physics of Fluids* **17** (3), 033103.

Kim, J., Hahn, S., Kim, J., Lee, D.-K., Choi, J., Jeon, W.-P. & Choi, H. 2004 Active control of turbulent flow over a model vehicle for drag reduction. *Journal of Turbulence* **5** (019), 1–12.

King, R., Becker, R., Garwon, M. & Henning, L. 2004 Robust and adaptive closed-loop control of separated shear flows. In *2nd AIAA Flow Control Conference*, p. 2519.

Kitamori, K., Manders, T., Dellink, R., Chateau, J., Magne, B. & van Vuuren, D. 2012 Oecd Environmental Outlook to 2050: The Consequences of Inaction. *Tech. Rep.*. OECD Publishing.

Krajnović, S. & Davidson, L. 2003 Numerical study of the flow around a bus-shaped body. *Journal of Fluids Engineering* **125** (3), 500–509.

Krajnović, S. & Fernandes, J. 2011 Numerical simulation of the flow around a simplified vehicle model with active flow control. *International Journal of Heat and Fluid Flow* **32** (1), 192–200.

Kremheller, A. 2014 The aerodynamics development of the new Nissan Qashqai. In *SAE 2014 World Congress and Exhibition*. SAE International.

Kremheller, A., LeGood, G., Annetts, I. & Moore, M. 2015 The aerodynamics development of a new light commercial vehicle concept under uniform and transient flow conditions. In *10th FKFS Conference*.

Kremheller, A., Moore, M., LeGood, G., Sims-Williams, D., Newborn, J. & Lewis, R. 2016 The effects of transient flow conditions on the aerodynamics of an LCV concept using CFD and wind tunnel experiments. In *International conference on vehicle aerodynamics 2016 : aerodynamics by design*. Coventry, England: IMechE.

Krüger, T., Kusumaatmaja, H., Kuzmin, A., Shardt, O., Silva, G. & Viggen, E. M. 2017 *The lattice Boltzmann method: principles and practice.*, 1st edn. Switzerland: Springer International Publishing.

Larsson, J., Kawai, S., Bodart, J. & Bermejo-Moreno, I. 2016 Large eddy simulation with modeled wall-stress: recent progress and future directions. *Mechanical Engineering Reviews* **3** (1).

Le Good, G. M. & Garry, K. P. 2004 On the use of reference models in automotive aerodynamics. *SAE Technical Paper* .

Leschziner, M. 2015 *Statistical Turbulence Modelling for Fluid Dynamics.*, 1st edn. London: Imperial College Press.

Leschziner, M. A. & Lardeau, S. 2011 Simulation of slot and round synthetic jets in the context of boundary-layer separation control. *Philosophical Transactions of the Royal Society A: Mathematical, Physical and Engineering Sciences* **369** (1940), 1495–1512.

Li, R., Barros, D., Borée, J., Cadot, O., Noack, B. R. & Cordier, L. 2016 Feedback control of bimodal wake dynamics. *Experiments in Fluids* **57** (10).

Littlewood, R. P. & Passmore, M. A. 2012 Aerodynamic drag reduction of a simplified squareback vehicle using steady blowing. *Experiments in Fluids* **53** (2), 519–529.

Ljung, L. 1987 *System Identification: Theory for the User.*, 1st edn. New Jersey, USA: Prentice-Hall, Inc.

Lucas, J.-M., Cadot, O., Herbert, V., Parpais, S. & Délery, J. 2017 A numerical investigation of the asymmetric wake mode of a squareback Ahmed body-effect of a base cavity. *Journal of Fluid Mechanics* **831**, 675–697.

Lumley, J. L. 1967 The structure of inhomogeneous turbulent flows. *Atmospheric turbulence and radio wave propagation* .

Manceau, R. & Bonnet, J.-P. 2002 Refined turbulence modelling. In *Proc. 10th ERCOFTAC (SIG-15)/IAHR/QNET-CFD Workshop*.

Meneveau, C. & Katz, J. 2000 Scale-invariance and turbulence models for large-eddy simulation. *Annual Review of Fluid Mechanics* **32** (1), 1–32.

Moin, P. & Mahesh, K. 1998 Direct numerical simulation: a tool in turbulence research. *Annual Review of Fluid Mechanics* **30** (1), 539–578.

Morrison, J. F. & Qubain, A. 2009 Control of an axisymmetric turbulent wake by a pulsed jet. In *Advances in Turbulence XII*, pp. 225–228. Springer.

Mukha, T., Rezaeiravesh, S. & Liefvendahl, M. 2019 A library for wall-modelled large-eddy simulation based on openFOAM technology. *Computer Physics Communications* .

Nicoud, F. & Ducros, F. 1999 Subgrid-scale stress modelling based on the square of the velocity gradient tensor. *Flow, Turbulence and Combustion* **62** (3), 183–200.

Oxlade, A. R., Morrison, J. F., Qubain, A. & Rigas, G. 2015 High-frequency forcing of a turbulent axisymmetric wake. *Journal of Fluid Mechanics* **770**, 305–318.

Park, H., Lee, D., Jeon, W.-P., Hahn, S., Kim, J., Kim, J., Choi, J. & Choi, H. 2006 Drag reduction in flow over a two-dimensional bluff body with a blunt trailing edge using a new passive device. *Journal of Fluid Mechanics* **563**, 389–414.

Pasquali, A., Schönherr, M., Geier, M. & Krafczyk, M. 2016 Simulation of external aerodynamics of the DrivAer model with the LBM on GPGPUs. *Advances in Parallel Computing* **27**, 391–400.

Pasquetti, R. & Peres, N. 2015 A penalty model of synthetic micro-jet actuator with application to the control of wake flows. *Computers & Fluids* **114**, 203–217.

Pastoor, M., Henning, L., Noack, B. R., King, R. & Tadmor, G. 2008 Feedback shear layer control for bluff body drag reduction. *Journal of Fluid Mechanics* **608**, 161–196.

Patankar, S. V. & Spalding, D. B. 1972 Paper 5 - a calculation procedure for heat, mass and momentum transfer in three-dimensional parabolic flows. *Numerical Prediction of Flow, Heat Transfer, Turbulence and Combustion* pp. 54–73.

Pavia, G., Passmore, M. & Sardu, C. 2018 Evolution of the bi-stable wake of a square-back automotive shape. *Experiments in Fluids* **59** (1), 20.

Perry, A.-K., Pavia, G. & Passmore, M. 2016 Influence of short rear end tapers on the wake of a simplified square-back vehicle: wake topology and rear drag. *Experiments in Fluids* **57** (11), 169.

Petrusma, M. 1992 Base pressure recovery for segmented trailing edge aerofoils. In *Australasian Fluid Mechanics Conference, 11th, University of Tasmania, Hobart, Australia*, pp. 787–790.

Pfeiffer, J. & King, R. 2012 Multivariable closed-loop flow control of drag and yaw moment for a 3D bluff body. In *6th AIAA Flow Control Conference*, p. 2802.

Piomelli, U. 1999 Large-eddy simulation: achievements and challenges. *Progress in Aerospace Sciences* **35** (4), 335–362.

Piomelli, U. 2008 Wall-layer models for large-eddy simulations. *Progress in Aerospace Sciences* **44** (6), 437–446.

Piomelli, U. & Balaras, E. 2002 Wall-layer models for large-eddy simulations. *Annual Review of Fluid Mechanics* **34** (1), 349–374.

Podvin, B., Pellerin, S., Fraigneau, Y., Bonnavion, G. & Cadot, O. 2021 Low-order modelling of the wake dynamics of an Ahmed body. *Journal of Fluid Mechanics* **927**, R6.

Pope, S. B. 2000 *Turbulent Flows*. Cambridge, England: Cambridge University Press.

Prandtl, L. 1910 Eine Beziehung zwischen Waermeaustausch und Stroemungswiderstand der Fluessigkeit. *Physikalische Zeitschrift* **11**, 1072–1078.

Pujals, G., Depardon, S. & Cossu, C. 2010 Drag reduction of a 3D bluff body using coherent streamwise streaks. *Experiments in Fluids* **49** (5), 1085–1094.

Rao, A. N., Minelli, G., Zhang, J., Basara, B. & Krajnović, S. 2018*a* Investigation of the near-wake flow topology of a simplified heavy vehicle using PANS simulations. *Journal of Wind Engineering and Industrial Aerodynamics* **183**, 243–272.

Rao, A. N., Zhang, J., Minelli, G., Basara, B. & Krajnović, S. 2018*b* An LES investigation of the near-wake flow topology of a simplified heavy vehicle. *Flow, Turbulence and Combustion* pp. 1–27.

Reichardt, H. 1951 Vollständige Darstellung der turbulenten Geschwindigkeitsverteilung in glatten Leitungen. *Journal of Applied Mathematics and Mechanics* **31** (7), 208–219.

Reynolds, W. C. 1990 The potential and limitations of direct and large eddy simulations. In *Whither turbulence? Turbulence at the crossroads*, pp. 313–343. Springer.

Rigas, G., Morgans, A. S., Brackston, R. D. & Morrison, J. F. 2015 Diffusive dynamics and stochastic models of turbulent axisymmetric wakes. *Journal of Fluid Mechanics* **778**.

Rigas, G., Oxlade, A. R., Morgans, A. S. & Morrison, J. F. 2014 Low-dimensional dynamics of a turbulent axisymmetric wake. *Journal of Fluid Mechanics* **755**.

Rintoul, S. R., Chown, S. L., DeConto, R. M., England, M. H., Fricker, H. A., Masson-Delmotte, V., Naish, T. R., Siegert, M. J. & Xavier, J. C. 2018 Choosing the future of Antarctica. *Nature* **558** (7709), 233.

Roshko, A. 1993 Perspectives on bluff body aerodynamics. *Journal of Wind Engineering and Industrial Aerodynamics* **49** (1-3), 79–100.

Rouméas, M., Gilliéron, P. & Kourta, A. 2009 Analysis and control of the near-wake flow over a square-back geometry. *Computers & Fluids* **38** (1), 60–70.

Roussopoulos, K. 1993 Feedback control of vortex shedding at low reynolds numbers. *Journal of Fluid Mechanics* **248**, 267–296.

Schmid, P. J. 2010 Dynamic mode decomposition of numerical and experimental data. *Journal of Fluid Mechanics* **656**, 5–28.

Schmid, P. J. & Sesterhenn, J. 2008 Dynamic mode decomposition of numerical and experimental data. In *61st Annual Meeting of the APS Division of Fluid Dynamics*.

Siegel, S. G., Seidel, J., Fagley, C., Luchtenburg, D. M., Cohen, K. & McLaughlin, T. 2008 Low-dimensional modelling of a transient cylinder wake using double proper orthogonal decomposition. *Journal of Fluid Mechanics* **610**, 1–42.

Smagorinsky, J. 1963 General circulation experiments with the primitive equations: The basic experiment. *Monthly Weather Review* **91** (3), 99–164.

Spalart, P. & Allmaras, S. 1992 A one-equation turbulence model for aerodynamic flows. In *30th aerospace sciences meeting and exhibit*, p. 439.

Spalding, D. B. 1961 A single formula for the "law of the wall". *Journal of Applied Mechanics* **28** (3), 455–458.

Stern, N. 2006 Stern review on the economics of climate change. *Tech. Rep.*. HM Treasury.

Strangfeld, C., Wieser, D., Schmidt, H.-J., Woszidlo, R., Nayeri, C. & Paschereit, C. 2013 Experimental study of baseline flow characteristics for the realistic car model DrivAer. *SAE Technical Paper* .

Taira, K., Brunton, S. L., Dawson, S. T. M., Rowley, C. W., Colonius, T., McKeon, B. J., Schmidt, O. T., Gordeyev, S., Theofilis, V. & Ukeiley, L. S. 2017 Modal analysis of fluid flows: An overview. *AIAA Journal* **55** (12), 4013–4041.

Taylor, G. I. 1916 Conditions at the surface of a hot body exposed to the wind. *Brit Adv Com Aero Rep Memor* **272**.

Temmerman, L. 2004 Large eddy simulation of separating flows from curved surfaces. PhD thesis, Queen Mary University of London.

Tennekes, H. & Lumley, J. L. 1972 *A First Course in Turbulence*. Cambridge, USA, and London, England: MIT press.

Thacker, A., Aubrun, S., Leroy, A. & Devinant, P. 2012 Effects of suppressing the 3D separation on the rear slant on the flow structures around an Ahmed body. *Journal of Wind Engineering and Industrial Aerodynamics* **107**, 237–243.

Tombazis, N. & Bearman, P. W. 1997 A study of three-dimensional aspects of vortex shedding from a bluff body with a mild geometric disturbance. *Journal of Fluid Mechanics* **330**, 85–112.

Tu, J. H., Rowley, C. W., Luchtenburg, D. M., Brunton, S. L. & Kutz, J. N. 2013 On dynamic mode decomposition: Theory and applications. *Journal of Computational Dynamics* .

Van Dam, C. P. 1999 Recent experience with different methods of drag prediction. *Progress in Aerospace Sciences* **35** (8), 751–798.

Versteeg, H. K. & Malalasekera, W. 2007 *An introduction to computational fluid dynamics: the finite volume method*. Pearson Education.

Viggen, E. M. 2014 The lattice Boltzmann method: Fundamentals and acoustics. PhD thesis, NTNU - Trondheim (Norwegian University of Science and Technology).

Volpe, R., Devinant, P. & Kourta, A. 2015 Experimental characterization of the unsteady natural wake of the full-scale square back Ahmed body: flow bi-stability and spectral analysis. *Experiments in Fluids* **56** (5), 99.

Wieser, D., Schmidt, H.-J., Müller, S., Strangfeld, C., Nayeri, C. & Paschereit, C. 2014 Experimental comparison of the aerodynamic behavior of fastback and notchback DrivAer models. *SAE International Journal of Passenger Cars-Mechanical Systems* **7** (2014-01-0613), 682–691.

WILCOX, D. C. 2006 *Turbulence modeling for CFD*, , vol. 2. California: DCW Industries Inc.

Appendix A: Pressure-Velocity Coupling

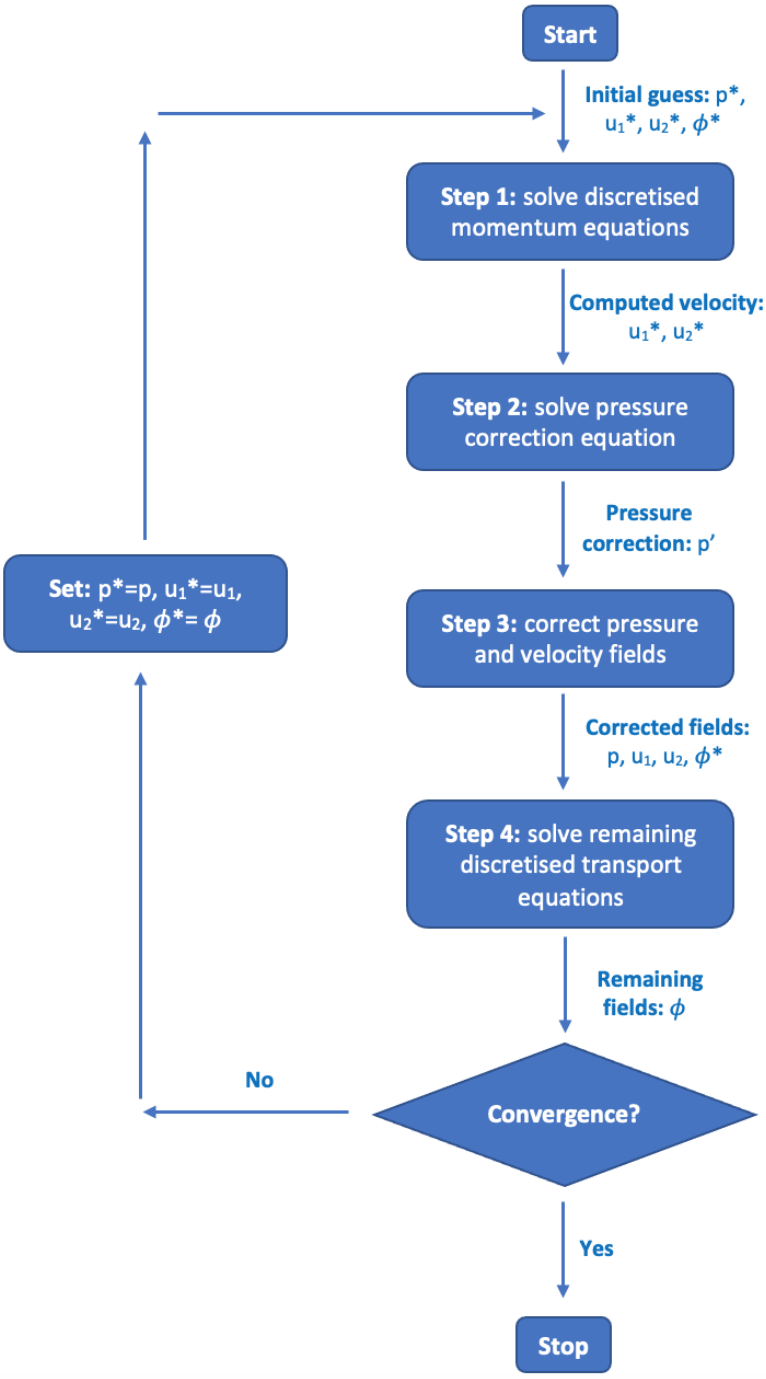


Fig. 7.1: Semi-Implicit Method for Pressure Linked Equations (SIMPLE) algorithm (Versteeg & Malalasekera, 2007)

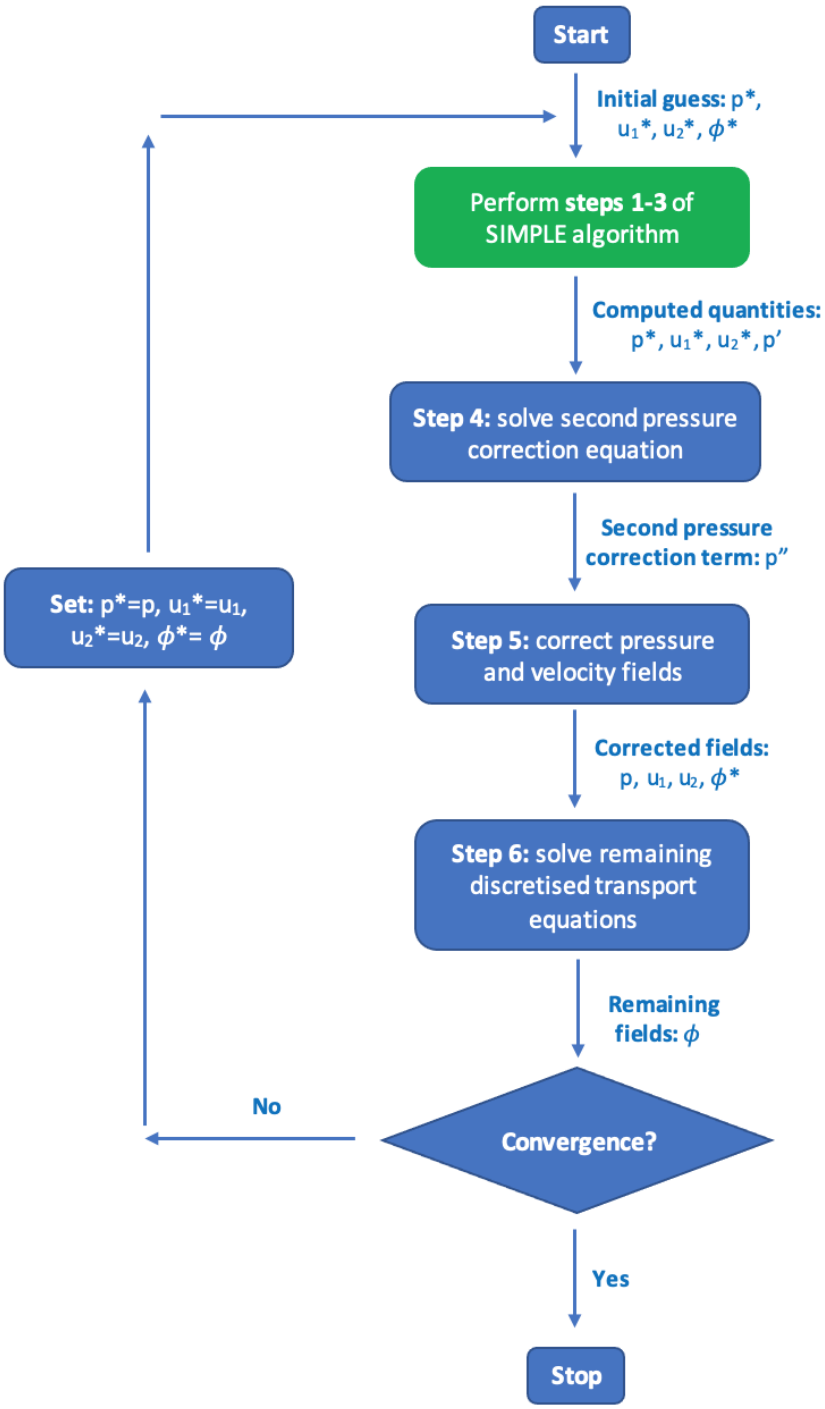


Fig. 7.2: Pressure Implicit with Splitting Operators (PISO) algorithm (Versteeg & Malalasekera, 2007)

Appendix B: Figure Usage Permission

Fig. No.	Fig. Source	Permission Granted
1.1	Edenhofer *et al.* (2014)	Yes - IPCC (Email from 20.02.19)
1.2	Cozzi *et al.* (2017)	Pending Email sent 16.02.19
1.3	Kremheller (2014)	Pending Email sent 16.02.19
1.4	Kremheller (2014)	Pending Email sent 16.02.19
2.1	Hucho (1998)	Yes - CCC
2.2	Choi *et al.* (2014)	Yes - CCC
2.3	Krajnović & Davidson (2003)	Pending Email sent 17.02.19
2.4	Grandemange *et al.* (2012)	Yes - SciPris
2.5	Grandemange *et al.* (2012)	Yes - SciPris
2.6a	Grandemange *et al.* (2013*a*)	Yes - CCC
2.6b	Evrard *et al.* (2016)	Yes - CCC
2.6c	Perry *et al.* (2016)	Yes - CCAL
2.7	Dalla Longa *et al.* (2019)	Yes - CCAL
2.8	Choi *et al.* (2008)	Yes - CCC
2.9a	Gilliéron & Kourta (2010)	Yes - CCC
2.9b	Choi *et al.* (2014)	Yes - CCC
2.10	Englar (2001)	Pending Email sent 24.02.19
2.12	Temmerman (2004)	Not contactable
2.13	Mukha *et al.* (2019)	Yes - CCC
2.14	Bose & Park (2018)	Yes - CCC
2.15	Piomelli & Balaras (2002)	Yes - CCC
3.1	Aram *et al.* (2010)	Yes
4.1	Dalla Longa *et al.* (2017)	CCAL
4.2	Dalla Longa *et al.* (2017)	CCAL
4.6	Dalla Longa *et al.* (2017)	CCAL
4.7	Pastoor *et al.* (2008)	Yes
4.8	Dalla Longa *et al.* (2017)	CCAL
4.16	Dalla Longa *et al.* (2017)	CCAL
4.21	Dalla Longa *et al.* (2017)	CCAL

Table 7.1: Permission for Figure Reproduction from Copyright Holder

16.02.19

Dear Intergovernmental Panel on Climate Change (IPCC),

I am completing my PhD thesis at Imperial College London entitled ‘Simulation and Feedback Control of Wake Dynamics for Vehicle Drag Reduction’.

I seek your permission to reprint, in my thesis a figure from ‘AR5 Climate Change 2014 – Mitigation of Climate Change’. The figure to be reproduced is figure 8.1.

I would like to include the figure in my thesis which will be added to Spiral, Imperial's institutional repository http://spiral.imperial.ac.uk/ and made available to the public under a Creative Commons Attribution-NonCommercial 4.0 International Licence (CC BY-NC).

If you are happy to grant me all the permissions requested, please return a signed copy of this letter. If you wish to grant only some of the permissions requested, please list these and then sign.

Yours sincerely,

Faron Hesse

Permission granted for the use requested above:

I confirm that I am the copyright holder of the figure above and hereby give permission to include it in your thesis which will be made available, via the internet, for non-commercial purposes under the terms of the user licence.

Signed:

Name:

Organisation:

Job title:

Dear Mr Hesse,

Thank you for your message concerning your request to reproduce IPCC material. Please be advised that we grant you non-exclusive permission to reproduce the figure in the manner as specified by you, provided that you acknowledge the original source with mention of the name of the IPCC report and a reference to the figure and publisher.

Please give the following credit line*:*

Figure 8.1 from Sims R., R. Schaeffer, F. Creutzig, X. Cruz-Núñez, M. D'Agosto, D. Dimitriu, M.J. Figueroa Meza, L. Fulton, S. Kobayashi, O. Lah, A. McKinnon, P. Newman, M. Ouyang, J.J. Schauer, D. Sperling, and G. Tiwari, 2014: Transport. In: *Climate Change 2014: Mitigation of Climate Change. Contribution of Working Group III to the Fifth Assessment Report of the Intergovernmental Panel on Climate Change* [Edenhofer, O., R. Pichs-Madruga, Y. Sokona, E. Farahani, S. Kadner, K. Seyboth, A. Adler, I. Baum, S. Brunner, P. Eickemeier, B. Kriemann, J. Savolainen, S. Schlömer, C. von Stechow, T. Zwickel and J.C. Minx (eds.)]. Cambridge University Press, Cambridge, United Kingdom and New York, NY, USA.

Thank you for your interest in the work of the IPCC.
Best regards,

Sophie Schlingemann

16.02.19

Dear International Energy Agency (IEA),

I am completing my PhD thesis at Imperial College London entitled ‘Simulation and Feedback Control of Wake Dynamics for Vehicle Drag Reduction’.

I seek your permission to reprint, in my thesis two figures from your ‘World Energy Outlook 2017’. The figures to be reproduced are (a) ‘Change in Global Oil Demand by Sector’ and (b) ‘Electric Car Fleet, 2016-2040’.

I would like to include the figures in my thesis which will be added to Spiral, Imperial's institutional repository http://spiral.imperial.ac.uk/ and made available to the public under a Creative Commons Attribution-NonCommercial 4.0 International Licence (CC BY-NC).

If you are happy to grant me all the permissions requested, please return a signed copy of this letter. If you wish to grant only some of the permissions requested, please list these and then sign.

Yours sincerely,

Faron Hesse

Permission granted for the use requested above:

I confirm that I am the copyright holder of the figure(s) above and hereby give permission to include it in your thesis which will be made available, via the internet, for non-commercial purposes under the terms of the user licence.

Signed:

Name:

Organisation:

Job title:

16.02.19

Dear Society of Automotive Engineers (SAE),

I am completing my PhD thesis at Imperial College London entitled ‘Simulation and Feedback Control of Wake Dynamics for Vehicle Drag Reduction’.

I seek your permission to reprint, in my thesis two figures from a 2014 publication titled ‘The Aerodynamics Development of the New Nissan Qashqai’. The figures to be reproduced are figures 5 and 18 of the publication.

I would like to include the figures in my thesis which will be added to Spiral, Imperial's institutional repository http://spiral.imperial.ac.uk/ and made available to the public under a Creative Commons Attribution-NonCommercial 4.0 International Licence (CC BY-NC).

If you are happy to grant me all the permissions requested, please return a signed copy of this letter. If you wish to grant only some of the permissions requested, please list these and then sign.

Yours sincerely,

Faron Hesse

Permission granted for the use requested above:

I confirm that I am the copyright holder of the figures above and hereby give permission to include it in your thesis which will be made available, via the internet, for non-commercial purposes under the terms of the user licence.

Signed:

Name:

Organisation:

Job title:

17.02.19

Dear American Society of Mechanical Engineers (ASME),

I am completing my PhD thesis at Imperial College London entitled ‘Simulation and Feedback Control of Wake Dynamics for Vehicle Drag Reduction’.

I seek your permission to reprint, in my thesis a figure from the publication ‘Numerical Study of the Flow Around a Bus-Shaped Body’ found within your 2003 Journal of Fluids Engineering. The figure to be reproduced is figure 10 of the above publication.

I would like to include the figure in my thesis which will be added to Spiral, Imperial's institutional repository http://spiral.imperial.ac.uk/ and made available to the public under a Creative Commons Attribution-NonCommercial 4.0 International Licence (CC BY-NC).

If you are happy to grant me all the permissions requested, please return a signed copy of this letter. If you wish to grant only some of the permissions requested, please list these and then sign.

Yours sincerely,

Faron Hesse

Permission granted for the use requested above:

I confirm that I am the copyright holder of the figure above and hereby give permission to include it in your thesis which will be made available, via the internet, for non-commercial purposes under the terms of the user licence.

Signed:

Name:

Organisation:

Job title:

24.02.19

Dear Society of Automotive Engineers (SAE),

I am completing my PhD thesis at Imperial College London entitled ‘Simulation and Feedback Control of Wake Dynamics for Vehicle Drag Reduction’.

I seek your permission to reprint, in my thesis a figure from a 2001 publication titled ‘Advanced aerodynamic devices to improve the performance, economics, handling and safety of heavy vehicles’. The figure to be reproduced is figure 6 of the publication.

I would like to include the figures in my thesis which will be added to Spiral, Imperial's institutional repository http://spiral.imperial.ac.uk/ and made available to the public under a Creative Commons Attribution-NonCommercial 4.0 International Licence (CC BY-NC).

If you are happy to grant me all the permissions requested, please return a signed copy of this letter. If you wish to grant only some of the permissions requested, please list these and then sign.

Yours sincerely,

Faron Hesse

Permission granted for the use requested above:

I confirm that I am the copyright holder of the figure above and hereby give permission to include it in your thesis which will be made available, via the internet, for non-commercial purposes under the terms of the user licence.

Signed:

Name:

Organisation:

Job title: